Polythermal glacier dynamics at Storglaciaren, Arctic Sweden, inferred using in situ geophysical techniques.

Gusmeroli, Alessio

Polythermal glacier dynamics at Storglaciären, Arctic Sweden, inferred using in situ geophysical techniques.

Alessio Gusmeroli

Submitted to the University of Wales in fulfilment of the requirements for the Degree of Doctor of Philosophy

Swansea University

June, 2010.

Polythermal glacier dynamics at Storglaciären, Arctic Sweden, inferred using in situ geophysical techniques.

Alessio Gusmeroli

Submitted in June, 2010, in accordance with the requirements for the degree of PhD
Swansea University, School of the Environment and Society

Abstract: Geophysical experiments were carried out to investigate spatial and temporal changes in the thermal regime and water-content of Storglaciären, a polythermal glacier located in Arctic Sweden. Thermal changes were observed by mapping the englacial transition between permanently frozen (cold) and temperate ice with a ground-penetrating radar in April 2009. The 2009 map was compared with surveys acquired in 1989 and 2001. The comparison shows that the thinning of the cold layer observed between 1989 and 2001 is still ongoing. The thinning rate in the two time windows analyzed is approximately similar ($\sim$0.75 m/a). A volume calculation shows that the cold surface layer has lost one third of its volume in 20 years.

Cross borehole zero offset radar profiles were employed to profile at high resolution, radar wave speed and power to $\sim$100 m depth at three sites on the glacier. Radio wave speeds, interpreted in terms of ice water-content, show that water-content in the temperate ice of Storglaciären is low (<1%) and homogeneous with depth in the upper part of the temperate ice. An increase of water-content due to strain-heating in the deepest part of the surveys (>70 m) was observed. Spatial variability due to complex interactions between water-content generated at the close-off and water-content produced by strain heating was observed at the three sites.

Seismic refraction surveys were used to estimate seismic-wave attenuation using the spectral ratio method for energy travelling in the uppermost ice with an average temperature of approximately -1°C. Attenuation values were derived between 100 and 300 Hz using the P-wave quality factor, Q_P, the inverse of the internal friction. By assuming constant attenuation along the seismic line, mean Q_P was 6$\pm$1. Q_P varied from 8$\pm$1 to 5$\pm$1 from the near-offset to the far-offset region of the line, respectively. Since the wave propagates deeper at far-offsets, this variation is interpreted by considering the temperature profile of the study area; far-offset arrivals sampled warmer and thus more-attenuative ice.

DECLARATION

This work has not previously been accepted in substance for any degree and is not being concurrently submitted in candidature for any degree.

Signed ..... (candidate)

Date 08.09.2010

STATEMENT 1

This thesis is the result of my own investigations, except where otherwise stated. Where correction services have been used, the extent and nature of the correction is clearly marked in a footnote(s).

Other sources are acknowledged by footnotes giving explicit references. A bibliography is appended.

Signed ..... (candidate)

Date 08.09.2010

STATEMENT 2

I hereby give consent for my thesis, if accepted, to be available for photocopying and for inter-library loan, and for the title and summary to be made available to outside organisations.

Signed ..... (candidate)

Date 08.09.2010

ACKNOWLEDGEMENTS.

This thesis and the research I had been luck enough to undertake in the last three years would have not been possible without the guidance, the advices, the support, the enthusiasm and the strength of many people. First, I sincerely thank Tavi Murray, my supervisor who offered me the invaluable opportunity to start a PhD project in Glaciology. Tavi's guidance, enthusiasm and dedication to science were always a model to follow during these three years. Whether preparing a paper, a proposal, a thesis chapter or dragging boxes on a glacier, Tavi patiently and promptly worked with me and for this I will be always grateful to her.

Luckily for Tavi also other people's patience was proven by my incessant asking help. Most notably I thank Peter Jansson in Stockholm, Roger Clark in Leeds, Adam Booth, Bernd Kulessa and Brian Barrett in Swansea, Rickard Pettersson in Uppsala, Andy Aschwanden in Fairbanks and Heinz Blatter in Zürich. Peter Jansson welcomed me in Tarfala, introduced me to the vast knowledge acquired at Storglaciären and always helped during the field operations and proposals writing related to this project, he also gave me the great opportunity to contribute to the research related to the cold layer. Roger Clark allowed me to spend a period at the University of Leeds where I learnt from him about seismology. Although primarily a good friend, Adam Booth had also a crucial academic role since he taught me many aspects of geophysics and he shared with me uncountable hours fiddling with tangled cables in various glaciated areas. I also thank my examiners, Danny McCarrol and Francisco Navarro for reading, commenting and discussing my thesis with me.

The nicest things about six field seasons in three years is probably the amount of people from whom you can learn something while they help you, or you help them on the glacier. Whether together with me in Svalbard, Tarfala, Valtellina or Greenland I would like to thank Doug Benn, Daniel Hjelm and his family in Kiruna, Fabio Villa, Henrik Törnberg and everyone at the Tarfala Research Station, Christian Helanow, Tavi Murray, Benedict Reinardy, Riccardo Scotti, Matteo Fransci, Tatjana Enzinger, Jonathan McGovern, Laura Cordero Llana, Richard Gravelle, Bernd Kulessa, Christine Dow, Glenn Jones, Sam Doyle and Alun Hubbard.

Even back from the field friends were fundamental in these years. My flatmates in Swansea and the Swansea Glaciology Group represented a family with who laugh, share time, go for a surf and chat about life. Tim and Kilian especially deserve a mention because of the numerous surf-trips to the Gower and the many nice moments on the beaches around Swansea. Finally on a more personal thought, I want to thank my mum and dad for their love and support, my family, my cousins and friends back home in the valley.

Contents

List of Figures

List of Tables

List of Notation

Roman Symbols **Page**

T_w	Travelime in water (ns)	148
$\tan\delta$	Loss tangent	36
u	Number of observations in kriging	74
u_{cts}	Emergence velocity at the CTS (m a^{-}1)	190
$\mathcal{V}$	Cold ice volume (hm^3)	83
v	Propagation speed	38
v_i	Radio wave speed in ice (m ns^{-1})	32
v_i'	Radio wave speed in ice with the air component removed (m ns^{-1})	197
v_m	Bulk radio wave speed in the mixture (m ns^{-1})	197
v_P	Propagation speed of Seismic P waves (m s^{-1})	37
v_S	Propagation speed of Seismic S waves (m s^{-1})	37
v_{snow}	Radio wave speed in snow (m ns^{-1})	80
v_w	Radio wave speed in water (m ns^{-1})	148
W	Volumetric water-content (%)	8
W_{cts}	Volumetric water-content at the CTS (%)	190
w_i	weights in kriging interpolation	74
X	Antenna separation (m)	101
X_H	Borehole top distance (m)	112
x	Distance along signal propagation path (m)	157
Z^*	Value of the variable Z to be predicted by kriging	74
z	Depth (m)	101
z_{RTS}	Depth of the radar transition surface measured using T_{RTS} (m)	69
z_{CTS}	Depth of the cold temperate transition surface (m)	80
z_{snow}	Snow thickness (m)	80

Greek Symbols **Page**

α	Attenuation coefficient (m^{-1})	38
β'	Rate of change of melting point with pressure (K Pa^{-1})	23

List of Acronyms

CO	Common offset	1
CRIM	Complex Refractive Index Model	34
CTS	Cold temperate transition surface	12
GPR	Ground penetrating radar	1
MWS	Macroscopic water system	13
mWS	Microscopic water system	13
RES	Radio echo sounding	20
RTS	Radar transition surface	55
SNR	Signal to noise ratio	63
ZOP	Zero offset profiles	92

Chapter 1

Introduction

One of the main branches of research currently faced by Earth Scientists is to predict the future behavior of Earth's ice-masses such as ice sheets and glaciers. It has indeed been recognized that during the 20th century, glaciers and ice caps have experienced widespread mass losses and have contributed to sea-level rise [*Solomon et al.*, 2007]. Poorly understood components of glacier dynamics such as basal motion, thermal stratification and glacier-hydrology provide the strongest limitation in predictive glacier-flow modeling and hence quantification of sea-level rise [*Solomon et al.*, 2007; *Lemke et al.*, 2007; *Alley et al.*, 2008].

The research presented in this thesis explores, by the means of three different experiments, the use of geophysical techniques in evaluating glaciological dynamics of the polythermal glacier Storglaciären, Northern Sweden. First, a series of common offset (CO) ground penetrating radar (GPR) lines, were used to map the thermal structure of the entire ablation area of the glacier. Second, borehole radar techniques are applied to measure the glacier-ice water-content distribution with depth. Finally, the attenuation of seismic waves in the ice, a rarely explored property, is measured as a potential tool to monitor glaciers' hydrothermal regimes.

1.1 Motivation

Recent acceleration [*Zwally et al.*, 2002; *van der Wal et al.*, 2008], and increases in discharge [*Howat et al.*, 2007] of many outlet glaciers of the Greenland Ice Sheet have modified the conventional view of glacier-derived sea-level variations, previously attributed mainly to changes in ice-mass surface mass-balance, but now also associated with variations in ice-dynamics [*Parizek and Alley*, 2004; *Alley et al.*, 2008]. The cause of these speed variations is still poorly understood [*Alley et al.*, 2008] and this severely limits our ability to quantity accurately the glacier-derived contribution to sea-level rise [*Lemke et al.*, 2007; *Alley et al.*, 2008].

Even though great attention is focused on the ice sheets, due in part to their potential to alter ocean circulation patterns, the largest observed contribution to the sea level rise currently comes from rapidly retreating small, mountain glaciers [*Meier et al.*, 2007; *Hock et al.*, 2009]. Just as better understanding of ice-sheet dynamics can improve predictive scenario under different climates [*Alley et al.*, 2008], more accurate knowledge of small glacier dynamics will improve predictive sea-level changes and also predictive retreat scenarios, critical for countries (e.g. in the European Alps, Himalaya and Andes) where the glaciated land represents a significant resource due, for example, to their use for mountaineering and skiing-related tourism and hydroelectric power supply.

Polythermal glaciers [*Hutter et al.*, 1988; *Blatter and Hutter*, 1991; *Moore et al.*, 1999; *Pettersson et al.*, 2003] are typically found in the Arctic and constitute an important part of the Earth's cryosphere, being present in Greenland, Canadian Arctic, Svalbard, Scandinavia and in the high altitude regions of European Alps and Himalaya. These polythermal glaciers are characterised by a cold (below pressure melting point) surface layer covering a temperate (at pressure melting point) core (Figure 2.2c). The difference between cold and warm ice is crucial: the former does not contain free-water, whereas temperate ice can contain intra-crystalline water. Such water bodies are thought to strongly influence ice viscosity [*Duval*, 1977], a major control on glacier-flow [*Glen*, 1955; *Paterson*, 1994]. Warming of ice-masses

have been documented in Arctic Sweden [*Pettersson et al.*, 2003], in the European Alps [*Vincent et al.*, 2007] and in the Bolivian Andes [*Gilbert et al.*, 2010]. Since such changes in thermal structure provide direct evidence of glaciers' response to climate change [*Lemke et al.*, 2007], monitoring studies of thermal dynamics in glaciers are particularly required.

A considerable volume of research has been focused on the thermomechanics of polythermal ice masses [e.g. *Fowler and Larson*, 1978; *Fowler*, 1984; *Hutter et al.*, 1988; *Blatter and Hutter*, 1991; *Aschwanden and Blatter*, 2005, 2009]. From these studies, it is possible to observe how the difference between cold and temperate ice can be summarised in terms of the internal energy of the system [*Hutter et al.*, 1988]. In cold ice, surplus energy will warm up the ice, whereas in temperate glaciers such energy will melt the ice [*Hutter et al.*, 1988; *Blatter and Hutter*, 1991]. More recently, *Aschwanden and Blatter* [2009] simplified the computation using an enthalpy balance approach, defining ice as cold if a change in enthalpy leads to a change in temperature alone and as temperate if a change in enthalpy leads to a change in water content alone. One of the main sources of water in temperate ice is known to be the heat of deformation [*Paterson*, 1971; *Pettersson et al.*, 2004; *Aschwanden and Blatter*, 2005]. As strain heating increases with depth in glaciers [*Paterson*, 1971], an increase of water content with depth is currently theoretically predicted for polythermal glaciers [*Aschwanden and Blatter*, 2005, 2009], but this needs validation [*Aschwanden and Blatter*, 2005].

The rheological properties of ice are fundamental in understanding glacier-motion and glaciers response to climatic variations (Section 2.1). Many studies [e.g. *Hubbard et al.*, 2003; *Chandler et al.*, 2008] have stressed the fact that the lack of knowledge of spatial variations in rheologically important properties such as water content and crystal orientation currently greatly limit advances in ice-flow modelling. Water content particularly is thought to play a key role in glacier motion since laboratory studies suggest that the strain rate of ice triples between 0.01% and 0.08% water content [*Duval*, 1977]. Published examples of water content estimates using various techniques vary from 0 to 9% [*Pettersson et al.*, 2004], but often without assessment

of the associated uncertainities. Recently, *Endres et al.* [2009] proposed a new petrophysical mixture model as the means by which glacier-ice volumetric water content and size of the inclusions can be estimated from radar and seismic surveys. Such model converts joint measurements of radar and seismic speed into water content estimates. *Endres et al.* [2009] suggested that their model can be improved by including two additional parameters: radar and seismic attenuation in glaciers. These two parameters are still poorly explored in glaciology and there are no examples of radar or seismic wave attenuation estimates applied for understanding ice properties.

1.2 Thesis aims

The overall aim of this project is investigate polythermal dynamics at Storglaciären using in situ radar and seismic techniques. Polythermal changes at Storglaciären between 1989 and 2001 were listed in the 2007 fourth assessment report of the IPCC as additional evidence of warming in the Arctic [*Pettersson et al.*, 2003; *Lemke et al.*, 2007], it is essential to provide updated observations of these dynamics. Limiting factor in understanding thermal changes in polythermal glaciers is knowledge on ice water content [*Pettersson et al.*, 2004, 2007]. Radar and seismic techniques can be used to measure thermal changes [*Pettersson et al.*, 2003] and ice water content [*Murray et al.*, 2000a; *Navarro et al.*, 2005; *Endres et al.*, 2009].

It is therefore important to (i) understand the changes that occurred within the polythermal structure of Storglaciären in the last 20 years by introducing novel observations of its thermal structure; (ii) measure the vertical distribution of water with depth and provide input for future models of polythermal glacier dynamics and (iii) introduce novel in situ geophysical techniques to monitor glacier's temperature and water content. Aim (i) will be addressed by mapping the thermal structure of the glacier using radar surveys acquired in 2009, recent thermal changes will be evaluated by comparison with the previous surveys; (ii) will be addressed by measuring spatial variability of vertical profiles of water content at three different sites on the

glacier whereas (iii) will be accomplished by accurately describing relatively novel geophysical application for glaciology: cross borehole zero offset radar profiling and the spectral ratio method to obtain seismic attenuation estimates.

1.3 Thesis outline

This thesis is structured as eight Chapters including this one. Chapters 1-3 contain introductory material and literature reviews. Chapter 4-6 are result chapters, whereas Chapter 7 discusses the main results observed in the results chapters. Chapter 8 will list the conclusions of this study. The Chapters of this thesis are the following:

- *Chapter 2*: This chapter provides the glaciological basis of this thesis. Glacier flow, thermal structure and glacier hydrology are discussed. Storglaciären, the study area is presented in considerable detail.

- *Chapter 3*: This chapter reviews the use of the techniques applied in the thesis. Previous application of radar and seismic techniques in glaciology are discussed. Particular emphasis is given to those studies which analyzed the hydrothermal structure of glaciers using radar and seismic techhniqeus.

- *Chapter 4*: This chapter will address an experiment provide updated observations of the thermal structure of Storglaciären. Here a detailed datastet of radar profiles acquired during spring 2009 will be used to map the extent of the permanently frozen cold surface layer. Such map will be compared to previous surveys collected in 1989 and 2001, and such a comparison will be used to provide important insights on the recent thermal changes within an Arctic polythermal glacier.

- *Chapter 5*: In this chapter the first application of cross-borehole zero offset radar profiles in glaciology will be described and analyzed. The profiles were

collected during two consecutive summer campaigns in 2008 and 2009 at Storglaciären. Variations of radio wave speed with depth will be interpreted in terms of glacier-ice unfrozen water-content.

- *Chapter 6*: In this chapter seismic refraction experiments collected at Storglaciären in summer 2008 will be analyzed to derive value the P-wave quality factor Q in order to understand its potential to explore the hydrothermal properties of glaciers. Such a parameter has been suggested in literature as a potential tool to measure water-content and temperature of glaciers.

- *Chapter 7*: In this chapter the glaciological implications of the findings in the results chapters will be discussed. In particular the spatiotemporal characteristics of the cold layer thinning of Storglaciären will be analyzed by using mass balance and thermo-mechanical modelling. Additionally, the water content distribution with depth obtained from borehole radar surveys in 2008 will be compared to independently made calorimetry-derived water content estimates at the same location. Spatial variability of water content will also be discussed.

- *Chapter 8*: Summarizes the findings of the thesis and provides suggestions for further work.

Chapter 2

Hydrothermal state of glaciers

This chapter will discuss some of the glaciological basis of the research presented in this thesis. In the first section the way that glacier-ice deforms and moves will be introduced with special emphasis on the relationships between glacier-ice strain rate and the physical properties investigated in this thesis, namely water-content and temperature. The second part of this chapter will review the different polythermal structures found in ice masses whereas the third section will deal with previous water-content estimates in glaciers. The fourth and last section will introduce the glacier where the experiments presented in this thesis were collected: Storglaciären.

2.1 Glacier flow

Glaciers movement can be caused by three processes: (*i*) internal deformation or *creep*, (*ii*) basal sliding and (*iii*) movement of ice coupled to a deforming bed [*Paterson*, 1994; *Benn and Evans*, 1998; *Hooke*, 2005]. The physical basis and theoretical treatment of the first will be discussed in this section, since the physical properties investigated in the thesis (water-content and temperature) inherently control the way how glacier-ice flows and deforms. The physical basis of all theoretical treatments of glacier flow is the relation between deformation rate and applied stress

[*Paterson*, 1994].

Polycrystalline aggregates of ice deform in a complex manner due to of several processes such as relative crystalline movement, dislocation, migration of crystal boundaries and dynamic recrystallization [*Paterson*, 1994]. A frequently mentioned simple expression for glacier-flow was firstly introduced by *Glen* [1955] who loaded polycrystalline ice in uniaxial compression. He observed that amount of deformation in ice initially decreases with time and subsequently stabilise on a steady-state behavior often called *secondary creep*. Such behavior can be described by relating the strain rate $\dot{\epsilon}$ to the applied stress σ [*Glen*, 1955]:

$$\dot{\epsilon} = \mathrm{A}\sigma^n, \tag{2.1}$$

where A is a viscosity parameter, often called the *rate factor*, that decreases as the ice becomes stiffer and n is an empirically determined constant often referred to as the stress exponent. The value of n is conventionally taken as 3 although it is known to vary from 1.5 to 4.2 [*Paterson*, 1994]. A is a measure of the viscosity of the ice. The viscosity depends on a number of factors. One of these factors is the temperature θ. By defining A_0 as the *standard* rate factor (independent of other parameters), the relationship between A and θ is described by [*Paterson*, 1994]:

$$\mathrm{A} = \mathrm{A}_0 \exp\left(-E_{\mathrm{creep}}/R\theta\right), \tag{2.2}$$

where E_{creep} is the activation energy for creep to occur in the ice, and R is the universal gas constant ($8.314 \mathrm{Jmol}^{-1}\mathrm{K}^{-1}$). The viscosity of ice is also influenced by small, intercrystalline water bodies whose contribution to the overall volume of ice is referred in this thesis as volumetric water-content, W (%). The dependance of the strain rate on the water content was found by performing mechanical tests on ice samples [*Duval*, 1977]: at constant applied stress the strain rate of ice increases linearly with water content. A plot of *Duval*'s [1977] experimental results is shown in Figure 2.1; by linear regression it thus follows that $\dot{\epsilon}$ is related to W:

$$\dot{\epsilon} = 2.8W + 1.4 \times 10^{-7} s^{-1}. \tag{2.3}$$

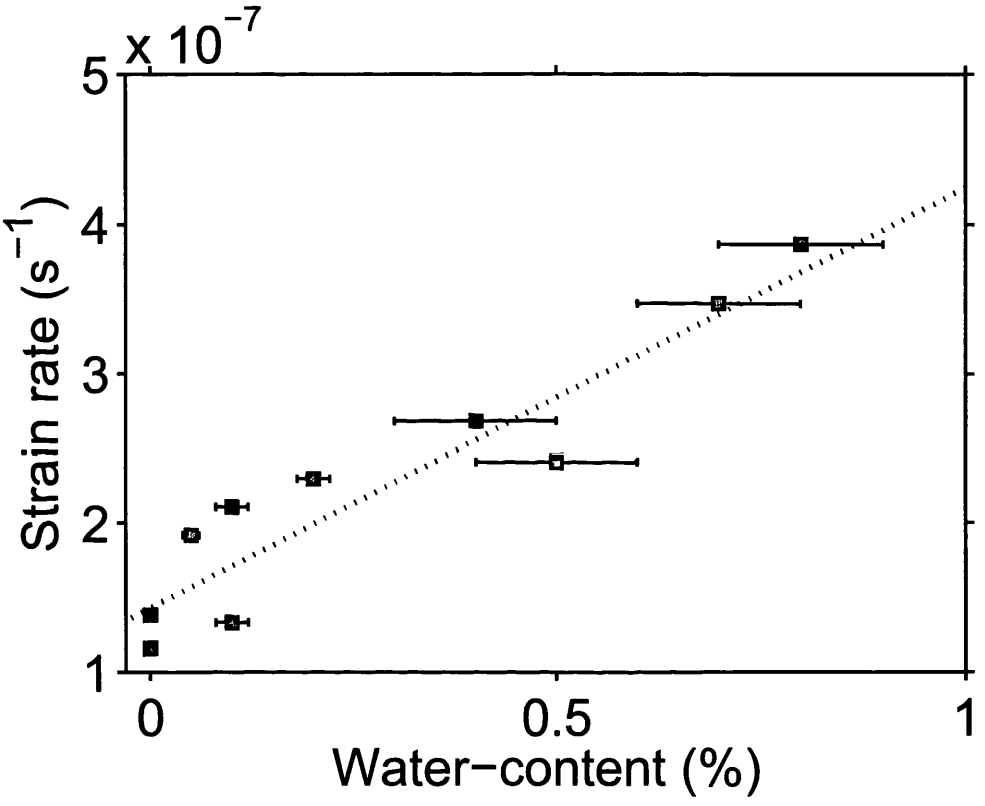

Figure 2.1: Variation in strain rate, $\dot{\epsilon}$ with water-content of the ice. Data reported by *Duval* [1977]. In the original figure [*Duval*, 1977] strain rate were reported in a^{-1}, here they are recalculated in s^{-1}. The linear regression illustrated by equation 2.3 is indicated.

Recently [*Chandler et al.*, 2008] used a relationship which combines equations 2.1, 2.2 and 2.3 and can be thus used as a generalised equation. This relationship allows strain rate to be calculated from the temperature, water content and follows a power-law dependence on stress:

$$\dot{\epsilon}_{ij} = A_0 \mathcal{E} \exp\left(-\frac{E_{\text{creep}}}{R\theta}\right) I_{II}^{n-1} \sigma_{ij} \ , \tag{2.4}$$

where $\dot{\epsilon}_{ij}$ and σ_{ij} are components ij of the strain rate and deviatoric stress tensors respectively, I_{II} is the second invariant of the deviatoric stress tensor and $\mathcal{E}$ is a dimensionless strain rate enhancement factor which include the effect of liquid water-content.

2.2 Polythermal glaciers

The temperature distribution in ice masses is intrinsically related to their movement. Using the equations outlined in section 2.1 it is possible to show that the deformation rate of ice is reduced by a factor of five when the temperature is reduced from -10°C to -25°C [*Paterson*, 1994]. Additionally a fundamental difference exists between the two simplest thermal states of glacier-ice: *cold* and *temperate* ice: the latter contains rheologically important intergranular water [*Raymond and Harrison*, 1975; *Duval*, 1977; *Fountain and Walder*, 1998]. *Paterson* [1994] listed four forms of temperature distributions (Figure 2.2)

- *Cold glaciers*: All glacier ice is below the pressure melting point (Figure 2.2a).
- *Warm-based glaciers*: Melting point is reached only at the bed (Figure 2.2b).
- *Polythermal glaciers*: Consist of regions of both temperate ice with temperature at the melting point, and regions of cold ice, with temperature below the melting point (Figure 2.2c).

- *Temperate glaciers*: All the ice is at the pressure melting point, only a thin surface layer is subject to seasonal variations in temperature and is therefore cold during the winter and the spring season (Figure 2.2d).

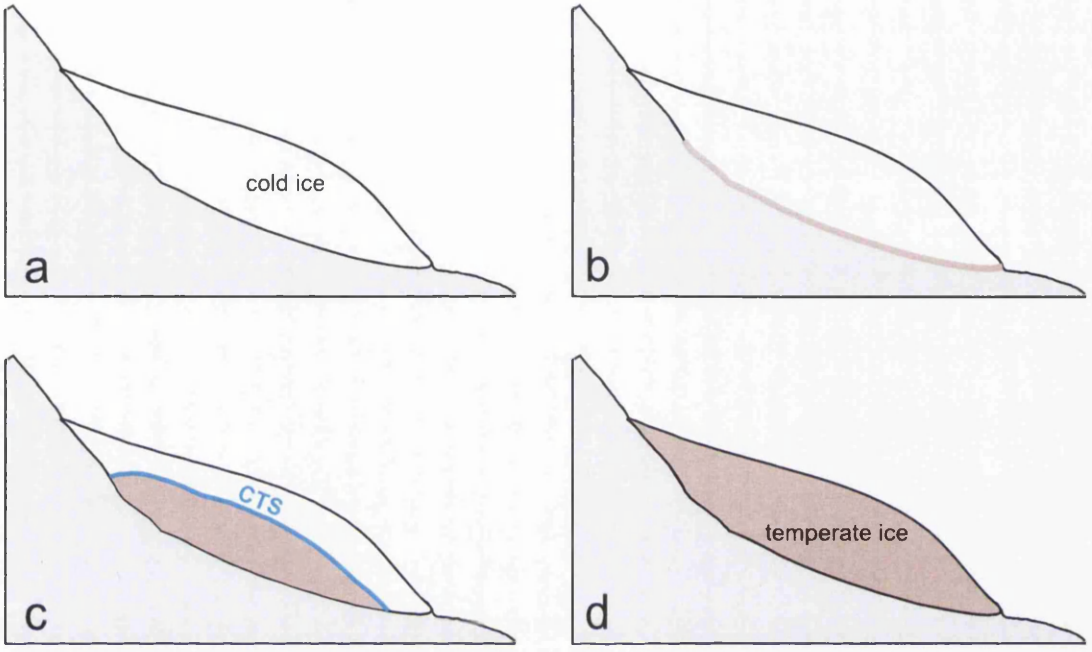

Figure 2.2: Forms of temperature distributions found in glaciers as listed by *Paterson* [1994]. (a) Cold, (b) Warm based, (c) Polythermal, (d) Temperate. The blue line marks the cold temperate transition surface CTS of a polythermal glacier.

Although the techniques used are applicable for any kind of glaciers, this research has focused on polythermal glaciers. The broad geographical (and thus climatical) distribution of such glaciers lead to a variety of thermal structures in the ice. Polythermal conditions are typically observed in Greenland [*Bull*, 1963; *Henry and White*, 1964; *Loewe*, 1966], Svalbard [*Dowdeswell et al.*, 1984; *Bamber*, 1987; *Kotlyakov and Macheret*, 1987; *Björnsson et al.*, 1996; *Murray et al.*, 2000b], the Himalaya and Karakorum mountains [*Maohuan*, 1990; *Gulley et al.*, 2009], European Alps [*Haeberli*, 1976; *Suter et al.*, 2001], Scandinavian mountains [*Schytt*, 1968; *Hooke et al.*, 1983], islands of the Canadian Arctic [*Blatter*, 1987; *Blatter and Kappenberger*, 1988; *Copland and Sharp*, 2001; *Irvine-Fynn et al.*, 2006], Yukon Territory [*Clarke and Goodman*, 1975], Alaska [*Rabus and Echelmeyer*, 1997] and in the Antarctic region [*Navarro et al.*, 2009].

Hutter et al. [1988] and *Hutter* [1993] stressed the importance of the englacial phase boundary that exists in polythermal ice masses. This interface, along which melting or freezing may occur is called the cold-temperate transition surface and is referred to as the CTS in this thesis (Figure 2.2c). Various types of CTS have been observed in glaciers and ice sheets. In figure 2.3 a modification of the figure originally proposed by *Blatter and Hutter* [1991] and subsequently modified by *Pettersson* [2004] is presented. This figure aims to describe different types of polythermal structure found in glaciers.

In particularly cold climates, such as the Canadian Arctic, almost no-melting occurs and glaciers are mostly cold except for a basal layer in the ablation area (Figure 2.3 a). Such basal sole is thought to generate from strain heating [*Hutter et al.*, 1988; *Blatter and Hutter*, 1991]. This kind of thermal structure is suspected also for the Khumbu Glacier in Himalaya as suggested by *Gulley et al.* [2009]. The occurrence of melting in the lower part of the accumulation area can generate the thermal structure depicted in Figure 2.3b. In such glaciers, the heat generated by the refreezing of meltwater within the snow-pack forms a temperate layer in an otherwise cold ice mass. This structure is suspected for the glacier Longyearbreen in Svalbard [*Gulley et al.*, 2009]. When spring melting is widespread in all the accumulation area the glacier in its upper part is entirely temperate (Figure 2.3c). However since the ice in the ablation area is not permeable to water, no percolation and refreezing can occur, thus the ice remains cold throughout the year. Polythermal glaciers such as the one shown in Figure 2.3 are observed in Svalbard [*Björnsson et al.*, 1996; *King et al.*, 2008] and in Scandinavia [*Hooke et al.*, 1983; *Holmlund and Eriksson*, 1989; *Pettersson et al.*, 2003]. In low-latitude, warmer climates (such as the European Alps), cold conditions are only observed in high-altitude regions [*Suter et al.*, 2001; *Vincent et al.*, 2007]. In these environments, glaciers are typically entirely temperate with the only exception of the uppermost part of the accumulation area (usually above 4000 m a.s.l. in the European Alps). The polythermal regime of Alpine glaciers is depicted in Figure 2.3d.

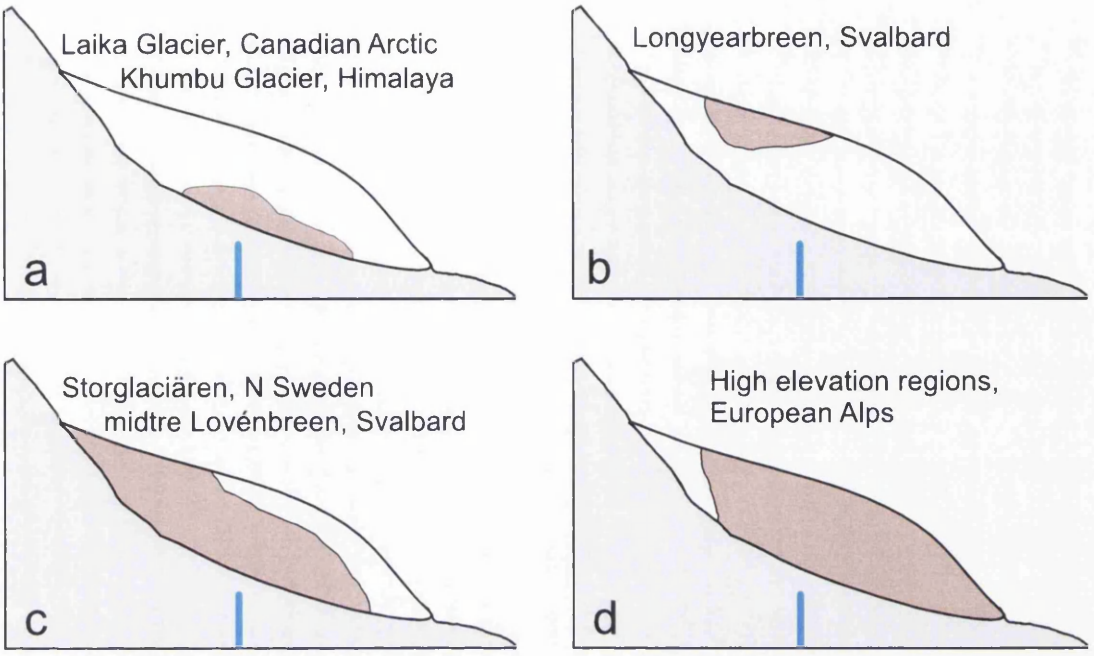

Figure 2.3: Various types of polythermal structures in glaciers after *Blatter and Hutter* [1991] and *Pettersson* [2004]. Cold and temperate ice regions parts are depicted in white and red respectively. The blue line indicate the approximate position of the average equilibrium line.

2.3 Water content in glaciers

Understanding the spatial distribution and the amount of liquid water within glaciers is essential because flow and thermal behavior of ice masses are directly linked to their englacial hydraulic system [*Duval*, 1977; *Fountain and Walder*, 1998; *Zwally et al.*, 2002; *Jansson et al.*, 2003; *Fountain et al.*, 2005]. Liquid water, generated from melting snow or direct input from rainfall, is routed downglacier by supraglacial streams. When such streams intersect vertical shafts (moulins), crevasses or fractures water can enter into the macroscopic englacial water system (MWS, Figure 2.4) mainly formed by a network of decimeter size, hydraulically connected fractures which can route macroscopic volumes of water to the bed of the glacier [*Fountain and Walder*, 1998; *Fountain et al.*, 2005].

Water in glaciers occurs also in a fundamentally different system unconnected from MWS: the microscopic water system (mWS, Figure 2.4). mWS is formed by small

(μm) water inclusions found in veins along three grain intersections, lenses on grain boundaries and in irregular shapes [*Raymond and Harrison*, 1975; *Nye*, 1989; *Mader*, 1992; *Fountain and Walder*, 1998]. Such water inclusions are primarily generated in the accumulation area where meltwater percolates in the porous firn and become part of the glacier-ice crystalline structure when pores closed for compaction [*Paterson*, 1971; *Lliboutry*, 1976; *Pettersson et al.*, 2004]. The mWS is primarily controlled by

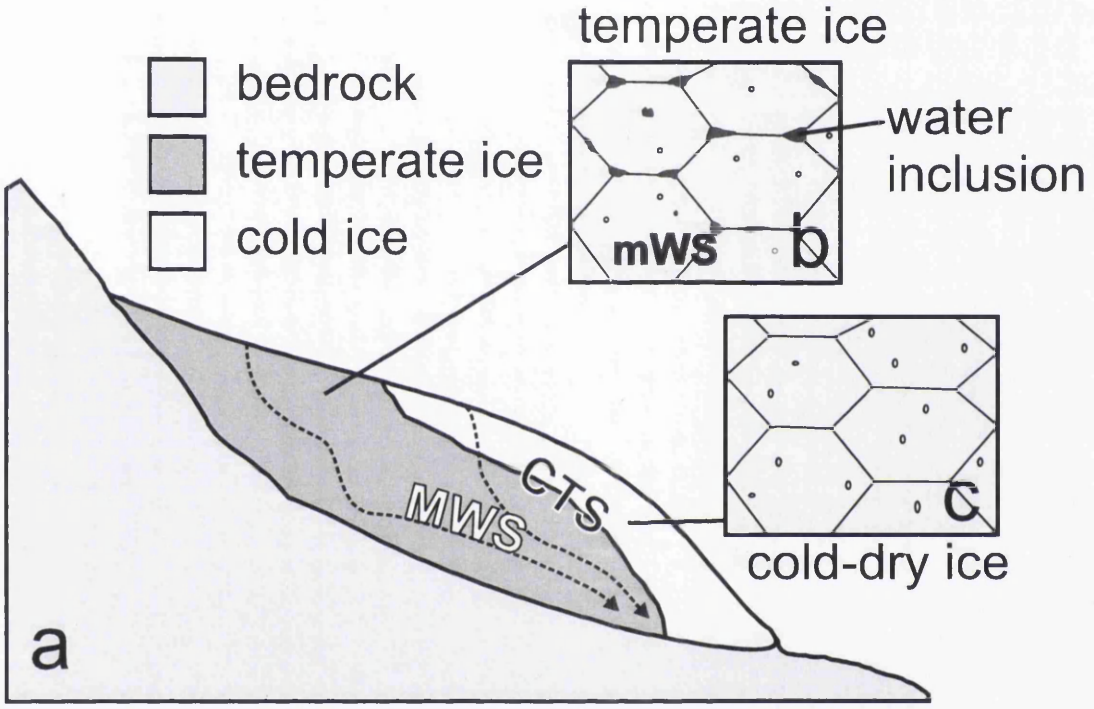

Figure 2.4: a) Sketch of a Storglaciären-type polythermal glacier with indication of terminology used in this paper. The macroscopic englacial water system (MWS) is indicated by the dashed lines whereas the microscopic water system (mWS) is shown in the inset (b). The cold temperate transition surface (CTS) is the englacial boundary which separates temperate ice (b) to the cold ice (c).

glacier ice temperature [*Paterson*, 1994] and is only present in those glaciers where ice temperature reaches the pressure melting point: temperate and polythermal glaciers. Recently *Aschwanden and Blatter*, 2009 treated glacier ice in polythermal glaciers as a continuous system dominated by entalphy: ice is defined as cold if a change in enthalpy leads to a change in temperature alone, as temperate if such change leads to a change in water content in mWS alone; across the CTS water

content in mWS jumps from zero values to positive volumetric percentages.

Values of water content quoted in literature suggest large variations (0-9%; *Pettersson et al.* [2004]). More specifically the estimates seem to depend sensitively on the methods used; for example measurements on cores tends to show low values (0-2%; *Vallon et al.* [1976]) while determinations using the backscattered power of radar signal (See Chapter 3 for details about the geophysical methodologies) give higher values, up to 9% [*Macheret and Glazovsky*, 2000]. Measurements using radar wave velocities (Chapter 3) seems to be the most effective method because they are in situ and they also provide the opportunity to obtain relatively high detailed vertical profile of the variations of the water content with depth [*Murray et al.*, 2000a]. Radar measurements can, however, overestimate water content since water features in MWS (cm to dm in size) are sampled in the measurements [*Murray et al.*, 2000a]. A list of water content estimates reported in literature is provided in Tables 2.1, 2.2 and 2.3.

2.4 Storglaciären

Storglaciären (67° 55'N, 18° 35'E) is a small polythermal valley glacier with a divided accumulation area located in the eastern side of Kebnekaise massif in Lappland, Arctic Sweden (Figure 2.5). Kebnekaise (2104 m a.s.l.) is the highest mountain in Sweden and is located in Lapland, about 150 kilometers north of the Arctic Circle; there are no higher peaks further north in Europe. It occupies the northern area of the Scandinavian Mountains, a mountain range that runs through the Scandinavian Peninsula. Storglaciären is 3.2 km long, the highest point is about 1730 m a.s.l. and the terminus is about 1120 m a.s.l. (Figure 2.6). In this region the melting season typically starts in June, reaches its peak in July and terminates at the end of September. Two cirque-type basins forming the accumulation area are thought to control two different portions of the flow: the major one is located in the northern part and the smaller one is to the south [*Jansson*, 1996].

Location	depth (m)	w(%)	Method	Reference
Saint Sorlin	2	0	C	*Dupuy* [1970]
	22	1	C	*Dupuy* [1970]
	55	1.2	C	*Dupuy* [1970]
Saint Sorlin	close off	0.6	C	*Vallon et al.* [1976]
	90	0.67	C	*Vallon et al.* [1976]
	110	0.7	C	*Vallon et al.* [1976]
	130	0.79	C	*Vallon et al.* [1976]
Abramov	h=32	0.49	CMP_r	*Macheret et al.* [1993]
	h=188	2.16	CMP_r	*Macheret et al.* [1993]
Falljökull	0	0.36	VRP_r	*Murray et al.* [2000a]
	2.5	3.77	VRP_r	*Murray et al.* [2000a]
	25	1.21	CMP_r	*Murray et al.* [2000a]
	30	4.26	CMP_r	*Murray et al.* [2000a]
	70	3.77	CMP_r	*Murray et al.* [2000a]
	93	3.04	CMP_r	*Murray et al.* [2000a]
	112-bed	0.15	CMP_r	*Murray et al.* [2000a]
Tsanflueron	h=39.8	1.18	CMP_r	*Murray et al.* [2007]
	h=39.8	3.9	CMP_r	*Murray et al.* [2007]
Tsanflueron	h=39.8	1.18	CMP_r	*Murray et al.* [2007]
	h=39.8	3.9	CMP_r	*Murray et al.* [2007]
	basal ice			

Table 2.1: Previous determination of water content in temperate glaciers. h: thickness of the layer with averaged water content w, w: water content, C: core-calorimetric, CMP: Common Mid Point, r: radio wave speed, VRP: vertical radar profile, s: seismic wave speed.

Location	zone	w(%)	Reference
Fritjovbreen	WLL	0.17	*Macheret et al.* [1993]
Hansbreen	WLL	1.68	*Macheret et al.* [1993]
Hansbreen	WML	0.56	*Macheret et al.* [1993]
	WLL	5.06	*Macheret et al.* [1993]
Hansbreen	WLL	0.39-3.9	*Moore et al.* [1999]
	WBI	0.8-1.5	*Moore et al.* [1999]
Fritdjovbreen	WLL	2.57	*Macheret and Glazovsky* [2000]
Fritdjovbreen	WLL	0.15	*Macheret and Glazovsky* [2000]
Hansbreen	WLL	1.66	*Macheret and Glazovsky* [2000]
Hansbreen	WML	5.29	*Macheret and Glazovsky* [2000]
Bakaninbreen	WLL	4.26	*Murray et al.* [2000b]
Hansbreen	spring	0.4	*Jania et al.* [2005]
Hansbreen	summer	2.1	*Jania et al.* [2005]
Bakaninbreen	WLL	1.77	*Murray et al.* [2007]
Bakaninbreen	WLL	1.4	*Endres et al.* [2009]
Hurd Glacier	-	0.1-1.6	*Navarro et al.* [2009]

Table 2.2: Previous determination of water content in polythermal glaciers using radio-wave speed. w: water content, WLL: warm lower layer, WBI: warm basal ice, WML: warm middle layer.

Location	zone	$w(\%)$	Reference
Fimbulisen	CTS	2.8	*Macheret and Glazovsky* [2000]
Tunabreen	CTS	2.9	*Macheret and Glazovsky* [2000]
Veteranen	CTS	3.6	*Macheret and Glazovsky* [2000]
Selfströmbreen	CTS	3.9	*Macheret and Glazovsky* [2000]
Mittag-Lefflerbreen	CTS	3.9	*Macheret and Glazovsky* [2000]
Nordenskjöldbreen	CTS	4.1	*Macheret and Glazovsky* [2000]
Chydeniusbreen	CTS	4.3	*Macheret and Glazovsky* [2000]
Hochstetterbreen	CTS	4.6	*Macheret and Glazovsky* [2000]
Formidablebreen	CTS	4.7	*Macheret and Glazovsky* [2000]
Wahlenbergbreen	CTS	5.2	*Macheret and Glazovsky* [2000]
Uversbreen	CTS	5.4	*Macheret and Glazovsky* [2000]
Vonbreen	CTS	5.5	*Macheret and Glazovsky* [2000]
Aavatsmarkbreen	CTS	5.9	*Macheret and Glazovsky* [2000]
Abrahamsenbreen	CTS	6.4	*Macheret and Glazovsky* [2000]
Eidenbreen	CTS	6.6	*Macheret and Glazovsky* [2000]
Fjortende Julibreen	CTS	7.1	*Macheret and Glazovsky* [2000]
Borebreen	CTS	7.2	*Macheret and Glazovsky* [2000]
Monacobreen	CTS	7.9	*Macheret and Glazovsky* [2000]
Kronebreen	CTS	7.9	*Macheret and Glazovsky* [2000]
Kongsvegen	CTS	9.1	*Macheret and Glazovsky* [2000]
Nansenbreen	CTS	9.1	*Macheret and Glazovsky* [2000]
Storglaciären	CTS	0.8	*Pettersson et al.* [2004]

Table 2.3: Previous determination of water content at the CTS of polythermal glaciers using radar backscatter strenght. w: water content.

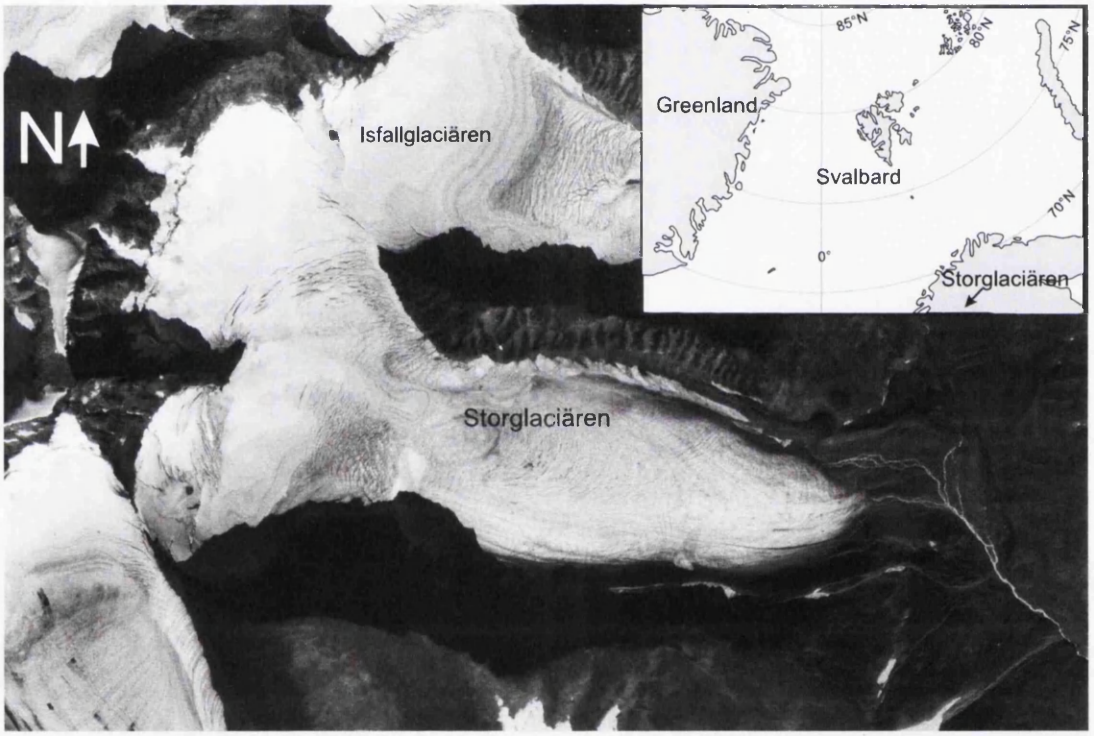

Figure 2.5: Aerial photo of Storglaciären and Isfallglaciären. Inset shows the geographical location of the study area.

Glaciological research at Storglaciären started just after the end of the second world war (see *Holmlund and Jansson* [2002] for further information). In 1945, the first mass balance measurements were performed on Storglaciären; since then the mass balance of the glacier (both winter and summer balance) has been measured annually with direct glaciological techniques. Radar techniques have been used for mapping the ice thickness, the bed topography and the hydrothermal structure of this glacier. *Björnsson* [1981] and *Eriksson et al.* [1994] used radio echo sounding (RES) to image the bed topography of Storglaciären; there are four over-deepened areas in the bed which would result in four lakes if the glacier were to melt away. The glacier has an average thickness of 95 m with a maximum thickness of 250 m in the upper part of the ablation area.

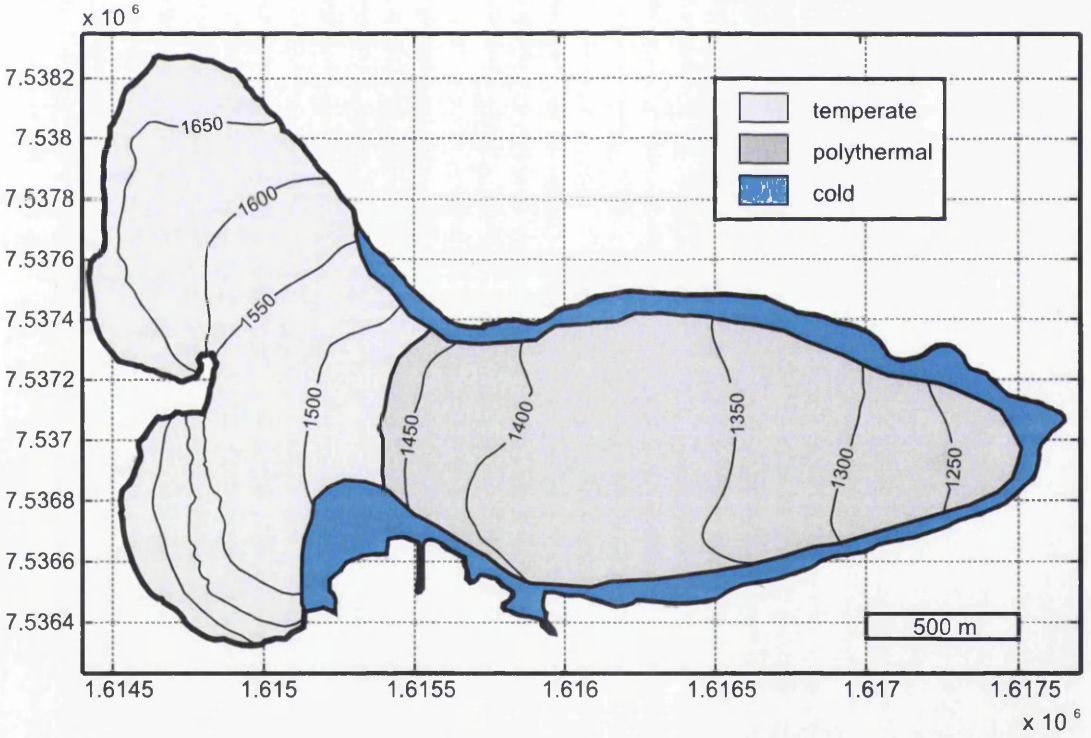

Figure 2.6: Map of Storglaciären with sketch of the thermal regime. Modified from *Holmlund and Jansson* [2002]. Coordinates are in Swedish grid.

The polythermal structure of the glacier was mapped using direct temperature measurements [*Schytt*, 1968; *Hooke et al.*, 1983] and GPR [*Holmlund and Eriksson*, 1989l; *Pettersson et al.*, 2003]. The glacier is temperate in most parts (~85%), except for

a cold surface layer in the ablation area. The cold layer is thickest at the terminus and at the margins (maximum thickness 60 m), while it is thinnest towards the centre of the glacier and towards the equilibrium line (Figure 2.6). The glacier is frozen to the bed close to its margins, over about 16% of its area [*Holmlund et al.*, 1996]. A comparison between comprehensive GPR surveys of the cold surface layer separated by 12 years (between 1989 and 2001) shows a thinning of the cold layer. ($\sim$ 22% of average thickness; [*Pettersson et al.*, 2003]). An increase of 1°C in winter air temperature since the mid-1980s was thought to be the cause of the observed thinning of cold surface layer [*Pettersson et al.*, 2007]. The thickness of the cold surface layer also contrasts whith that of nearby glaciers: on Mårmaglaciären, located 20 km north-east of Storglaciären and with the same shape and size, 27% of the ice is cold based and the 40% of its volume consists of cold ice; the difference in the proportion of cold ice is related to the glacier mass balance turnover. Mårmaglaciären has a thinner insulating snow cover and has a lower ablation rate than Storglaciären [*Holmlund et al.*, 1996].

The water-content at the cold-temperate transition surface (CTS) is typically low, less than 1% in an area close to the equilibrium line [*Pettersson et al.*, 2004]. Spatial variations in water-content at the CTS were also observed, showing a distinct pattern with higher values in the northern side of the glacier [*Pettersson et al.*, 2004]. This variability is believed to be a consequence of ice originating from two different cirques having different properties [*Pettersson et al.*, 2004]. Observations of the hydraulic state of Storglaciären are, however, limited to the CTS and the water-content distribution with depth is still unknown. *Aschwanden and Blatter* [2005] quantified the meltwater production due to strain heating along the kinematic centre line of the glacier; they predict that this source is important, especially near the bed in the ablation area, where they calculate water-contents greater than 1%.

2.5 Thermal structure of Storglaciären

This thesis will investigate the hydrothermal structure of Storglaciären using geophysical experiments acquired during three subsequent field-seasons: summer 2008, spring 2009 and summer 2009. Since the propagation of geophysical signals is an indirect method of imaging the glacier subsurface, often additional evidence, other than geophysics, are required to strenghten the glaciological interpretation of geophysical surveys. For this thesis an important additional dataset was the glacier-ice temperature distribution with depth provided by Dr. Rickard Pettersson (Uppsala University) and Prof. Peter Jansson (Stockholm University).

Temperature profiles were available for a thermistor string located in the upper ablation area of the glacier, at the altitude of $\sim$ 1350 m (Figure 2.7). That string was installed to monitor changes of the thermal state of the glacier over time. The vertical temperature distribution was obtained using 18 RTI Electronics Inc. ACCU-curve (ACCX-003) thermistors spaced 2 m apart to a depth of 18 m and a 0.5-m separation below 18 m. When the thermistor string was installed, the deepest thermistor had a depth of 29.5 m. The absolute depth for the thermistors changed over time due to ablation at the surface. Traditional ablation readings of a stake placed next to the thermistor string were done on a semi-weekly basis during the melt season to monitor these depth changes.

Glacier-ice temperatures were acquired and processed in the same manner described in *Pettersson et al.* [2003] and *Pettersson et al.* [2004] by Rickard Pettersson. The accuracy of the temperature data is $\pm$ 0.05°C [*Pettersson et al.*, 2003, 2004]. Two temperature profiles were available. The first one (Figure 2.7b dashed line, white cicles) was acquired on the 21^{th} of July 2008 when the borehole radar surveys discussed in Chapter 5 were acquired. The second profile (Figure 2.7b solid line, black cicles) was from the 14^{th} of April 2009 when the surface radar lines discussed in Chapter 4 were collected. The seismic refraction experiments illustrated in Chapter 6 also refer to the temperature profile acquired in July 2008. The thermal structure of the glacier at this location was firstly presented in *Gusmeroli et al.* [2010a] and

Gusmeroli et al. [2010b].

Glacier-ice temperatures in the upper 7 m of the ice column were directly influenced by the air temperatures since the summer profile (Figure 2.7b dashed line, white cicles) shows higher values than the spring profile (Figure 2.7b dashed line, white cicles). At the depth of 10 m however the two profiles have the same value and there is no difference between the two profiles at greater depth (Figure 2.7b). The thermal structure is polythermal with an upper layer of cold ice overlying a temperate lower layer, however, this interpretation requires the definition of the melting point temperature which varies with depth in a glacier and can be written as [*Paterson*, 1994]:

$$\theta = \theta_0 - \beta' P, \tag{2.5}$$

where θ_0 is the triple-point temperature of water, $\beta' = 9.8 \times 10^{-8}$ K/Pa is the change of melting point with pressure, P, [*Paterson*, 1994]. By using equation 2.5 on the range of depth sampled by the thermistors in Figure 2.7 we obtain that the pressure melting point at 30 m differs from θ_0 of only 0.01 K: well lower than the accuracy of the measurements. It thus follows that the CTS was defined on the first thermistor including the melting point in its accuracy range. For the summer 2008 temperature profile the value of 0.05 ± 0.05°C was reached at 21 m; the same value was observed in the spring 2009 dataset The position of the CTS and thus cold layer thickness did not change over time from summer 2008 to spring 2009.

2.5.1 Changes in the cold surface layer of Storglaciären

The first observations of the temperature distribution of Storglaciären were collected by Prof. Walter Schytt by installing four thermistors at depths in 1965 [*Schytt*, 1966]. The temperature profiles collected at the time revealed that the glacier was not isothermal, a temperature gradient was discovered and the observation that glacier-ice temperature at depth remain stable over short period of time was made (Figure 2.8, [*Schytt*, 1966]). After these pioneering discoveries the temperature measurements were intensified at more location and results revealed that the ice temper-

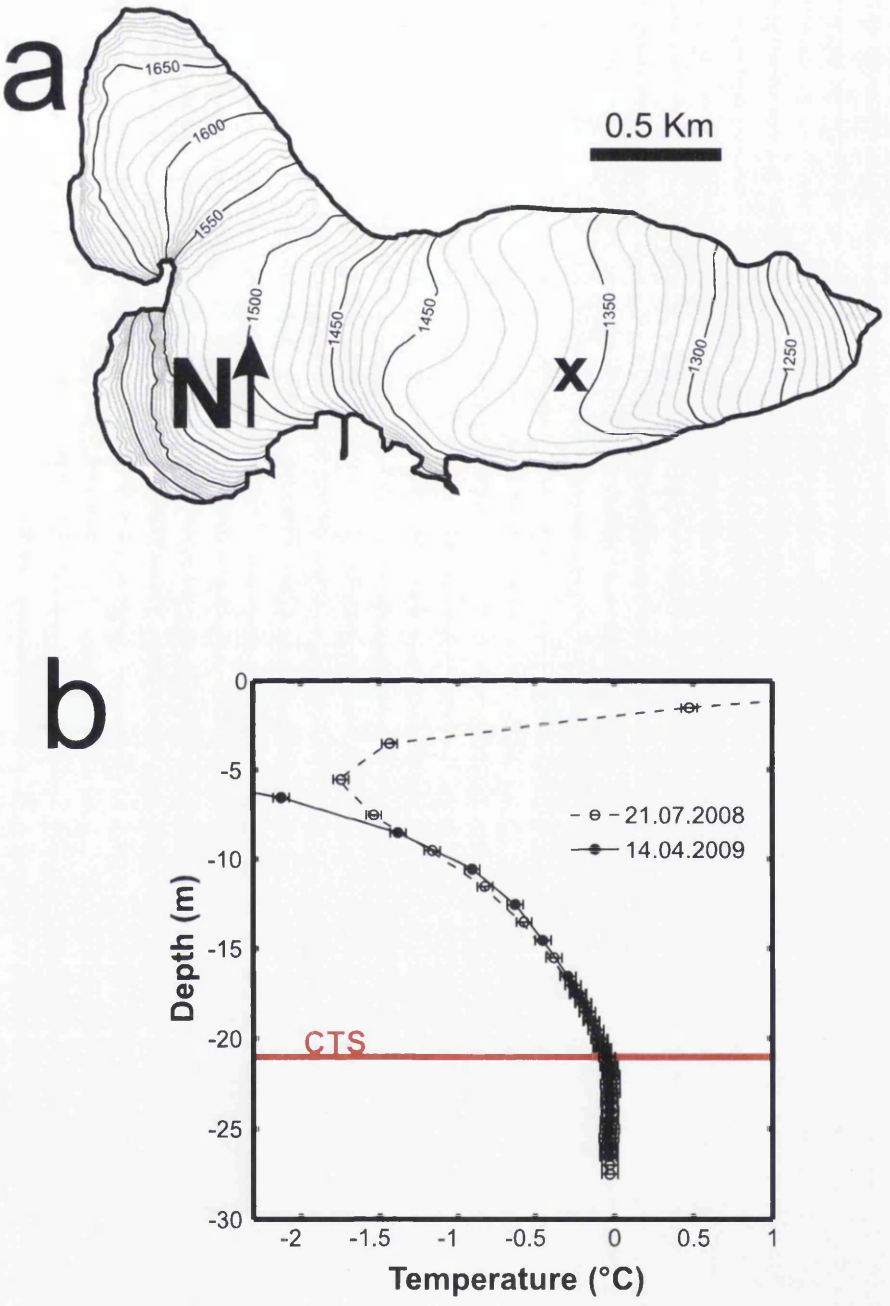

Figure 2.7: (a) Location map of the thermistor string located in the upper ablation area of the glacier. (b) Temperature profile with depth collected from the thermistors on the 21^{st} of July 2008 (White circles, dashed line) and on the 14^{th} of April 2009 (Black circles, solid line). The position of the CTS for the two temperature profiles is indicated by the horizontal line

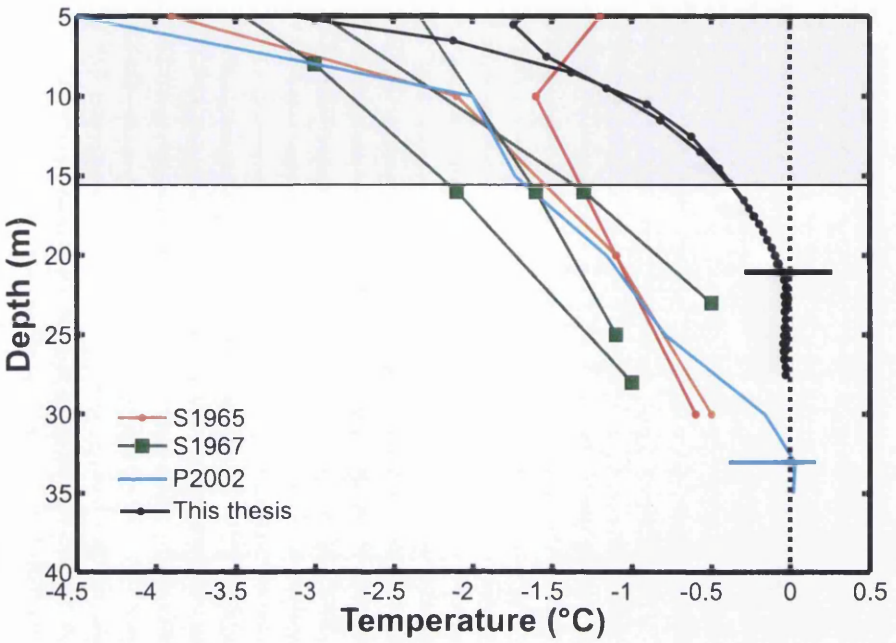

Figure 2.8: Ice temperature profiles at different locations at Storglaciären. The grey area marks the upper 16 meters of the ice column. In this area ice temperature is affected by air-temperature's fluctuations [*Schytt*, 1968]. S1965 were collected in May and November at 1350 m [*Schytt*, 1966]. S1967 are mean annual values from June 1966 to June 1967 from *Schytt* [1968]. P2002 is the temperature profile extracted from *Pettersson et al.* [2003]. Temperature profiles for the year 2009 used in this thesis are also indicated. The horizontal lines indicate the CTS in *Pettersson et al.* [2003] and in this thesis [*Gusmeroli et al.*, 2010a]. The dotted line indicates the melting point.

ature at the depths of 2, 4 and 8 meters is affected by air-temperature fluctuations [*Schytt*, 1968]. Spatial variations in ice temperature with depth were also observed (Figure 2.8) and the idea that a positve temperature gradient with depth could lead to a polythermal structure arose [*Schytt*, 1968].

Temperature measurments (Figure 2.8) suggested the presence of a perennially cold surface layer in the lower part of the glacier [*Schytt*, 1966, 1968]. Additional measurements by *Hooke et al.* [1983] confirmed the ideas in *Schytt* [1968]: temperature profiles from the central part of the tongue of Storglaciären showed a minimum at $\sim$ 4 m below the surface, below this depth the temperature increases to the pressure melting point at the depth of $\sim$ 40 m [*Schytt*, 1968; *Hooke et al.*, 1983]. At the same time radioglaciological works started focusing on the large dielectric contrast

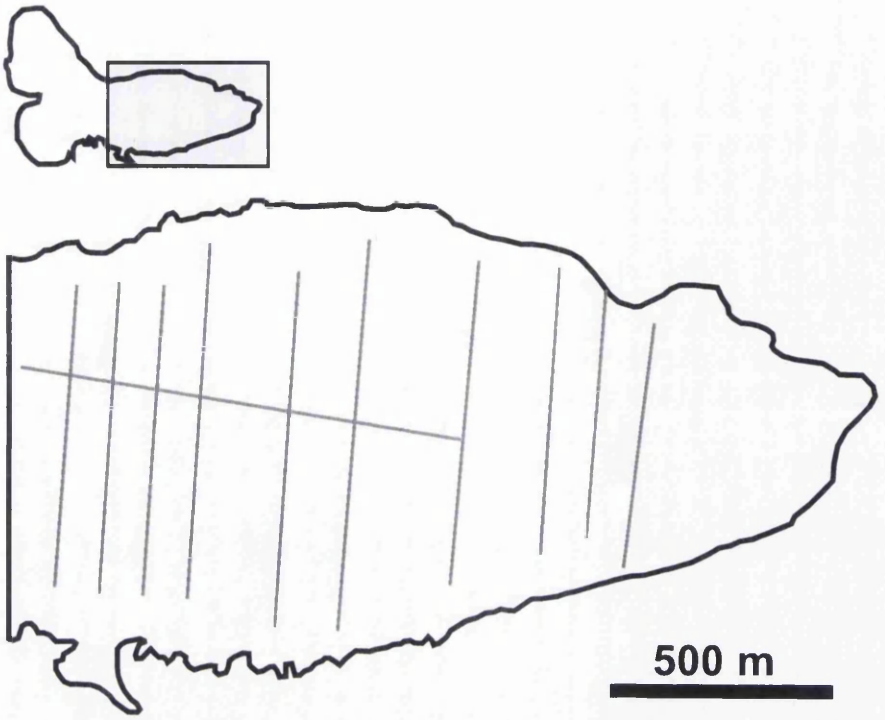

Figure 2.9: Radar profiles acquired in the ablation area of Storglaciären (grey box) in April 1989 [*Holmlund and Eriksson*, 1989] and April 2001 [*Pettersson et al.*, 2003]. These radar profiles were interpolated by *Pettersson et al.* [2003] in order to produce the maps showed in Figure 2.10.

between ice and water [*Smith and Evans*, 1972]; englacial water bodies were thought to be the cause of measurable retuns in RES at Storglaciären [*Walford et al.*, 1986] and at Variegated Glacier [*Jacobel and Anderson*, 1987].

The presence of a polythermal structure and the growing ideas that radio-echo sounding could detect water was successfully exploited by *Holmlund and Eriksson* [1989] with the first survey of the cold surface layer on Storglaciären. The idea in *Holmlund and Eriksson* [1989] was that a cold, water-free layer is underlain by a water-rich temperate layer could cause a detectable transition in the radargram. The radar profiles in the ablation area reported in *Holmlund and Eriksson* [1989] (Figure 2.9) have been subsequently repeated in April 2001 (Figure 2.9). The comparison between the two datasets (1989 and 2001) taken from *Pettersson et al.* [2003] is illustrated in Figure 2.10.

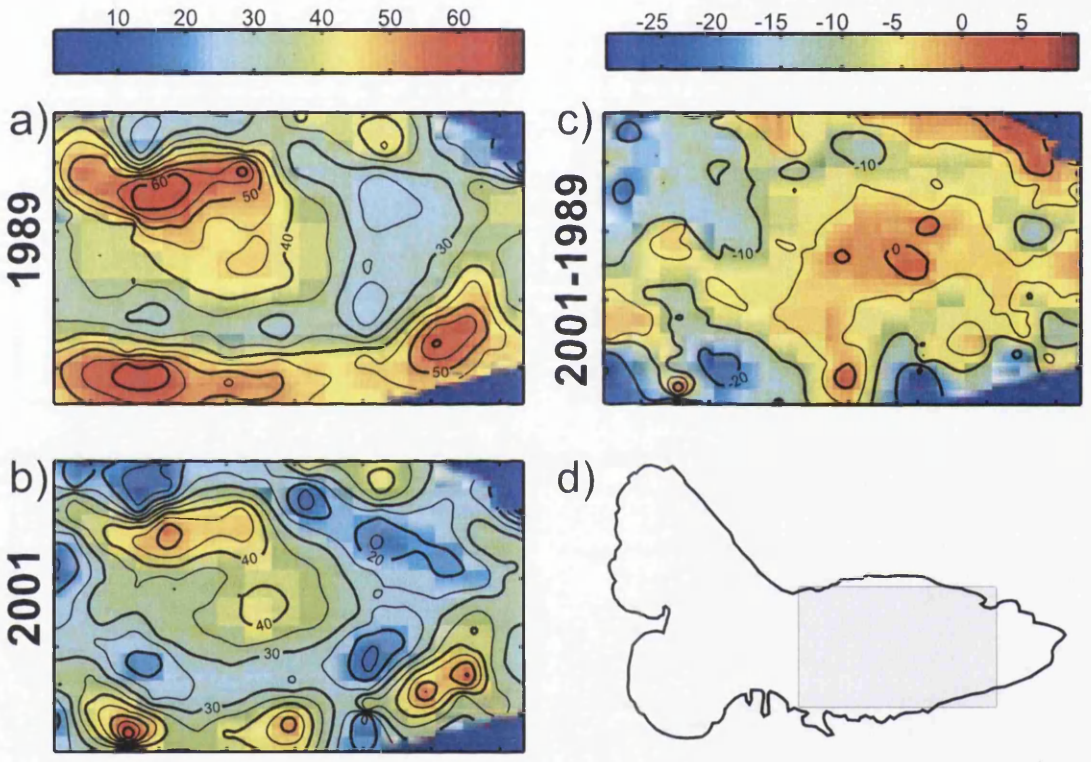

Figure 2.10: Maps of the cold layer thickness in the ablation area of Storglaciären as mapped in 1989 by *Holmlund and Eriksson* [1989](a) and 2001 by *Pettersson et al.* [2003](b). (c) Difference between the two maps. (d) Glacier outline with indication of the maps' location. This figure is modified from *Pettersson et al.* [2003]. Data courtesy of R. Pettersson.

2.6 Summary

In this chapter the glaciological background of the thesis has been discussed. This thesis will investigate temperature and water-content distribution within Storglaciären, because both are known to affect ice viscosity (Equations 2.2 and 2.3). Water content within glaciers is a poorly understood parameter which has been measured to vary between 0 and 9%. Storglaciären is a polythermal glacier, is thus composed by both cold (below freezing) and temperate ice. The thermal structure of Storglaciären varied between 1989 and 2001. In detail the cold, permanently frozen layer thinned by $\sim$ 22% on average during this period. Such thinning was connected to climate, but lack of knowledge of glacier-ice water-content does not allow a full understanding of polythermal glaciers' dynamics.

Chapter 3

Radar and seismic techniques for glaciology

This research uses artificially generated geophysical signals, such as electromagnetic and seismic waves, to explore and quantify glacier-ice properties. These techniques have been widely used by glaciologists in the last 40 years in order to measure ice thickness of ice sheets (e.g. *Drewry* [1983]), understand their basal conditions (e.g. *Blankenship et al.* [1986] and *Smith et al.* [2005]), and their hydrological regime [*Fountain et al.*, 2005]. Since direct investigations are logistically challenging and often simply *not possible* these methodologies are becoming part of the glaciological field science. A considerable amount of research has been undertaken to constrain ice water content using in situ geophysical techniques. Since the propagation speed and attenuation of radar and seismic waves is strongly dependent on water-content, estimates of geophysical variables (radar and seismic speed, radar and seismic attenuation) can be used to estimate water content in glaciers [*Looyenga*, 1965; *Paren*, 1970; *Endres et al.*, 2009].

The propagation speed of radio waves [*Macheret et al.*, 1993; *Bradford and Harper*, 2005; *Murray et al.*, 2000a, 2007], and seismic and radar waves [*Benjumea et al.*, 2003; *Navarro et al.*, 2005; *Endres et al.*, 2009] have been classically inverted in

literature to estimate the water-content in temperate and polythemal glaciers. Other studies (e.g. *Hamran et al.* [1996]; *Macheret and Glazovsky* [2000]; *Pettersson et al.* [2004]) exploited the internal layering in polythermal glaciers to quantify the water-content-dependent backscattered radar energy from the CTS. Although radar and seismic attenuation has been suggested as a powerful potential indicator of water-content [*Endres et al.*, 2009] there are no published examples which directly relate attenuation to water-content.

In this chapter background information about the geophysical techniques used in this study are provided. Firstly radar techniques will be introduced with special emphasis on the use of GPR in mapping glaciers' thermal structure and water content distribution. Secondly seismic techniques will be introduced in section two with a detailed discussion about the attenuation of seismic waves in glaciers.

3.1 Ground penetrating radar

Ground penetrating radar (GPR) is one form of RES operating in a range of frequency between 10 and 1000 MHz [*Davis and Annan*, 1989]. This technique provides a remote method to estimate the physical properties within glaciers. Comprehensive reviews about GPR are provided by *Davis and Annan* [1989], *Reynolds* [1997] and *Daniels* [2004]. GPR transmits electromagnetic waves from the glacier surface through the ice; such waves are partially reflected when they meet inhomogeneities in electrical properties within the ice or at the ice-bed interface; the reflected energy travels back to the surface and a receiver registers the signal.

Strong dielectric contrasts between ice, water, sediments of rocks make possible the identification of the thickness of ice [*Drewry*, 1983], the spatial extent of water-free cold ice in polythermal glaciers [*Pettersson et al.*, 2003], the hydraulic properties of the ice-bed interface [*Murray et al.*, 2008], the presence of water channels [*Stuart et al.*, 2003], crevasses and moulins within an ice sheet [*Catania et al.*, 2008] and the internal structure of glaciers [*Murray et al.*, 1997]. Table 3.1 provides a

Material	Speed, m/ns	Dielectric Coefficient
Air	0.300	1
Snow	0.194-0.252	1.2-2.0(dry)
		1.5-3.3(wet)
Cold dry ice	0.167-0.170	3-4
Warm ice	0.14-0.16	1.9-2.1
Warm ice W=6%	0.14	
Warm ice W=3.4%	0.15	
Warm ice W=1.5%	0.16	
Warm ice W0*1.5%	0.16-0.167	
Water	0.033	80
Sediment-rich ice	0.122	6
Permafrost	0.12-0.15	4-6.3
Till(porosity=0.15)	0.087	12
Till(porosity=0.3)	0.071	18
Shales and mudstone	0.09	5-15
Granite	0.13	4-6

Table 3.1: Propagation speeds and dielectric permittivities for Materials Common in the Glacial Environment (from *Murray et al.* [2000b], modified). Sources are: Bogorodsky1985, *Davis and Annan* [1989], *Macheret et al.* [1993], *Murray et al.* [2000a], *Annan* [1999].

comprehensive list of radio wave speeds commonly found in glacial environments.

Radar wave propagation through a medium is basically controlled by two principal properties: the magnetic permeability, μ, and dielectric permittivity, ε [*Davis and Annan*, 1989]. Therefore, the speed of propagation of electromagnetic waves in vacuum, c, is governed by equation 3.1 *Griffiths* [1999]:

$$c = \frac{1}{\sqrt{\mu\varepsilon}} \tag{3.1}$$

where μ and ε are the magnetic permeability and the dielectric permittivity in free space. Ice is non-conductive and non-magnetic, so that its magnetic permeability is very close to the value in free space; therefore the radio wave speed in ice v_i is in general governed by its dielectric permittivity and the equation 3.1 can be written

using the dielectric permittivty of ice , ε_i:

$$v_i = \frac{c}{\sqrt{\varepsilon_i}} \,. \tag{3.2}$$

3.1.1 Thermal state of glaciers from radar surveys

Radio-echo sounding (RES) and ground-penetrating radar (GPR) techniques, applied at a variety of radio frequencies, are commonly used in glaciology to explore ice-masses' interior and structure. Classic examples of comprehensive reviews about Radioglaciology are *Bogorodsky et al.* [1985] and *Dowdeswell and Evans* [2004]. The importance of radar techniques in glaciology is undisputable since they allow quick, effective and cheap estimates of the most important quantity in such science: the thickness and therefore the shape of the ice masses. The basic principle of the technique is that a transmitted electromagnetic signal travels within the ice and is reflected back to the receiver when a material with different electrical properties (e.g. water, air, rocks) is encountered. In a simple ice sheet example, the signal is radiated by the transmitter, travels througout the whole ice mass, bounces back from the ice-rock interface and is recorded at the receiver after travelling the entire thickness. Such process allows thickness measurements with little uncertainty. For example *Dowdeswell and Evans* [2004] quote the error of $\pm$ 3 m for 1000 m depth.

The most effective limiting factor in thickness estimates using RES is the signal absorption which is proportional to ice temperature [*Bogorodsky et al.*, 1985; *Dowdeswell and Evans*, 2004]. Dielectric absorption causes signal power loss, decreases penetration depth and can prevent ice-thickness estimates. Despite these facts, signal absorption is useful when mapping the thermal regime of polythermal glaciers. *Dowdeswell et al.* [1984] observed discrepancies between RES returns at different frequencies in Spitsbergen glaciers. The high frequency (620 MHz) showed shallower reflections than the low frequency (60 MHz) one. Further work [*Bamber*, 1987] suggested that such shallow reflections are internal reflecting horizons (IRH) originating at the CTS, the bounday between low-absorption areas (cold ice) and high-absorption areas (temperate ice) in polythermal glaciers. Such idea was then

confirmed by joint GPR and temperature observations in Svalbard [*Björnsson et al.*, 1996; *Ødegård et al.*, 1997; *Moore et al.*, 1999; *Murray et al.*, 2000b] and Scandinavia [*Holmlund et al.*, 1996; *Pettersson et al.*, 2003]: radar surveys on polythermal glaciers allow quantitative separation between cold and temperate ice. This is because the radio-response in both kinds of ice is different: high temperature and the presence of water in temperate ice causes increases in both signal absorption and scattering.

The accuracy of these measurement was discussed by *Ødegård et al.* [1997] who observed that the first change in the relative amplitude of the radar signals corresponded to the pressure-melting point isotherm with the accuracy of ± 2-4 m. Such precision was somewhat improved by *Pettersson et al.* [2003] at Storglaciären where using high frequency (345 and 800 MHz) radar the CTS was mapped with the accuracy of ± 1 m. Recent studies in Svalbard [*Murray et al.*, 2007; *King et al.*, 2008; *Barrett et al.*, 2008] and Switzerland [*Eisen et al.*, 2009] used the concept of cold surface layer in an estabilished way: scattering-free (transparent), with low-returned radar energy) regions in radargrams are interpreted as cold ice whereas scattering-rich zones are interpreted as temperate ice. However, *Brown et al.* [2009] using multiple radar frequencies imaged a transparent layer up to 50 m deep in the ablation zone of the temperate Bench glacier in Alaska. This evidence [*Brown et al.*, 2009] shows that radar surveys can only provide useful insights about the thermal structure of glaciers. Temperature measurements are still required to validate the radar-inferred temperature distribution.

3.1.2 Water content from radio-wave speed

The strong contrast between the electrical properties of water and ice provide a potential remote method to detect and map the hydrothermal state of polythermal glaciers and measure ice liquid water content. If glacier ice is assumed to be a two-component mixture with random inclusions of water with characteristic dimensions much less than the radar-signal wavelength, then a speed-depth profile can be considered equivalent to a water-content-depth profile; the radar speed of ice with

randomly distributed water inclusions has been modelled using three approaches: (see Fig.3.1):

The first approach is to consider the inclusions to be randomly distributed linear water bodies using Paren's mixture formula (*Paren* [1970]; *Smith and Evans* [1972]) which relate water content W to the dielectric permittivities of dry glacier ice, ε_i , and water, ε_w , the measured speed of propagation in the wet ice, v_i, and the speed of electromagnetic radiation in free space, c.

$$W = \frac{3}{\varepsilon_w}\left(\frac{c^2}{{v_i}^2} - \varepsilon_i\right) \tag{3.3}$$

The second approach introduced by *Looyenga* [1965] give higher values (Fig. 3.1) and makes no assumption about particle shape (e.g. *Barrett* [2007]). The Looyenga mixture formula [*Looyenga*, 1965] is the most commonly used in the previous work focused on the determination of water content using radio waves speed (e.g. *Macheret et al.* [1993], *Murray et al.* [2000a], *Benjumea et al.* [2003], *Murray et al.* [2007]):

$$W = \frac{(c/v_i)^{2/3} - \varepsilon_i^{1/3}}{\varepsilon_w^{1/3} - \varepsilon_i^{1/3}}. \tag{3.4}$$

Both equations are valid for speeds lower than 0.167 $\mathrm{m/ns^{-1}}$ which are typical speeds found in temperate wet glacier ice, higher values are associated either to dry cold ice or firn; typically, such speed values are ignored for the analyisis concerning water quantification using GPR. (*Macheret et al.* [1993], *Navarro et al.* [2005]).

Another method quoted in literature but less often used in glaciological applications is the Complex Refractive Index Methods (CRIM) introduced by *Greaves et al.* [1996]. This method is different from those cited above because it is independent of geometry and considers the fractional volume n_k and ε_k the dielectric constant of the k^{th} model and thus the relative proportion of each phases.

The generalized form of the CRIM model is:

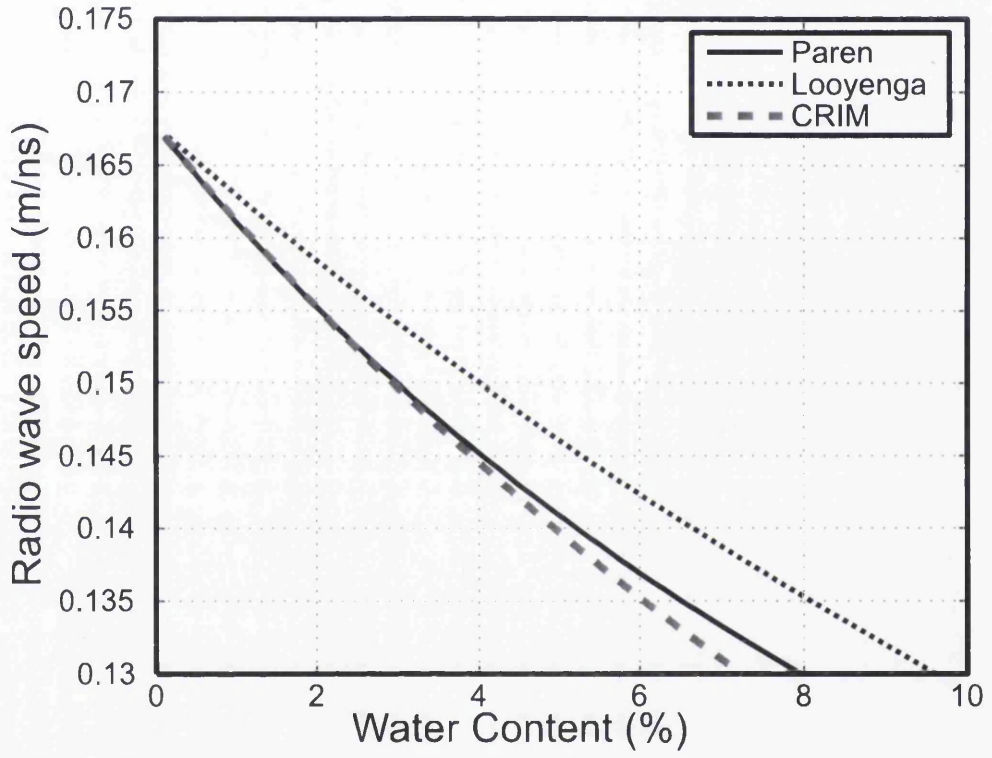

Figure 3.1: Radio wave speed vs. water content as given by Equations 3.4,3.3 and 3.6 using $\varepsilon_i = 3.2, \varepsilon_w = 80$ and $c = 3 \times 10^8 ms^{-1}$.

$$\frac{c}{v_m} = \sum_{i=1}^{k} n_k \sqrt{\varepsilon_k}, \tag{3.5}$$

where v_m is the bulk radio wave speed in the mixture. Using the model for the two-phase (ice and water) system of glacier ice where $n_1 = 1 - n_2$ the equation becomes:

$$W = \frac{c/v_i - \sqrt{\varepsilon_i}}{\sqrt{\varepsilon_w} - \varepsilon_i}. \tag{3.6}$$

3.1.3 Radar wave attenuation

A propagating radio wave loses energy when it travels within ice masses. In the case of a radio echo from the bottom of a glacier the returning echo is smaller in amplitude than the original radiation emitted by the transmitter at the surface. The total change in power of the signal during its travel to the reflector (e.g. the bedrock) and back to the receiver N_Σ can be described by [*Bogorodsky et al.*, 1985]:

$$N_\Sigma = N_G + N_R + N_\phi + N_D + N_A + N_P, \tag{3.7}$$

where N_G denotes geometrical spreading losses, N_R losses due to reflections from interfaces, N_ϕ changes in signal strength due to focusing effects, N_D losses due to scattering, N_A losses due to signal absorption in the ice, and N_P apparent losses due to polarisation. Signal absorption N_A is the key parameter since it can be related to variations in ice properties such as temperature and water content [*Endres et al.*, 2009]. Specifically it is possible to express the total signal attenuation using the specific absorption $N_A(\theta)$ [*Bogorodsky et al.*, 1985]:

$$N_\Sigma = -20\log(\mathcal{G}\lambda) + 20\log H + N_A(\theta)h + 40.7, \tag{3.8}$$

where $\mathcal{G}$ is the antenna gain coefficient, λ is the wavelength, H is ice thickness and $N_A(\theta)$ can be calculated by experimental data [*Bogorodsky et al.*, 1985]:

$$N_A = 8.68\frac{\omega}{2c}\sqrt{\varepsilon_i}h\tan\delta, \tag{3.9}$$

where ω, and $\tan\delta$ denote circular frequency and the loss tangent (the usual way to express the absorption of electromagnetic energy).

3.2 Seismic techniques

Exploration seismology uses artificially generated elastic waves to locate mineral deposits (including hydrocarbons, ores, water, geothermal reservoirs, etc.), archaeological sites and to obtain information about the geological composition of the ground and the physical properties of glaciers and ice sheets. The basic technique of seismic exploration consists of generating seismic waves and measuring the time required for the waves to travel from the source to a series of receivers (geophones), usually along a straight line. Knowledge on travel time is required to reconstruct the paths of the seismic waves.

Seismic sources generate several type of waves including two types of body waves termed *P-waves* known also as dilatational, longitudinal, irrotational or compressional waves; and *S-waves* called also shear, transverse or rotational waves; P-waves are longitudinal (motion in direction of propagation), S-waves are transverse (motion is perpendicular to the direction of propagation). Different propragation speeds are found for P and S waves, in detail P-waves are always faster than S-waves, the speed of both are described by the following equations [*Sheriff and Geldart*, 1995]:

$$v_P = \sqrt{\frac{(K + 2\mu_s)}{\rho}}, \tag{3.10}$$

$$v_S = \sqrt{\frac{\mu_s}{\rho}}. \tag{3.11}$$

where v_P and v_S are the speeds of P and S waves respectively, ρ is the density of the material, K and μ_S are the bulk modulus (often mentioned as modulus of incompressibily) and the rigidity modulus respectively. The value of K depends sensitively on porosity [*Sheriff and Geldart*, 1995] which is simply defined as the pore volume per unit volume; if we assumed temperate glacier ice as a two component mixture of ice and water with all pores filled by water the speed of seismic waves in wet glacier ice is therefore lowered by the presence of intergranular water bodies.

3.2.1 Seismic waves attenuation

The attenuation of seismic energy is usually quantified using the non-dimensional seismic quality factor Q, or its inverse, Q^{-1}, the internal friction. Q is a fundamental property of rocks and Earth-materials, and is defined by the fractional energy loss per cycle experienced by a propagating seismic wave [*Knopoff*, 1964; *Toksöz and Johnston*, 1981; *Sheriff and Geldart*, 1995]. High Q values (500–1000) are expected for non-attenuative materials such as massive crystalline rocks, and low Q values (10s) are typical for attenuative materials such as porous and/or fractured rocks. Although there are many definitions of Q in the seismological literature, in this thesis will be used the one provided by *Aki and Richards* [2002], which is the definition typically used in other glaciological studies [*Clee et al.*, 1969; *Bentley and Kohnen*, 1976]:

$$Q = \frac{\pi f}{\alpha v}, \tag{3.12}$$

where f, v and α are frequency, propagation speed and attenuation coefficient respectively. Q values in frozen rocks are very much higher than those observed in unfrozen rocks [*Spetzler and Anderson*, 1968; *Toksöz et al.*, 1979]. The degree of water saturation also influences seismic attenuation. In some cases Q values are known to be similar for dry and fully saturated materials, but are significantly lower for partial degrees of saturation [*Winkler and Nur*, 1982]; in fact partial saturation allows space for fluid squirt-flow (pressure-induced, intra-granular fluid flow) between and within fractures, microcracks on grain surfaces, and pore spaces [*Toms et al.*, 2007].

Only a few measurements of seismic attenuation are available in the glaciological literature. Comprehensive reviews of seismic attenuation studies in polar ice are also provided by *Smith* [1997, 2007]. Some workers measured seismic attenuation using time-domain analysis of the attenuation coefficient, α, [*Robin*, 1958; *Westphal*, 1965; *Jarvis and King*, 1993] whereas others [*Clee et al.*, 1969; *Bentley and Kohnen*, 1976]

Workers	Location	θ(° C)	Q_P	f (Hz)
Westphal, 1965	Blue Glacier	~ 0	129-172*	25000
Clee and others, 1969	Athabasca Glacier	~ 0	65	120 - 1000
Bentley and Kohnen, 1976	Byrd Station	-28	526-1667	136
Jarvis and King, 1993	Larsen Ice Shelf	-10 to -12**	50-160*	100 - 300***

Table 3.2: Examples of Q_P estimates in polar and alpine ice masses from previous studies. θ is ice temperature . * recalculated from published α using equation 3.12. ** temperature from *Reynolds* [1981]; *Vaughan and Doake* [1996]; *Smith* [1997]. *** recalculated from α in this frequency-range to facilitate comparison with this study.

used Q^{-1}. The results of this prior research show that the P-wave quality factor, Q_P, is generally higher for cold-ice ($Q_P \sim 500 - 1700$, Bentley and Kohnen, 1976) than that for temperate ice ($Q_P \sim 65$ at Athabasca Glacier; *Clee et al.* [1969]). This evidence is also supported by *Kuirowa* [1964], who conducted laboratory measurements of the internal friction in natural polycrystalline glacier-ice. He observed that Q_P increases (attenuation decreases) from low values ($Q_P \sim 40$) near the melting point to very high values (Q_P up to 1000) around -30°C. Despite this, it is very difficult to obtain a clear range of Q_P estimates in glacier-ice since previous workers measured attenuation over different frequency-ranges, using different methods, equations and assumptions. Table 3.2 shows a compilation of previous Q_P estimates (in some cases recalculated) from different glaciological settings.

In situ Q_P estimates are always made as effective attenuation ($1/Q_{\text{eff}}$) in the medium. These values are controlled by intrinsic effects such as material properties and also by apparent attenuation processes such as scattering from inclusions, heterogeneities, rough interfaces, and/or interference between direct arrivals and short-path multiples. Effective attenuation is related to intrinsic ($1/Q_{\text{int}}$) and apparent ($1/Q_{\text{app}}$) attenuation by the following relationship [*Spencer et al.*, 1982]:

$$\frac{1}{Q_{\text{eff}}} = \frac{1}{Q_{\text{int}}} + \frac{1}{Q_{\text{app}}}. \tag{3.13}$$

Modelling [*Dvorkin and Nur*, 1993] and observations [*Sams et al.*, 1997] of attenuation mechanisms show that seismic Q is frequency dependent when considered over

several orders of magnitude (e.g. 10^{-3} to 10^{4} Hz). However, other studies suggest that the frequency dependence is negligible [*Johnston et al.*, 1979].

3.3 Summary

In this chapter radar and seismic techniques and their application in glaciology were presented. Radar techniques have been used to map ice-thickness, temperature distribution and water content of glaciers. Seismic techniques measured ice-thickness, basal properties and subglacial till thickness. Radio wave speed is the most commonly applied method in inferring ice water-content, fewer studies have used seismic speeds for the same purpose. Radar and seismic wave attenuation represent potential parameters in measuring water-content.

Chapter 4

The cold surface layer of Storglaciären

Changes in thermal structure of Storglaciären were mentioned in the latest IPCC report [*Lemke et al.*, 2007] as an indicator of warming in the Arctic. Such changes were documented by mapping with ground penetrating radar (GPR) the depth of the cold temperate transition surface (CTS) of the glacier's ablation area in 1989 (Figure 2.10a [*Holmlund and Eriksson*, 1989]) and 2001 (Figure 2.10b [*Pettersson et al.*, 2003]). Further details about the thermal structure of Storglaciären and the previous cold layer maps are given in Section 2.5.1. The difference between the two GPR surveys shows an overall decrease of 8.3 m (22% of average thickness) of the CTS depth in 12 years (Figure 2.10c [*Pettersson et al.*, 2003]). Temporal variations in cold surface layer thickness are due to surface ablation and downward migration of the CTS [*Blatter and Hutter*, 1991; *Pettersson et al.*, 2003]. During the 12 years spanning the two surveys, the mass balance of Storglaciären was in equilibrium [*Holmlund and Jansson*, 1999], and so the observed decrease was explained by a decrease in downward migration of the CTS caused by a weak temperature gradient throughout the cold layer (e.g. warmer air temperature) [*Pettersson et al.*, 2003]. A small increase in average winter air temperature was suggested as the explanation of the observed changes [*Pettersson et al.*, 2003, 2007].

The maps in *Pettersson et al.* [2003](Figure 2.10) were obtained using 11 GPR CO lines. The number of samples used to interpolate the map was 152 in 1989 and 218 in 2001 (Figure 2.9). In this chapter a new denser dataset of 60 CO lines are used to obtain $\sim$ 5000 CTS depth estimates from which a new, highly-detailed, map of the cold layer of Storglaciären in 2009 was interpolated. This map will represent useful reference for future comparisons and will be compared to the previous map in order to provide updated observations of the cold surface layer dynamics.

4.1 Common offset (CO) GPR surveys

Common offset (CO) GPR surveys (Figure 4.1) can be employed to map ice-thickness and infer the thermal state of glaciers [*Murray et al.*, 2000a,b; *Pettersson et al.*, 2003; *King et al.*, 2008; *Eisen et al.*, 2009; *Brown et al.*, 2009]. CO surveys are undertaken by acquiring radar traces along a line keeping the distance between transmitting and receiving antennas constant. This way of surveying is particularly useful in qualitatively imaging subsurface features since, for example, returns from an horizontal planar reflector beneath the survey line will occur at the same travel time throughout the whole profile, provided the subsurface velocity remains constant (e.g. arrivals 1 and 2 in Figure 4.1). In the same way, if the position of the reflector changes, returns will occur at higher (arrivals 3 and 4 in Figure 4.1) or lower travel-times depending on wether the reflector is shallower or deeper respectively.

In this survey GPR data were acquired with a commercially available *Måla Geoscience* GPR system with 100 MHz antennas. Forty-five CO GPR profiles (grey lines in Figure 4.2) were collected by pulling the radar with snow scooter on the 11^{th} of April 2009. Coverage was increased by acquiring 15 additional profiles on skis on the 18^{th} of April (dotted lines in Figure 4.2). The additional profiles were located in the northern side of the ablation area where occurrence of small crevasses or steep topography did not allow surveying with snow scooters. Surveys location were acquired using a Garmin handheld GPS connected to the radar system. The

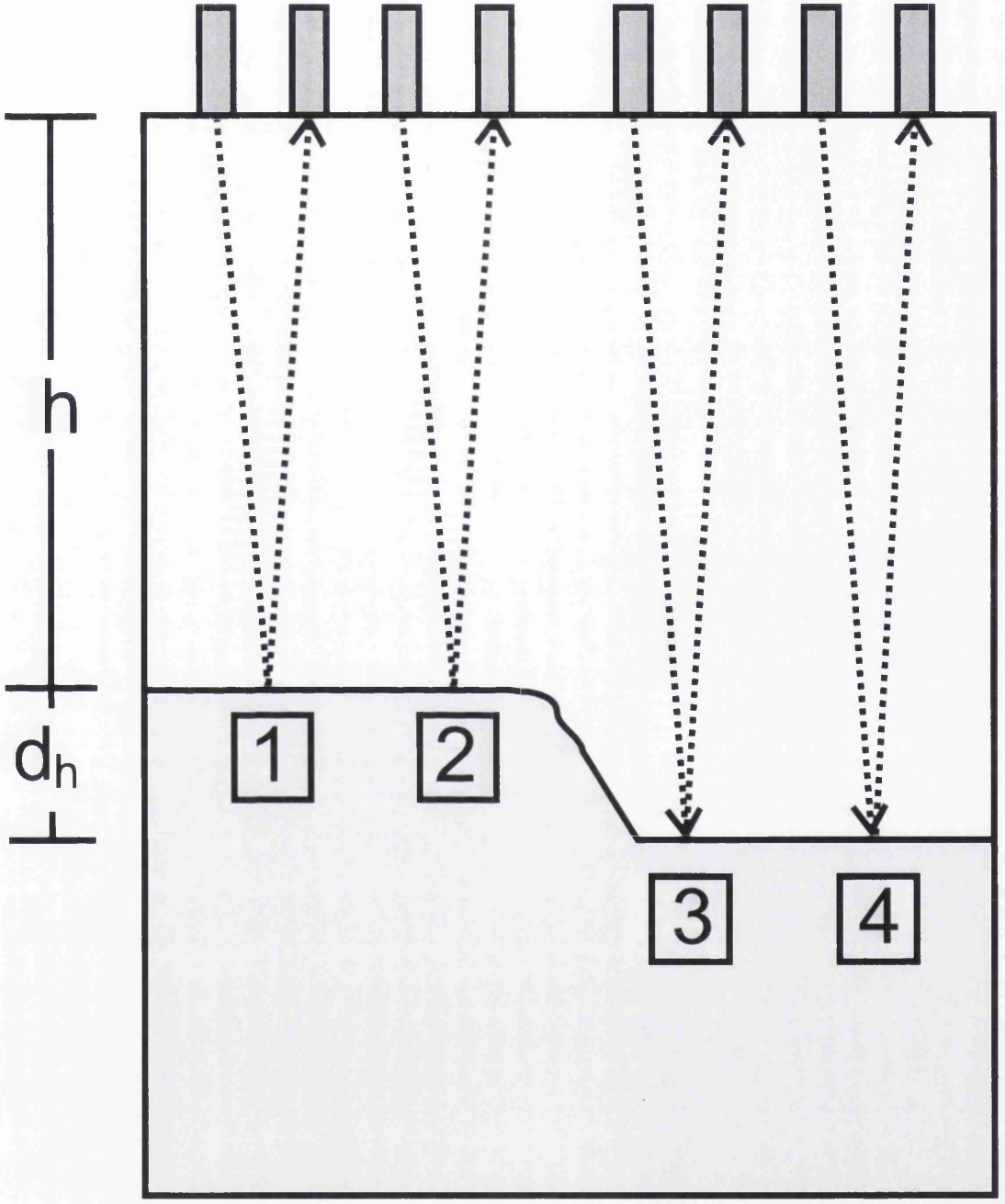

Figure 4.1: (a) Schematic of a common offset radar survey over a layered subsurface. The upper and lower layer have distinct dielectric properties, and thus radar wave speeds. The interface between the two layers represents a reflector which generates radar returns recorded in the radargram.

horizontal accuracy was ± 5 m. The GPS system stored the position of radar trace

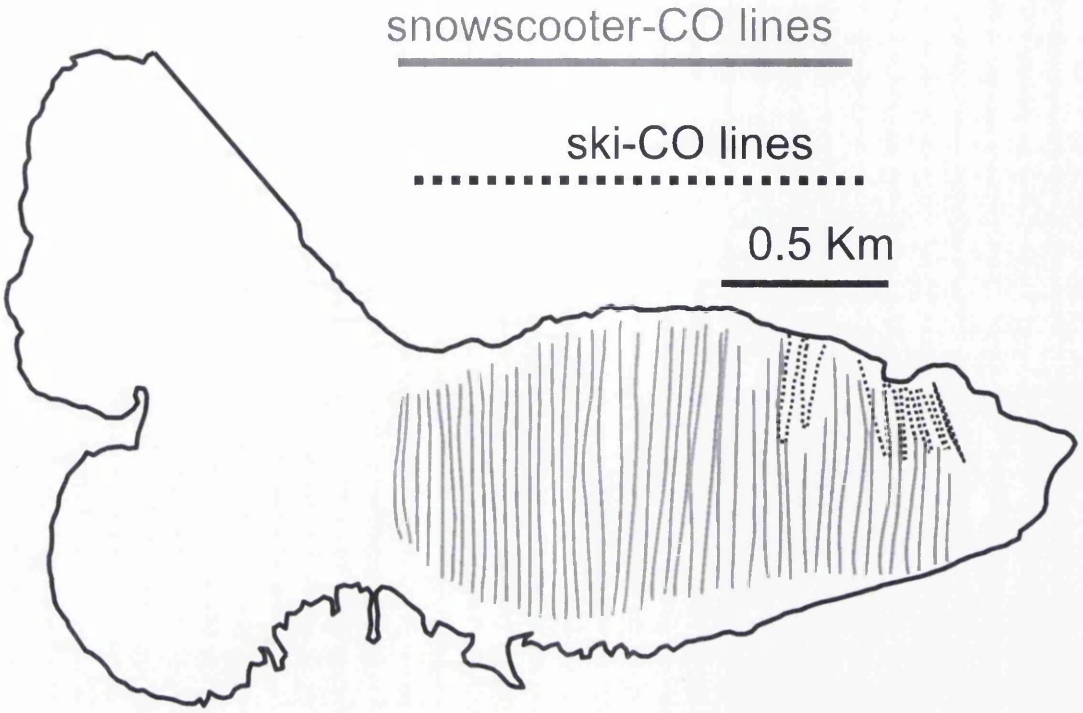

Figure 4.2: Map of Storglaciären with the locations of the GPR surveys used for the cold-layer map

every 2 seconds which was ~ 40 radar traces. The survey collected in 2009 is denser than the surveys used for the comparison in *Pettersson et al.* [2003] (Figure 4.3). The CTS depth was typically sampled every 2-3 m and this sampling/density is ~ 10 higher than that reported in *Pettersson et al.* [2003] (Figure 4.3) which was variable but typically, every 30 m [*Pettersson et al.*, 2003]. The fundamental feature of the radargrams explored in this chapter was the CTS. Although radar studies on polythermal glaciers typically provides also ice-thickness estimates (e.g. *King et al.* [2008]) in the radar data discussed in this thesis the bed reflections were not recovered in the profiles. This was presumably because of the signal losses due to absorption. Thus cold layer thickness will be presented by itself and, unfortunately, it was not possible to obtain an accompanying ice thickness map of the glacier.

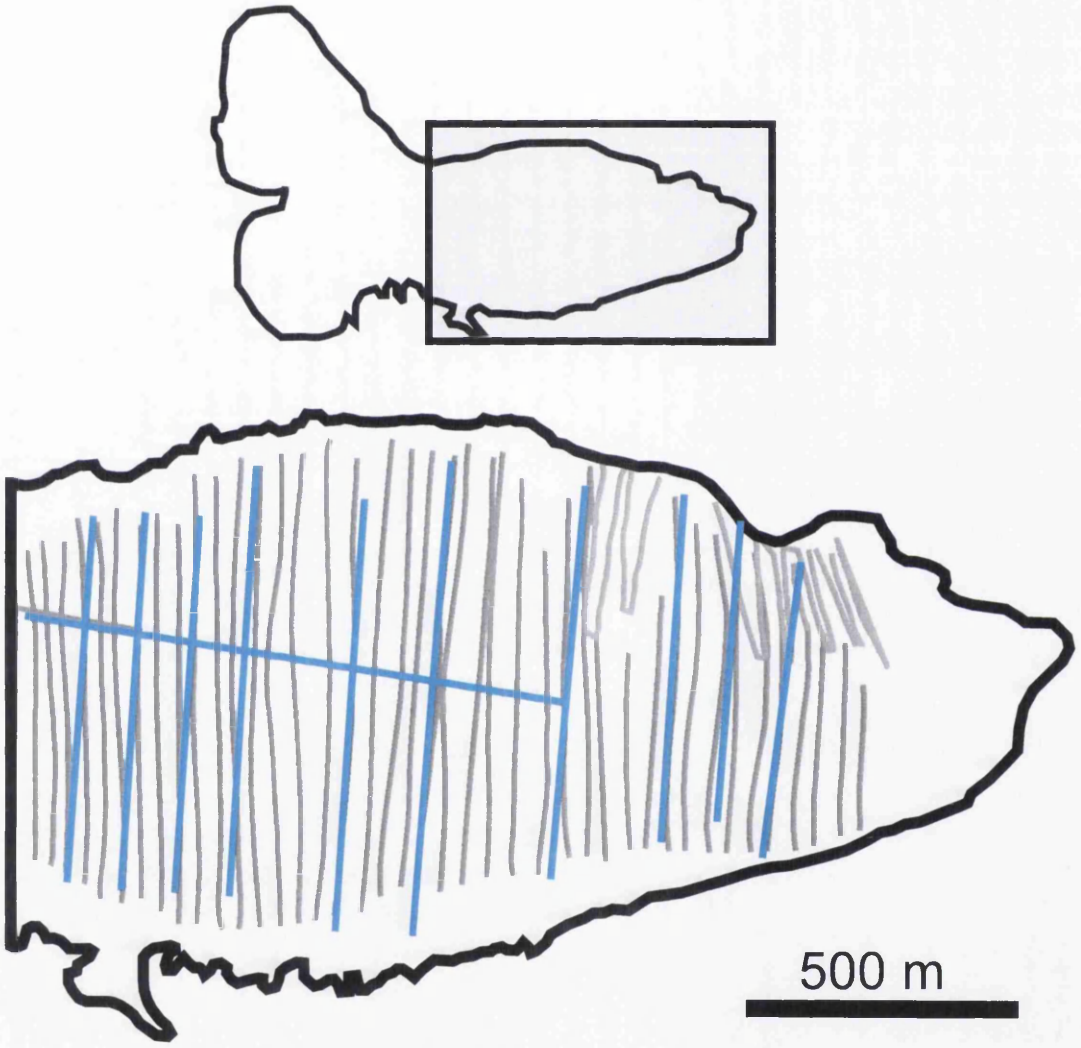

Figure 4.3: The 2009 survey (gray) lines was denser than the surveys reported in [*Pettersson et al.*, 2003] (blue).

4.2 GPR processing

The GPR CO lines were exported from the radar system and processed using the processing package ReflexW (Version 3.5.7, by Sandmeier Software). Processing steps for all the profiles of Figure 4.2 are those usually involved in radioglaciological studies (e.g. *Murray et al.* [2000a]; *Irvine-Fynn et al.* [2006]; *King et al.* [2008]; *Barrett et al.* [2008]; *Brown et al.* [2009]). In Figure 4.4a, a sample unprocessed radargram is shown. From this radargram it is not possible to extract reliable information about the thermal structure of the glacier since: (i) it is affected by a low frequency noise called *wow* typically observed in GPR data; (ii) travel times are not calibrated to the real time zero; and (iii) travel times need to be transformed into distances by the means of a certain radio wave speed. This section will illustrate the processing steps that led to CTS depth estimates from radargrams such as the one depicted in Figure 4.4.

4.2.1 Dewow

Dewow filters minimise the low frequency noise called wow generated by instrument electronics in GPR data. The wow observed in the CO lines collected at Storglaciären is represented by a whole-trace negative shift (Figure 4.6a, the amplitude of the trace has negative values). Dewow filters provided by ReflexW operate independently on each trace of the radargram, a running mean value is calculated for each value of each trace and this value is subtracted from the central point of the running-mean window. Dewow filters are conventionally applied in glaciological literature (e.g. *Murray et al.* [2000a]; *Hambrey et al.* [2005]; *Irvine-Fynn et al.* [2006]; *Barrett et al.* [2008]; *Brown et al.* [2009]), although published examples of their performance are scarce: usually dewow filters are only mentioned as a classic processing step with no details.

The unprocessed radargram in Figure 4.4 a does not allow clear inferences of Storglaciären's thermal structure whereas by applying a simple dewow operation, scat-

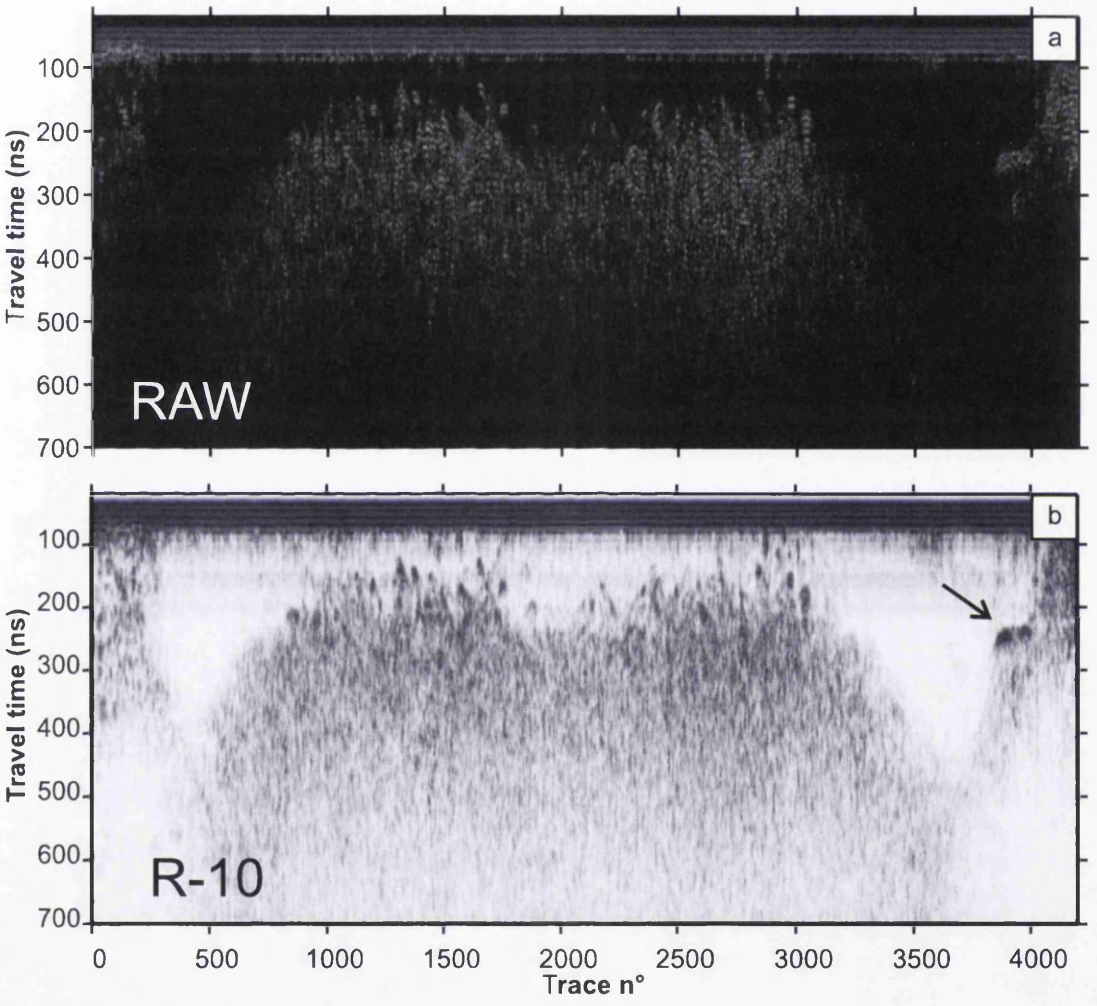

Figure 4.4: (a) Unprocessed radargram and (b) dewowed radargram using 10 ns running mean.

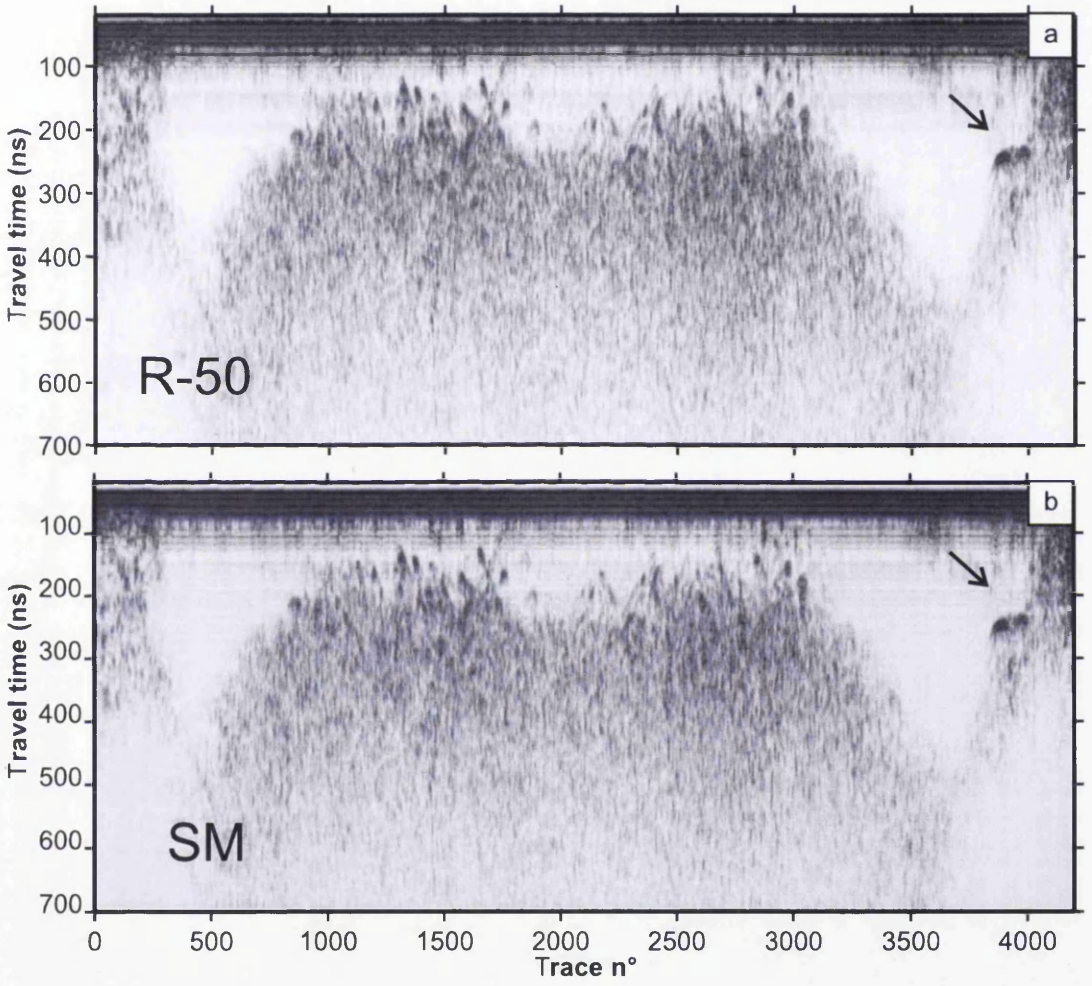

Figure 4.5: Test of two dewow filters: (a) 50 ns running mean (b) pre signal mean subtraction.

tering and non-scattering zones are distinguishable (Figures 4.4 b and 4.5). Tests on dewow filters were undertaken by changing the time windows for the running mean in ReflexW. An alternative filter designed in Matlab which subtracted the pre-signal mean, SM, was also tested. Dewowed radargrams did not differ for different filters and the position of features in the radargrams (e.g. the bright reflector indicated with arrow in Figures 4.4 and 4.5) was unaffected by different dewow filters. Further detail was thus obtained by considering the wavelets produced by the different filters. The first arrival in the unprocessed wavelet for a sample trace is of negative polarity and shifted according to the zero-phase position at $\sim$ -700 amplitude (Figure 4.6 a). All the dewow filters tested re-locate the first arrivals at 0 amplitude (Figures 4.6 b, 4.6 c and 4.6 d) but introduced minor artifacts. The running mean on a 10 ns time-window (Figure 4.6 b) preserved the timing of the first-arrival but changed its polarity. The running mean on a 50 ns time-window (Figure 4.6 c) preserved the polarity of the main first arrival but introduced artificial precursors such as those observed by *Irvine-Fynn et al.* [2006]. These artifacts are however insignificant to be a concern in this analysis.

The pre-signal subtraction dewow (Figure 4.6 d) only shifted unprocessed traces to correct zero-amplitude positions without introducing changes in polarity or precursor. Dewow-induced artifacts in all the filters are however limited to low travel-times, leaving unchanged the part of the trace which contains the CTS meaning that all three filters could be used for this analysis. The filter chosen was SM (Figure 4.6 d) which completely removed the low frequency negative shift and did not introduce visible artifacts in the early data.

4.2.2 Time zero correction

The time zero correction in GPR CO surveys is a commonly applied process. Travel times in unprocessed and dewowed radargrams are not real travel-times but they are instead affected by instrumental delay which corrupt true interpretation. This problem is usually solved by considering that the first break in each trace is a radio

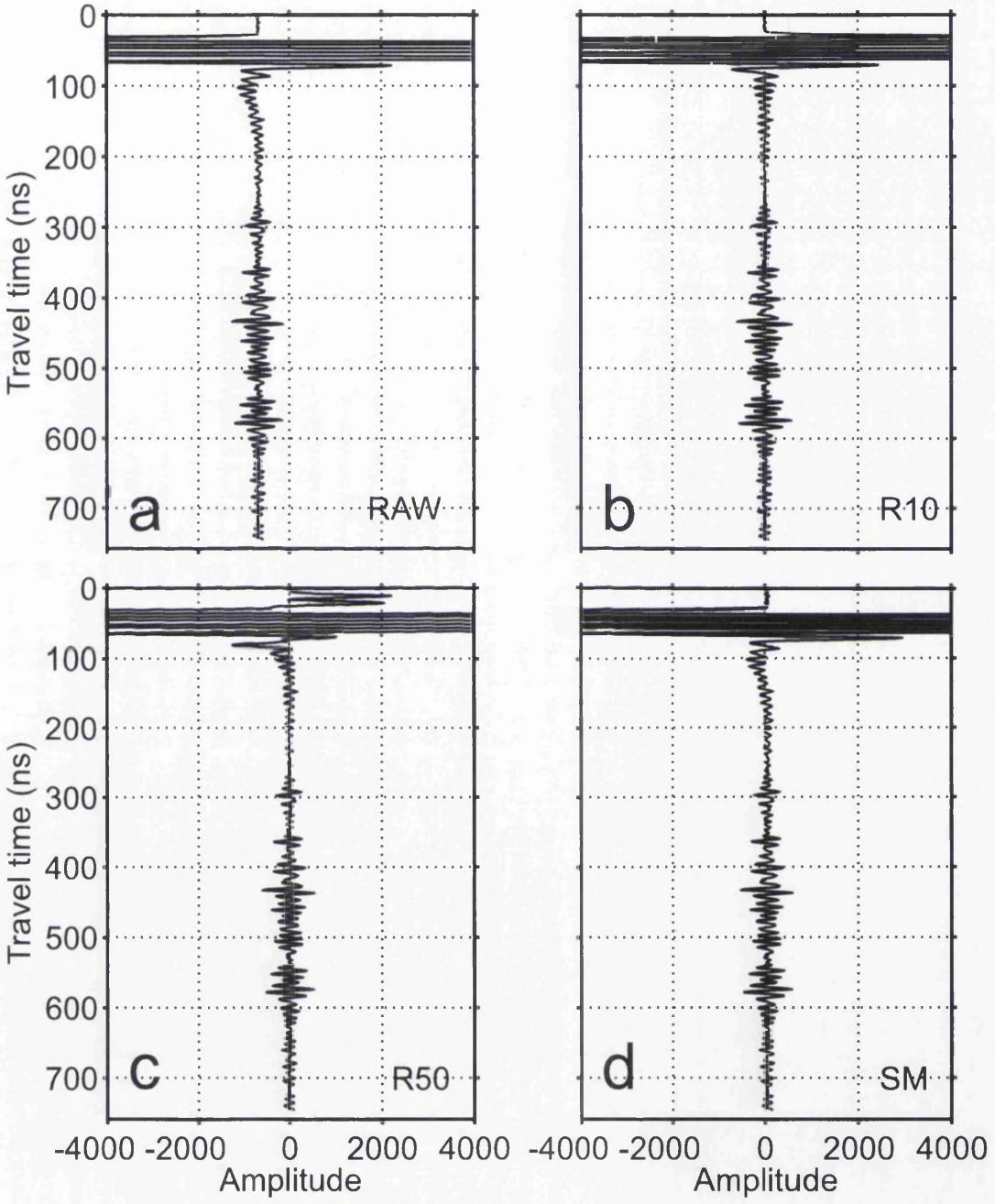

Figure 4.6: Test of three dewow filters and comparison with (a) the unprocessed wavelet. (b) 10 ns ReflexW dewow filter, (c) 20 ns ReflexW dewow filter and (d) Fixed window mean subtraction (d). The filter chosen was (d) because it completely removed the negative shift without introducing artifacts

wave propagating in the air (with speed c=0.3 m/ns) between the two antennas separated by a distance x. Published studies rarely provide explanation on how the time zero has been defined. The time zero correction requires measurement of the first break in each trace. In recent radioglaciological studies the time zero correction has been only mentioned as a processing step (as in *Brown et al.* [2009]), briefly explained with no definition of the first-break (as in *Barrett et al.* [2008]) or not mentioned (as in *King et al.* [2008] and *Kulessa et al.* [2008]).

Figure 4.7 shows a trace from the sample profile uncorrected to time zero. The first arrival is picked as the first sample with amplitude greater than the noise level (quantified by the maximum amplitude in the noise window, NW in Figure 4.7). The first break in Figure 4.7 arrives on the radargram at 22.82 ns, which is erroneous since at the antenna separation used in the survey (1 m) the first break should be at 3.33 ns. The whole trace was thus corrected for time zero by shifting the first arrivals by 19.49 ns. Such a correction will be referred in this chapter as sytem delay correction T_{DEL} .

The time zero correction is affected by uncertainities. In Figure 4.7 it is possible to observe that the error in the first break estimate is dependent on the sampling rate. At the sampling rate used in this study (1 sample = 0.99 ns) the maximum uncertainity (worst case scenario) in the picked first break is ± 1 sample thus ± 0.99 ns. However, a more realistic error is obtained by considering half of that range (±0.5 ns). This is because the preceding sample (arriving at 21.8 ns in Figure 4.7 b) still lies in the noise level whereas the following sample an amplitude that is twice as much the one measured for the sample indicated as a first break in the Figure 4.7. It is thus likely than the first arrivals is at the sample indicated in Figure 4.7 with an uncertainty of 1/2 sample (± 0.5 ns). Uncertainty in the CTS position due to the time-zero correction is thus very small and quantified as ±0.2 m using a typical radio wave speed of 0.168 m/ns for cold ice [*Bogorodsky et al.*, 1985; *Robin*, 1975].

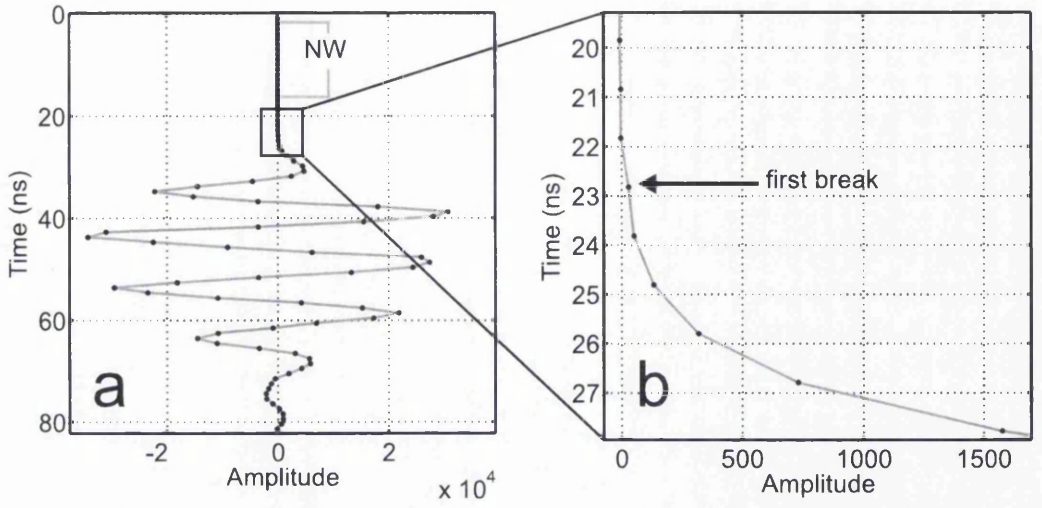

Figure 4.7: First break definition in trace 1 of the sample profile. (a) Full wavelet of the first arrival propagating between the antennas. (b) enlargement of the box in (a) which shows the first break. NW is the noise window

4.2.3 Gain and radar data visualisation

All the radar data plotted in this chapter were processed with constant gain. The colour scale chosen had the white colour on zero amplitude and two dark colours (dark-blue and black) for maximum and minimum amplitude respectively. This colour scale strategy is appropriate for this study since the polarity of the wavelets is of negligible importance. Indeed, this study relies on the difference between zero amplitude zone of the radargram (e.g. the transparent-cold ice) and high amplitude zone.

4.2.4 Migration

A commonly applied technique which repositions data elements to make their location appropriate to the location of the associated reflector or diffractor is migration [*Sheriff and Geldart*, 1995]. Migration in glaciology is typically applied to re-locate the apparent position of the reflector to their true positions (e.g. *Dowdeswell and Evans* [2004]). Migration should be applied in all the radar datasets in order to re-

move the apparent hyperbolic shape of reflectors. Migration should be applied also in this study, however, migration of radar data requires accurate information about the geometry of the survey; a good migration can only be performed when the traces are equally separated and accurately positioned (e.g. on a tape measurement). Since the dataset presented in this chapter was composed by radar traces unevenly distributed the migration process is difficult and could introduce undesired artifacts. For this primary reason radar data for the 2009 cold layer map were not migrated. A second and equally important reason is consistency: the two previous radar study on the cold layer did not migrate the radar profiles [*Holmlund and Eriksson*, 1989; *Pettersson et al.*, 2003].

4.3 Temperature-derived and radar-derived CTS

On the 14^{th} of April 2009, two 100 MHz CO lines have been acquired in the location where a thermistor string was placed in the glacier (Figure 4.8). The location of this experiment was the same as site B treated in Chapter 5 (Section 5.1.1) and for the seismic refraction experiments discussed in Chapter 6 and in *Gusmeroli et al.* [2010a]. The two radar lines were collected in a cross so that the position of the thermistor string, indicated with an ablation stake supporting the datalogger, was in the middle of the cross (Figure 4.8). Details of the thermistor measurements and of the thermal state of Storglaciären in this area are given in Section 2.5 and showed in Figure 2.7. The two lines were collected using the same survey methodology used in *Barrett et al.* [2009]: a measurement tape was lined on the snow to mark the survey line and the a stop-and-go survey method was used, in which the the surface GPR system was held motionless at 0.5 m sampling intervals. The length of both GPR lines was 100 m.

At the location where THERM1 and THERM2 were acquired (Figure 4.8) the CTS is located at the depth of 21 m (Figure 2.7). It thus follows that, at this location, the time that a radio-pulse will require to travel to the CTS and back, T_{CTS}, can be

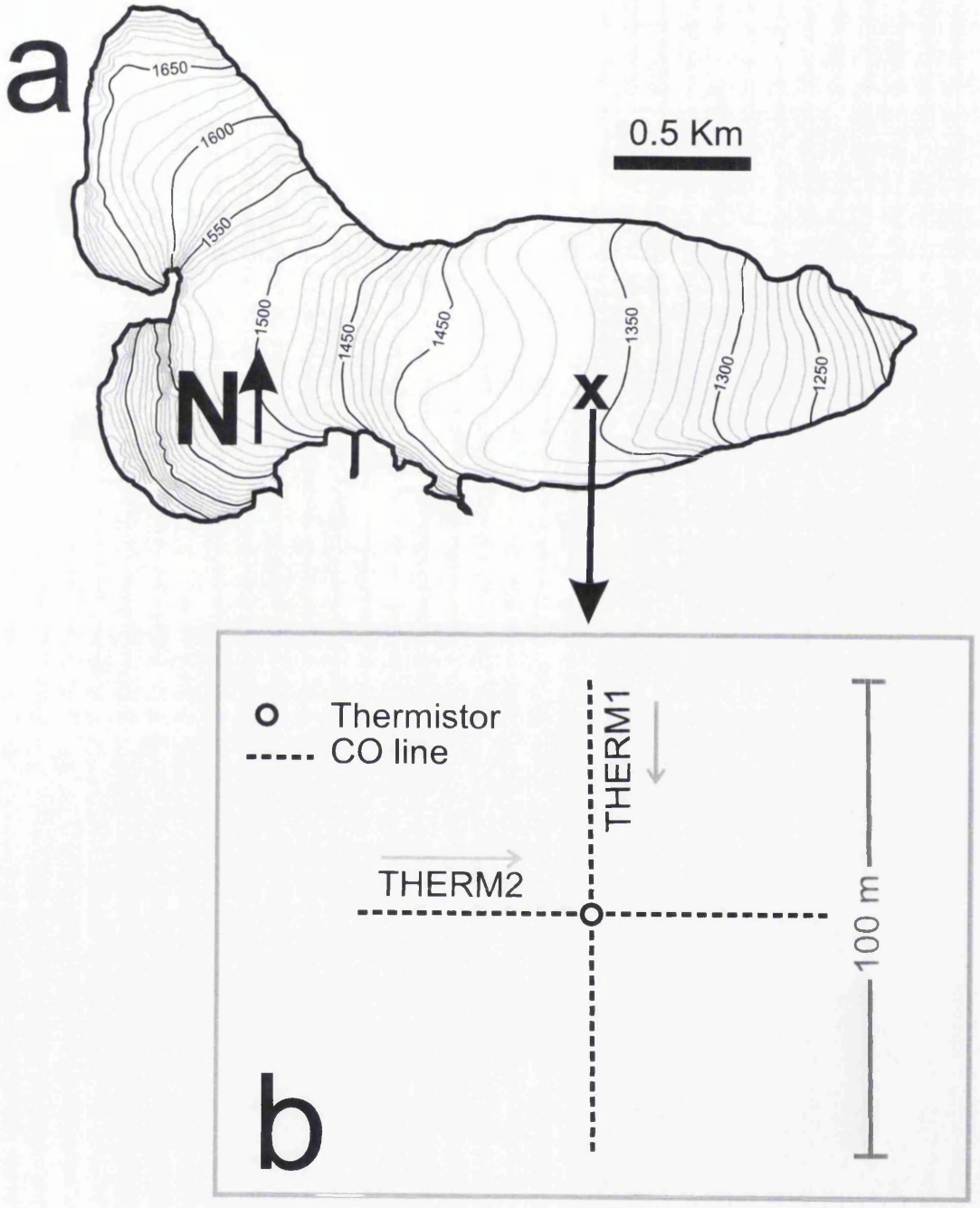

Figure 4.8: (a) Location map of the GPR surveys at the thermistor string. (b) shows the outline of the surveys. Arrows indicate survey direction

calculated by:

$$T_{CTS} = 2 \times \frac{21}{v_i}, \tag{4.1}$$

by plotting T_{CTS} for the radio wave speed range of 0.169±0.002 m/ns we can directly compare the radar and temperature-inferred CTS (Figure 4.9). In the radargrams an upper transparent region is divided by a lower scattering region with an undulating upper boundary. T_{CTS} traced across the profiles (Figure 4.9, horisontal line) shows that the radar transition surface (RTS) is located nearby the CTS.

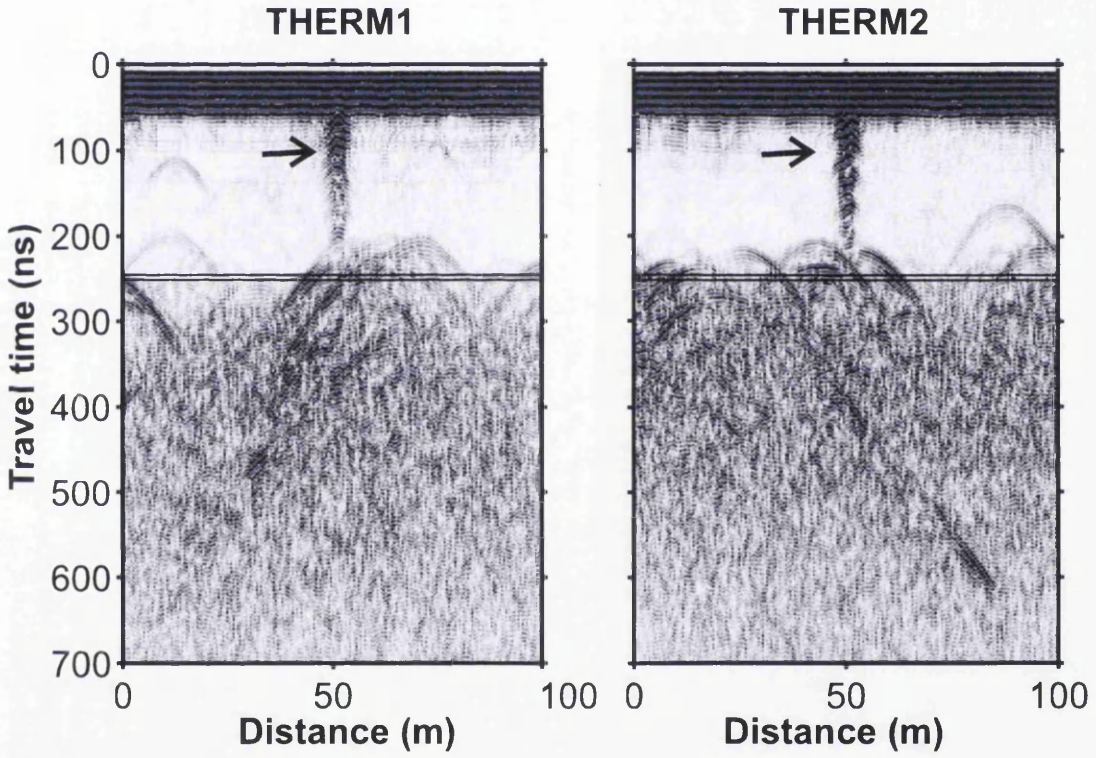

Figure 4.9: GPR CO lines THERM1 and THERM2 (see Figure 4.8 for location and outline of the survey) with T_{CTS} (Equation 4.1) superimposed. The arrows indicates the position of the thermistor

Further details of THERM1 and THERM2 with the interpreted RTS are given in Figure 4.10. The RTS do not match with the CTS but it approximates its depth within an accuracy of about ± 2 m (± 24 ns m at 0.168 m/ns). Figures 4.9 and 4.10 indicate that at the thermistor location the RTS is located at ∼ 18 m. Since temperature data provided in Figure 2.7 suggest that the temperature at 19 m is

-0.19°C it is possible to speculate that scattering objects are present in the cold ice. However, the shape of the undulating upper boundary of the scattering zone is primarily determined by the presence of reflection hyperbolas (Figure 4.9).

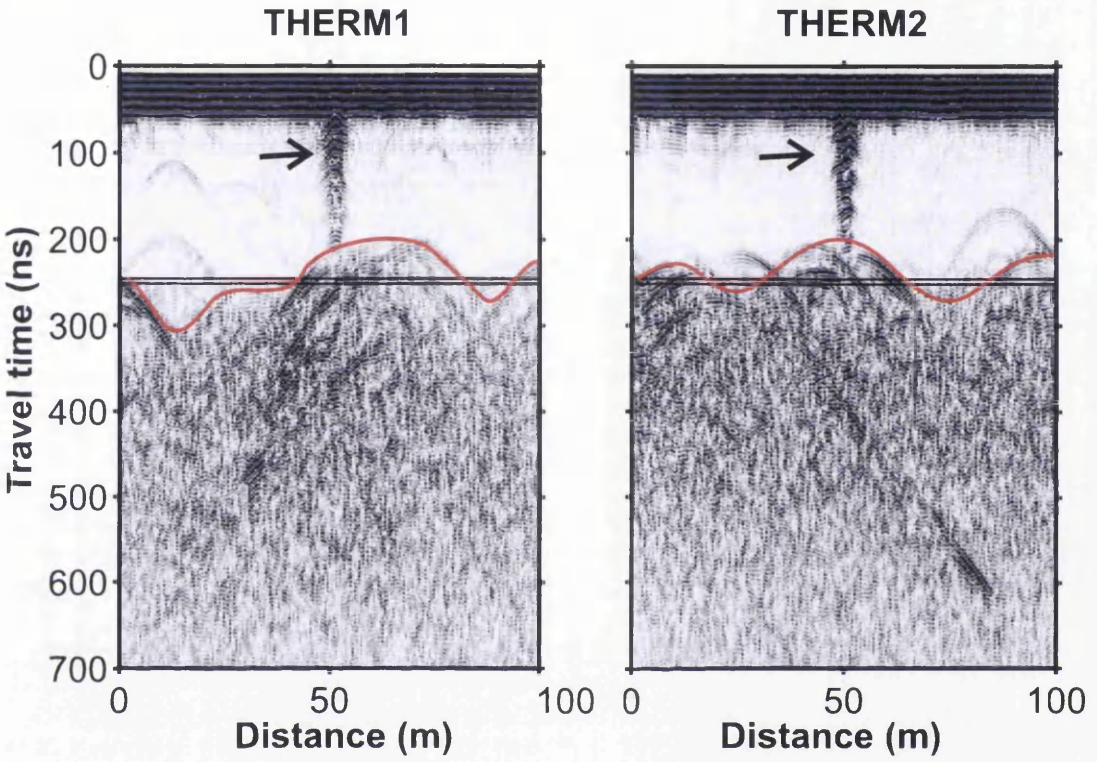

Figure 4.10: GPR CO lines THERM1 and THERM2 (see Figure 4.8 for location and outline of the survey) with T_{CTS} (Equation 4.1) superimposed. The arrows indicates the position of the thermistor. The interpeted RTS is is also superimposed.

By migrating the data is possible to collapse these hyperbolas [*Sheriff and Geldart*, 1995]. Migration of glaciological CO lines acquired in the same way as the one showed in Figure 4.9 was applied in *Barrett et al.* [2008] to explore the undulating upper boundary of the scattering region in radargrams from Bakaninbreen, Svalbard. Migration of radar profiles can collapse many of the hyperbolic events that comprise the scattering regions; however, the undulating shape of the upper boundary of scattering was still present [*Barrett et al.*, 2008]. Following the procedures illustrated in *Barrett* [2007] and *Barrett et al.* [2008] high amplitude events such as the first arrivals and the thermistor string in Figure 4.9 were muted (Figure 4.11) prior to migration.

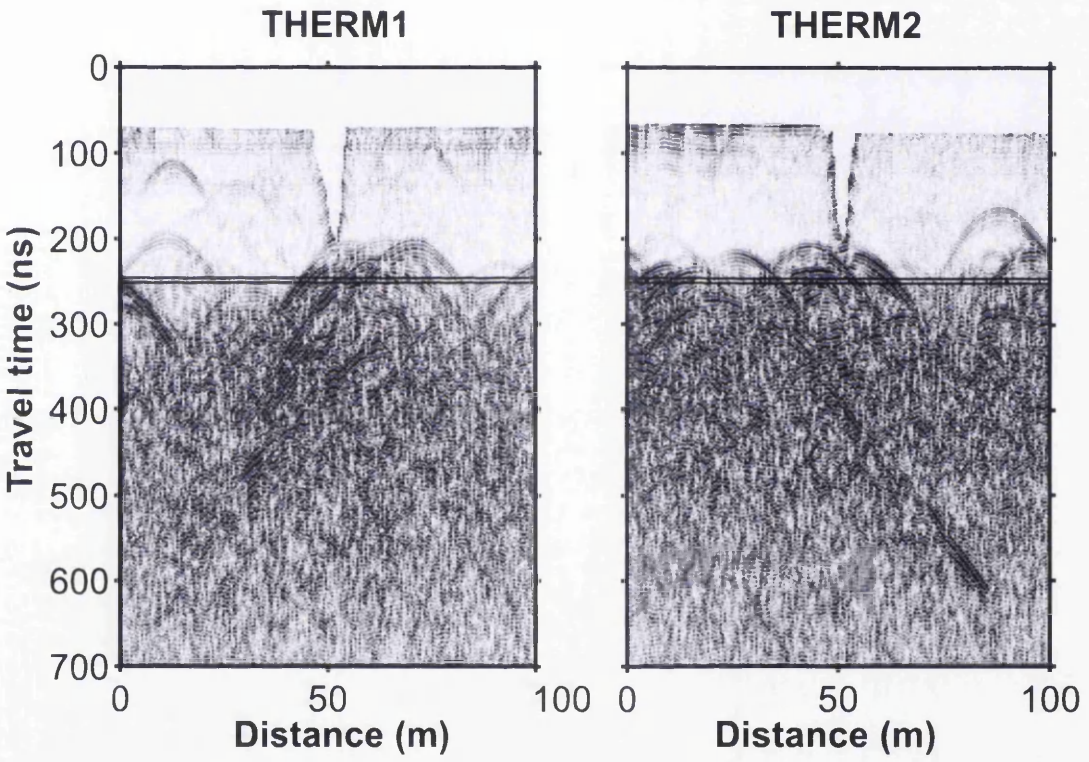

Figure 4.11: Muted profiles THERM1 and THERM2 (see Figure 4.8 for location and outline of the survey) with T_{CTS} (Equation 4.1) superimposed.

Migration was tested for THERM1 and THERM2 in order to understand whether the collapse of the hyperbolic events would modify the interpretation showed in Figure 4.10. Kirchoff-migrated profiles for THERM1 and THERM2 are shown in Figure 4.12 for the migration speed of 0.168 m/ns. This radio wave speed is typical for cold glacier ice [*Robin*, 1975], do not introduce migration artifact such as the so-called *migration smiles* [*Sheriff and Geldart*, 1995] and is also supported by the measurements illustrated in Chapter 5. The interpreted RTS for the unmigrated profile traced in Figure 4.10 is superimposed at the migrated profiles (Figure 4.12). Migration did manage to collapse the hyperbolic events of the unmigrated profiles, however, the upper undulating boundary of the scattering region is still observable in the migrated profile as it was in the pre-migration derived RTS. In spite of the difference between Figures 4.10 and 4.12 resulting from the migration process, the CTS derived from the pre-migration and post-migration profiles do not differ substantially.

The ± 2 m uncertainty between T_{CTS} and RTS observed for the unmigrated profiles (Figure 4.10) is still present after migration (Figure 4.12). We can therefore conclude that a direct comparison between temperature measurements and 100 MHz CO radar profiles acquired at Storgläciaren at the frequency of 100 MHz in April 2009 shows that CTS position can be mapped with the radar with an accuracy of ± 2 m. A similar accuracy (but up to ± 4 m) was found using the same methodology (comparison between radar and temperature profiles) by *Ødegård et al.* [1997] for the CTS of Finsterwalderbreen. The higher precision quoted in *Pettersson et al.* [2003] (± 0.7 m at 800 MHz and ± 1.3 m at 345 MHz) presumably derives from the higher frequencies used in their study (800 MHz and 345 MHz as opposed to the 100 MHz frequency used in this study).

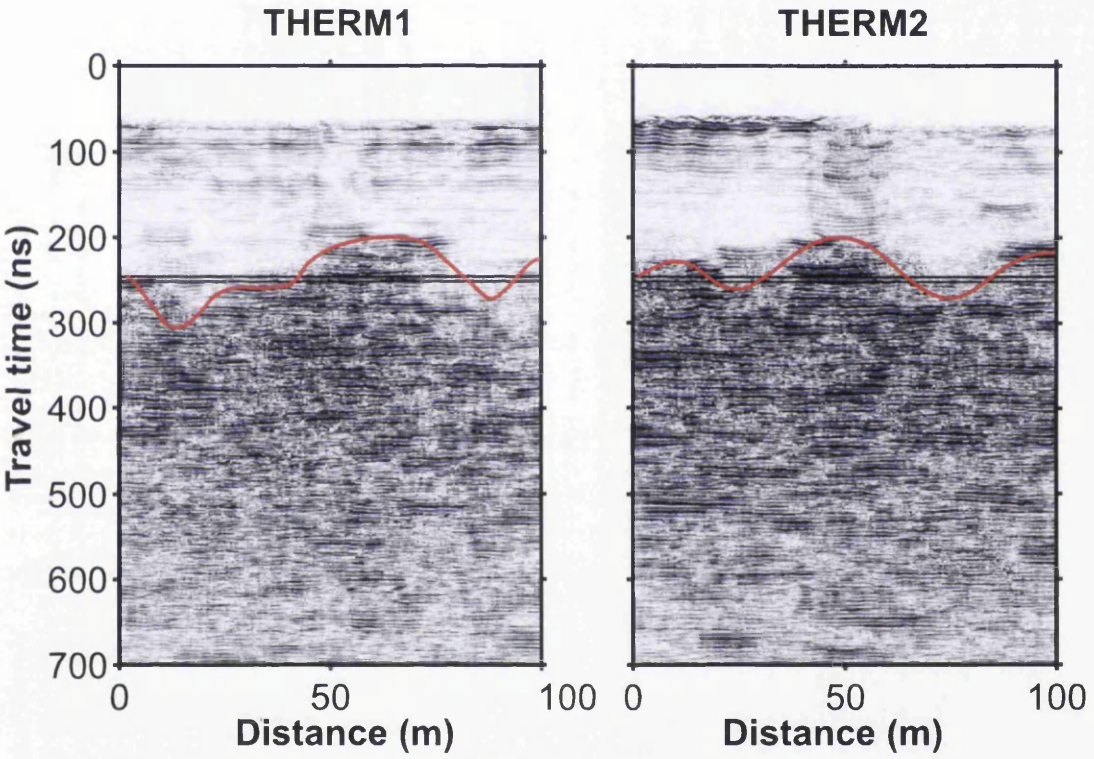

Figure 4.12: Kirchoff-migrated profiles THERM1 and THERM2 (see Figure 4.8 for location and outline of the survey). T_{CTS} (black, horisontal line; Equation 4.1) and the pre-migration derived RTS (Figure 4.10 are superimposed.

4.4 Picking the RTS

Dewowed but unmigrated radargrams (see Appendix for plots of all the profiles) were then analyzed to obtain RTS depth-estimates for each profile. This process commonly consist in picking manually the boundary between low-backscatter and high-backscatter zones of the radargrams [*Moore et al.*, 1999; *Pettersson et al.*, 2003; *Eisen et al.*, 2009; *Brown et al.*, 2009]. In this section the classic manual approach is supported by quantitative observation on the sample radar profile (4.4, 4.5) discussed in this chapter.

4.4.1 RTS picking, manual approach

Digitization was done in ReflexW by manually drawing on each profile the RTS. As previously observed by *Pettersson et al.* [2003] this process is subjective since there are no quantitative parameters involved in the process and the RTS digitalised by one person can be slightly different to the RTS digitalised by another. Figure 4.13, shows the RTS for the sample radargram as picked by 30 different digitization-experiments.

The 30 digitizations depicted in Figure 4.13 for the sample profile were used to calculate the mean RTS (Figure 4.14 a) in each radar profile. The standard deviation calculated at each data point is also shown in Figure 4.14b and lie in a range between 3 and 21 ns with a mean value of 9 ns (indicated with the gray horizontal line in Figure 4.14b). The maximum value of standard deviation observed in Figure 4.14n (21 ns) represents the maximum error associated in the manual picking of the RTS. The worst-scenario error of $\pm$ 21 ns ($\pm$ 1.8 m in RTS depth) is $\sim$ similar to the maximum discrepancy observed between RTS and CTS in THERM1 and THERM2 (Section 4.3, Figure 4.9). The intermediate scenario using the mean standard deviation of $\pm$ 9 ns suggest that the RTS can be mapped with a precision of $\pm$ 0.8 m.

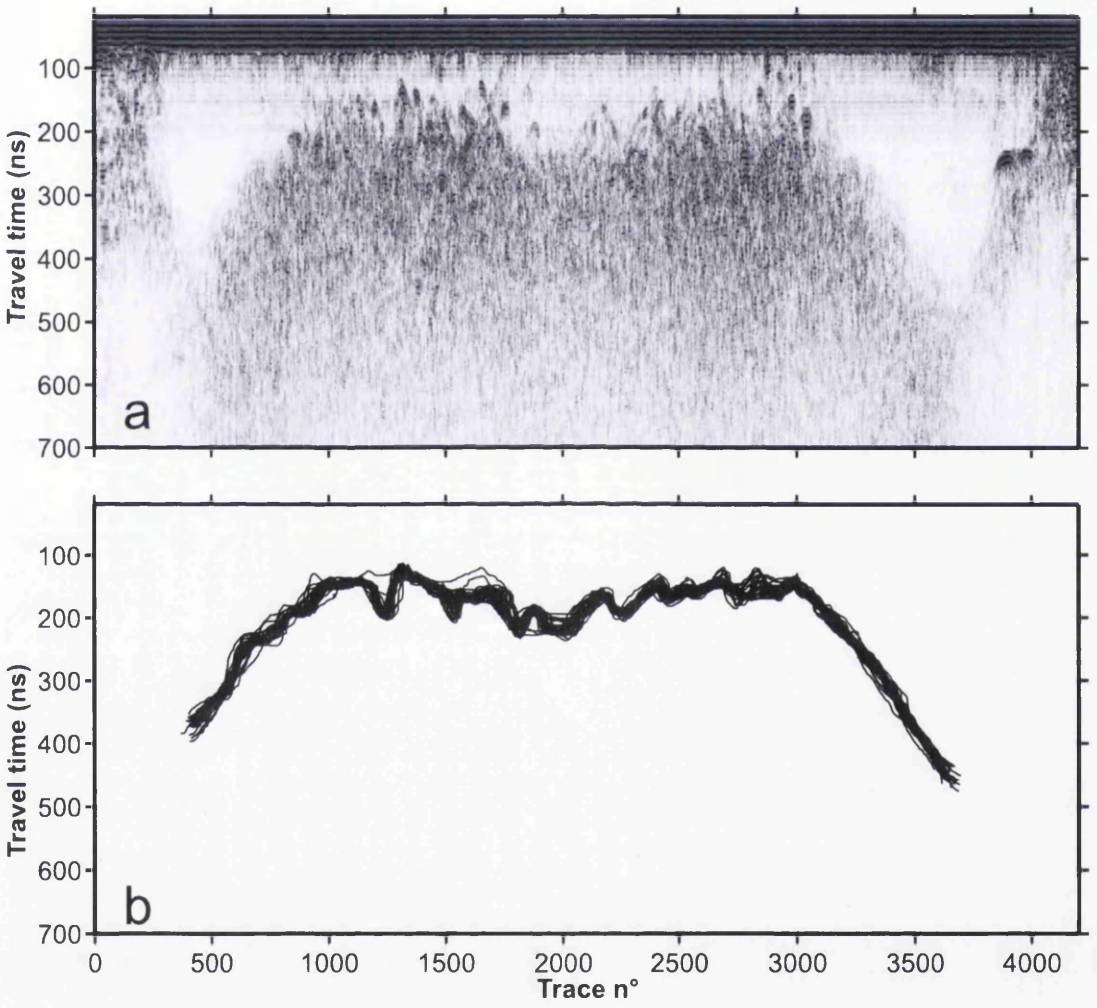

Figure 4.13: Dewowed radargram (a) and RTS as picked by 30 different digitizations for the sample profile treated in this chapter.

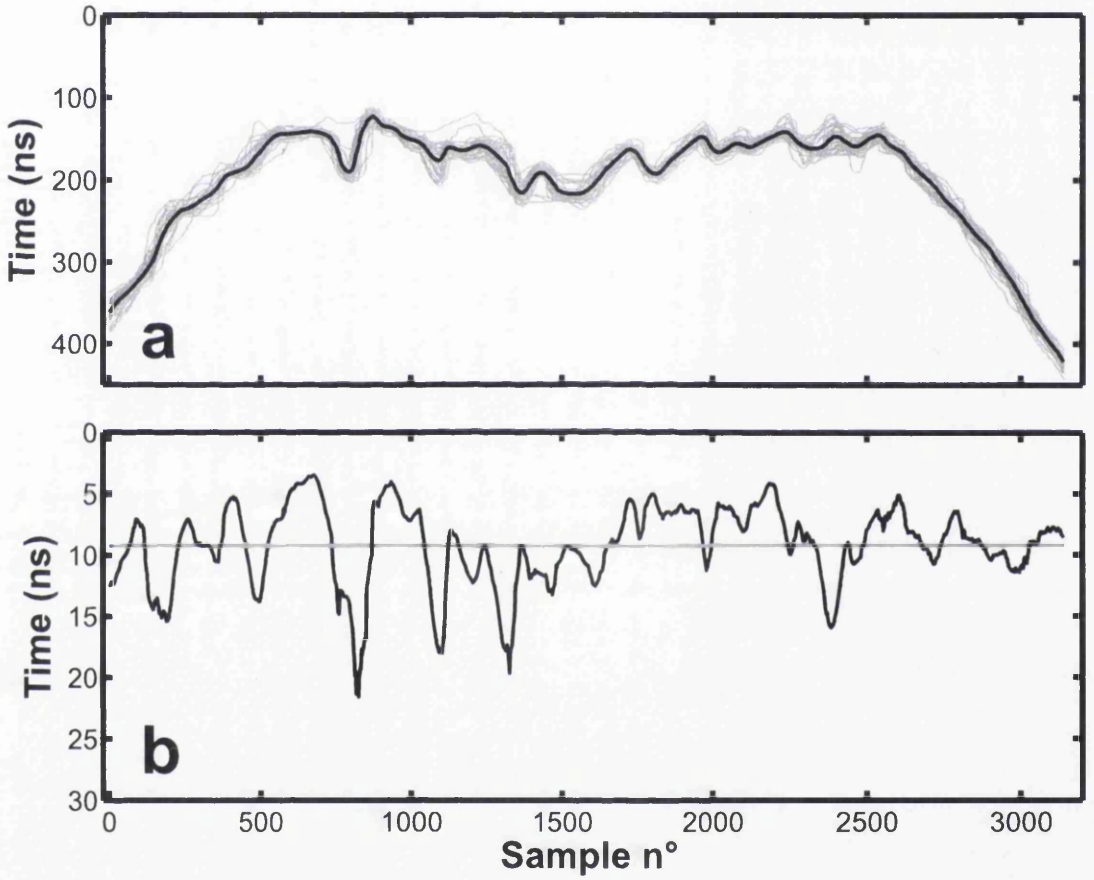

Figure 4.14: (a) Picked RTS (grey lines) and mean RTS (black thick line) from the sample profile. (b) Standard deviation of RTS calculated over the 30 digitization for the sample profile. The horizontal line indicates the mean standard deviation of 9 ns.

4.4.2 RTS picking, quantitative considerations

CTS depth estimates from GPR surveys in polythermal glaciers are possible because of the increased scattering from water inclusions present on the temperate side of the CTS [*Pettersson et al.*, 2003; *Pettersson*, 2005]. Studies reported in the literature have rarely used a quantitative approach to undertake CTS mapping. *Pettersson et al.* [2003] picked the RTS manually and observed that the returned intensity in the radargram was increased by $\sim$ 10 dB on the temperate side of the CTS. *Brown et al.* [2009] also manually traced the RTS and mentioned that the signal-to-noise ratio increased from $\sim$ 6 to 17 dB by passing from the low-backscatter to the high-backscatter side of the RTS.

Following the approach of *Brown et al.* [2009], different portions of the sample profile have been extracted for radar power analysis. The test was undertaken by randomly selecting four areas in the cold ice (Figure 4.15 upper insets) and four areas in the temperate ice (Figure 4.15 lower insets). A preliminary qualitative analysis (Figure 4.15) show that the backscattered energy in the cold ice (Figure 4.15 a,b,c,d) is clearly lower than in the temperate ice (Figure 4.15 e,f,g,h). Differences in the cold ice are also observed since samples taken in the central part of the cold layer contain some scattering-objects (Figure 4.15 b,c) whereas samples at the margin (Figure 4.15 a,d) are typically more transparent.

Signal-to-noise ratio, SNR was quantified by measuring the maximum amplitude of the pre-signal noise, A_{noise} and the maximum amplitude of the signal, A_{signal}, in each of the boxes depicted in Figure 4.15. A_{noise} was taken from the noise window (NW) in Figure 4.7. Amplitudes were converted into power values (P_{noise}=A^2_{noise} and P_{signal}=A^2_{signal}). SNR, measured in dB is thus given by:

$$SNR = 10\log_{10}\left(\frac{P_{\text{signal}}}{P_{\text{noise}}}\right). \tag{4.2}$$

Signal amplitudes for all the traces extracted from the sample-boxes are given in Figure 4.16. Results for SNR calculated on the 8 samples are listed in Table 4.1. Table 4.1 also reports the amplitude range (maximum amplitude minus minimum

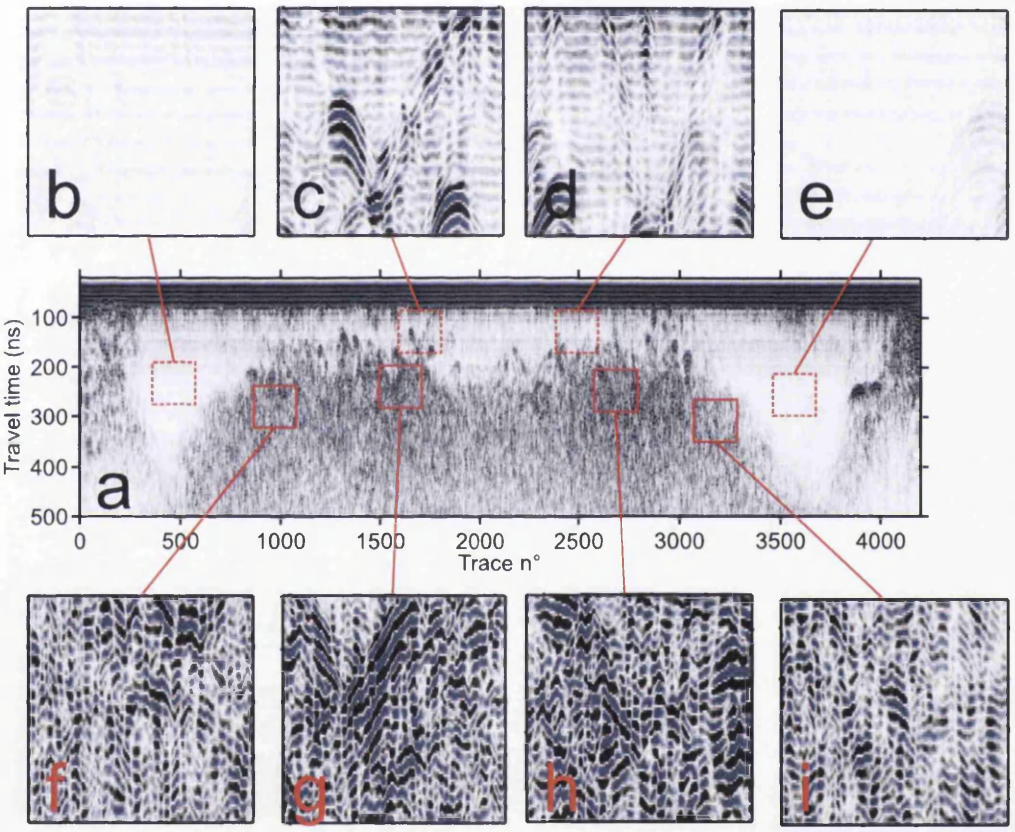

Figure 4.15: Location of the sampling area for the signal-to-noise ratio calculation. (a) Sample radargram. (b), (c), (d), (e), (f), (g) and (h) are samples discussed in the text.

Sample	SNR (dB)	Amplitude range
C1	44.4	286
C2	90.0	2663
C3	87.7	2321
C4	47.1	332
T1	90.42	3065
T2	96.9	4085
T3	96.8	3766
T4	88.2	2677

Table 4.1: SNR calculated for 8 samples in different regions of the sample radargram as shown in Figure 4.15. Amplitudes are plotted in Figure 4.16

amplitude). Amplitudes in the marginal regions of the cold ice are the lowest ob-

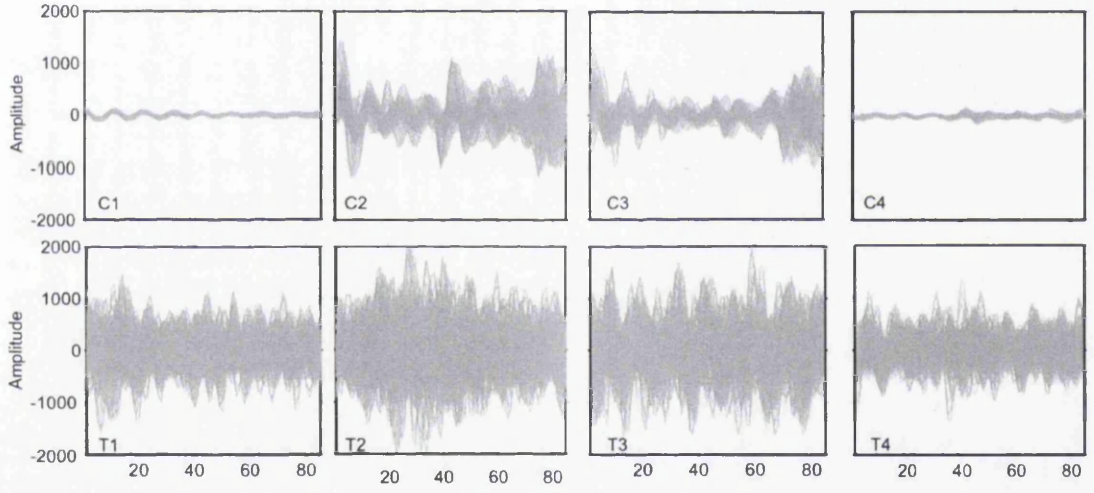

Figure 4.16: Amplitudes plotted for all the traces of the samples extracted in Figure 4.15. SNR values are listed in Table 4.1

served (Figure 4.16 C1 and C4), SNR for these regions is typically 2 times lower than those measured in the temperate ice (Table 4.1). Anomalously high SNR (in the same range as those measured for the temperate ice) are also observed in the central part of the sample line. High SNR in the cold ice are caused by scattering objects in the cold ice, such as the reflection hyperbolas distinguishable in Figures 4.15c and 4.15d.

On the basis of amplitude values listed in Table 4.1, an automatic-picking test has

been undertaken. Since the aim of the test was detecting the CTS, the upper part of the dewowed radargram (between 0 and 100 ns) was muted out. The algorithm detected for each trace of the dewowed radargram the first sample equal or greater than a given value. Three tests, named A_M, $A_M/2$ and $A_M/3$, respectively picked the arrival time of the absolute maximum amplidue, of its half and its third respectively. Values of A_M in the sample profile are shown in Figure 4.17. The maximum amplitude recorded at each trace relates with cold layer thickness Figure 4.17. More specifically A_M is lower in the margins of the profile where the cold layer is thicker; even the slight thickening of cold layer observed in the centre of the line cause decrease in A_M. This behaviour is reasonable since the thicker the layer the higher are absorption and geometric spreading (Section 3.1.3) which contribute decreasing radar amplitudes. The absolute maximum in amplitude in the whole profile is represented by a sharp, consistent, positive spike at trace 3897 (Figure 4.17). Such peak is consistent with the strong reflection observed in the radargrams (e.g. arrow in Figure 4.5 a).

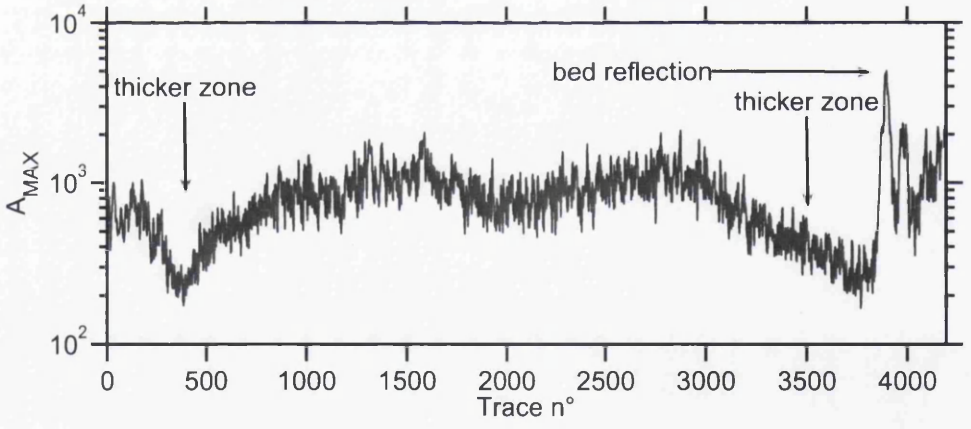

Figure 4.17: A_M computed for each trace throughout the whole sample profile

Results of the quantitative picking tests are illustrated in Figures 4.18. The automatic pickings performed by $A_M/3$ (Figure 4.18 a), $A_M/2$ (Figure 4.18 b) and A_M (Figure 4.18 c) are highly scattered and can not be compared to the previous CTS estimates by *Holmlund and Eriksson* [1989] and *Pettersson et al.* [2003]. $A_M/3$ is limited by the coherent noise at around 150 in the data which is picked throghout

the profile instead of the CTS (Figure 4.18 a), characteristics hyperbolae are also picked towards the centre of the profile. $A_M/2$ (Figure 4.18 b) also show many datapoints on the 150 ns noise line and the general trend of the datapoints do not differ greatly from $A_M/3$. The coherent-noise is avoided by A_M but the greater part of the datapoints fell well into the warm ice. In Figure 4.18 the range of the mean hand-picked RTS with is shown for comparison with the automatic picking.

4.4.3 RTS picking, summary

Two different methodologies which independently produce estimates of the travel-time position of the RTS were tested on the sample profile treated in this chapter. The two methods were: (i) manual digitization of the RTS based on visual differences between the commonly cited (*Pettersson et al.* [2003]; *Eisen et al.* [2009]; *Brown et al.* [2009]) high-backscatter and low-backscatter regions of radargrams, and (ii) automatic picking of the RTS based on quantitative observations from absolute amplitude measured on the sample profile. Results show that the manual picking of the RTS has quantitative consistency with the automatic picking. The automatic picking was represented by a non-smooth series of datapoints which were all, in large majority, bounded upperly by the manually traced RTS. The automatic picked was contaminated by the presence of noise and scattering objects, presumably air or water pockets, within the cold ice. However, amplitude maxima, half of the maxima and one-third of the maxima were for the vast majority within the warm ice. The manually traced RTS acted as a filter onto the largely scattered automatic picks and thus represented a way to trace the RTS without being conditioned by noisy datapoints or scattering-objects. The map of the cold layer will be produced by hand-picking the travel time from the RTS (T_{RTS}), as it has been done in recent radioglaciological studies [*Pettersson et al.*, 2003; *Eisen et al.*, 2009; *Brown et al.*, 2009].

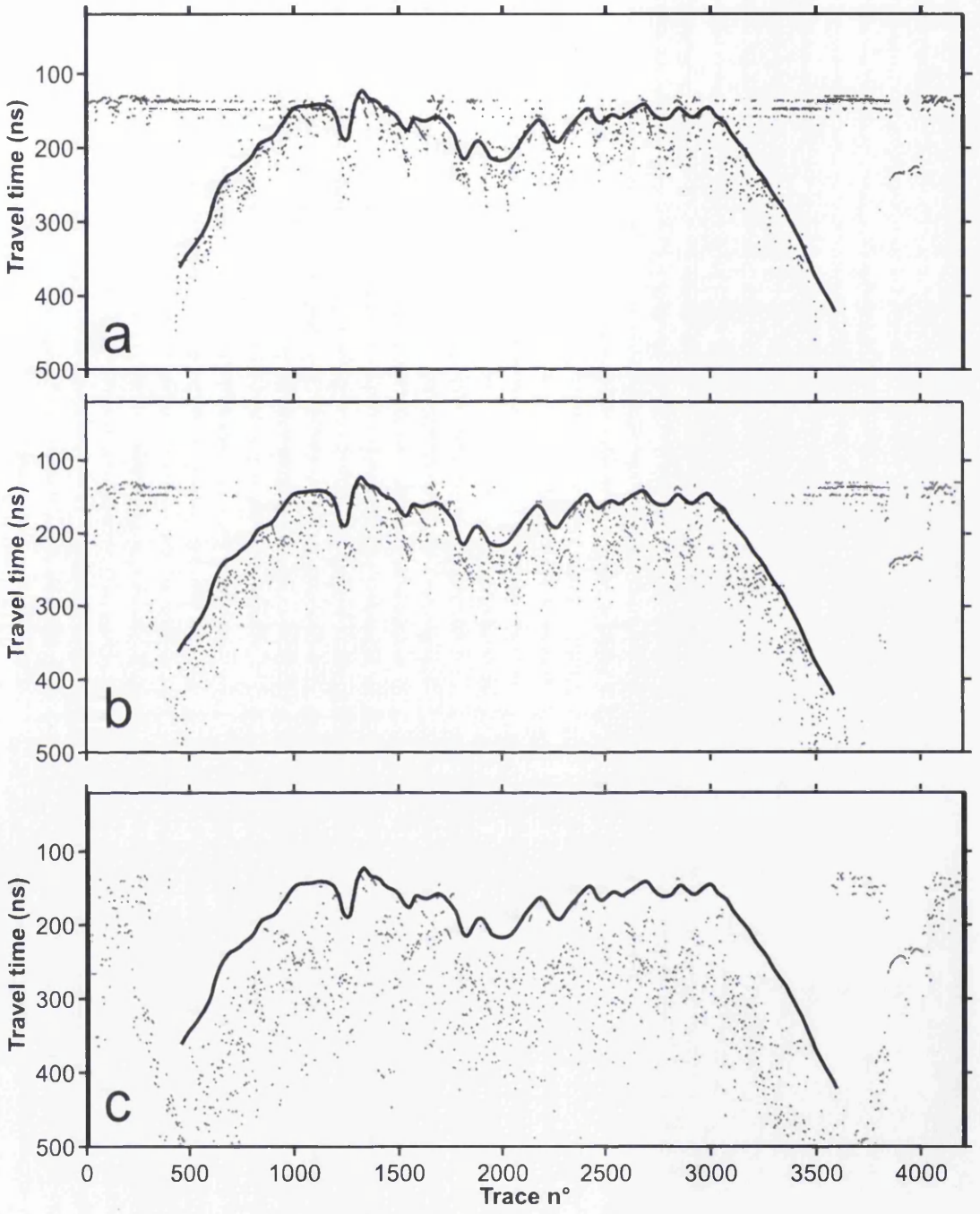

Figure 4.18: Results of automatic picking of the RTS. (a) $A_{\mathrm{M}}/3$. (b) $A_{\mathrm{M}}/2$. (c) A_{M}. The solid black line indicates the mean hand-picked CTS. The black dots are individual picks for each trace

4.5 Depth of the RTS

The depth of the radar transition surface, z_{RTS}, was computed in all the profiles using T_{RTS}:

$$z_{RTS} = (T_{RTS}/2)v_i, \tag{4.3}$$

Figure 4.19 shows three representative profiles of RTS depth estimates throughout the glacier. The number of RTS depth estimates on each profile is typically between 80 and 100 (Figure 4.19, black dots), this sampling rate is considerably higher than the one used in *Pettersson et al.* [2003] which was typically between 10 and 20 CTS depth estimates per profile. The accuracy of RTS depth estimates is quantifiable using the standard deviation of T_{RTS} picks which is indicated with a solid line on the profiles in Figure 4.19. RTS depth accuracy considering the standard deviation is ± 2 m as worst case scenario (± 1 m for the best scenario). This value is considerably higher than the precision associated in radio wave speed uncertainities (v_i in Equation 4.3). By considering that radio wave speeds in the cold-ice varied at Storglaciaren between 0.166 and 0.170 m/ns (Chapter 5), the value of 0.168 ± 0.002 m/ns is a satisfactory range. This speed range cause errors in RTS depth of ± 0.5 m for the worse case scenario (± 0.2 m for the best scenario). By considering the 100 MHz wavelength the radar resolution is of ~ 1.5 m.

4.6 Interpolation of GPR surveys

The series of profiles shown in Figure 4.2 represents a series of irregularly spaced datapoints throghout the ablation area of the glacier (Figure 4.20). The spatial sampling rate was limited by the GPS system which acquired the position of the collected trace every 2 seconds, typically every 30th-40th trace. The distances between two subsequent samples was on average ~ 5 m. This dataset only provides spatially limited data-points since is impossible to get exhaustive values of data at every desired point (e.g. in the gap marked with an arrow in Figure 4.20). However, since the final aim of this chapter is to obtain a clear picture of the cold layer thickness, a

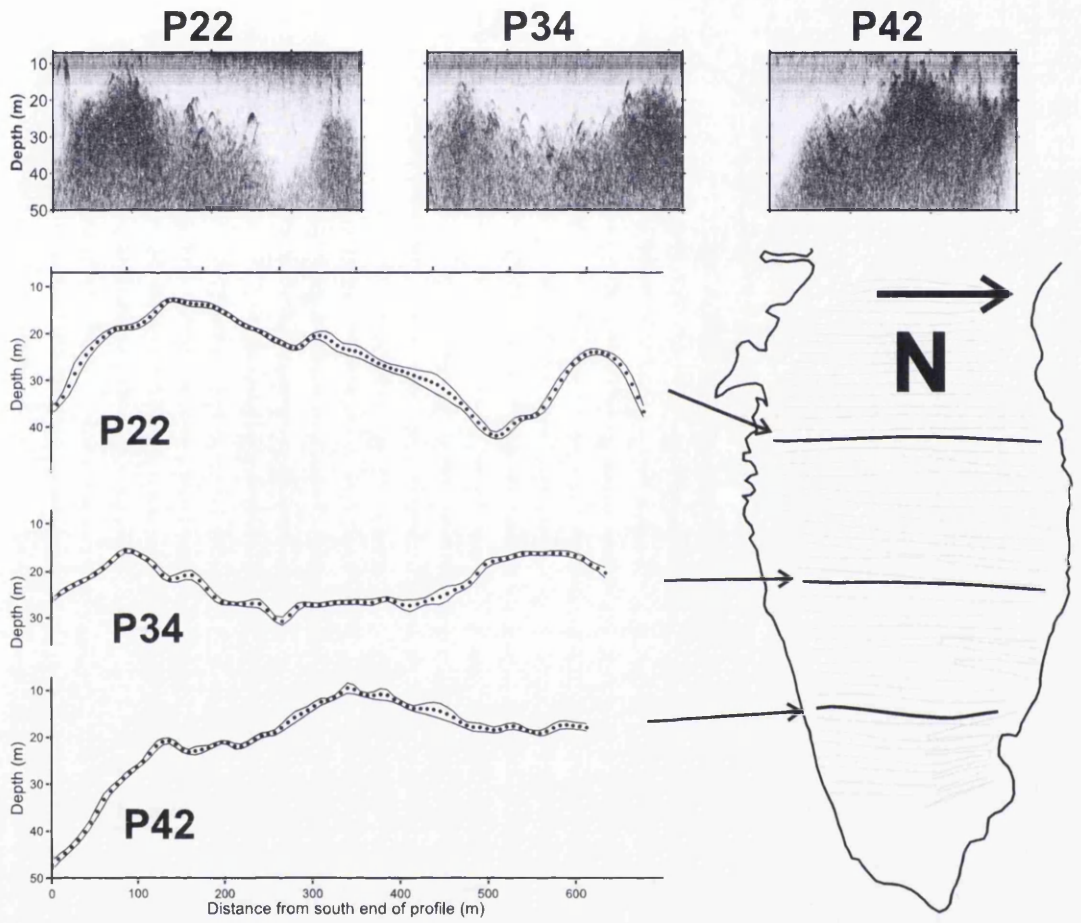

Figure 4.19: Representative examples of RTS depth estimates from CO radar profiles in April 2009. CTS values (black circles) will be interpolated to obtain the map of the cold surface layer in 2009. The range ± one standard deviation from 30 picking experiments on each profile is between the two solid black lines.

geostatistical procedure needs to be applied in order to interpolate GPR profiles. In geostatistical interpolations, a variable is estimated at an unmeasured location from observed values at surrounding locations. This procedure is widely used especially in applied sciences such as petroleum geology, ore geology, hydrogeology and hazard management, where predicting unmeasured values and produce maps is a fundamental requirement to meet.

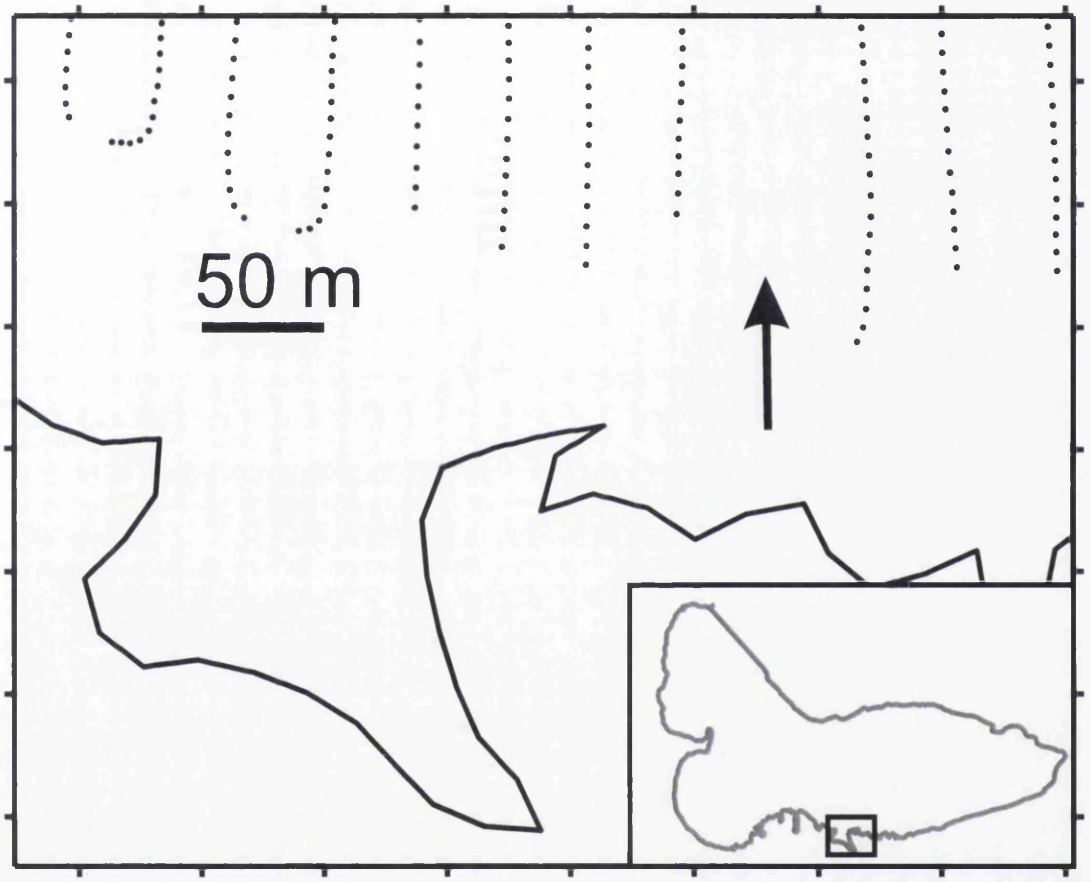

Figure 4.20: Detail of the datapoints of the southern side of the ablation area. The arrow indicate a large gap ($\sim$ 50 m) between two radar profiles. Storglaciären's outline and the location of the area is shown in the inset.

The basic principles of a geostatistical problem applied to the case study discussed in this chapter are schematically depicted in Figure 4.21. A cold surface layer $\sim$ 30 m thick thins towards the left side of the figure to $\sim$ 10 m. The thickness was measured at four different points (A, B, C and D) and a geostatistical interpolation aim to predict the value in a and b on the basis of the four datapoints measured. Intuitively,

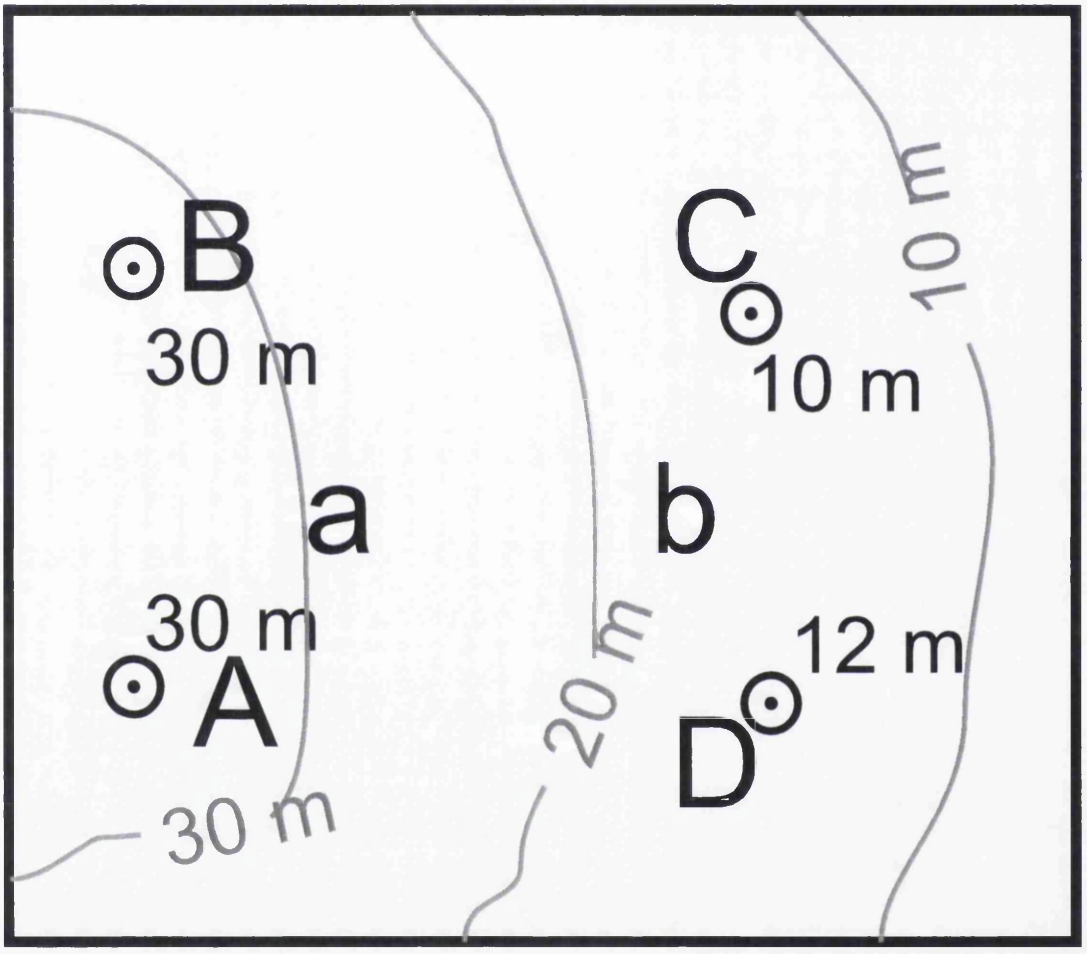

Figure 4.21: Example of a geostatistical problem. A certain physical quantity (e.g. the cold layer thickness) has been measured in four different points (A,B,C and D). Contour lines for such quantity are indicated in gray lines. Intuitively the predicted value of a will be closer to 30 than the predicted value of b.

the value of a should be closer to the one of A and B than the one of C and D. In the same way the value of b should be similar to C and D. The general thinning of the cold layer from right to left will therefore be predicted by the interpolated contour surface (gray lines in Figure 4.21). In this section the process that allow sparce measurements such as A, B, C and D to lead to the production of contour lines in Figure 4.21 will be illustrated and discussed.

4.6.1 Kriging interpolation

The kriging interpolation-method is based on the regression of observed values of surrounding data points, weighted according to spatial covariance values [*Isaaks and Srivastava*, 1989]. The two previous maps of the cold layer of Storglaciären published in *Pettersson et al.* [2003] and depicted in Figure 2.10 were obtained using kriging. However, this method is not only used for thermal mapping in glaciology but it has also been used to map the bed topography of Storglaciären [*Herzfeld et al.*, 1993] and Trapridge Glacier [*Flowers and Clarke*, 1999]. Beyond glaciology, the recent literature in natural sciences show a wide use of this method in numerous topics such as forest ecology [*Garbarino et al.*, 2010], groundwater quality [*Nas and Berktay*, 2010], tectonics [*Martinez et al.*, 2008] and hydrological sciences [*Janetti et al.*, 2010].

Kriging is popular because of the method used for estimating unknown datapoints. The vast majority of geostatistical interpolations (inverse distance squared, radial basis functions, splines, triangulation) predict values at unknown locations as a weighted sum of values at surrounding locations. Weights in these methods are assigned according to functions that give a decreasing weight with increasing separation distance. Instead kriging assigns weights according to a data-driven weighting function (called a semi-variogram), rather than an arbitrary function. Differences between different interpolation algorithms are however very small [*Isaaks and Srivastava*, 1989]. For example, if we have a dense set of observations, the final model produced by kriging will be very similar to the one produced by triangulation.

A geostatistical interpolation using kriging consists of two different stages. At first data have to be studied, the predictability of values from place to place is estabilished by the means of a graph known as a semi-variogram which models the differences between observations according to the distance and direction between them. The second stage, also known as *ordinary kriging*, estimates values at unknown location by using a weighted average of neighbouring samples. The weights are optimized using the semi-variogram model. Ordinary kriging also provides standard errors which can thus be used to quantify confidence levels. The basic idea of the kriging method is that the predicted value of the variable Z^* at the location b surrounded by u measured data $Z(b_i)$ at locations b_i will be given by:

$$Z^*(b) = \sum_{i=1}^{u} w_i Z(b_i), \tag{4.4}$$

where w_i are the weights given by the semivariogram analysis.

4.6.2 Underlying theory of semivariograms

Semivariogram analysis is the characterisation of spatial correlation between datapoints in geostatistics. Spatial correlation is a geostatistical problem since e.g. two different datasets can be similar as far as the descriptive statistic is concerned (e.g. same mean, same standard deviation, same population, same histogram) but totally different in terms of variations in space. A semivariogram is a plot of semivariances Υ versus distances h between ordered data in a graph. Υ is defined in spatial statistics as:

$$\Upsilon(b) = \frac{1}{2}\frac{1}{u}\sum_{i=1}^{u}\Big(Z(b_i + h) - Z(b_i)\Big)^2, \tag{4.5}$$

Intuitively if h=0, the semivariance is calculated between two points with the same value. For this reason, in the ideal case, a semivariogram passes through the origin of the axes. As h increases, Υ should also increase until h is great enough that two samples are independent and no correlation is observed between Υ and h. This behaviour, also known as spherical-model is recognized as the ideal-case of a semivariogram, and it can be seen with the same significance that the normal distribution

has in descriptive statistics. The spherical-model is mathematically described as:

$$\Upsilon(h) = O\left(\frac{3}{2}\frac{h}{a} - \frac{1}{2}\frac{h^3}{a^3}\right) \text{ where } h \leq a, \tag{4.6}$$

$$\Upsilon(h) = O \text{ where } h \geq a, \tag{4.7}$$

where O and a are the sill and the range of the variogram (Figure 4.22).

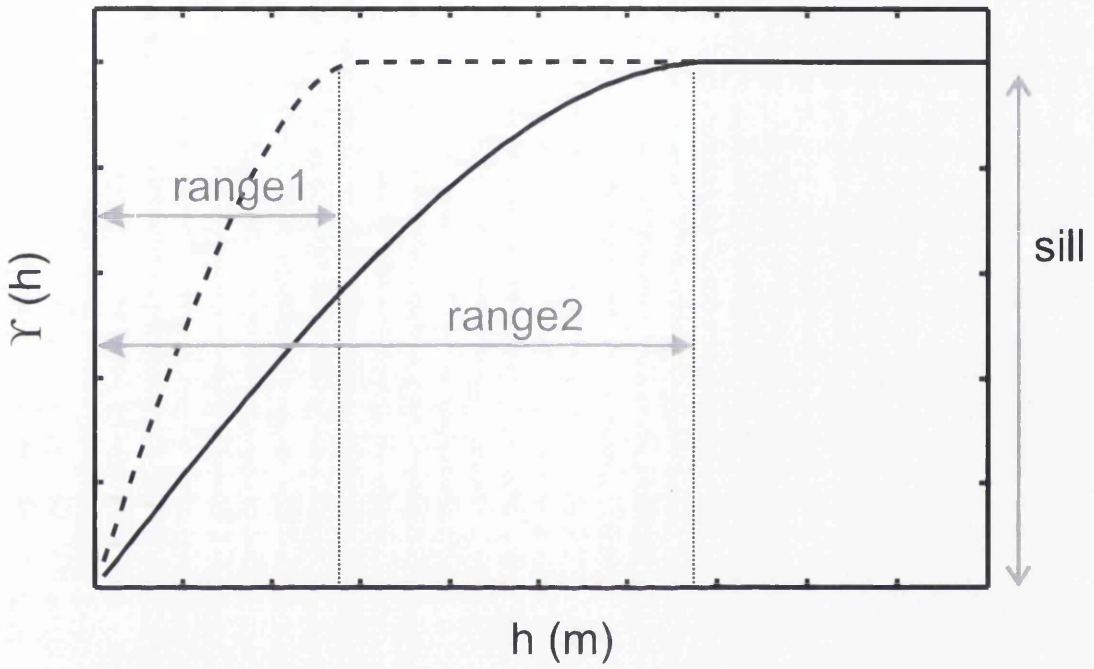

Figure 4.22: Representation of the spherical model according to Equations 4.6 and 4.7. Dashed and solid line indicates two models with same sill and different range.

Two different spherical semivariograms are illustrated in Figure 4.22. The differences between the two are usually expressed in geostatistics with the term *range*. The sill in Figure 4.22 express the variance of the dataset whereas the range is the distance at which the variogram reach the sill. The spatial variability of a given dataset can be describe by such semivariograms: in the case presented in Figure 4.22, the dashed line shows higher spatial variability since for the same given h higher values of semivariance Υ are observed below the sill.

4.6.3 Semivariogram at Storglaciären

Tests on semivariogram-performances for the CO profiles at Storglaciären was obtained using the geostatistical package *Golden Software Surfer 8.* The Surfer variogram grid stores information about the variance between data point pairs based on the distance and angle between points. The variogram operated by Surfer is a three dimensional function, built on two independent variables (direction, Θ, and distance, h) and one independent variable ($\Upsilon(\Theta, h)$). The example of the variogram plot in Figure 4.22 is a radial slice from the spherical variogram grid, which can be seen as a funnel shaped surface. Surfer produces an omni-directional variogram which is thus an average measure of the spatial correlation of the dataset.

The omnidirectional semivariogram computed from the 4284 CTS depth estimates is showed in Figure 4.23a. Such a plot is a statistically-based, quantitative description of the spatial variability in the datasets. Υ shows the average dissimilarity (in terms of semivariances, see Equation 4.5) between points separated distance h. The semivariogram for the CTS depths (Figure 4.23a) shows characteristics of a spherical variogram since a prominent *sill* (the value in the ordinate at which the variogram levels off) is observed. When the variogram reaches the sill there is no-spatial correlation between the data. The semivariogram obtained from the standard deviation of T_{RTS} (Figure 4.23b) shows no-spatial correlation since the sill is reached at very low h and Υ do not increases with h. The semivariogram of the standard deviation (Figure 4.23) does not add evidence to this study and and is included here only to provide an example of a spatially-uncorrelated dataset.

Another peculiar characteristic of the experimental variograms in Figure 4.23 is that there is a non-zero intercept on the vertical axis, the magnitude of the intercept is called the *nugget.* Nuggets can be representative of the measurement errors present in the datasets. Once the variogram has been computed the kriging interpolation can be done. Such interpolation will require a model in which *sill*, *nugget* and *range* reproduce the trend observed in the experimental variograms.

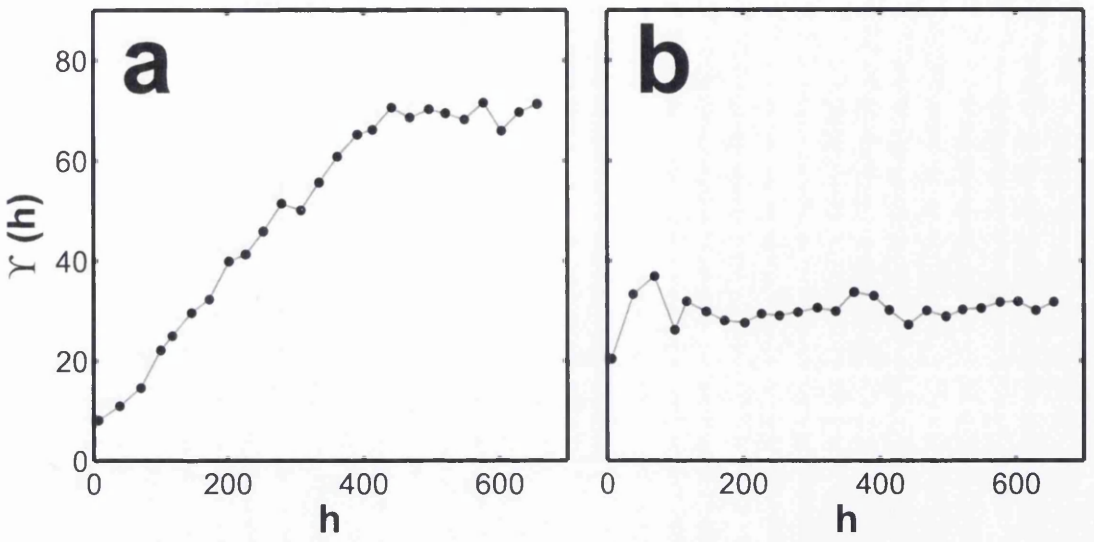

Figure 4.23: Semivariogram computed using *Surfer* for the CTS depth estimates from the radar profiles and 30 picking test on each profiles (a). Semivariogram of the standard deviation (b).

4.6.4 RTS depth map

The experimental variogram shown in Figure 4.23 is the basis on which a variogram model is chosen to perform the kriging interpolation. The interpolation weights, which will be applied on the datapoints, are in fact direct functions of the variogram model. There are thousands of different ways to construct variogram models by changing the sill, range, nugget and slope of the model. In this chapter, three different variogram models are tested and compared. The models are illustrated in Figure 4.24. The first model (Figure 4.24 a) is a linear variogram with an intercept shifted towards the nugget level observed in the data. The nugget correction is not incorporated in the second linear model (Figure 4.24 b). The spherical (Figure 4.24 c) model included the nugget correction.

The RTS map was produced using the same spatial grid of the maps reported in *Pettersson et al.* [2003](Figure 2.10). The spatial grid used is thus 10 × 10 m. The pattern of the interpolated cold layer thickness is the same using different variogram models (Figure 4.25), however, ignoring the nugget effect in the variogram introduces numerical instabilities (Figure 4.26). Insignificant differences were observed between the linear and spherical model (Figures 4.25 and 4.26).

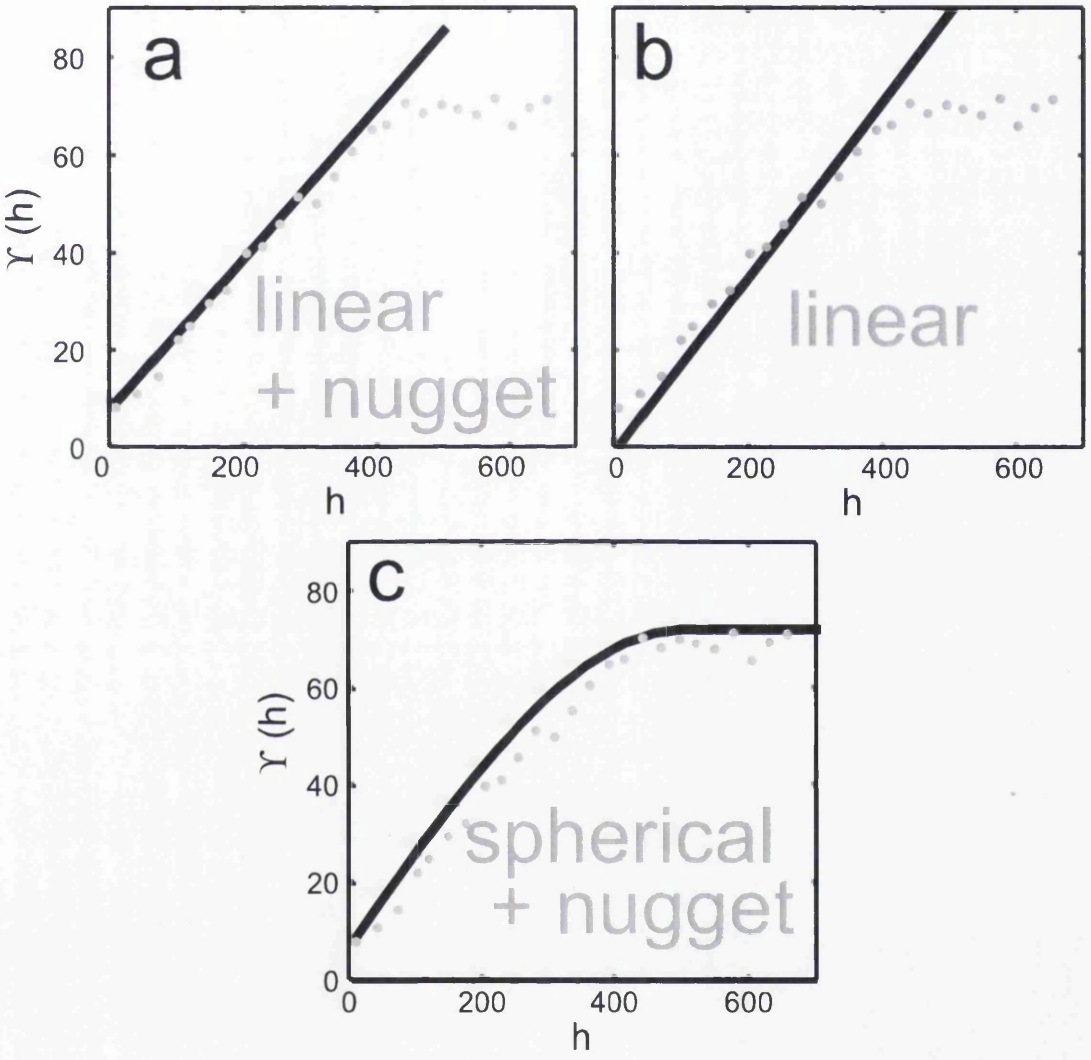

Figure 4.24: Semivariogram models (black line) used for the Kriging interpolation. The experimental semivariogram is shown with gray dots

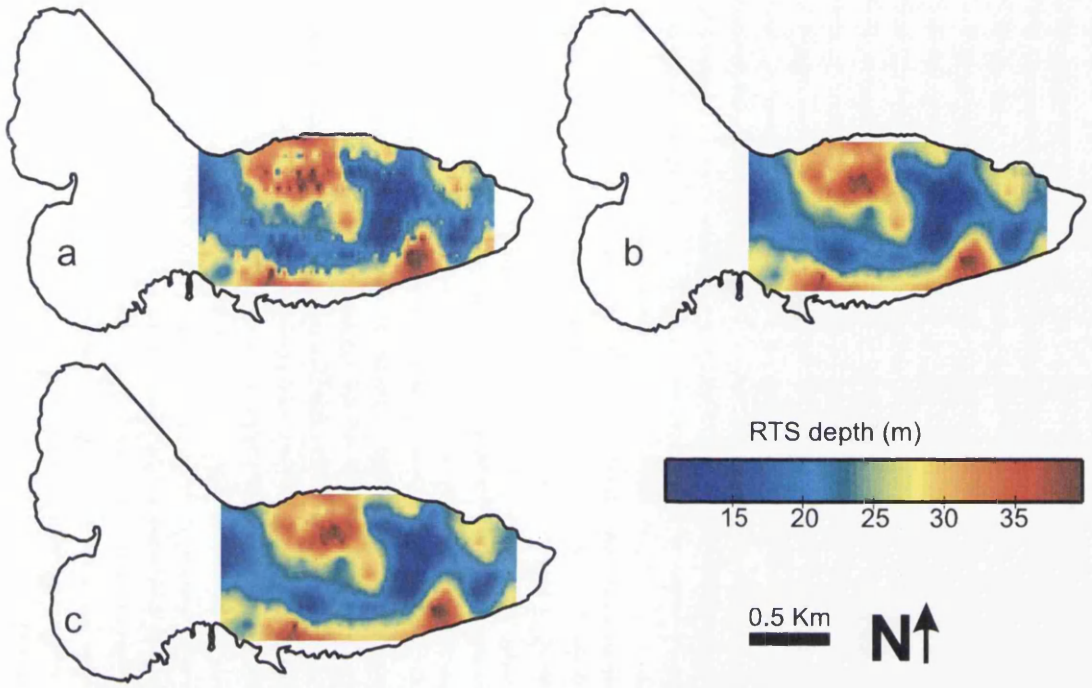

Figure 4.25: Map of the RTS depth interpolated using the kriging algorithm on the basis of the three different models illustrated in Figure 4.24. (a) Linear model. (b) Linear model with nugget. (c) Spherical model with nugget.

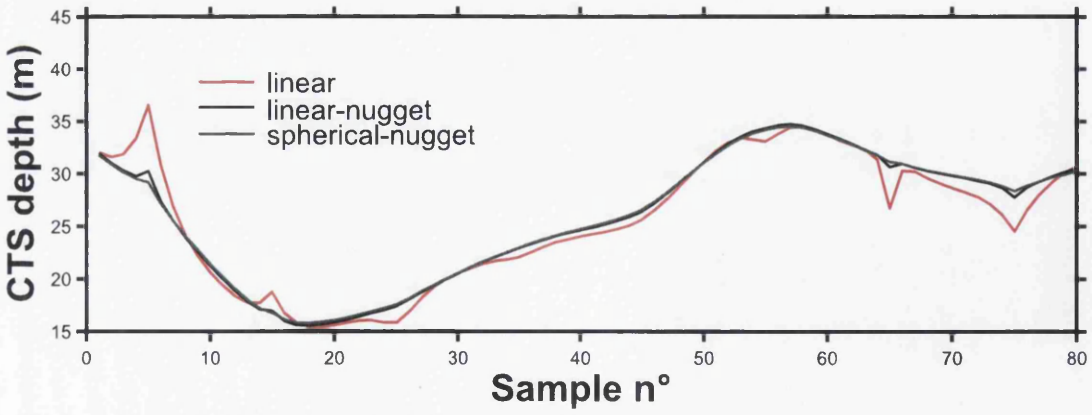

Figure 4.26: Sample RTS depth profiles using three different kriging methods. The differences are minor, however compensation for the nugget effect removed some numerical instabilities.

4.6.5 Depth of the CTS, correcting for the snow-cover

The interpolated RTS map slightly differs from the CTS map because is still affected by a systematic depth-overestimation due to the snow layer. By starting with equation 4.3 we can write $T_{RTS}/2$ as the combination of two travel-paths, one within the snowpack and one within the ice:

$$z_{RTS} = \left(\frac{z_{snow}}{v_{snow}} + \frac{z_{CTS}}{v_i}\right) v_i, \tag{4.8}$$

where z_{CTS},z_{snow} and v_{snow} are the CTS depth, snow-thickness and radio wave speed within the snowpack respectively. The depth of the CTS below the ice surface is thus given by:

$$z_{CTS} = v_i\left(\frac{z_{RTS}}{v_i} - \frac{z_{snow}}{v_{snow}}\right). \tag{4.9}$$

z_{SNOW} can be calculated using the snow thickness values collected by the Tarfala Research Station in April 2010 (Figure 4.27). Snow thickness in the area where the survey was collected was homogeneous on values between 1-2 m. However, for some profiles (e.g. in the southern side), snow depths reached up to 4 m and therefore the effect for the snow-layer may be important. Correction for the snow-layer was calculated in *Pettersson et al.* [2003] using the empirical relationship illustrated in *Kohler et al.* [1997]. However, since *Kohler et al.* [1997] relationship was a geometrically corrected version of the speed-density equation [*Robin*, 1975], the original relationship from *Robin* [1975] will be used instead. We can relate v_s to snow density ρ_s [*Robin*, 1975]:

$$v_{snow} = \frac{c}{1 + (0.851)}\rho_S. \tag{4.10}$$

Equation 4.10 gives v_{snow}=0.24±0.02 m/ns for a range of ρ_s between 200 and 400 kg/m^3. This range is between the minimum value quoted for settled snow (200 Kg/m^3) and the maximum value for wind packed snow (400 Kg/m^3) in *Paterson* [1994]. v_{snow} allows calculation of the travel time in the snow pack, which is very small which is subtracted from the RTS map. The correction map (Figure 4.28) shows the differences between Z_{CTS} and Z_{RTS} which are very small ($\sim$ 0.5 m) for the vast majority of the surveyed area. However, in some regions this correction

reaches up to 4 m (Figure 4.28). Uncertainty in the correction map are very small and mostly dependent on uncertainties in ρ_s and v_{snow}. v_{snow} error of 0.02 m/ns correspond of uncertainty in the correction of $\sim$ 0.3 m. This value is negligible by considering the accuracy of CTS depth estimates of $\pm$ 2 m. Low uncertainities in the correction factor (as low as 0.18 m) were also observed by *Pettersson et al.* [2003].

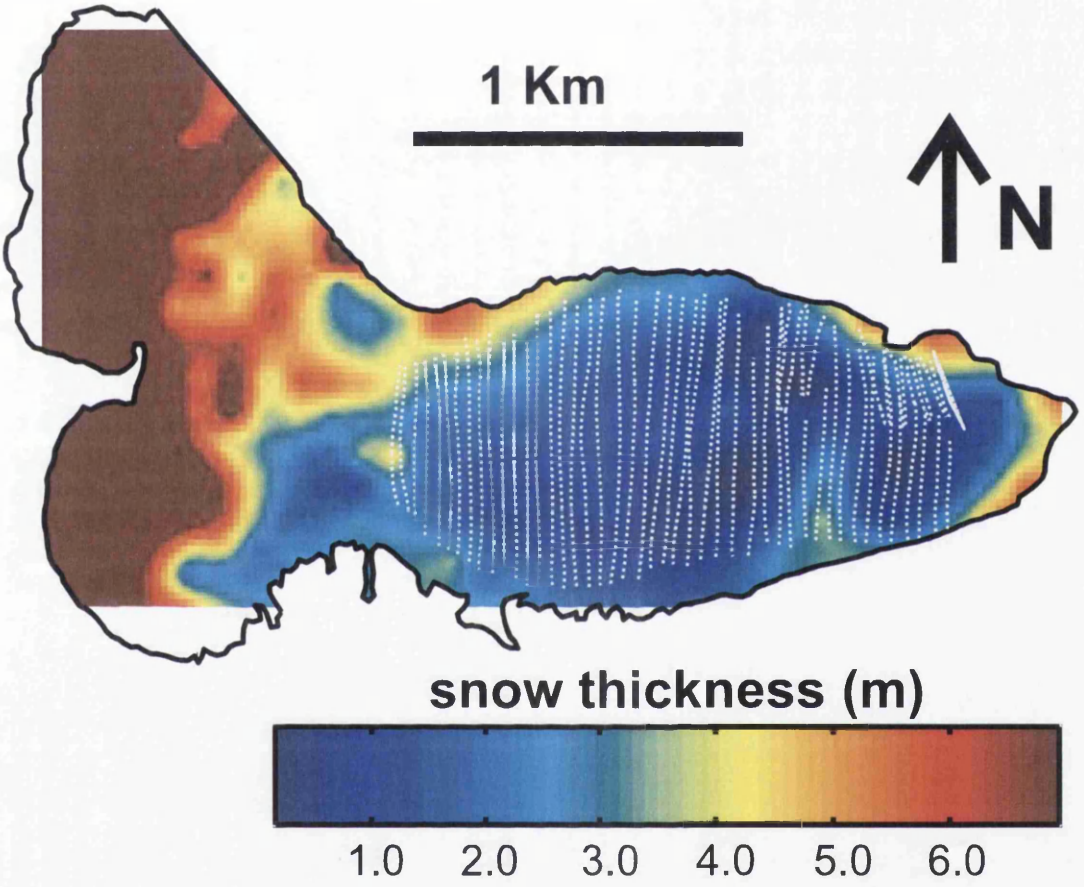

Figure 4.27: Snow thickness map from the snow-depth measurements collected at the Tarfala Research Station in April 2009, data courtesy of P. Jansson. The dotted lines superimposed indicate the GPR surveys.

4.6.6 The 2009 cold layer map

Since the spherical model mostly resembled the experimental semivariogram (Figure 4.24) the RTS map based on this model (Figure 4.25c) was chosen as the final RTS map. The final CTS map (Figure 4.29) was obtained by correcting the RTS for the

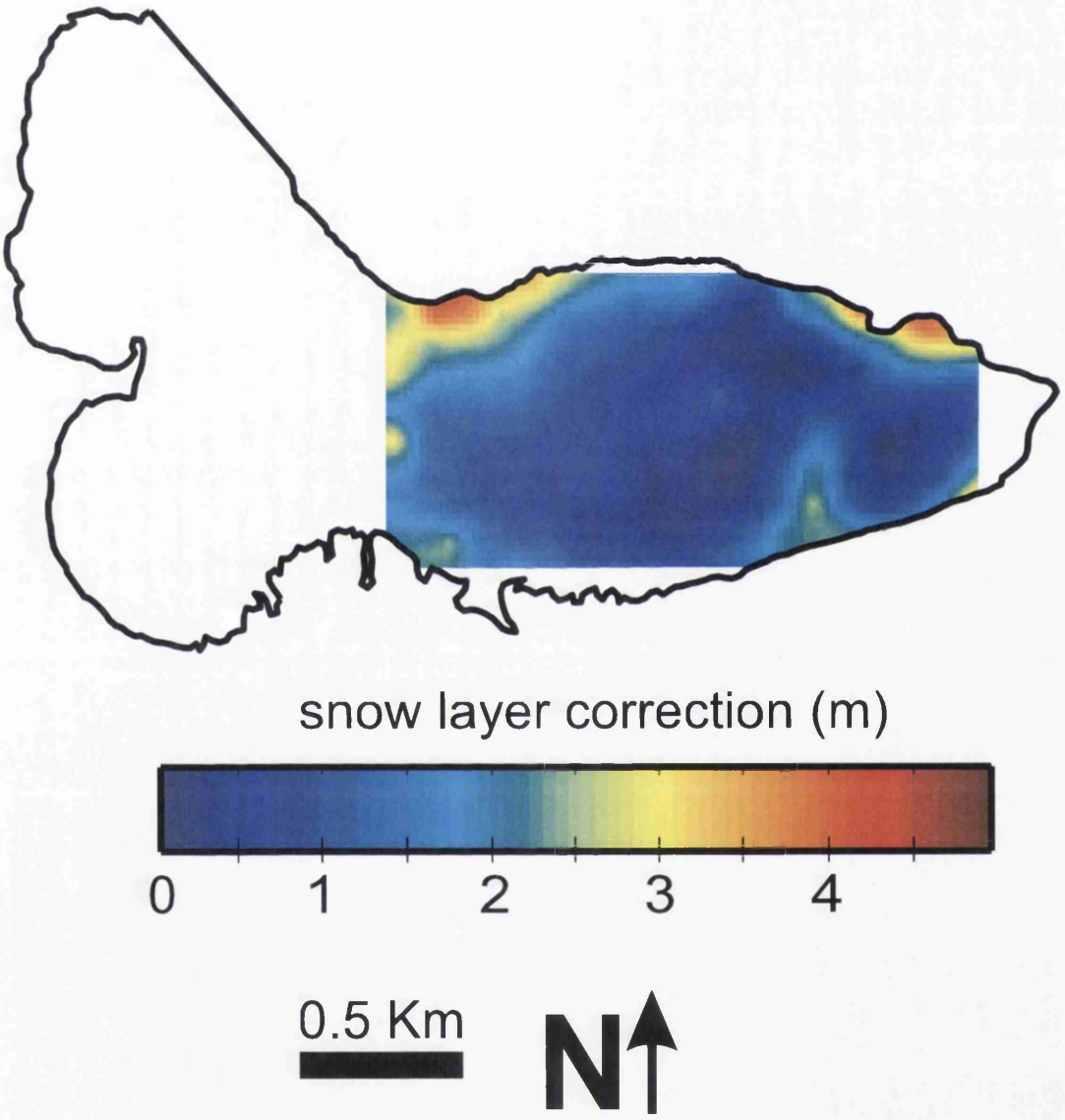

Figure 4.28: The snow layer correction in CTS depth estimates.

snow layer (Equation 4.9, Figure 4.28). The cold layer has a minimum thickness of 11 m, a maximum thickness of 42 m and an average of 25 m. The spatial pattern of the cold surface layer agrees with the background knowledge acquired throghout the years by *Holmlund and Eriksson* [1989] and *Pettersson et al.* [2003]: the thickest layer is observed in the southern margin and in the northwesterly part of the survey-area (A in Figure 4.29). The thinnest part of the layer is in center of the tongue (B in Figure 4.29) and in a region just south of the centre line which runs parallel to the glacier-flow (C in Figure 4.29). A distinct thick area which extends from the southern margin towards the centre of the glacier is also observed in the lower ablation area (D in Figure 4.29).

4.7 Comparison with previous surveys

The cold layer thicknesses as mapped by *Holmlund and Eriksson* [1989], *Pettersson et al.* [2003] and in this study are shown in Figures 4.30 a, 4.30 b and 4.30 c respectively. The thinning-trend reported by *Pettersson et al.* [2003] appears to have continued since the cold layer of Storglaciären was substantially thicker in 2001 than 2009 (Figure 4.30). In detail, the thicker bulge (B in Figure 4.29) toward the northern side of the glacier, which was $\sim$ 60 m thick in 1989, (Figure 4.30 a) lost about 50 % of its thickness and now (2009) has thickness values $<$ 35 m (Figure 4.30b). The thin region (<30 m), which runs, parallel to the glacier flow, just south of the bulge (TS in Figure 4.29), is extending since it was only a $\sim$ 20 m extend stripe in 1989 and 2001, has now doubled in length and is extending across most of the ablation area of the glacier.

These qualitative observations are supported by the thinning maps presented in Figure 4.31. The map is divided in $\mathcal{N}$ elements of area $\mathcal{A}$=100 m^2. The volume of cold ice stored in each element is thus $z_{CTS}\mathcal{A}$ The cold ice volume V is is thus given by

$$\mathcal{V} = \sum_{i=1}^{\mathcal{N}} (z_{CTS}(i))\mathcal{A}, \tag{4.11}$$

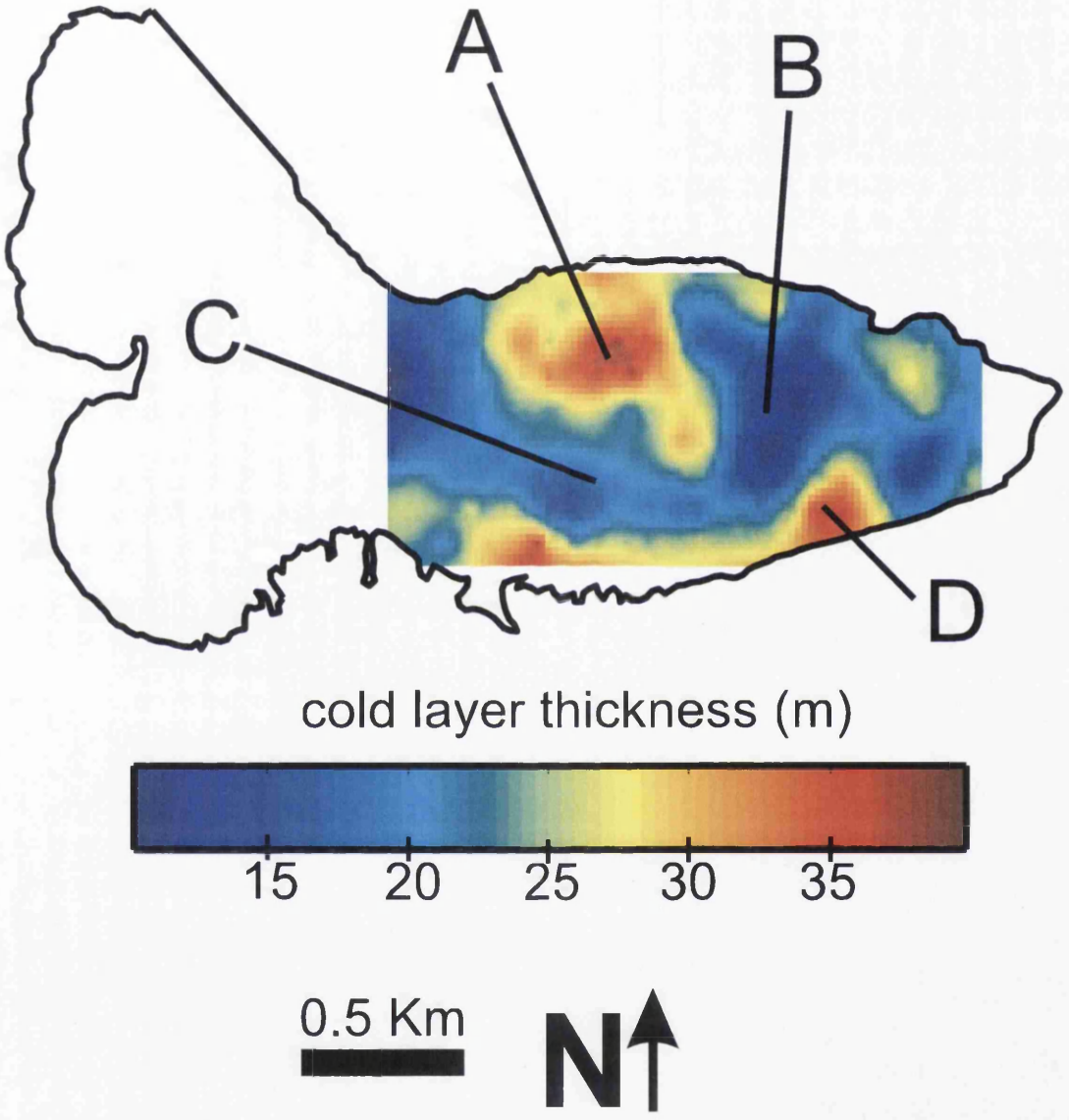

Figure 4.29: The cold surface layer of Storglaciaren in 2009. Features of the cold layer labelled here are frequently discussed in the text. This map was obtained using the spherical kriging interpolation method.

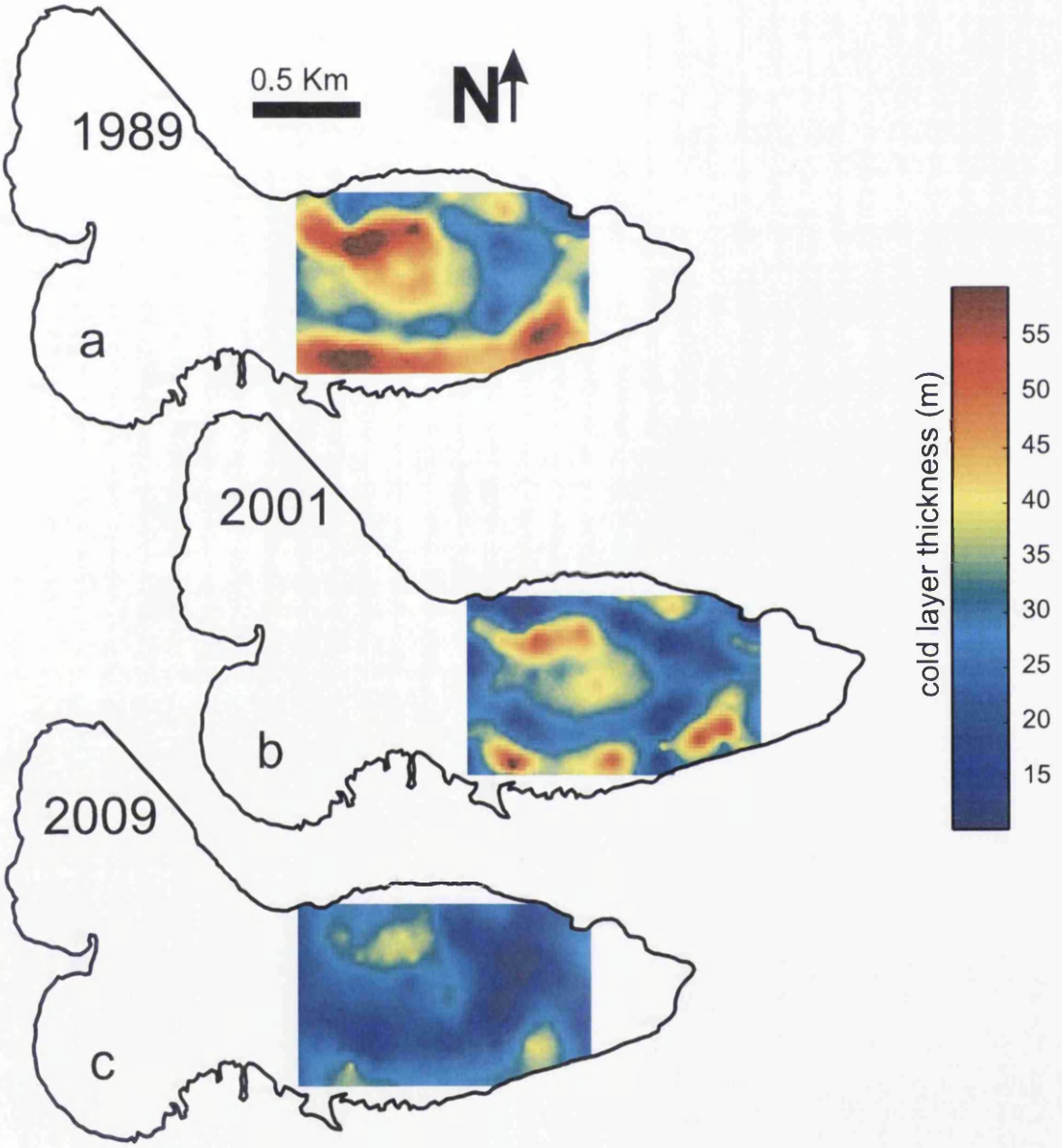

Figure 4.30: Cold layer thickness maps for 1989 (a), 2001 (b) and 2009 (c).

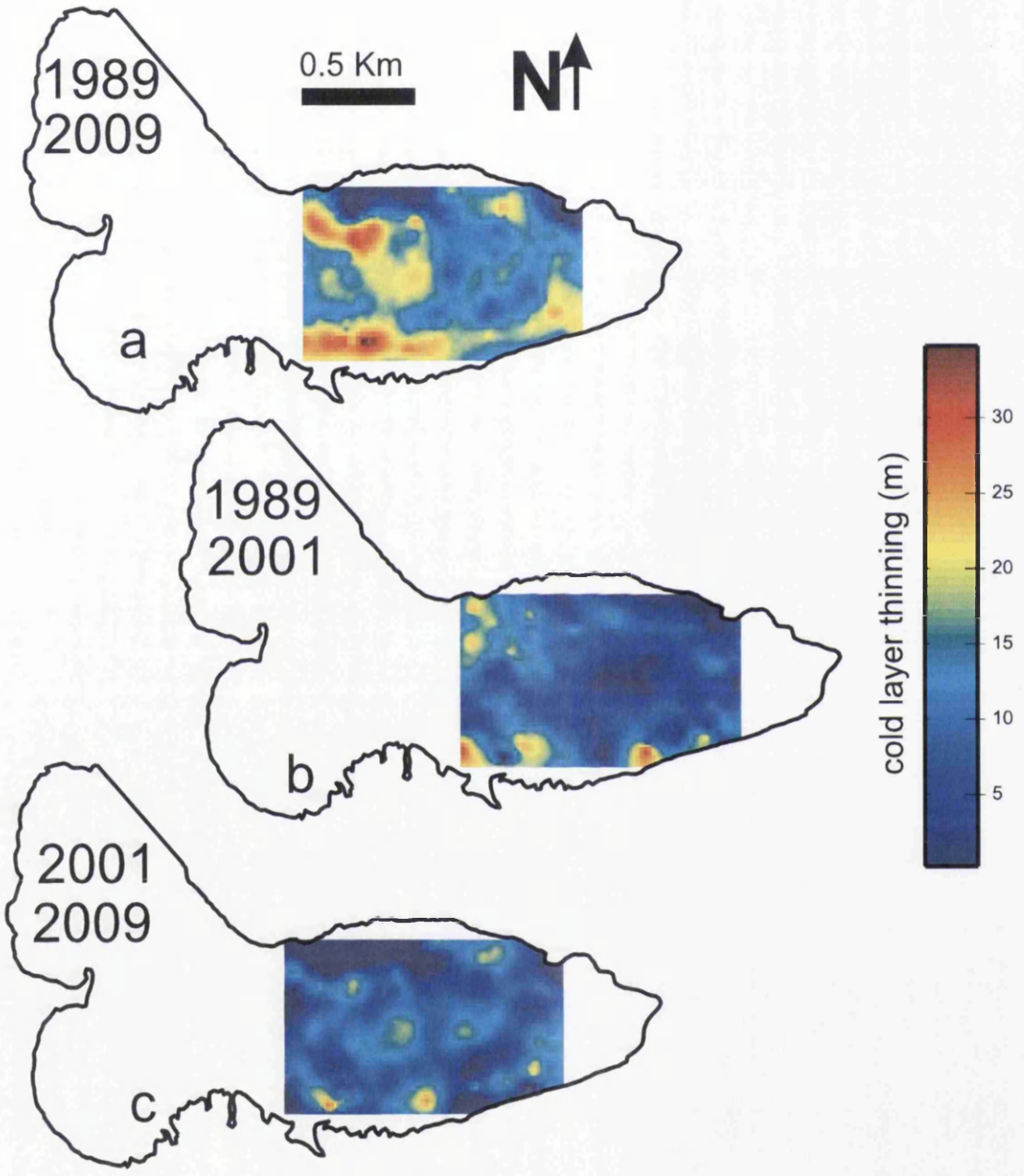

Figure 4.31: The thinning of the cold surface layer of Storgläciaren by comparing different GPR surveys. (a) 1989-2009. (b) 1989-2001. (c) 2001-2009.

similarly the error in V can be calculated from the error in CTS depth $\delta_{z_{CTS}}$ by considering that the minimum volume estimate derive from an underestimation of $\delta_{z_{CTS}}$ at each grid point on the map. Conversely the maximum estimate will be quantified by an overestimation at each grid point. The error in volume is thus given by:

$$\delta_V = \mathcal{N}\delta_{z_{CTS}}\mathcal{A}. \tag{4.12}$$

By considering CTS uncertainty in each map being ± 3 m (a lower precision than stated in *Pettersson et al.* [2003] but coherent with the experiment discussed in Section 4.3) cold ice volume is estimated to be 44.2 ± 3.4 hm^3 for 1989, 34.9 ± 3.4 hm^3 for 2001 and 27.1 ± 3.4 hm^3 in 2009. The volume calculation showed in Figure 4.32 suggest that the rate of cold layer thinning is only slightly higher for the comparison reported in this PhD study. This is also confirmed by the average thickness of the cold layer which was 38 m in 1989, 30 m in 2001 and 23 m in 2009. The thinning rate slightly increased from 0.67 to 0.87 m/a with an averaged overall rate of 0.75 m/a. Spatiotemporal variations in the cold layer are discussed in detail in section 7.1 of this thesis.

4.8 Cold based regions

The margins of the ablation area of the glacier are known to be frozen to the bedrock [*Pettersson et al.*, 2003]. Previous studies focused on the cold layer thickness and details about the cold based portions of the glacier have not been discussed in further details. In this PhD study the boundary between cold-based regions and warm based region has been picked manually on each radargram (e.g. the distinction in Figure 4.33). From each profile the position on the radargram was obtained by picking the transition. The trace number on the radargram typically corresponded to a pair of GPS coordinate which were plotted on a map in order to visualise the extent of the cold based region.

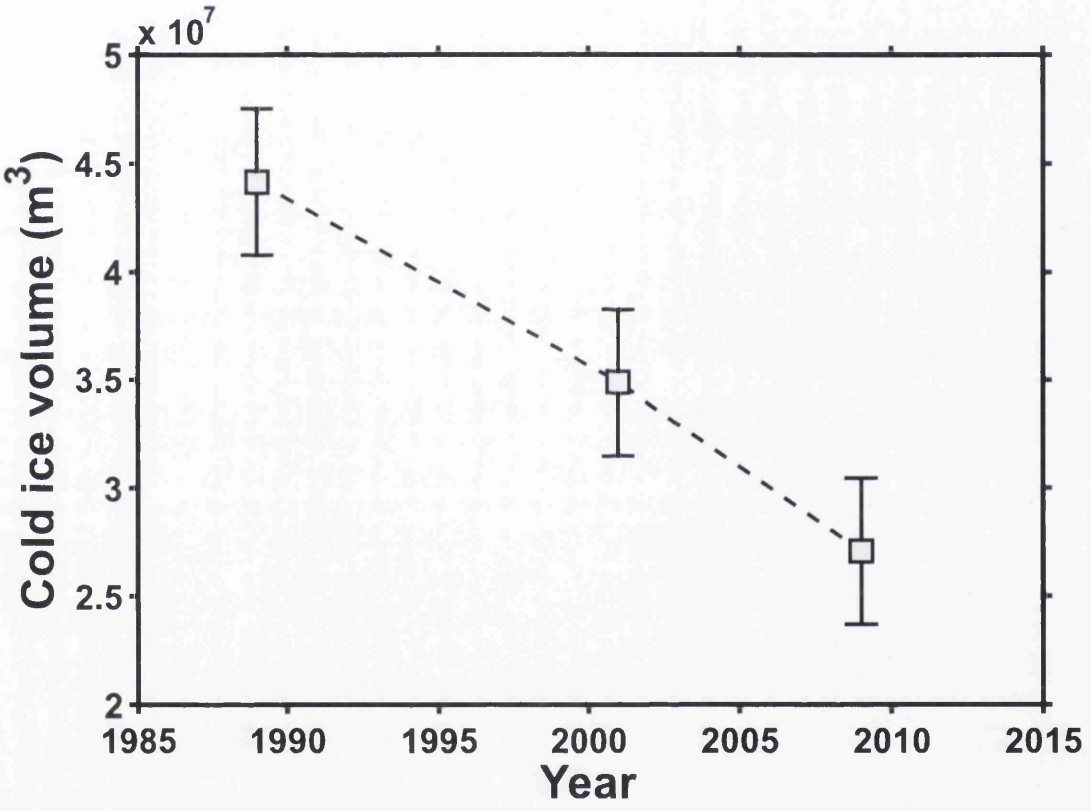

Figure 4.32: Cold ice volume computed using cold layer maps from 1989, 2001 and 2009.

Figure 4.34 shows the comparison between the cold based region in 2001 taken from *Pettersson et al.* [2003] and the cold based region obtained in this study. The comparison shows that, unlike the cold layer thickness, the areal extent of the cold-based portion of the glacier has not changed significantly from what has been previously reported.

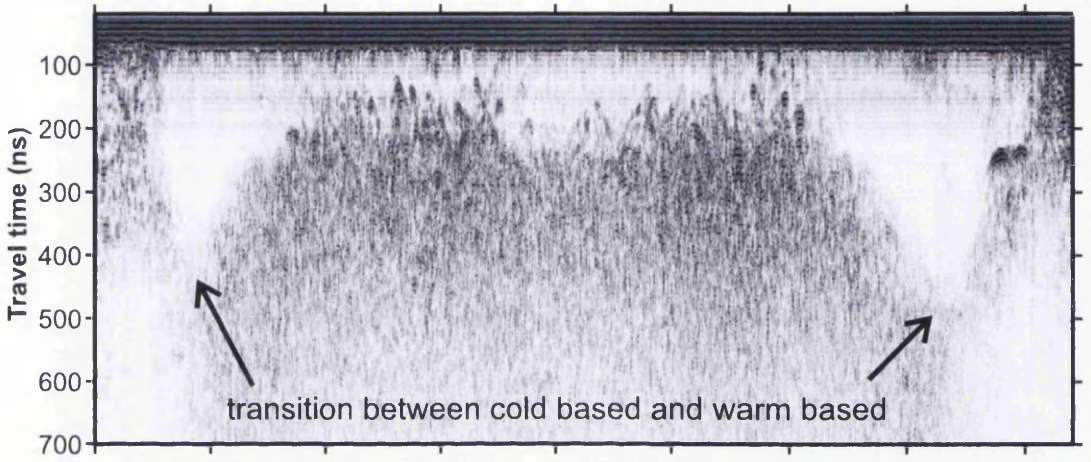

Figure 4.33: Cold based and warm based regions on the sample radargram.

4.9 Summary

A detailed set of 60 ground penetrating radar (GPR) common offset (CO) surveys collected in April 2009, have been used to map the thermal structure of the ablation area of Storglaciären. The technique allows the separation in a radargram of scattering-free and scattering-rich regions which are interpreted to be cold ice and temperate ice respectively. Direct comparison between 100 MHz radar data and temperature data showed that the accuracy in CTS mapping for this study is ± 2 m, a lower precision than previously reported for higher frequencies. CTS depth estimates were obtained by assuming a constant radio wave speed in the cold ice of 0.168 m/ns. Kriging interpolation and variogram performance was tested in order to produce a map of cold-ice thickness. The resulting map of the year 2009 was compared with maps collected in 1989 and 2001. The comparison shows that the

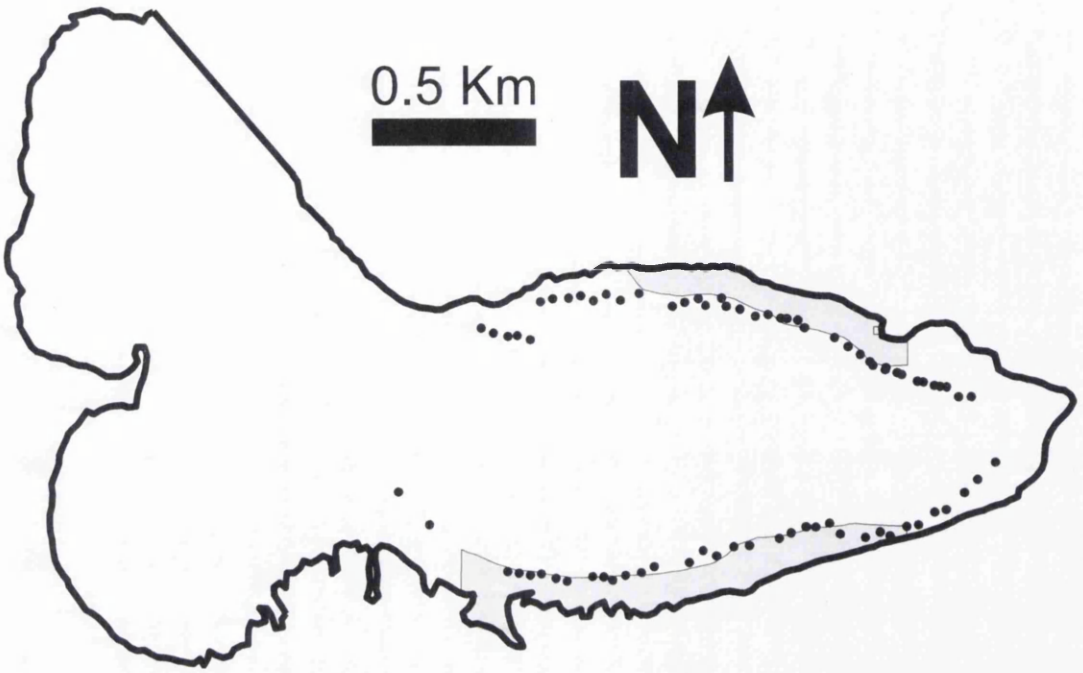

Figure 4.34: Cold based regions of Storglaciären. The gray area was redrawn from *Pettersson et al.* [2003] to visualise the cold based portion reported for the year 2001. The dots indicate results from this study. No significant changes occurred between 2001 and 2009.

recent thinning of the cold layer between 1989 and 2001 is still ongoing. The thinning rate (or cold ice volume-loss) in the two time windows analyzed (1989-2001; 2001-2009) appear to be very similar with only a minor increase in the last decade. The thinning pattern changed spatially, however, as the highest thinning from the 1989-2001 comparison was observed in the margins as compared with preferential thinning in the centre of the glacier between 2001 and 2009. On average the thicker part of the cold layer measured in 1989 in the northwesternly part of the study area has lost about $\sim$ 40 % of its entire thickness between 1989 (50 m) and 2009 (30 m). A volume calculation showed that the cold surface layer of Storglaciären has lost one third of its volume in 20 years with a mean thinning rate of 0.75 m/a.

Chapter 5

Vertical distribution of water with depth

Considerable research has been focused on defining theoretical principles and numerical modeling of polythermal glaciers [*Fowler and Larson*, 1978; *Fowler*, 1984; *Hutter et al.*, 1988; *Blatter and Hutter*, 1991; *Aschwanden and Blatter*, 2005, 2009]. A vital component of such models is knowledge about the temperature and water content distribution since they both strongly affect ice viscosity *Glen* [1955]; *Duval* [1977]. The viscosity parameter A (also known as the rate factor) varies with temperature T and percentage water content W according to [*Paterson*, 1994]:

$$A(\theta, W) = A_0(W) \exp(-E_{creep}/RT), \tag{5.1}$$

where $A_0(W)$ is a temperature independent, water-content dependent ice viscosity [*Duval*, 1977; *Paterson*, 1994], E_{creep} and R are the activation energy for creep in ice (139 kJ/mol for T >-10°C [*Paterson*, 1994] and the universal gas constant (8.134 J/mol K), respectively.

Equation 5.1 shows that accurate quantification of both T and W is required to predict the mechanical behavior of polythermal glaciers. Despite this fact, there is a lack of data providing detailed experimental evidence of coincident measurements of

temperature and water-content distributions in polythermal glaciers. Many workers have reported temperature profiles with depth for polythermal glaciers in Scandinavia [*Hooke et al.*, 1983], Canadian Arctic [*Blatter and Kappenberger*, 1988], China [*Maohuan*, 1990] and Svalbard [*Björnsson et al.*, 1996], but there are only two polythermal glaciers in which temperature and water-content estimates (published with measurement error) have been compared. These two glaciers are Bakaninbreen in Svalbard [*Murray et al.*, 2000a, 2007] and Storglaciären [*Pettersson et al.*, 2004]. These studies rigorously reported temperature profiles within the ice column, but only gave one single estimate of W in the temperate ice. Since *Murray et al.* [2000a, 2007] obtained a bulk average W = 1.29 (+1.68, -1.14) % for the whole 40 meter thick temperate layer of Bakaninbreen, and [*Pettersson et al.*, 2004] estimated average W=0.8±0.3% at the CTS of Storglaciären, it is clear that there is a lack of knowledge on how water content in mWS varies with depth in polythermal glaciers and how we can include this parameter in modelling ice rheology.

Current understanding of the spatial distribution of water content within glaciers comes largely from geophysical investigations, because changes in the propagation speed and attenuation of radio and seismic waves can be related to variations in the water content of glaciers [*Looyenga*, 1965; *Paren*, 1970; *Bradford and Harper*, 2005; *Endres et al.*, 2009]. The strong dielectric contrast between glacier ice and liquid water makes radio-wave speed profiling particularly efficient when describing the hydrothermal state of ice masses. Speeds higher than 0.168 m/ns are typical of dry, water-free ice, while lower speeds are typical of ice which contains some volumetric percentage of liquid water [*Macheret et al.*, 1993; *Murray et al.*, 2000a; *Bradford and Harper*, 2005; *Gusmeroli et al.*, 2008]. However, the presence of air in wet ice can complicate this interpretation [*Bradford and Harper*, 2005; *Gusmeroli et al.*, 2008].

In this chapter vertical profiles of water content with depth at Storglaciären are presented. Such estimates were obtained using detailed radio-wave speed profiles acquired by borehole radar zero offset profiling (ZOP) [*Peterson*, 2001; *Binley et al.*, 2001; *Huisman et al.*, 2003]. Published examples of borehole radar techniques for glaciology are scarce. *Murray et al.* [2000a] used vertical radar profiles from Iceland

and ZOP is a relatively novel application in the glaciological science. Parts of this Chapter are published in *Gusmeroli et al.* [2010b].

5.1 Data collection

ZOP profiles at Storglaciären were collected over two consecutive summer seasons lasting three month in total in summer 2008 and summer 2009. In the 2008 campaign the ZOP experiments were tested at only one study area in the upper ablation area of the glacier. The 2009 campaign exploited the survey experience gained during 2008 and two additional locations of the glacier were explored. These location were near the equilibrium line and in the lower ablation area of the glacier. Annual variations were also investigated by repeating ZOP surveys in the same study area as in 2008. Figure 5.1 shows the three study areas investigated in this study, whereas Table 5.1 lists details for all the ZOP surveys acquired in the two campaigns. Geometry and relative distances between boreholes involved in the study are illustrated in detail in Figure 5.2.

5.1.1 Study sites

The three study areas differ considerably in terms of glaciological regime (Figures 5.1 and 5.3). Study area A is located in the higher part of the accumulation area, not very far from the equilibrium line altitude (ELA in Figure 5.1) at the altitude of ~1395 m. A is located at the higher boundary of the so called *flat area* of Storglaciären. Steepness of the glacier surface is considerably higher upglacier than A. Site A also presented other two peculiarities: (i) it is located where the NW thick flow-units join with the rest of the glacier, and (ii) being the higher site studied it still preserved some slush-snow at the end of August whereas at site B and C there was no sign of remaining snow cover since mid-July in both years. The presence of snow (Figure

Site	Survey	$\overline{Z}(m)$	f (MHz)	Date	$\Omega(°)$	z(m)	x (m)	X(m)	Fig.
A2009	Ah1h2	1394	100	25.08	8	112	29.4	42.2	5.1b
	Ah1h3	1394	100	27.08	56	64	37.5	51.2	5.1b
	Ah2h3	1394	100	27.08	106	64	21.4	29.2	5.1b
	Ah3h5	1394	100	28.08	82	64	41.7	47.2	5.1b
	Ah4h5	1394	100	28.08	101	74	23.8	28.8	5.1b
B2009	Bh1h3	1353	100	01.08	86	86	29.4	30.0	5.1c
	Bh2h3	1353	100	04.08	136	87	22.6	38.1	5.1c
B2008	B2h1h2	1359	100	21.07	2	84	25.3	25.5	5.1d
	B2h1h3	1359	100	21.07	26	74	30.5	39.0	5.1d
C2009	Ch1h2	1280	100	11.08	0	96	27.0	29.7	5.1e
	$Ch1h2_1$	1280	100	12.08	0	96	27.0	29.7	5.1e
	Ch2h3	1280	100	13.08	138	90	40.6	44.9	5.1e
	Ch3h4	1280	100	14.08	2	90	33.2	34.1	5.1e
	$Ch3h4_1$	1280	250	14.08	2	90	33.2	34.1	5.1e
	Ch5h6	1280	100	19.08	46	90	31.2	52.6	5.1e
	$Ch5h6_1$	1280	250	19.08	46	90	31.2	52.6	5.1e

Table 5.1: Details of the ZOP surveys collected in the two campaigns. $\overline{Z}$ is the mean altitude derived from dGPS measurements; f is frequency; Ω is the azimuth of the ZOP survey; z is the maximum depth investigated; x and X indicate minimum and maximum antenna separation respectively. Differences in $\overline{Z}$ estimated with the dGPS at site B summer 2008 and 2009 are due to ablation.

5.3) did not facilitate choosing the drilling site since channelized supraglacial flow (necessary to obtain melt-water for drilling) was scarce.

Site *B* (1359 m) was located in the upper ablation area and was the only site investigated in both years. Its position was slightly to the south of the center line of the glacier. The topography of this area is essentially flat (Figure 5.1). Crevasses and moulins were noticeably absent in this area and the glacier was overridden by numerous decimetric-wide meltwater channel which made the area very convenient for drilling operation. The drilling site B was chosen because of the presence of a thermistor-string which was already in-place at the time of the first campaign (July 2008). The site was upglacier of the transverse bedrock ridge called *the riegel* which is known to underlie Storglaciären in its lower ablation area [*Jansson*, 1995, 1996]. Subglacial hydrology of this part of the ablation area is known to be dramatically different of those observed at the site C located downglacier from the riegel at 1278 m [*Jansson*, 1995]. Water pressures measured above the riegel are relatively constant while down-glacier from it they vary significantly [*Jansson*, 1995]. The lower part of the ablation area (of which site C is representative) accelerates in response to weather-induced peaks in basal water pressure whereas the upper part (site B) does not. *Jansson* [1995] suggested that the upper part may be weakly coupled to the lower part during these peaks.

5.1.2 ZOP, Zero Offset radar Profiling

ZOPs were collected in both seasons using a Måla Geoscience RAMAC GPR system. ZOP is a commonly used geophysical method to obtain high resolution radio-wave speed reconstruction of the subsurface. This method has been successfully used to monitor hydrogeological dynamics in the unsaturated zone of aquifers [*Binley et al.*, 2001, 2002] and the spatial distribution of biogenic gas in peatlands [*Comas et al.*, 2005]. In a ZOP survey, an EM pulse is radiated from a transmitting antenna (Tx), located in one borehole, and recorded at the receiving antenna (Rx), located in an adjacent borehole (Figure 5.4). The antennas are then progressively lowered down

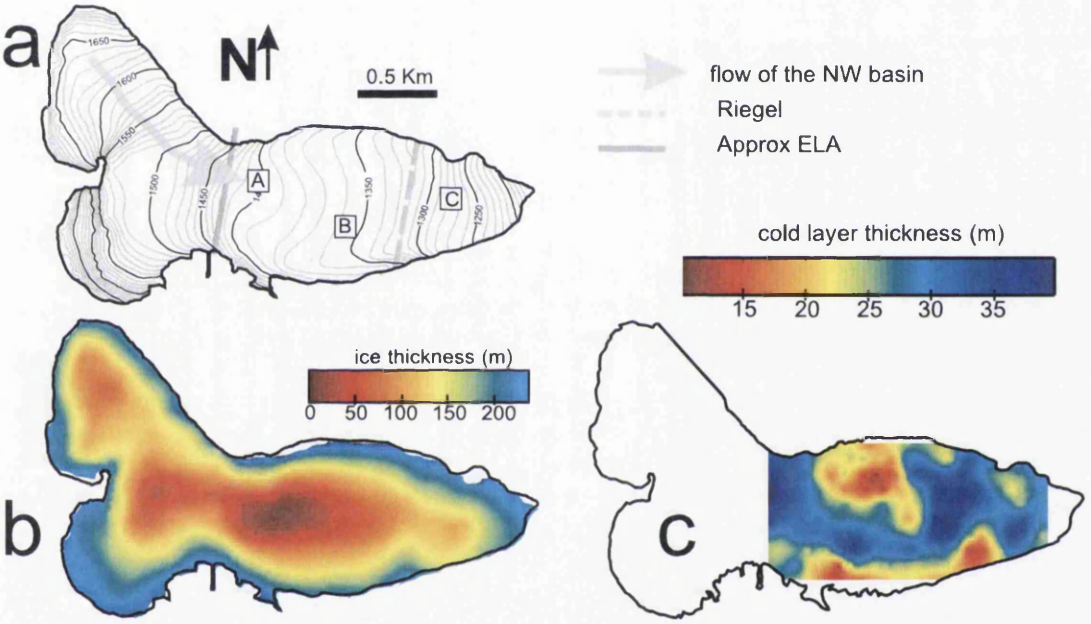

Figure 5.1: (a) Map of the location of the ZOP experiments presented in this chapter. Study area B was surveyed in both summer 2008 and summer 2009 whereas A and C were surveyed in 2009 only. The ice thickness map (b, data courtesy of P. Jansson and Tarfala Research Station) and the cold layer thickness map (c, from Chapter 4) are also shown to provide glaciological background to the ZOP surveys.

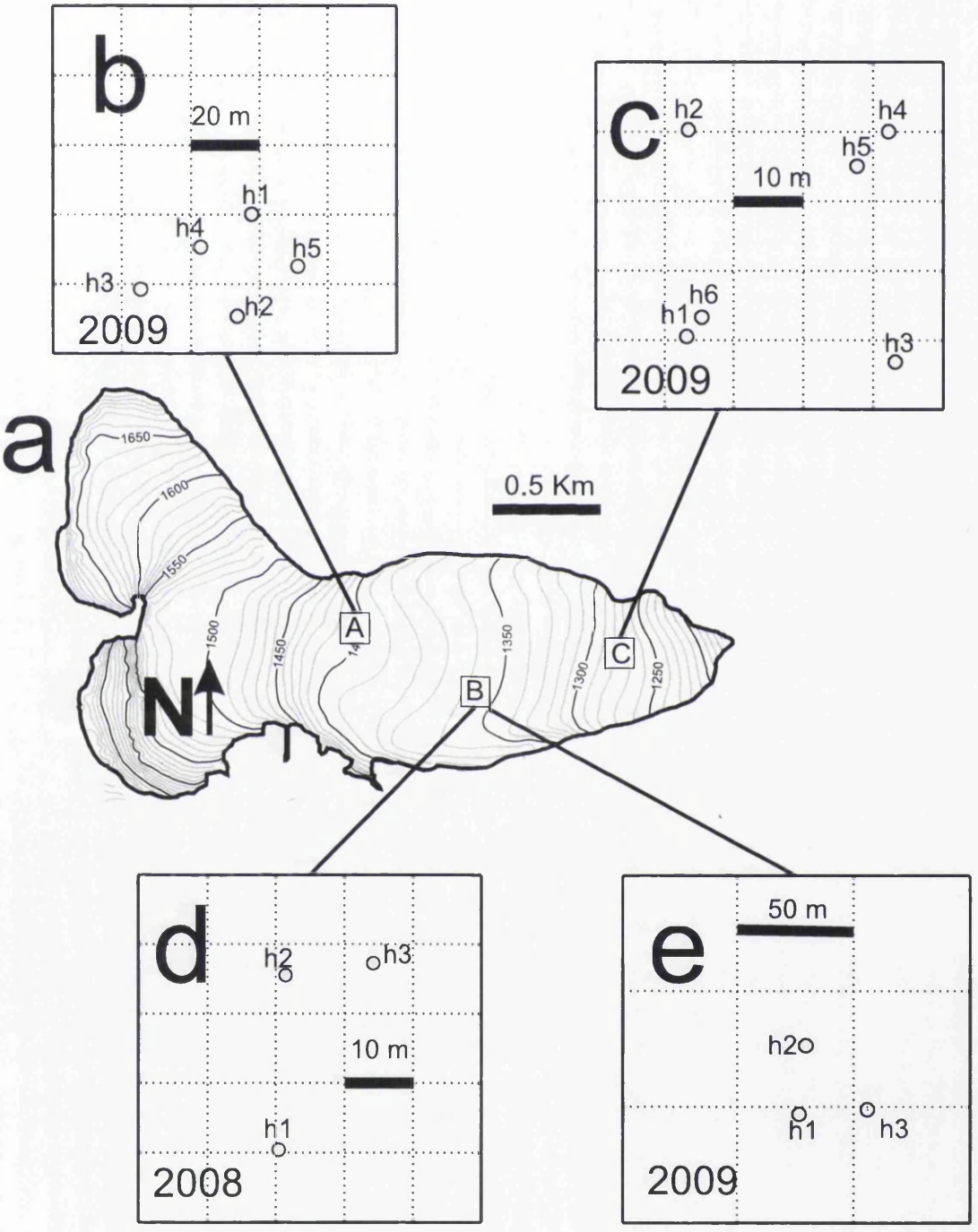

Figure 5.2: Map of the boreholes used for ZOP profiling in this chapter.

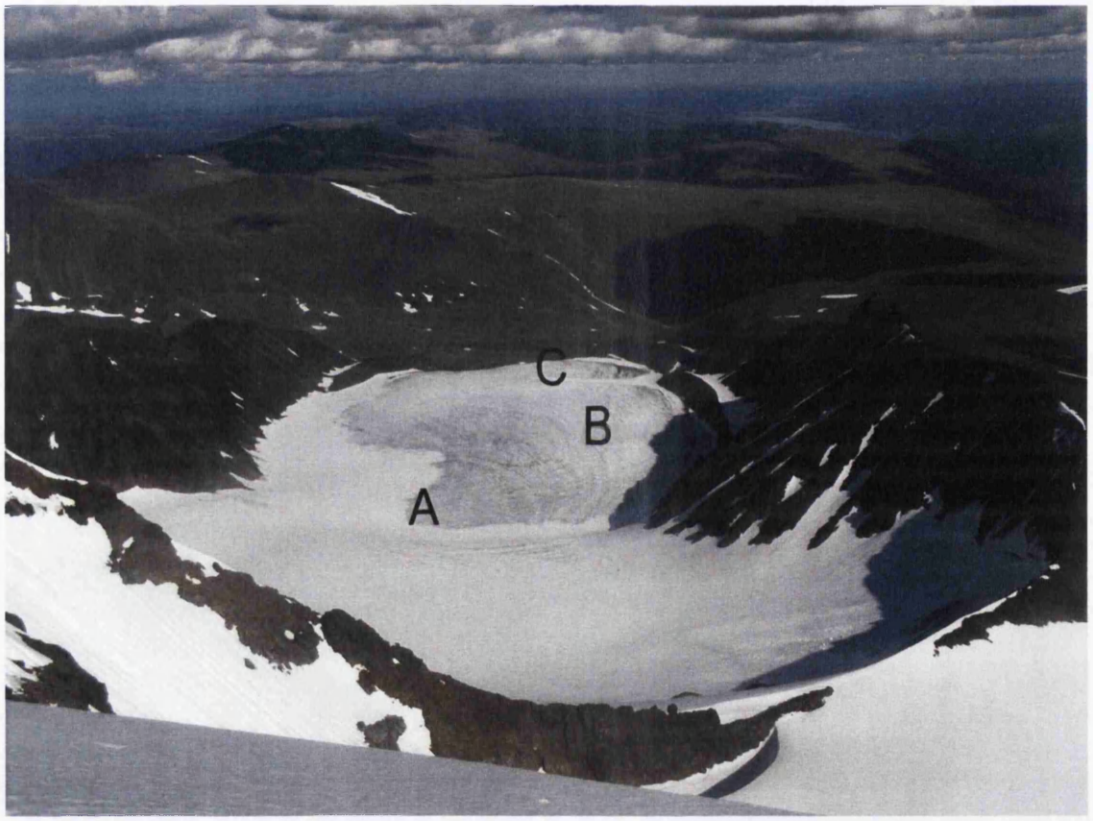

Figure 5.3: Storglaciären from Kebnekaise on the 27.07.2008. From this picture, taken from Sweden's highest point, is possible to see all the sites listed in Figures 5.1 and 5.2.

the two boreholes with the transmitter and receiver at the same depth in each. We used a 1-m depth step and, for each antenna depth, the time required for EM radiation to travel through the inter-borehole region was measured. This type of survey also provides the opportunity to measure amplitudes of the EM pulse at each depth. At the beginning and end of every survey, a few traces were collected in the air at a known antenna separation to provide a time-zero calibration. Survey tripods were used to hold the antennas still during measurements. All the boreholes were termi-

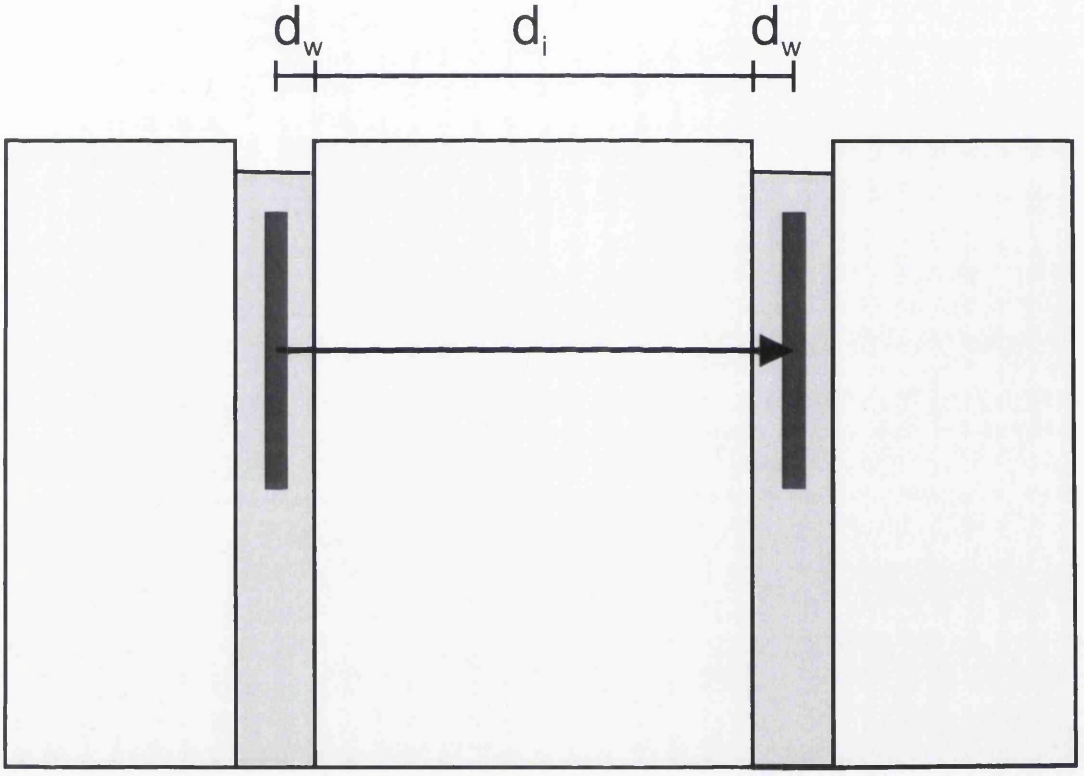

Figure 5.4: Sketch illustrating the geometry of a ZOP survey; d_w and d_i are the propagation paths in water and ice respectively.

nated englacially to reduce the likelihood of subglacial drainage. The holes remained water-filled for the duration of the study suggesting that no efficient hydraulic connection was established between the boreholes and the englacial water system. The location of the top of the boreholes was surveyed using differential GPS observations, while the geometry of the holes (i.e., how they deviate from vertical) was measured using an inclinometer (MI-3 Digital Borehole Survey Tools from Icefield

Instruments Inc). This instrument determines the geometry of a borehole relative to its top at a series of measurement stations down its length. The orientation is represented by the measured dip and azimuth readings. Measurement stations (or shots) were collected every 2 m downhole.

Obtaining ZOP on glaciers is not simple, there are many logistic challenges that need to be addressed, not least the transport with an helicopter of an hot-water drill, together with sufficient quantities of gasoline and diesel to run the engines. The basic description of the hot-water drill operations is that running meltwater is redirected into a boiler by the means of a pressurizing pump. The boiler heats up the water and such water is redirected by the means of hoses into a drill-end which is the actual drill. Boreholes need to be wide enough to allow inserting of the radar antennas and such wideness has to be preserved throughout the whole length of the borehole. The shortest surveys collected in the campaigns (e.g. in Ah1h3, Ah2h3, and Ah3h5; see Table 5.1) were due to insufficient wideness of one the boreholes (hole 3 at site A) which did not allow deeper investigations. The maximum depth reached by the boreholes was highly variable (see Table 5.1), in a range between 112 and 96 m.

5.1.3 ZOP radargrams

The outcome of a ZOP is a radargram on which the arrival travel time of a radio-wave propagating between the inter-borehole region can be estimated. Dewowed radargrams (see Chapter 4 for details about dewow filters) for the three sites are shown in Figures 5.5, 5.6 and 5.7. All the radargrams present similar clear first arrivals in the ice. Additional features common for all the ZOP radargrams are (i) a weak series of radar returns at low-depth and early travel-times with linear increase of travel time with depth (particularly clear in Figure 5.5 b just below the letter *b*) and (ii) an hyperbolic series of returns which arrive after the first arrivals in the ice. Such event is very clear in some radargrams (e.g. in Figures 5.7 g to l and Figure 5.5d and 5.5e) whereas is nearly absent in others (Figures 5.6c, 5.6d, 5.6e, 5.7a and

5.7b. A clear illustration of the events recognizable from a sample ZOP radargram is given in Figure 5.8.

We can approximate the travel-path of a propagating radio wave using geometric optics. With such procedure travel-path and consequent travel-times can be modelled to correctly identify the events depicted in Figure 5.8. Given the radio wave velocity in ice v_i, radio wave velocity in air c, antenna separation distance X , the depth z the propagating time of a direct wave in the ice and a reflected wave from the ice air interface T_D and T_R respectively:

$$T_D = \frac{X}{v_i}, \tag{5.2}$$

$$T_R = 2\sqrt{\left(\frac{x^2}{2} + Z^2\right)}, \tag{5.3}$$

A third arrival, the critically refracted travel-path should also be considered. Although such arrivals rarely bring useful information about subsurface's properties few workers have studied their characteristics in order to avoid misinterpretation in radioglaciology [*Gusmeroli et al.*, 2008] and hydrogeology [*Rucker and Ferré*, 2004; *West and Truss*, 2006]. This is because a pulse generated at depth will refract critically at the boundary along the glacier-air interface, the traveltime of the critically-refracted raypath is thus given by :

$$T_{\text{refr}} = \frac{X}{c} + Z\left(\frac{2}{v_i \cos i_c} - \frac{2\tan i_c}{c}\right), \tag{5.4}$$

[*Rucker and Ferré*, 2004], where z is depth, and i_c is the critical angle defined by the Snell's Law:

$$i_c = \sin^{-1}\left(\frac{v_i}{c}\right). \tag{5.5}$$

Modelled travel-times for the three different arrivals using equations 5.2, 5.3 and 5.4 for X=25 m and v_i=0.168 m/ns are shown in Figure 5.8. The modelled travel-times coincide nicely with the events observed in reality and therefore the interpretation shown in Figure 5.8a and 5.8b is valid for all the ZOPs illustrated in this chapter.

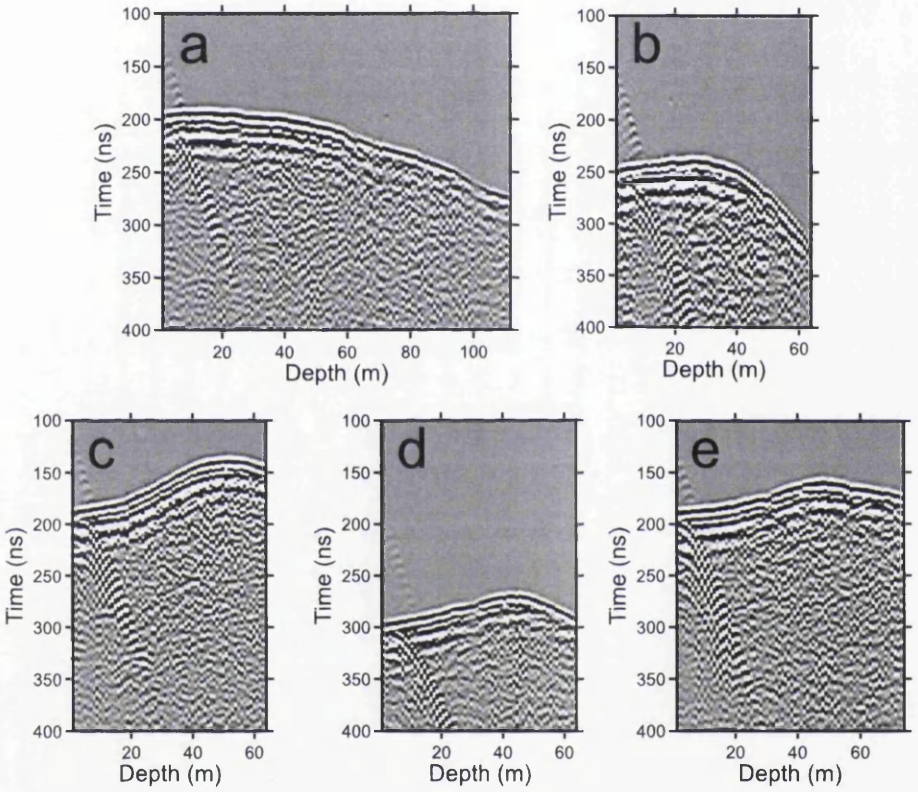

Figure 5.5: ZOP radargrams collected at site A. Details of the surveys are listed in Table 5.1. Maps of the surveys are shown in Figure 5.2. (a) Ah1h2; (b) Ah1h3; (c) Ah2h3; (d) Ah3h5; (e) Ah4h5.

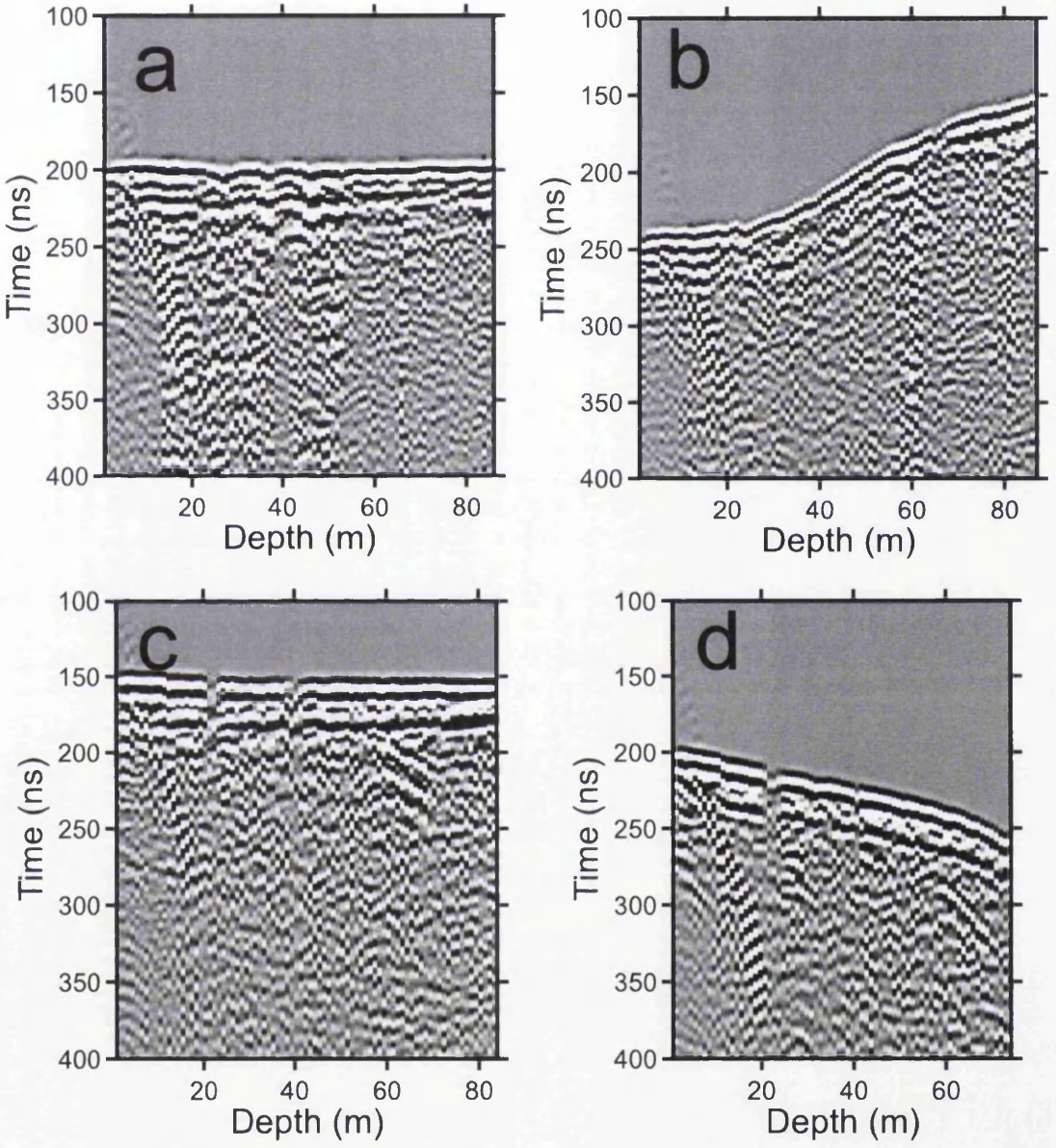

Figure 5.6: ZOP radargrams collected at site B. Details of the surveys are listed in Table 5.1. Maps of the surveys are shown in Figure 5.2. (a) Bh1h3; (a) Bh2h3; (c) B2h1h2; (d) B2h1h3.

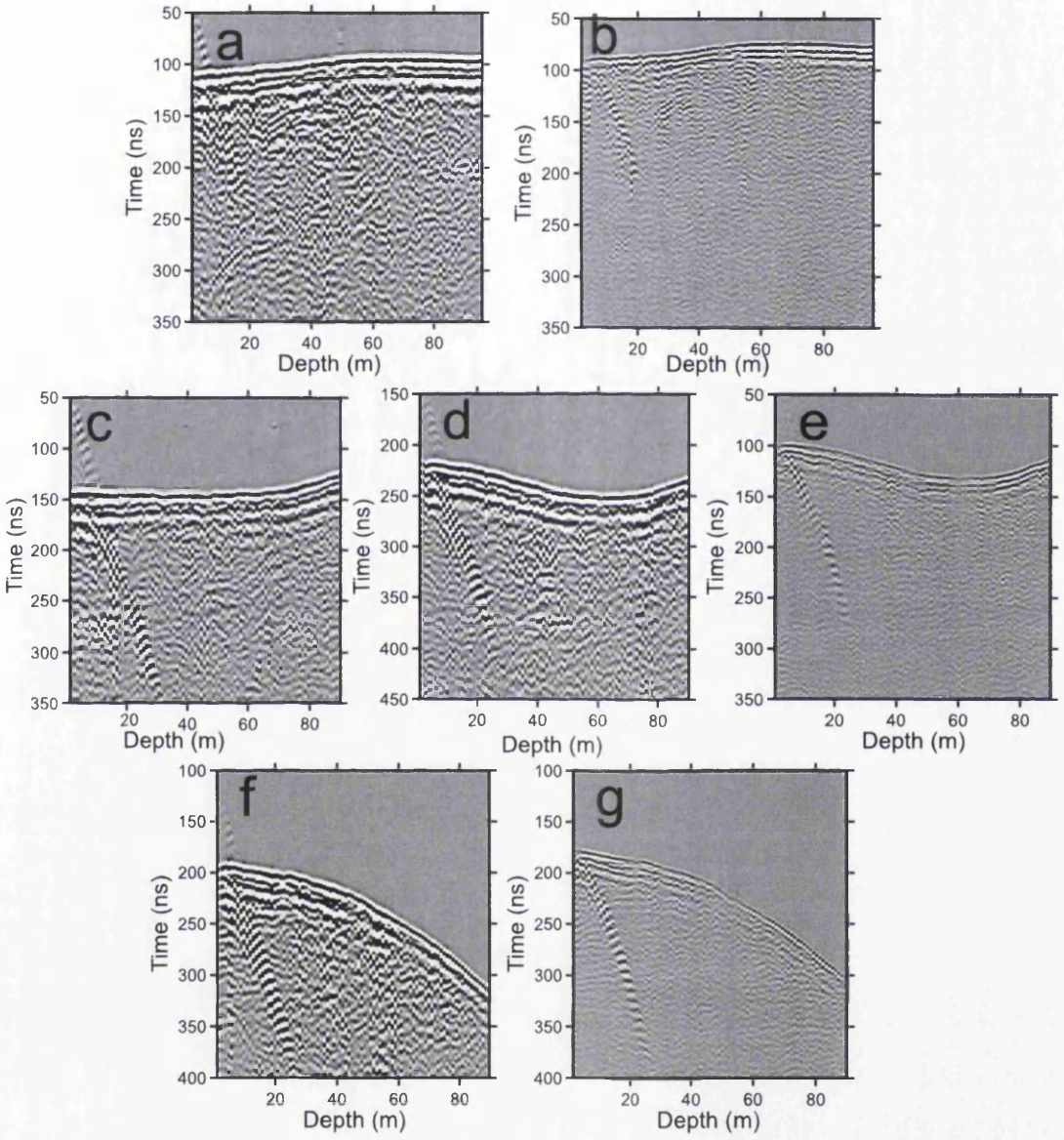

Figure 5.7: ZOP radargrams collected at site C. Details of the surveys are listed in Table 5.1. Maps of the surveys are shown in Figure 5.2. (a) Ch1h2; (b) $Ch1h2_1$; (c) Ch2h3; (d) Ch3h4; (e) $Ch3h4_1$; (f) Ch5h6; (g) $Ch5h6_1$.

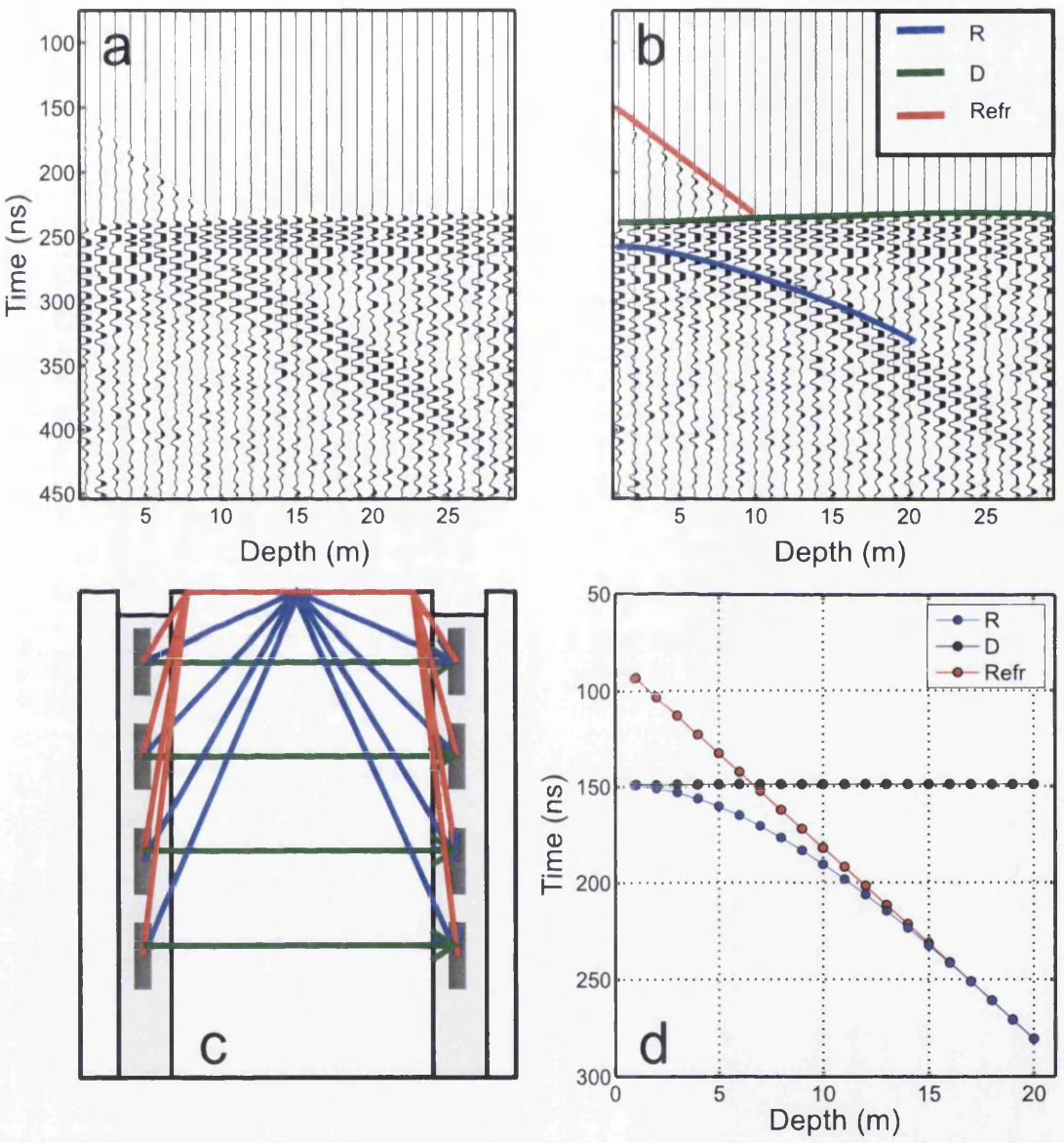

Figure 5.8: Ah2h3 (a) with direct arrivals in the ice (D), reflected arrivals from the ice-air interface (R) and critically refracted arrivals (Refr) shown in (b). (c) Schematic of a ZOP survey with the main travelpath indicated. Modelled travel-times for the three different arrivals using equations 5.2, 5.3 and 5.4 for X=25 m and v_i=0.168 m/ns.

5.2 Radio-wave speed estimates and measurement error

5.2.1 Obtaining speed estimates

The radar system used in this study required a time zero calibration due to a time delay in the electronics. If the survey is started with both antennas in the boreholes, the radar pulse arrives at Rx at an unknown delay which prevents radio-wave speed estimates. Such problem was avoided starting the survey by acquiring a few traces holding both antennas in the air at known antenna separation X. Since EM velocity in air is $c = 0.300$ m/ns the time delay in the system T_{DEL} is given by:

$$T_{DEL} = T_a - \frac{X}{c}, \tag{5.6}$$

where T_a is the first break of the wave propagating in the air. After this calibration the ZOP survey can start and at any depth we can calculate the the true travel time between the transmitted and recorded signal , $T_M = T_P - T_{DEL}$, where T_P is the first break of the in-hole recorded wave. The time calibration was repeated at the end of the survey to detect any drift in the time zero which could cause misinterpretation.

Distances between the tops of the two boreholes were computed using the Easting and Northing coordinates from the GPS surveys. Variations in borehole separation with depth were adjusted using the inclinometry data whereas, since at any depth the antenna positions are geometrically described by their easting (E) and Northing (N), the actual distance in ice D_M is given by:

$$D_M = \sqrt{(E_1 - E_2)^2 + (N_1 - N_2)^2}, \tag{5.7}$$

where the subscripts 1 and 2 indicate the transmitting and receiving antennas respectively. The radio-wave speed v_i in the glacier-ice mixture is then given by D_M/T_M.

Radio wave speed estimates are sensitively dependent on the definition of the first break. The first break of a propagating radio wave has been discussed in Section 4.2.2 (Figure 4.7). For the ZOP surveys presented in this chapter an additional complication to the definition given in Section 4.2.2 is introduced by the presence of the critically refracted waves (Figure 5.8) and by the presence of random noise which corrupted the automatic picking. For these reasons first breaks were picked manually for each trace as the first sample exceeding the noise floor. Figure 5.9 shows a detail of the picked first breaks for Ah1h2.

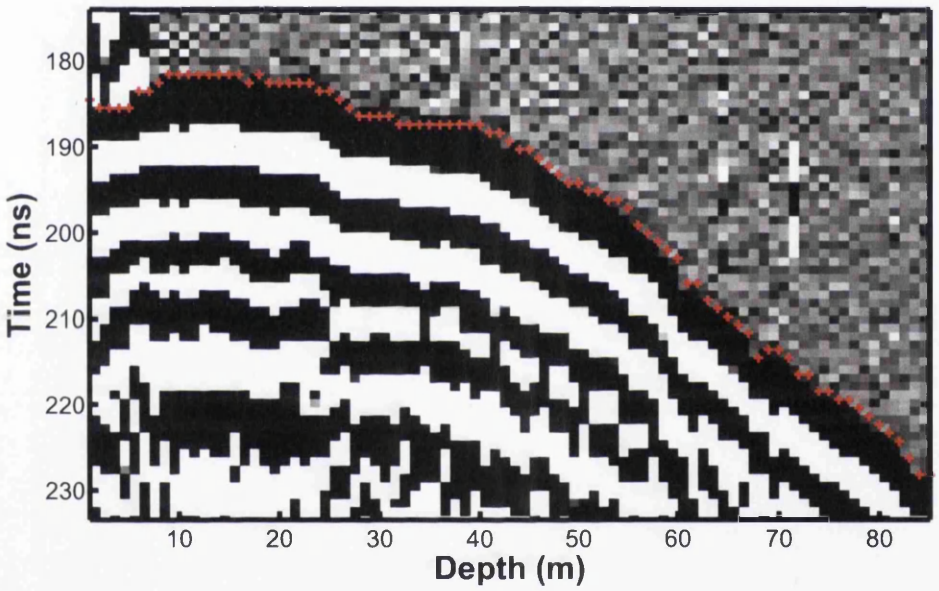

Figure 5.9: Picked first breaks for Ah1h2. Amplitudes are scaled in the way that the maximum amplitude is at 5% above noise level.

5.2.2 Measurement error

The error associated with radio wave speed estimates is the final error which derives from the combination of the uncertainties in measuring each parameter used in the calculation. Therefore since errors will affect the estimates of delay T_D (Equation 5.22), time T_M and distance D_M (Equation 5.7) the treatment of the total error will follow the rules of error propagation for compound quantities [*Topping*, 1972]. The

standard rules for treating errors [*Topping*, 1972] are commonly used to estimate the error of compound quantities, this methodology has been previously used in estimating geophysical quantities in glaciers by *Barrett et al.* [2007], *Gusmeroli et al.* [2008] and *Gusmeroli et al.* [2010a]. These rules are defined as:

$$\delta_{m1m2} = \sqrt{m_1^2\delta_{m2}^2 + m_2^2\delta_{m1}^2}, \tag{5.8}$$

for the standard error of the product of m1 and m2 which have standard errors δ_{m1} and δ_{m2} respectively;

$$\delta_{m1\pm m2} = \sqrt{\delta_{m1}^2 + \delta_{m2}^2}, \tag{5.9}$$

for the sum or the difference of the two quantities;

$$\delta_{m1^p} = (pm_1^{p-1})\delta_{m_1}, \tag{5.10}$$

for the quantity m_1 raised to the power of p;

$$\delta_{km_1} = k\delta_{m1}, \tag{5.11}$$

for the quantity m_1 multiplied by a constant k.

By applying these rules and defining δ_X, $\delta_{X/c}$ and δ_{T_a} as the standard errors in X, X/c and T_a respectively, we can demonstrate that the error in estimating the system delay $\delta_{T_{DEL}}$ is given by:

$$\delta_{T_{DEL}} = \sqrt{\delta_{X/c}^2 + \delta_{T_a}^2}, \tag{5.12}$$

similarly, the error in measured travel time within the inter-borehole region δ_{T_M} is given by considering the error in picking δ_{T_P}:

$$\delta_{T_M} = \sqrt{\delta_{T_P}^2 + \delta_{T_{DEL}}^2}, \tag{5.13}$$

The computation of the error in distance δd has been done using the simple error associated with the easting and northing measurements (Equation 5.7). The error in $E_1 - E_2$ and $N_1 - N_2$, $\delta_{E_1-E_2}$ and $\delta_{N_1-N_2}$ respectively are given by (eq 5.9):

$$\delta_{E_1-E_2} = \sqrt{\delta_{E1}^2 + \delta_{E2}^2}, \tag{5.14}$$

$$\delta_{N_1-N_2} = \sqrt{\delta_{N1}^2 + \delta_{N2}^2}; \tag{5.15}$$

the error in $(E_1 - E_2)^2$ and $(N_1 - N_2)^2$, $\delta_{(E_1-E_2)^2}$ and $\delta_{(N_1-N_2)^2}$ respectively are given by (eq 5.10):

$$\delta_{(E_1-E_2)^2} = (2(E_1 - E_2))\delta_{E_1-E_2}, \tag{5.16}$$

$$\delta_{(N_1-N_2)^2} = (2(N_1 - N_2))\delta_{N_1-N_2}; \tag{5.17}$$

the error in $(E_1 - E_2)^2 + (N_1 - N_2)^2$, $\delta_{(E_1-E_2)^2+(N_1-N_2)^2}$ is given by (eq. 5.9):

$$\delta_{(E_1-E_2)^2+(N_1-N_2)^2} = \sqrt{\delta_{(E_1-E_2)^2}^2 + \delta_{(N_1-N_2)^2}^2}, \tag{5.18}$$

by defining $\alpha = (E_1 - E_2)^2 + (N_1 - N_2)^2$, combining equation 5.7 and equation 5.10, the error of the argument under square root in equation 5.7 is:

$$\delta_d = (0.5(\alpha)^{-0.5})\delta_\alpha, \tag{5.19}$$

δ_{T_M} is then converted into δ_{1/T_M} using the power law (equation 5.10):

$$\delta_1/T_M = -1(T_M^{-2})\delta_{TM}, \tag{5.20}$$

The last step to calculate the total error associate with velocity estimates, δ_v, is combining Topping's product rule (equation 5.8) with equations 5.19 and 5.20; (v = *distance/time*):

$$\delta_v = \sqrt{d^2\delta_{1/T_M}^2 + \left(\frac{1}{T_M}\right)^2 \delta_d^2}, \tag{5.21}$$

5.2.3 Radio wave speed estimates, wavelet analysis

Measurements of the actual travel time within the inter-borehole region were done by assigning the time zero using few traces acquired holding the antennas in the air 5 meters apart (Figure 5.10, upper event) and, for some surveys, at the top of the borehole (Figure 5.10). Such calibration was repeated at the end of every survey.

This was because in the summer 2008 campaign the radar system appeared to be affected by a time-zero shifting: the travel time recorded by holding the antennas 5 meters apart differs substantially (e.g. more than 5 ns) between the beginning and at the end of many surveys. These surveys were discarded because there was no way to understand whether the traveltimes measured within the glacier were affected to such time-shifting.

Figure 5.10 shows the two events used for the time zero assignment in Ah1h2. T_a for Equation 5.22 was picked manually on each trace acquired in the air. The vast majority of the surveys acquired presented no appreciable difference between the pre-survey and the post survey T_a measurement (Table 5.2). However in three surveys (Ah4h5, Bh2h3 and Ch5h6 - Table 5.2) T_a differences of $\sim$ 3 ns were observed. Surveys affected by such appreciable change in time zero calibration will be assessed carefully in the interpretation section.

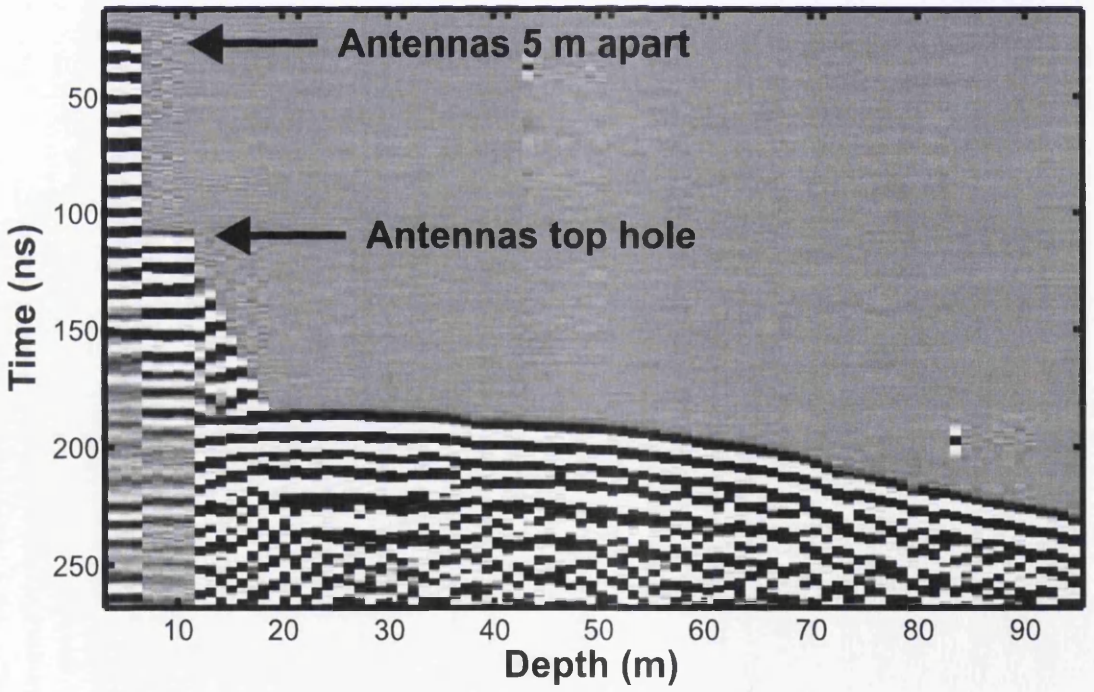

Figure 5.10: Sequence of pre-surveys events acquired in Ah1h2.

Radio wave speed profiles as computed using the different T_a listed in Table 5.2 are shown in Figure 5.11, measurement error throughout the profiles are deliberately

Survey	$\overline{T_a}$ - 5 m(1)	$\overline{T_a}$ - top hole (1)	$\overline{T_a}$ - 5 m(2)	$\overline{T_a}$ - top hole (2)
Ah1h2	19.62 ns	105.47 ns	20.00 ns	104.88 ns
Ah1h3	16.23 ns	132.89 ns	16.37 ns	132.89 ns
Ah2h3	14.24 ns	99.54 ns	15.30 ns	99.83 ns
Ah3h5	21.37 ns	163.15 ns	22.89 ns	163.96 ns
Ah4h5	16.70 ns	99.83 ns	20.39 ns	102.36 ns
Bh1h3	21.44 ns	-	21.44 ns	-
Bh2h3	17.13 ns	-	19.88 ns	-
B2h1h2	3.88 ns	-	3.88 ns	-
B2h1h3	22.31	-	22.31	-
Ch1h2	-	20.15 ns	-	19.75 ns
$Ch1h2_1$	-	4.09 ns	-	4.49 ns
Ch2h3	-	15.71 ns	-	13.34 ns
Ch3h4	23.89 ns	120.42 ns	23.89ns	120.03ns
$Ch3h4_1$	-	6.58 ns	-	6.23 ns
Ch5h6	9.71 ns	102.70 ns	8.73 ns	99.22 ns
$Ch5h6_1$	-	90.48 ns	-	89.53 ns

Table 5.2: Values of the average first break in the air , $\overline{T_a}$ (ns), for all the ZOP acquired at Storglaciären in the two campaigns. This value is necessary for the time-zero determination (Equation 5.22). (1) and (2) indicates pre and post survey acquisition respectively.

omitted to highlight the dependence that radio wave speed estimates have on T_a. All the speed estimates (Figure 5.11) fall in the range of 0.158-0.172 m/ns. Magnitude of the profiles depends sensitively on the value of T_a: Speed profiles obtained by T_a estimated holding the antenna 5 m apart are typically slower than those computed using T_a measured at the borehole tops (Figures 5.11a, 5.11b. 5.11c, 5.11d, 5.11o and 5.11q). As observed in Section 5.2.1, few surveys (Ah4h5, Figure 5.11e; Bh2h3, Figure 5.11g and Ch5h6, Figure 5.11q) are affected by differences in pre and post survey T_a determination. Surveys with only one profile (e.g. Bh1h3, Figure 5.11f; B2h1h2, Figure 5.11h; B2h1h3, Figure 5.11i; Ch1h2, Figure 5.11m) were those with no difference observed in T_a (Table 5.2). Differences in T_a cause difference in speed magnitude but not in the relative variation of speed with depth (Figure 5.11).

For those surveys where the double calibration was acquired (e.g. T_a estimated either holding the antennas 5 m apart and a top of the boreholes) a quality check was performed. By defining X_H as the antenna separation when the antennas are held at the tops of the boreholes the difference in distances X_H-5=T_{aH} c - T_{a5} c can be compared using what was measured by the dGPS (X_H-5) and what is measured by the radar system (T_{aH} c - T_{a5} c). Table 5.3 shows the results of the computation. Radar-derived X_H-5 values overestimate the distance by $\sim$ 1 m in all the 6 surveys (Table 5.3). Overestimate of the radar-derived distance can be due to either overestimates of T_{aH} or underestimates of T_{a5}. In other words, in order to fit the value of Δ_X on zero T_{aH} should arrive earlier whereas T_{a5} should arrive later. Figure 5.12 shows individual traces with T_{aH} and T_{a5} used for Ah1h2 indicated. It is clear that T_{a5} can not arrive considerably later than the sample indicated in Figure 5.12b since it fall well into the signal-wavelet (Figure 5.12a). Conversely the first break of T_{aH} can be earlier than the one indicated in Figure 5.12b, and be obscured by the pre-signal noise.

Uncertainties listed in Table 5.3 are not acceptable for the glaciological interpretations used in this study. From Table 5.3 we can observe that the radar-derived distance has an accuracy of $\pm$ 1 m. This error in distance is generated by uncertainty in both T_{a5} and T_{aH} which can be calculated using the Equations of formal error

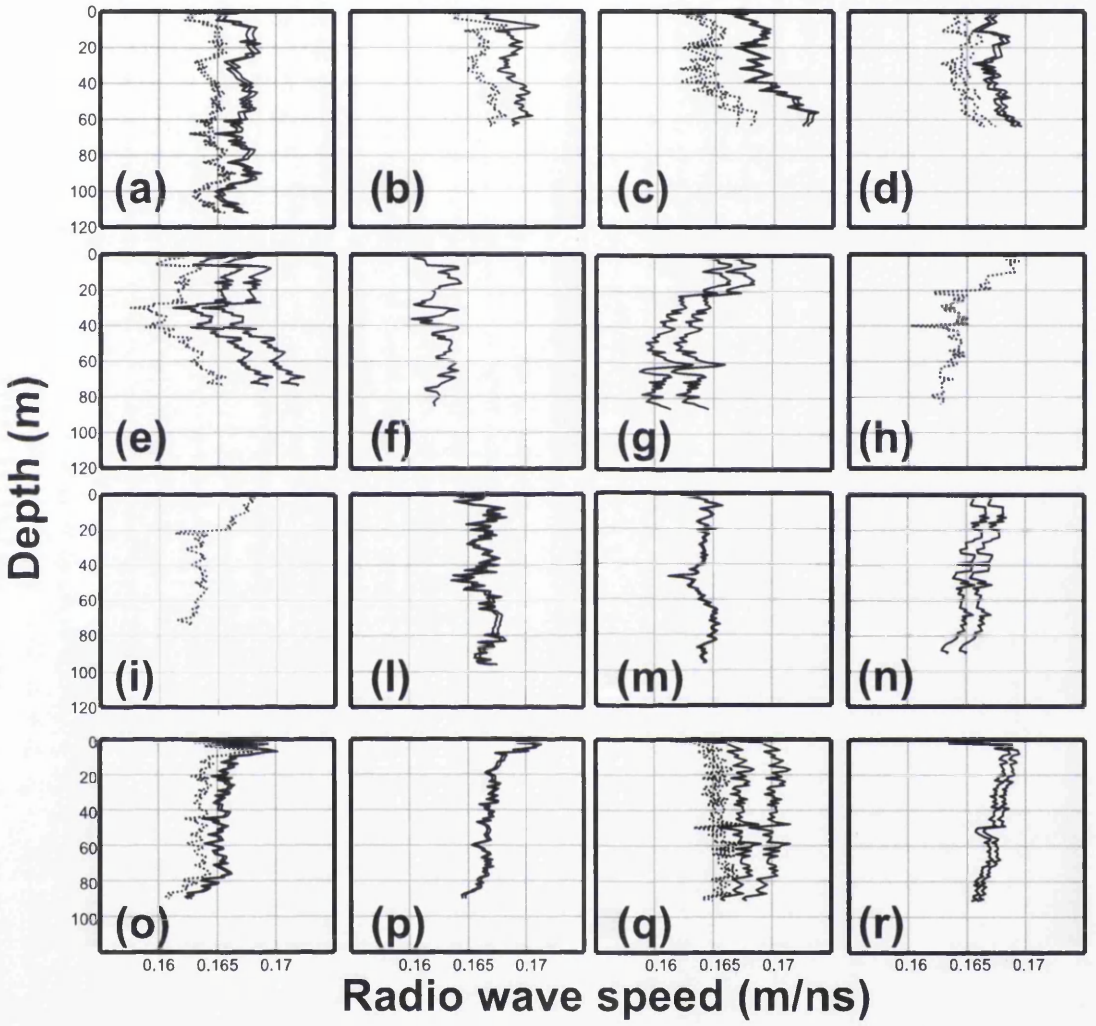

Figure 5.11: Radio wave speed profiles with depth as measured with ZOP surveys at Storglaciären. Each plot shows different profiles according to the number of T_a acquired (see Table tab:tadetermination). Dotted-line profiles were computed using T_a acquired holding the antennas 5 m apart whereas for solid-line profiles T_a was measured holding the antennas at the top of the boreholes. (a) Ah1h2, (b) Ah1h3, (c) Ah2h3, (d) Ah3h5, (e) Ah4h5, (f) Bh1h3, (g) Bh2h3, (h) B2h1h2, (i) Bh2h1h3, (l) Ch1h2, (m) Ch1h2_1, (n) Ch2h3, (o) Ch3h4, (p) Ch3h4_1, (q) Ch5h6, (r) Ch5h6_1.

Survey	X_H-5	$T_{aH}c - T_{a5}c$	Δ_X
Ah1h2	24.71 m	25.75 m	1.04 m
Ah1h3	33.83 m	34.99 m	1.16 m
Ah2h3	24.21 m	25.59 m	1.38 m
Ah3h5	41.21 m	42.54 m	1.33 m
Ch3h4	28.19 m	28.96 m	0.77 m

Table 5.3: Quality control on ZOP calibration and T_a values. Δ_X is the difference between the radar derived and dGPS derived X_H-5=$T_{a(H)}c - T_{a(5)}c$.

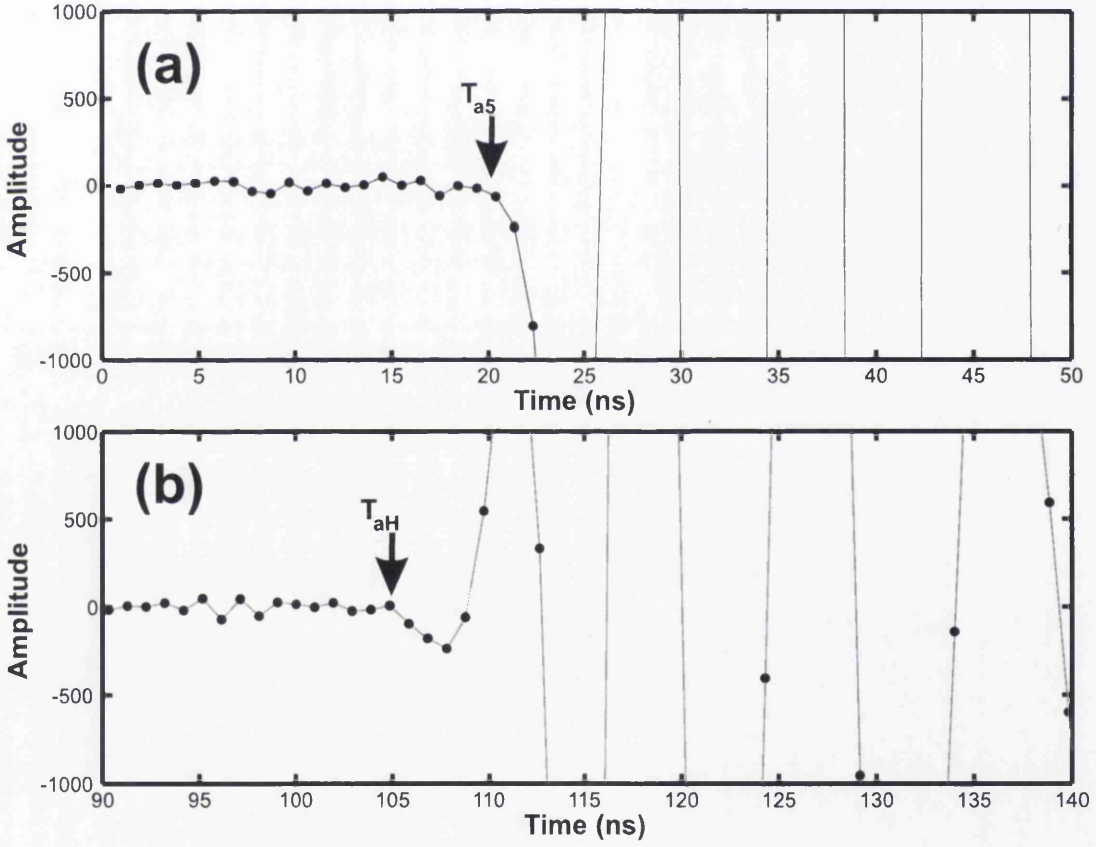

Figure 5.12: Picked first breaks in the air for in the case of antennas held 5 m apart (a) and positioned at two boreholes tops (b). The picked first break T_{a5} and T_{aH} are shown. The waveform is different because the geometrical losses at 5 m are consierably lower than those observede at top boreholes which were typically $\sim$ 30 m apart.

propagation (Equations 5.11 and 5.9). The error of ± 1 m is generated by errors in picking the first break of ± 2.5 ns which would consequently cause errors in radio wave speeds of ± 0.003 m/ns (Estimated with Equation 5.21 considering X of 30 m and v_i of 0.168).

The uncertainty of 0.003 m/ns in the magnitude of radio wave speed estimates can be reduced. A second approach, where T_{a5} and T_{aH} were picked at the amplitude peak was also tested to improve measurement accuracy (Figure 5.13). Unlike the first break, which has zero amplitude (Figures 4.7 and 5.12) and thus ambiguous arrival time, the amplitude peak is uniquely defined in all the traces (Figure 5.13). Δ_X values calculated using the amplitude peak are clearly more accurate (Table 5.4) as compared at those computed using the first break (Table 5.3). By taking Ah1h2 as example the error in radar-derived distance of ± 0.2 m is caused by uncertainities in picking of ± 0.5 ns (~ half of the sampling rate) which will, in turn propagate into an error in speed of ± 0.0007 m/ns: a considerable improvement.

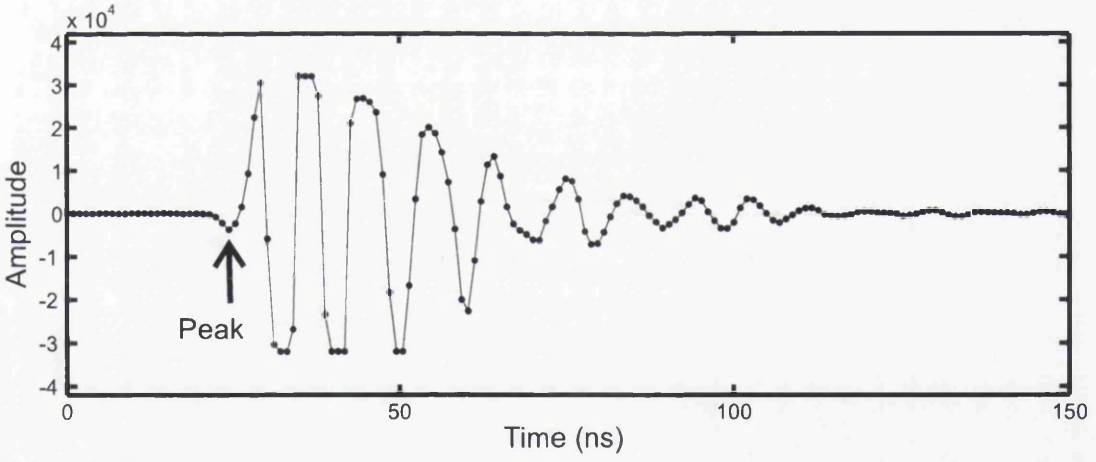

Figure 5.13: The wavelet peak for a trace acquired with the antennas in the air, 5 m apart.

The improvement of accuracy observed with wavelet-analysis was included in the speed analysis by modifying Equation 5.12. By defining T_c as the time required to complete a cycle from the fist to the third consequent zero crossing (Figure 5.14) and T_p as the time of the amplitude peak (Figure 5.14) the system delay as measured

Survey	X_H-5	$T_{aH}c - T_{a5}c$	Δ_X
Ah1h2	24.71 m	24.93 m	0.23 m
Ah1h3	33.83 m	34.08 m	0.26 m
Ah2h3	24.21 m	24.47 m	0.26 m
Ah3h5	41.21 m	41.66 m	0.45 m
Ch3h4	28.19 m	28.26 m	0.07 m

Table 5.4: Quality control on ZOP calibration and T_a values obtained picking the Amplitude peak instead of the first break. Δ_X is the difference between the radar derived and dGPS derived X_H-5=$T_{a(H)}c - T_{a(5)}c$.

using T_p is:

$$T_{DEL} = T_p - (T_c/4) - \frac{X}{c}, \tag{5.22}$$

radio wave speed profiles as computed using T_p, instead of T_a are are shown in Figure 5.15, the plot shows also the speed profiles measured with T_a (such as Figure 5.11) for comparison. Measurement errors throughout the profiles are still omitted to highlight the importance of the detailed wavelet analysis illustrated in the previous paragraphs. The improvements introduced by peaking the amplitude peak are appreciable since the differences observed in Figure 5.11 were eliminated. For example the speed profile for Ah1h2 computed using T_a acquired holding the antennas 5 m apart (Figure 5.11a, dotted line) was slower than the profile computed using T_a at the borehole-top (Figure 5.11a, solid line). By using the peak amplitude of both events such difference is only minor (Two black solid lines in Figure 5.15 a). Generally using the peak amplitude T_p instead of the first break removed differences in the radio wave speed estimates. Differences between the solid lines in each single plot reflect the precision of the estimates (Figure 5.15).

5.2.4 Radio wave speed estimates, profiles

Final radio wave speed profiles for the three sites are illustrated in Figures 5.16. Speed estimates fall within the range typically considered as *glaciological* between 0.160 and 0.170 m/ns. At site A (Figure 5.16 from (a) to (e)) speeds lay for the vast

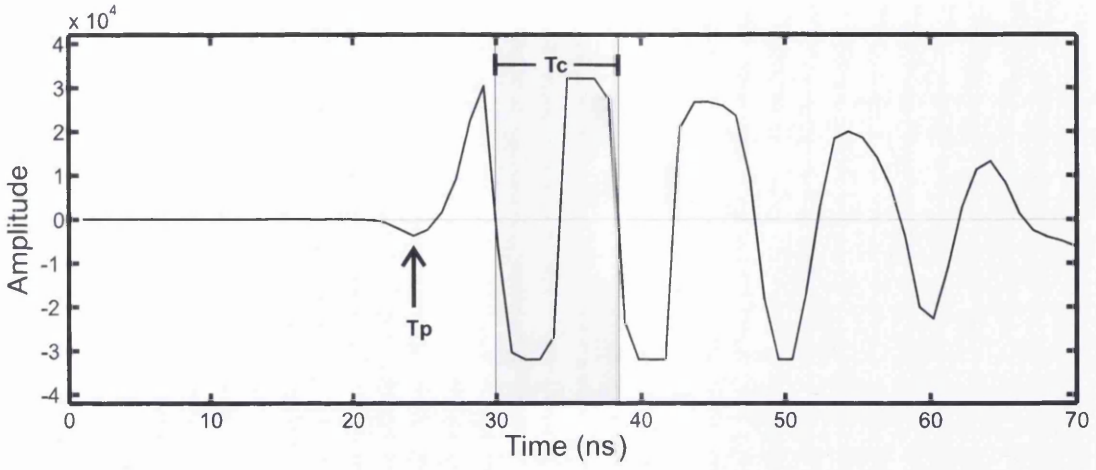

Figure 5.14: The wavelet acquired with the antennas in the air, 5 m apart with definitions of the time required to complete a cycle T_c and the first amplitude peak T_p.

majority in the range between 0.165 and 0.170 m/ns. The deepest survey collected in the two campaign (Ah1h2) do not show appreciable variation throghout the ice column with the only possible exception of a slow layer located between 100 and 120 m. Stability and relatively high speeds were also observed two days later in Ah1h3 (Figure 5.16b) where speeds were always higher than the solid ice velocity of 0.168 m/ns. Ah2h3 (Figure 5.16c) show a peculiar high-speed region at $\sim$ 60 m. Such increasing of speed was also observed in the other two surveys collected at site A (Ah3h5 and Ah4h5; Figures fig:thevelplotc and d). The lowest speed of the site was measured in Ah4h5 at the depth of $\sim$ 30 m. On average variations in radio-wave speed with depth at site A can be defined as minor and there were no evidences of particularly low radio wave speeds.

At site B (Figure 5.16) the speed structure shows peculiar characteristics. The survey Bh2h3 was affected by uncontrolled time-zero-drift (Figures 5.16g) and therefore is not included in Figure 5.16. The only survey collected in 2009 (Bh1h3, Figure 5.16f) provides evidence of stability with depth: speed appear to be stable at the value of 0.165 m/ns. Surveys collected in 2008 appear to be considerably different with a two layer structure (Surveys B2h1h2 and B2h1h3 - Figures 5.16g and 5.16h). In the 2008 surveys there is a distinct upper high-speed layer $\sim$ 20 m thick with radio-wave speeds higher than $\sim$ 0.165 m/ns. This high-speed layer is separated by a sharp

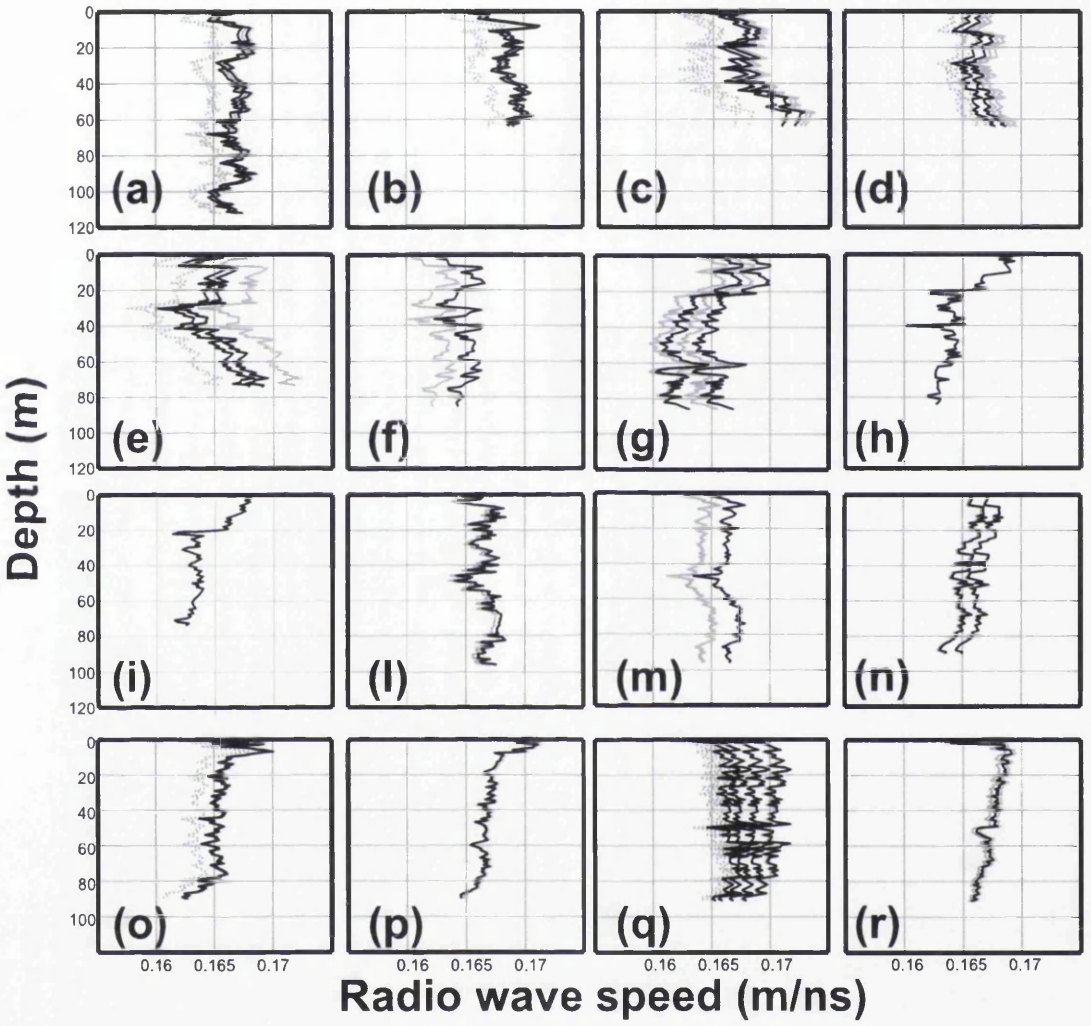

Figure 5.15: Radio wave speed profiles (black lines) with depth as measured with ZOP surveys using T_p instead of T_a at Storglaciären. Each plot shows different profiles according to the number of T_a acquired (see Table tab:tadetermination). Gray lines in the background of each plot are the same of Figure 5.11. (a) Ah1h2, (b) Ah1h3, (c) Ah2h3, (d) Ah3h5, (e) Ah4h5, (f) Bh1h3, (g) Bh2h3, (h) B2h1h2, (i) Bh2h1h3, (l) Ch1h2, (m) Ch1h2_1, (n) Ch2h3, (o) Ch3h4, (p) Ch3h4_1, (q) Ch5h6, (r) Ch5h6_1. This figure gives a general overview of the ZOP results. Final radio wave speed profiles are plotted singularly from Figure 5.25 to Figure 5.38.

transition from a lower low-speed layer. Speeds in the lower layer appear to stabilise on values of $\sim$ 0.164 m/ns. The two surveys collected on the same date (21.07.2008 B2h1h2 and Bh1h3, Figure 5.16g and Figure 5.16h) shows the same speed-structure.

At site C the 100 MHz survey collected in Ch5h6 was discarded because it was affected by uncontrolled time-zero-drift (Figure 5.11q). At this site a multi-frequency experiment was also tested. Three ZOP surveys (Ch1h2, Ch3h4 and Ch5h6) were repeated using different antennas (100 and 250 MHz). In all the multi-frequency surveys the two frequencies were tested in the same day with no significant delay between the two surveys. No frequency-dependence of radio wave speed is shown by looking at the resulting speed profiles (Figures 5.11): radio wave speeds measured at different frequencies were essentially the same and within the accuracy of the estimates. Radio wave speed profiles recorded at site C provide the most convincing evidence of a decrease of speed with depth. Speeds in Ch1h2 (Figure 5.16a) remain stable on the value of $\sim$ 0.166 $\pm$ 0.001 with a slow region at 50 m. The remaining surveys show a slight decrease of speed with depth with the slower speed, indicative of wet-ice, recorded at around 90 m depth.

5.3 Radar attenuation from ZOP

General principles of englacial radar attenuation are outlined in Section 3.1.3. *Matsuoka et al.* [2010] recently estimated radar attenuation from within the ice of central West Antarctica and provided a set of equations which can be used in this analysis. Attenuation values in *Matsuoka et al.* [2010] were obtained from radar power reflected back from the interior of the ice sheet. Despite the fact that scale, geographical and glaciological settings are different, quantitative treatments in *Matsuoka et al.* [2010] can be used for the ZOP at Storglaciären. Following the basis illustrated by *Bogorodsky et al.* [1985] the returned power $[P]_{dB}$ from within ice is a function of the radar instrument $[S]_{dB}$ and of ice properties $[I]_{dB}$ along the propagation path from a reflector located at depth z . $[P]_{dB}$ it is also affected by geometrical spreading

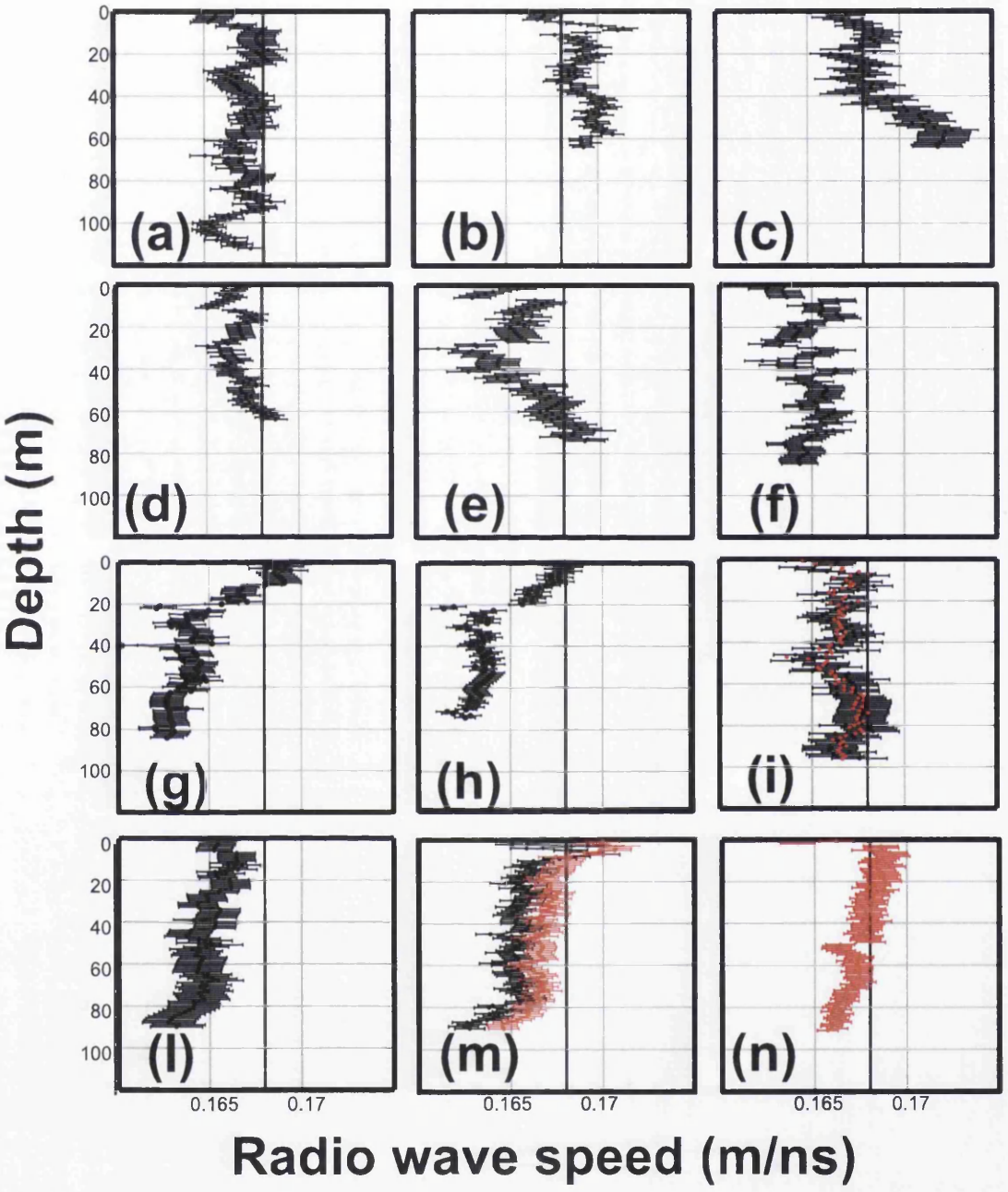

Figure 5.16: Radio wave speed profiles with measurement error with depth as measured with ZOP surveys at Storglaciären. (a) Ah1h2, (b) Ah1h3, (c) Ah2h3, (d) Ah3h5, (e) Ah4h5, (f) Bh1h3, (g) B2h1h2, (h) Bh2h1h3, (i) Ch1h2 (100 MHz, black dots; 250 MHz, red dots) , (l) Ch2h3, (m) Ch3h4 (100 MHz, black dots; 250 MHz, red dots), (n) Ch5h6 (100 MHz, black dots; 250 MHz, red dots). In Figure differs from Figure 5.15 by the fact that measurement errors are included and that multi-frequency surveys (e.g. (i), (m) and (n)) are plotted together.

$[G]_{dB}$ [*Bogorodsky et al.*, 1985; *Matsuoka et al.*, 2004, 2010]:

$$[P]_{dB} = [S]_{dB} + [I]_{dB} - [G]_{dB}. \tag{5.23}$$

where the term $[G]_{dB}$ for the case of an airborne radio pulse emitted at height H above the surface and travelling into a subsurface with mean relative permittivity ε, is derived by *Matsuoka et al.* [2010]:

$$[G]_{dB} = 2\left[H + \frac{z}{\sqrt{\varepsilon}}\right]_{dB}. \tag{5.24}$$

For the ZOP surveys treated in this chapter equation 5.24 simply become $[GP]_{dB} = D_M/\sqrt{\varepsilon_i}$. Thus the geometrically corrected returned power [*Matsuoka et al.*, 2010] is:

$$[P^c]_{dB} = [P]_{dB} + [G]_{dB}. \tag{5.25}$$

5.3.1 Radar power profiles

Radar power variations within the ice column were investigated by studying the first arrivals of the radar pulse propagating within the inter-borehole region. In power analysis the initial amplitude of a radio-wave pulse is calculated from the radargrams. Several criteria for measuring amplitude can be used. These include measuring the amplitude of the first peak, from the first peak to the first trough or calculating it from a frequency spectrum [*Peterson*, 2001]. Amplitude peaks of the first half cycle of the dewowed wavelet (e.g., from the first break to the following subsequent zero crossing) were measured at each antenna depth for all the ZOP radargrams illustrated in Figures 5.5, 5.6 and 5.7 by measuring the the first peak of the wavelet Amplitude measurements were transformed to power (amplitude squared) as in many publications about englacial radar attenuation (e.g. *Matsuoka et al.* [2004], *MacGregor et al.* [2007] and *Matsuoka et al.* [2010]); additionally calculations using power can be directly compared regardless the polarity of the arrivals since the squared power of negative amplitudes is a positive value.

Measured radar power was normalized to the mean pre-signal noise in order to obtain power in dB. As in Equation 4.2, the received power in dB $[P]_{dB}$ can be measured using the measured power P_{signal} with the mean power of pre-signal noise P_{noise} :

$$[P]_{dB} = 10 \log_{10}\left(\frac{P_{\text{signal}}}{P_{\text{noise}}}\right). \tag{5.26}$$

P_{noise} was measured by manually selecting pre-signal portions of the surveys (e.g. the solid-line box in Figure 5.17) which avoided pre-signal critical refractions (the dotted line box in Figure 5.17) and random noisy datapoints (e.g. the dashed box in Figure 5.17). From the *noise box* (solid box in Figure 5.17) the mean noise used as P_{noise} in Equation 5.26 was calculated as the mean value of the vector containing the maximum noise value for each trace.

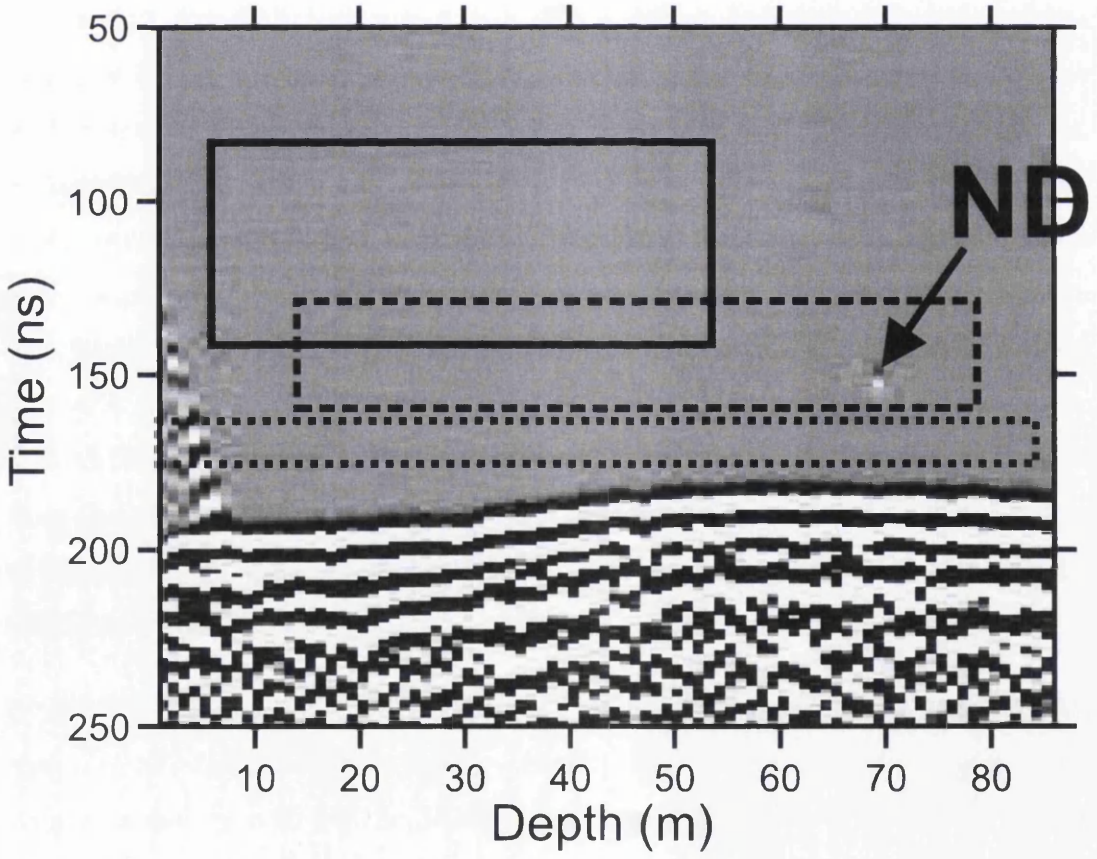

Figure 5.17: Selection of the noise box for the calculation of P_{noise} from ZOP Ch1h2. The solid line box is unaffected by critically-refracted arrivals, present in the dotted box and noisy datapoints (NB) present in the dashed box.

$[P]_{dB}$ values were then converted into geometrically corrected returned power $[P^c]_{dB}$ using Equation 5.25. Figure 5.18 shows $[P^c]_{dB}$ with depth for all the ZOP profiles collected in the two campaigns. $[P^c]_{dB}$ measured in 2008 all coherently lie in the same range between 50 and 100 dB whereas power measured in 2008 are clearly higher ($\sim$ 50 dB) than those obtained in 2009 (Figure 5.18, solid and dashed lines). This presumably is due to the fact that in 2008, different antennas with a different control unit were used. $[P^c]_{dB}$ values measured in the upper 5 m of the ice column are consistently lower than those measured at greater depths and this is because in the upper part of the survey, direct arrivals from within the ice interfere with the critically refracted waves (Figure 5.8).

$[P^c]_{dB}$ profiles with depth plotted singularly for all the surveys are illustrated in Figure 5.19. Powers in the upper part of the surveys (e.g. the upper 5 m points in Figure 5.19 a) are not representative of a radio pulse propagating within glacier ice because they are corrupted by the interference with critically refracted arrivals. At representative depths (e.g. when $[P^c]_{dB}$ values stabilise on $\sim$ 100 dB in Figure 5.19a) geometrically corrected power profiles varied from survey to survey. At site A the whole spectrum of measured $[P^c]_{dB}$ spanned from $\sim$ 40 to 100 dB with mean of $\sim$ 80 dB. In two surveys (Ah1h2, Figure 5.19a and Ah1h3, Figure 5.19 b) a slight decreases of $[P^c]_{dB}$ with depth is observed. In other surveys (Ah2h3, Figure 5.19c and Ah4h5, Figure 5.19e) $[P^c]_{dB}$ values were relatively stable and rarely changed from the range 80-100 dB. In one survey (Ah3h5, Figure 5.19d) two distinct area of low power, between 27 and 34 m and at $\sim$ 50 m are identifiable in an otherwise relatively stable survey.

At site B (Figures 5.19f, 5.19m and 5.19n) absolute values were much higher in 2008 (mean $\sim$ 130 dB) than 2009 (mean $\sim$ 90 dB). Figure 5.18 shows how 2008 values clearly exceed by $\sim$20 dB the 2009 range. In Bh1h3 (Figure 5.19f) $[P^c]_{dB}$ values are relatively stable on values of between 80 and 100 dB. $[P^c]_{dB}$ values for the 2008 surveys (Figures 5.19m and 5.19m) are generally higher than $\sim$ 130 dB throughout the ice column with low-power regions at 21-24 m and at 40 m.

The multifrequency experiment tested at site C (Figure 5.19; from g to l) shows that $[P^c]_{dB}$ values measured with the 100 MHz antennas are generally higher than those acquired with the higher frequency of 250 MHz. As observed at the other sites, power values exhibit general stability with no large fluctuations with depth. Noticeably there are few areas of relatively high $[P^c]_{dB}$ (e.g. between 5 and 15 m depth in Ch1h2 and Ch2h3, Figure 5.19g and h), however the difference between such high regions and the mean values is quantifiable as ~20 dB. The overall picture which emerges from multifrequency radar power profiles acquired at site C is little variation with depth and frequency-dependance of $[P^c]_{dB}$ values.

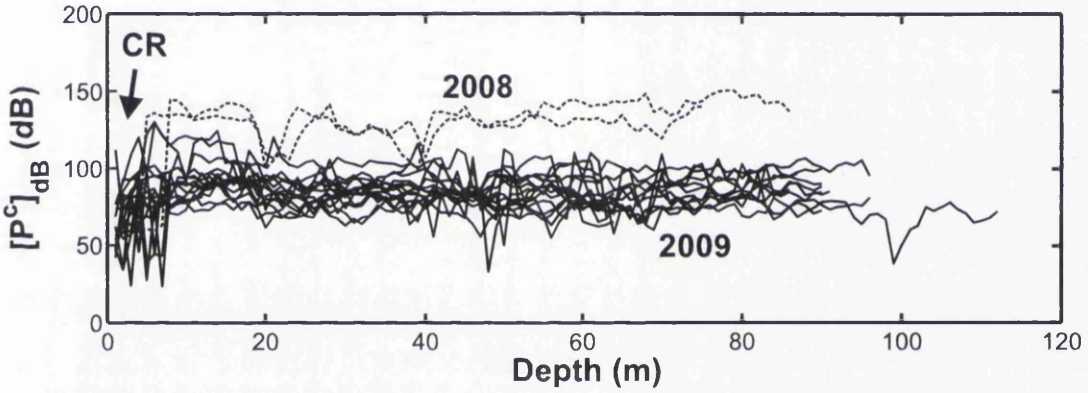

Figure 5.18: $[P^c]_{dB}$ values for all the ZOP collected in the two campaigns. The dashed lines indicate the surveys acquired in summer 2008 whereas the solid line indicate those collected in 2009. CR indicate the upper region of the survey where power values of the first arrivals are distorted by the interference with the critically refracted waves.

5.4 Meteorological data during ZOP surveying

As a first step in the interpretation of the results listed in this chapter meteorological data recorded by the nearby Tarfala Research Station were analysed. Since radio wave speed and radio wave attenuation are strongly sensitive to variations in water-content and temperature respectively, it is critical to determined whether or not changes in weather conditions (e.g. strong rainfalls or high melt rates due to high temperatures) have an effect on ZOP surveys. The weather station was located

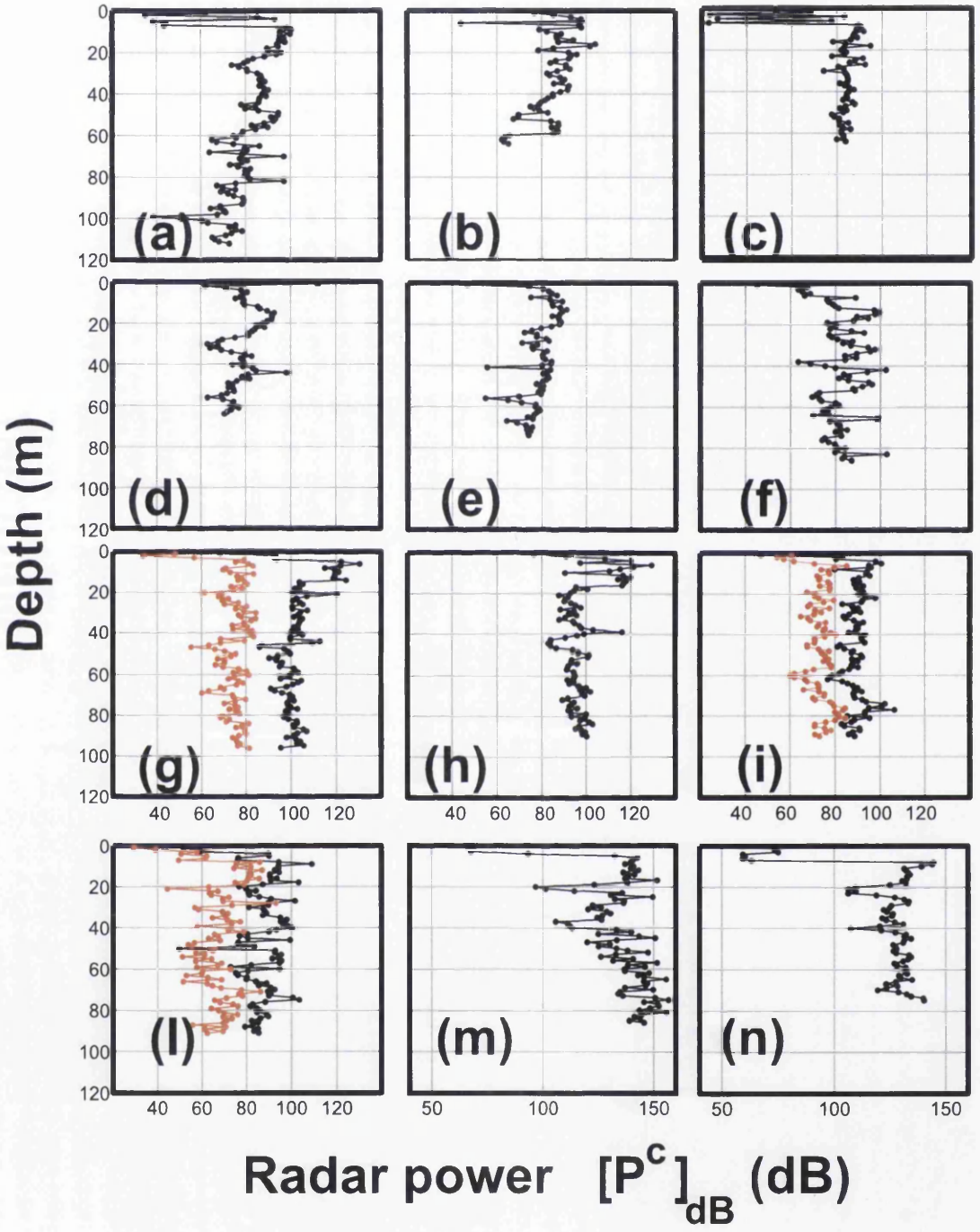

Figure 5.19: $[P^c]_{dB}$ values for the ZOP collected at Storglaciären. (a) Ah1h2; (b) Ah1h3; (c) Ah2h3; (d) Ah3h5; (e) Ah4h5; (f) Bh1h3; (g) Ch1h2; (h) Ch2h3; (i) Ch3h4; (l) Ch5h6; (m) B2h1h2; (n) B2h1h3.

in the middle of the Tarfala valley ~1 km away from the glacier and can provide useful insights about the general meteorological pattern during ZOP surveys. Tarfala Research Station meteorological data have often been used to interpret dynamics occurring on Storglaciären (e.g. *Jansson* [1995]; *Grudd and Schneider* [1996]; *Jansson* [1996]).

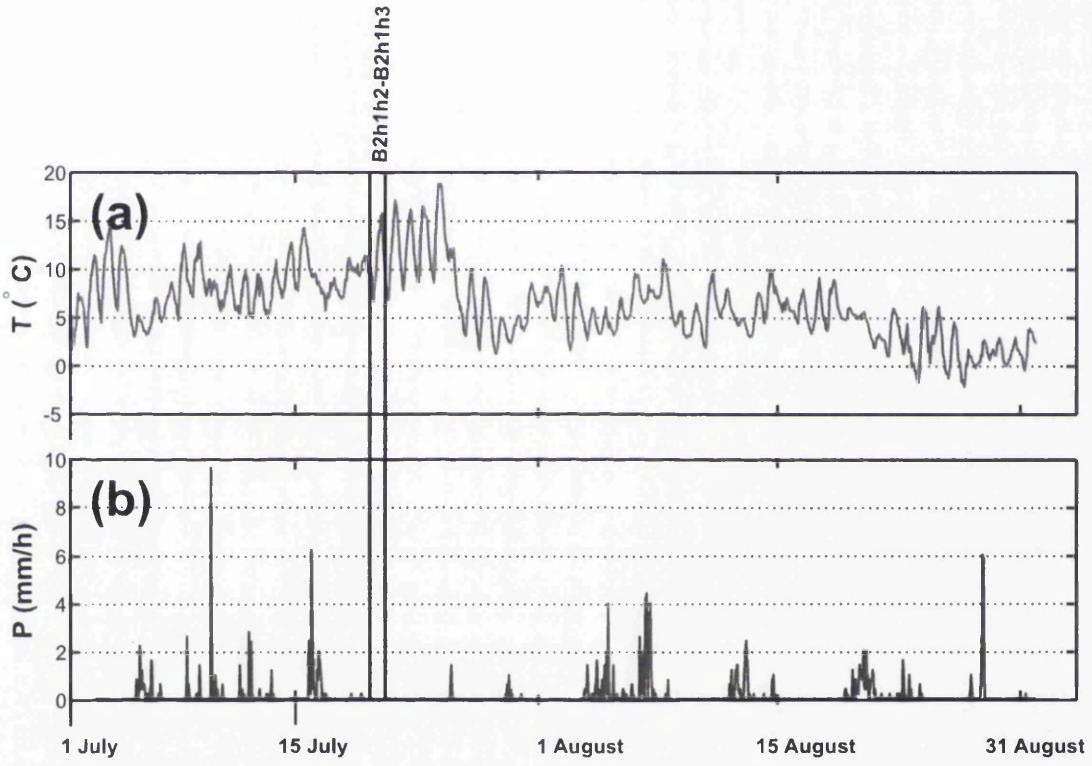

Figure 5.20: Temperature (a) and precipitation data (b) for July and August 2008 measured at the nearby Tarfala Research Station.

Temperature and precipitation data for the period July-August 2008 and 2009 are shown in Figures 5.20 5.21. The 2008 acquisition (Figure 5.20 was carachterised by dry condition, there is no evidence supporting particular high ablation-rates in the period immediatly before the survey. In 2009 ZOP acquisition started just after the largest wet period of the end of July. Warmer and colder conditions were recorder during survey periods at site B and site C respectively whereas, with the only exception of Bh1h3 and Ch5h6, no significant rainfalls were coincident (Bh1h3) or preceeded (Ch5h6) ZOP surveying. Absence of precipitation and stable temperature characterised the acquisition at site C. Strikingly, the peak temperature on the 4^{th}

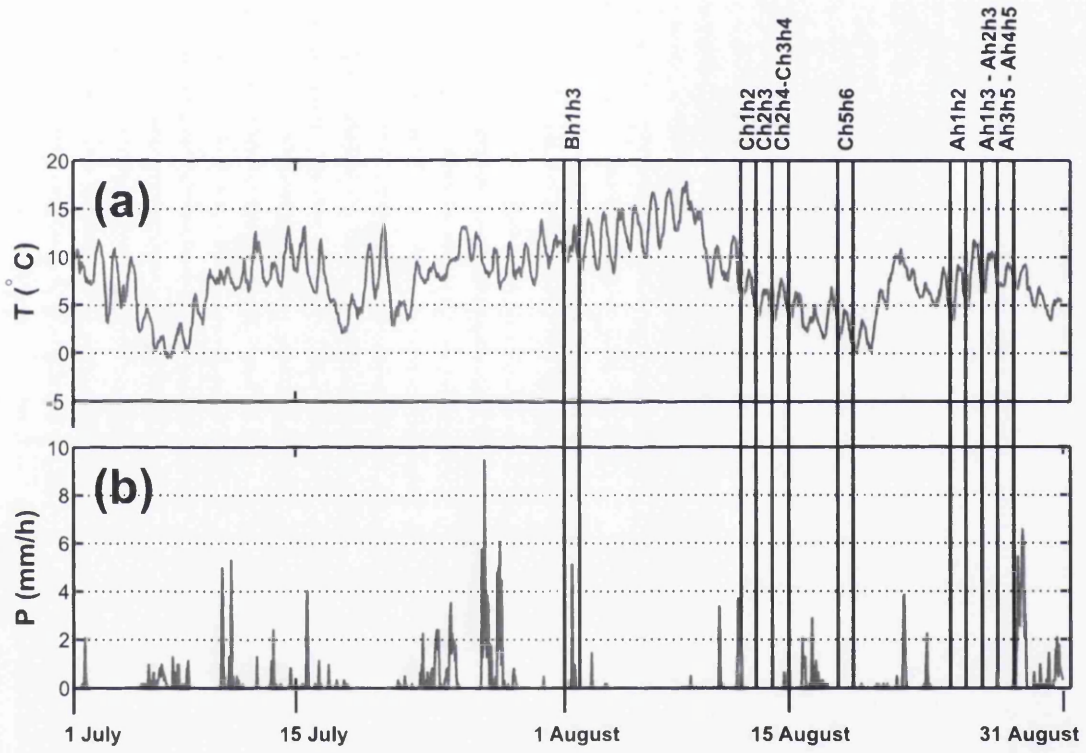

Figure 5.21: Temperature (a) and precipitation data (b) for July and August 2009 measured at the nearby Tarfala Research Station.

of August, the day when Bh2h3 was acquired, was some 15s °C higher than the 18^{th} of August (Ch5h6).

5.5 Inclinometry data

Inclinometry data were used to measure the distance between the two boreholes in each survey. These data are illustrated in Figures 5.22, 5.23 and 5.24 for the ZOP surveys at site A, B and C respectively. Boreholes at sites B and C were considerably straight (Figures 5.23 and Figures5.24) whereas the larges deviation from vertical was observed at site A (Figure 5.22). Inclinometry data will be considered in the interpretation of the ZOP results. For example results from Ah3h4 and Ah4h5 (Figures 5.22d and 5.22e) will be critically discussed since the inclination of the antennas in the boreholes reached dip as low as 40°. The data quality is unequivocal for those surveys acquired in straight boreholes (e.g. B2h1h2, Figure 5.23a and Ch1h2, Figure 5.24a).

5.6 ZOP results, summary

Radio wave speed and power profiles were plotted together for every single ZOP collected at Storglaciären in the two campaigns discussed in this chapter. Plot for site A are given in Figures 5.25, 5.26, 5.27, 5.28 and 5.29. The only ZOP survey acquired at site B in 2009 is shown in Figure 5.30 whereas those collected in 2008 are given in Figures 5.31 and 5.32. Finally, results from site C are illlustrated in Figures 5.33, 5.34, 5.35, 5.36, 5.37, and 5.38. These profiles were corrected to compensate the effect of borehole width and the corrected speeds are given in Figure 5.16. Since low radio wave speed in glacier ice is generally interpreted as indicator of the presence of water bodies within glaciers [*Macheret et al.*, 1993; *Murray et al.*, 2000a; *Bradford and Harper*, 2005; *Endres et al.*, 2009] this summary will use the words *dry* and *wet*

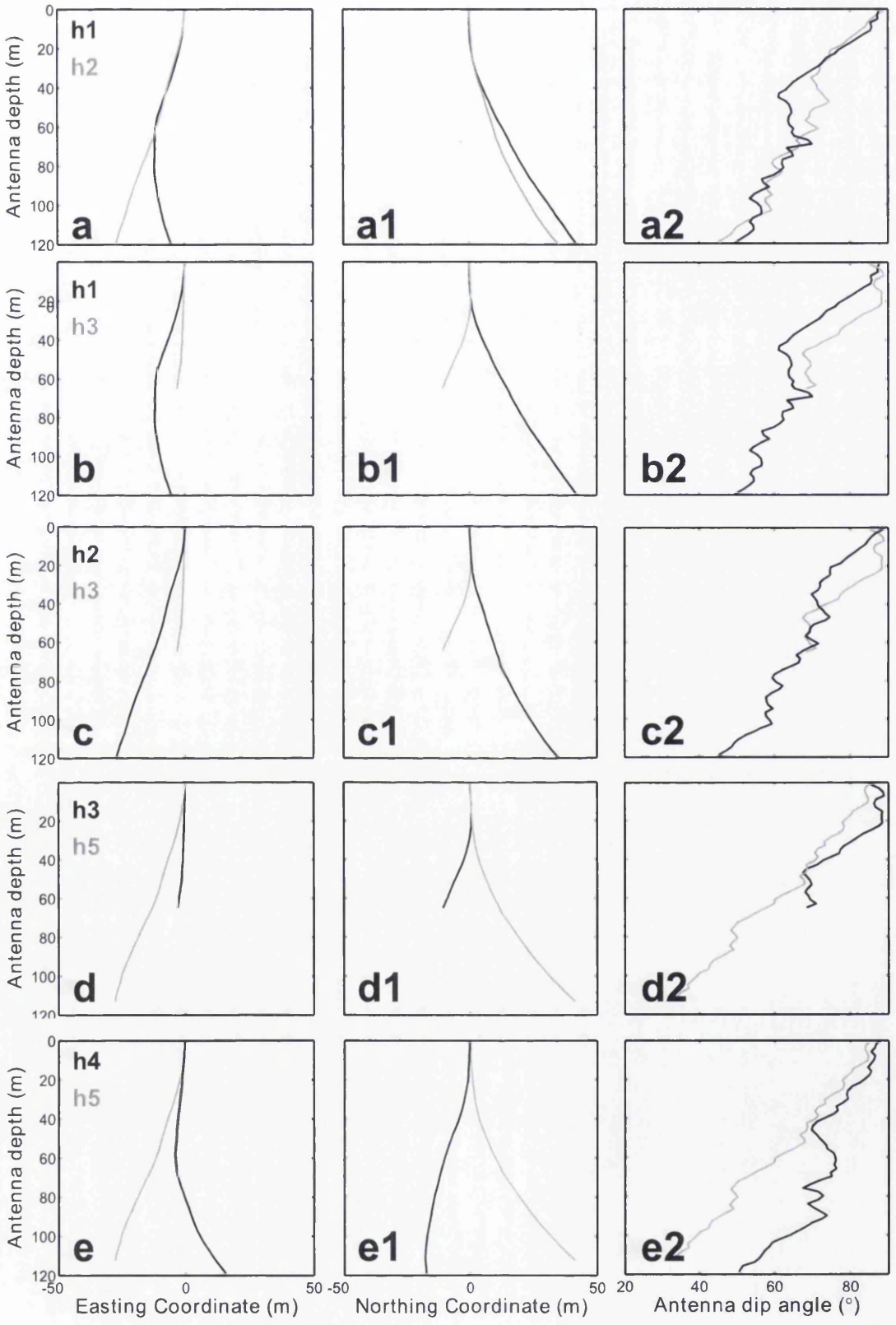

Figure 5.22: Inclinometry data at site A for (a) Ah1h2, (b) Ah2h3, (c) Ah3h4 and (d) Ah3h5.

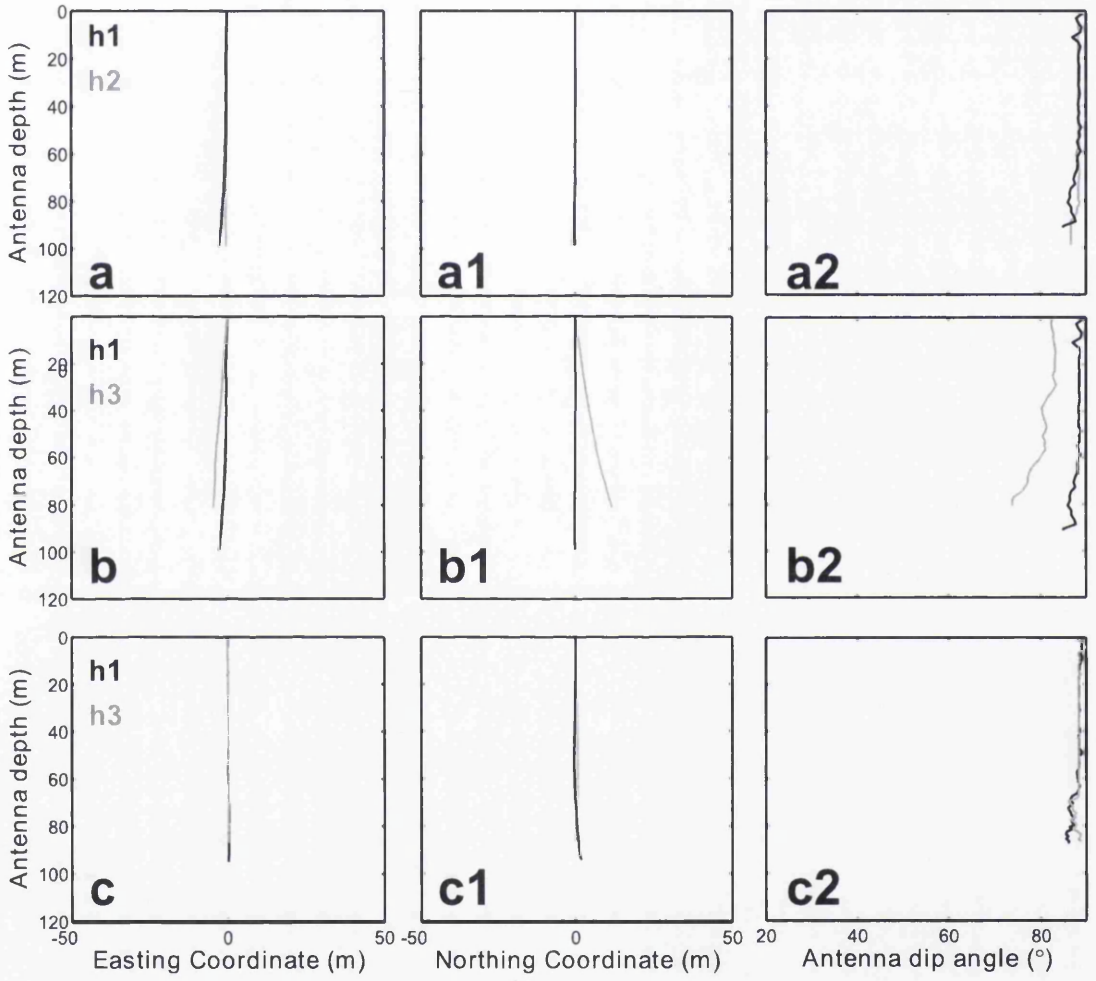

Figure 5.23: Inclinometry data at site B for (a) B2h1h2, (b) B2h1h3 and (c) Bh1h3.

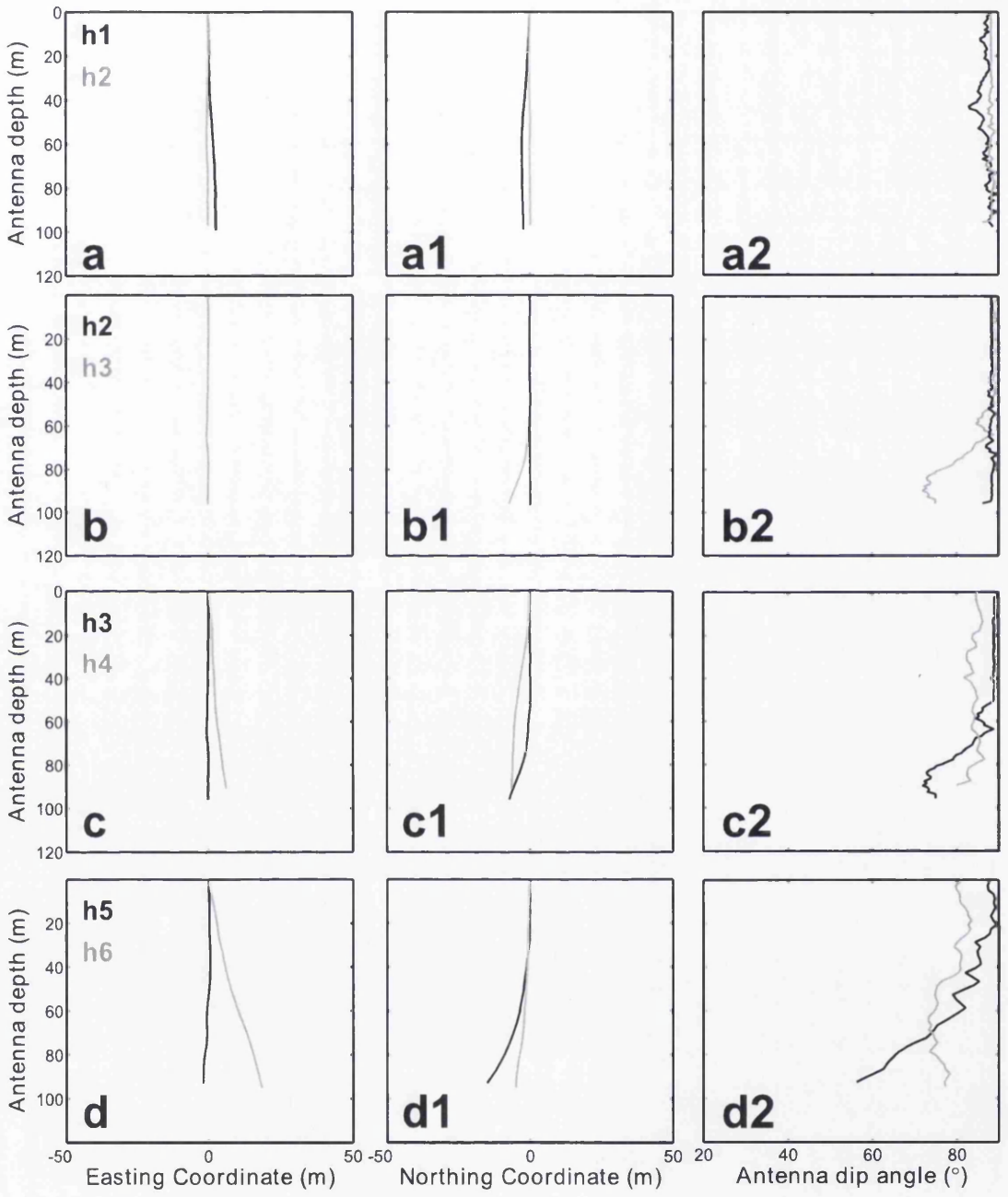

Figure 5.24: Inclinometry data at site C for (a) Ch1h2, (b) Ch2h3, (c) Ch3h4 and (d) Ch5h6.

to qualitatively describe spatial and temporal variability of radio-wave propagation at Storglaciären.

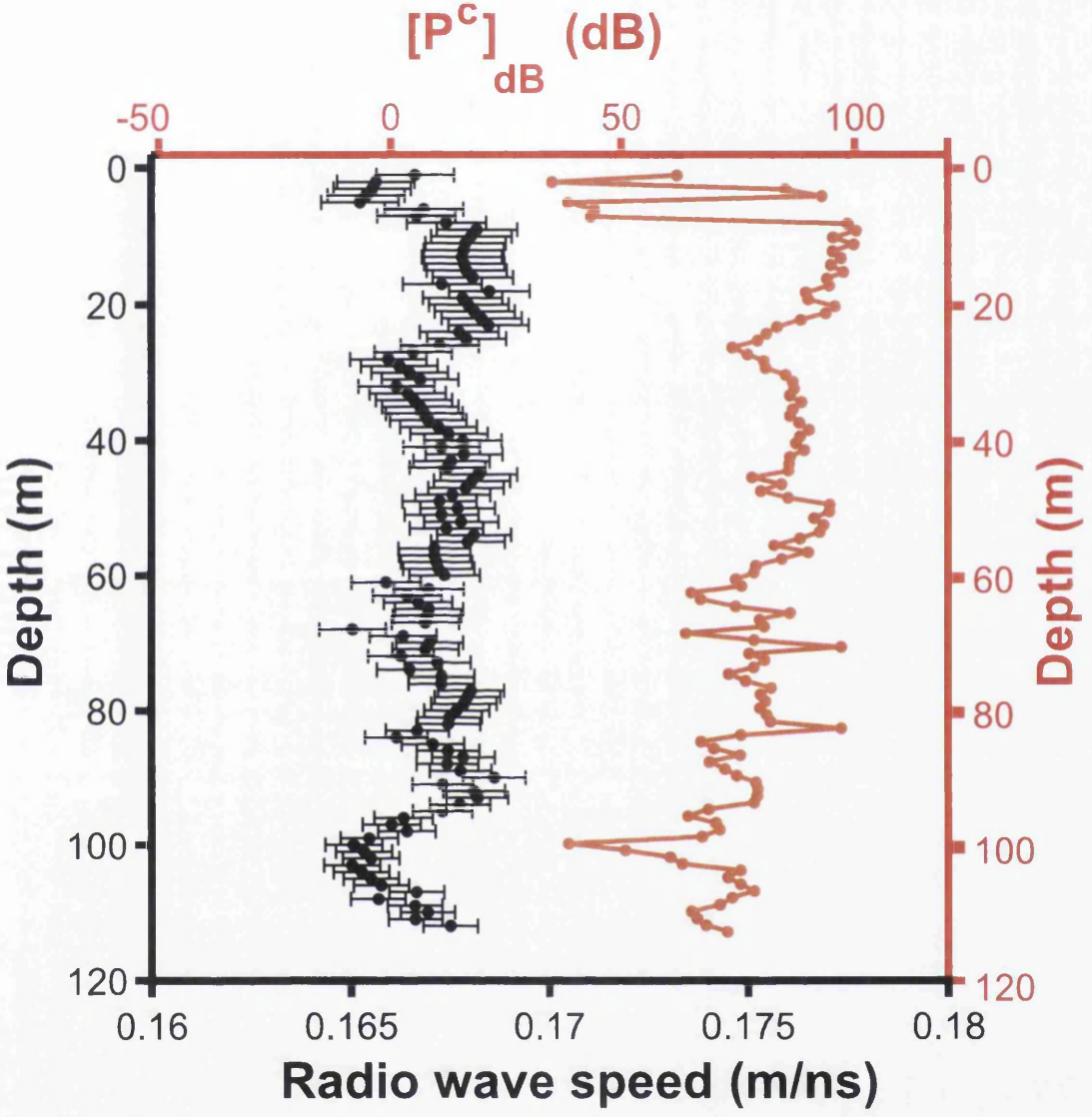

Figure 5.25: Radio wave speed (black) and $[P^c]_{dB}$ (red) profile for the survey Ah1h2

At site A, located nearby the equilibrium line altitude, 5 differently orientated 100 MHz ZOP surveys shows spatial variations in radio wave speed and radar power profiles with depth. A general dry and uniform situation, in which radio wave speed is rarely slower than the average throughout the ice-column, is observed in two surveys (Ah1h2, Figure 5.25 and Ah1h3, Figure 5.26). A distinct dry region was identified by radio wave speeds as high as 0.172 m/ns at $\sim$ 60 m in the survey Ah2h3 (Figure

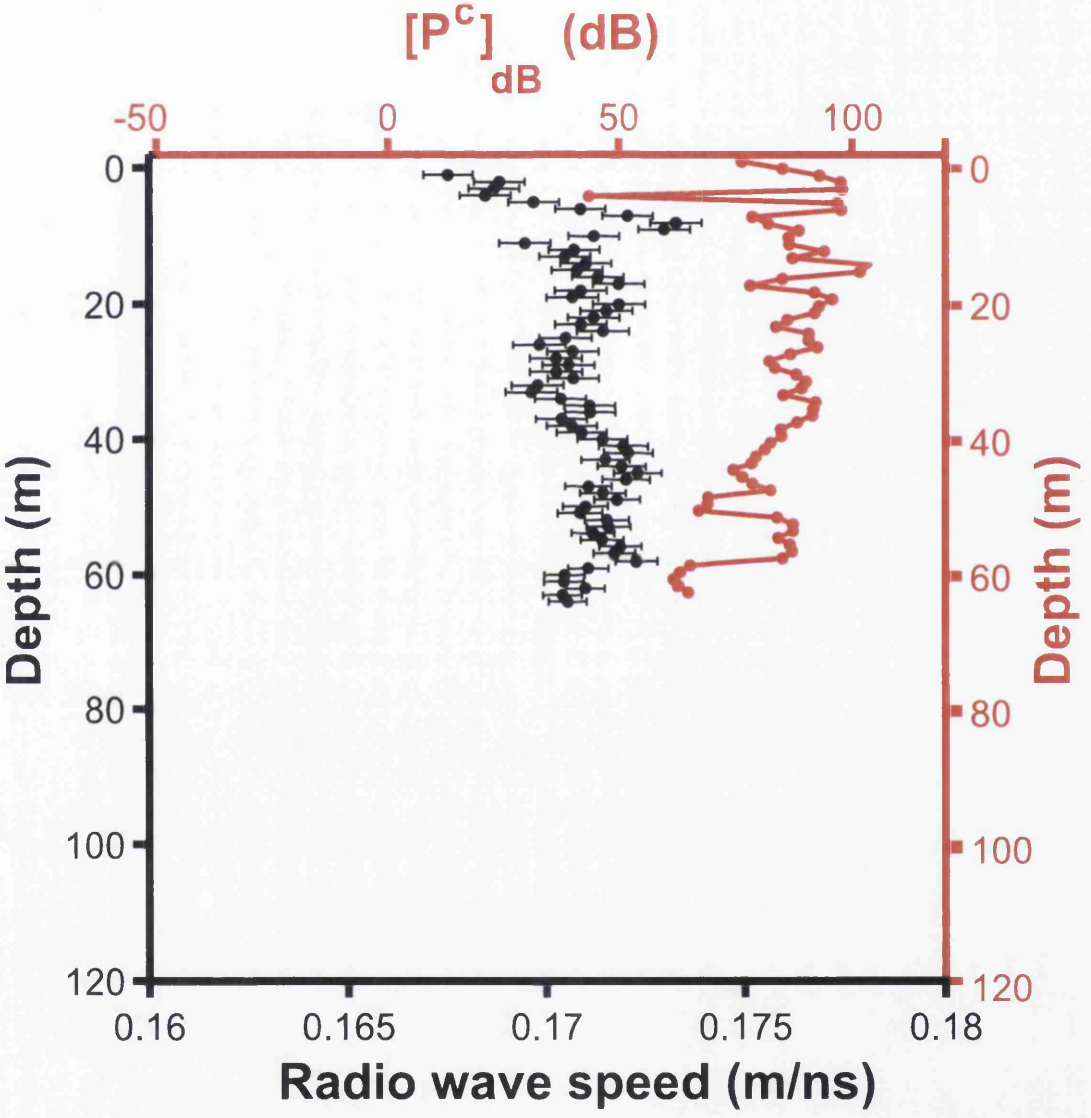

Figure 5.26: Radio wave speed (black) and $[P^c]_{dB}$ (red) profile for the survey Ah1h3

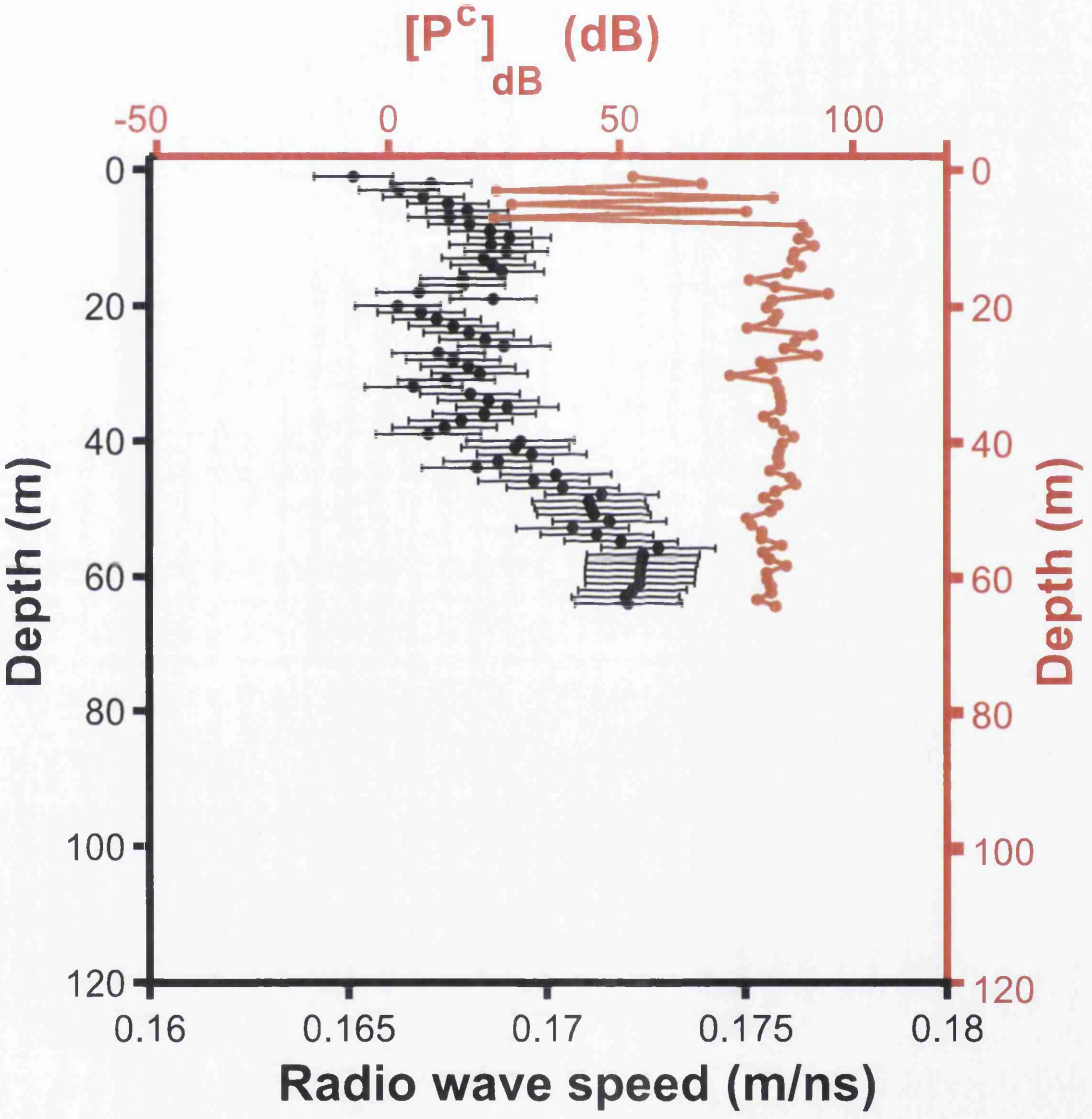

Figure 5.27: Radio wave speed (black) and $[P^c]_{dB}$ (red) profile for the survey Ah2h3

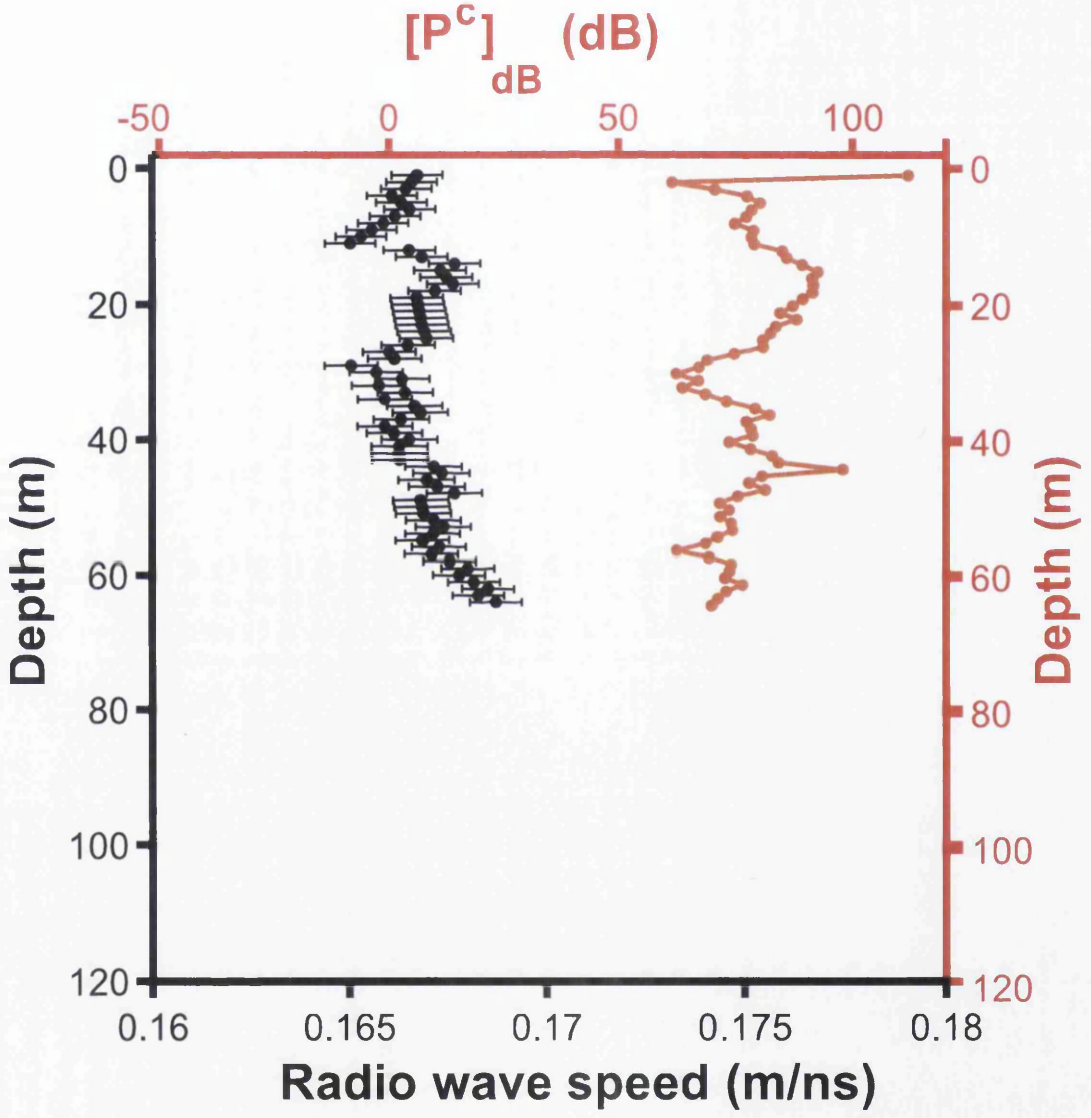

Figure 5.28: Radio wave speed (black) and $[P^c]_{dB}$ (red) profile for the survey Ah3h5

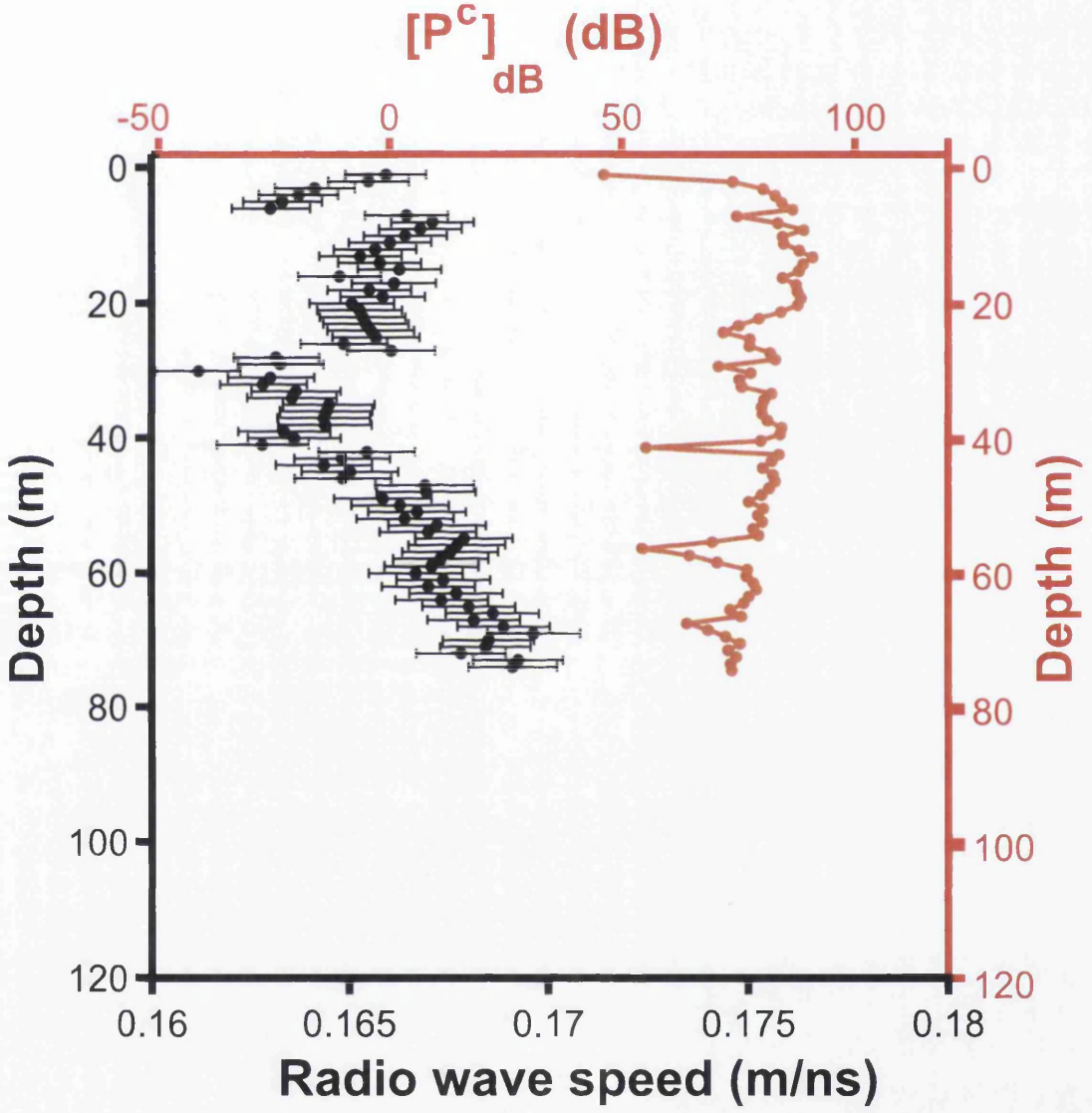

Figure 5.29: Radio wave speed (black) and $[P^c]_{dB}$ (red) profile for the survey Ah4h5

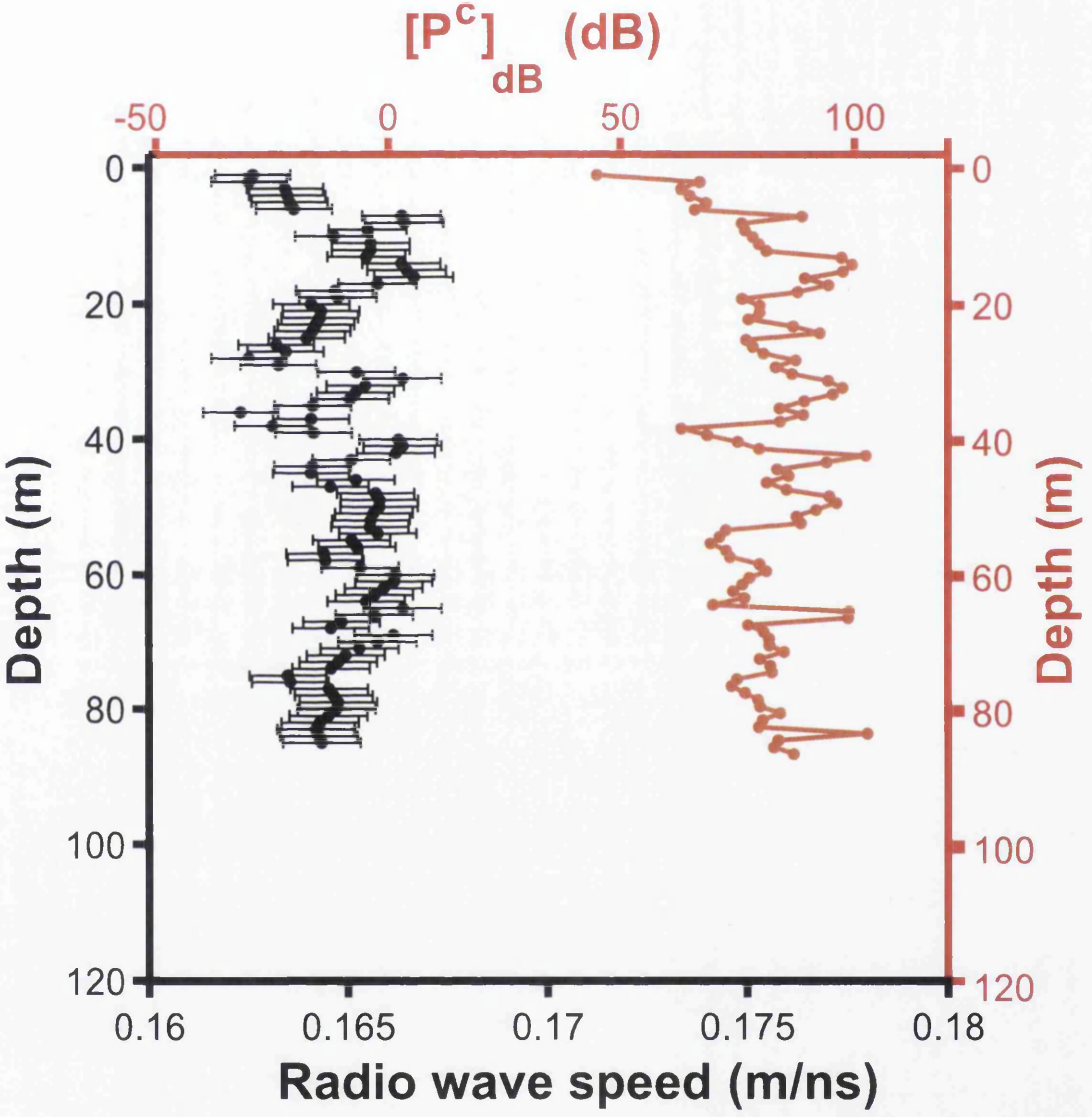

Figure 5.30: Radio wave speed (black) and $[P^c]_{dB}$ (red) profile for the survey Bh1h3

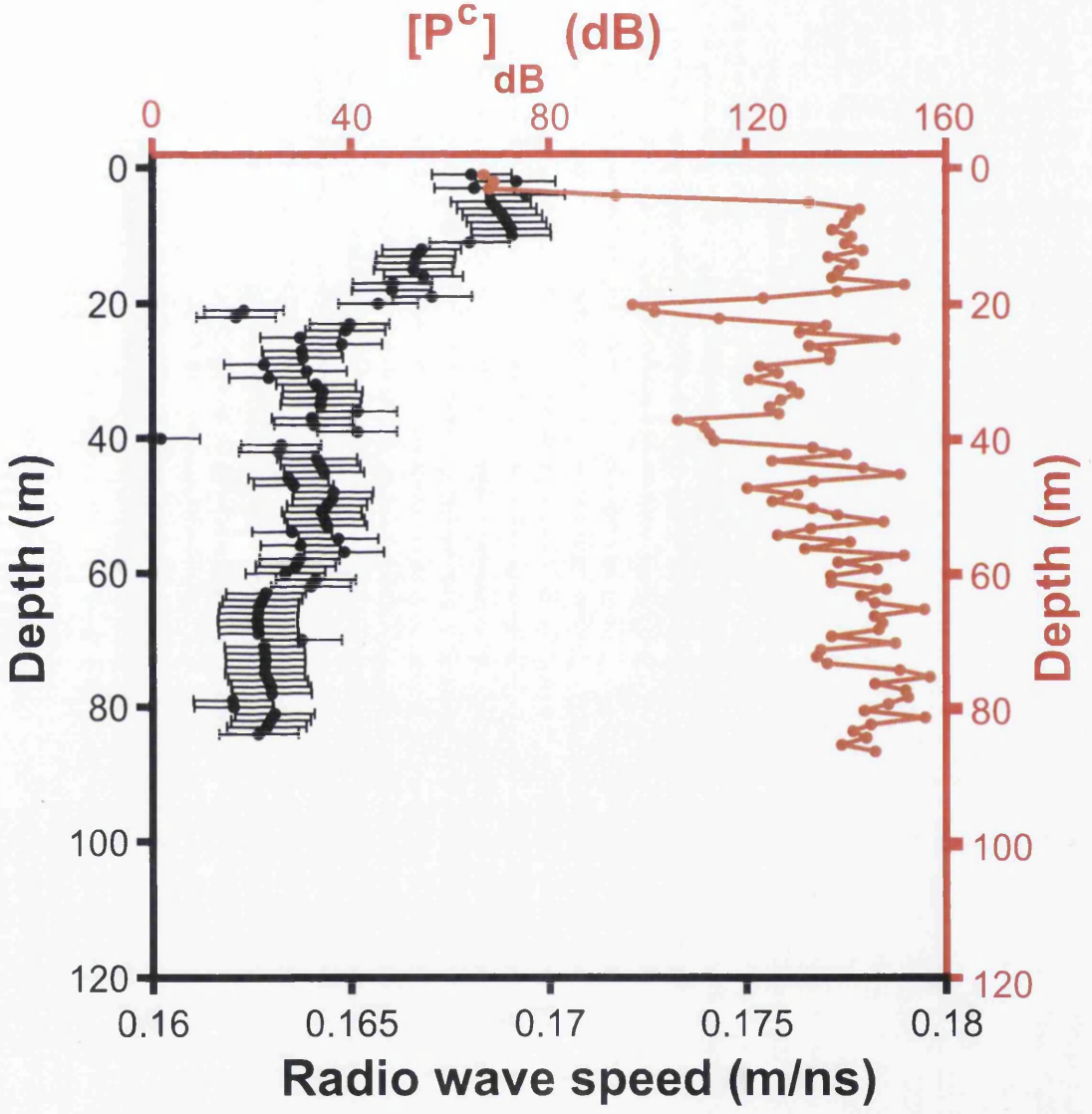

Figure 5.31: Radio wave speed (black) and $[P^c]_{dB}$ (red) profile for the survey B2h1h2

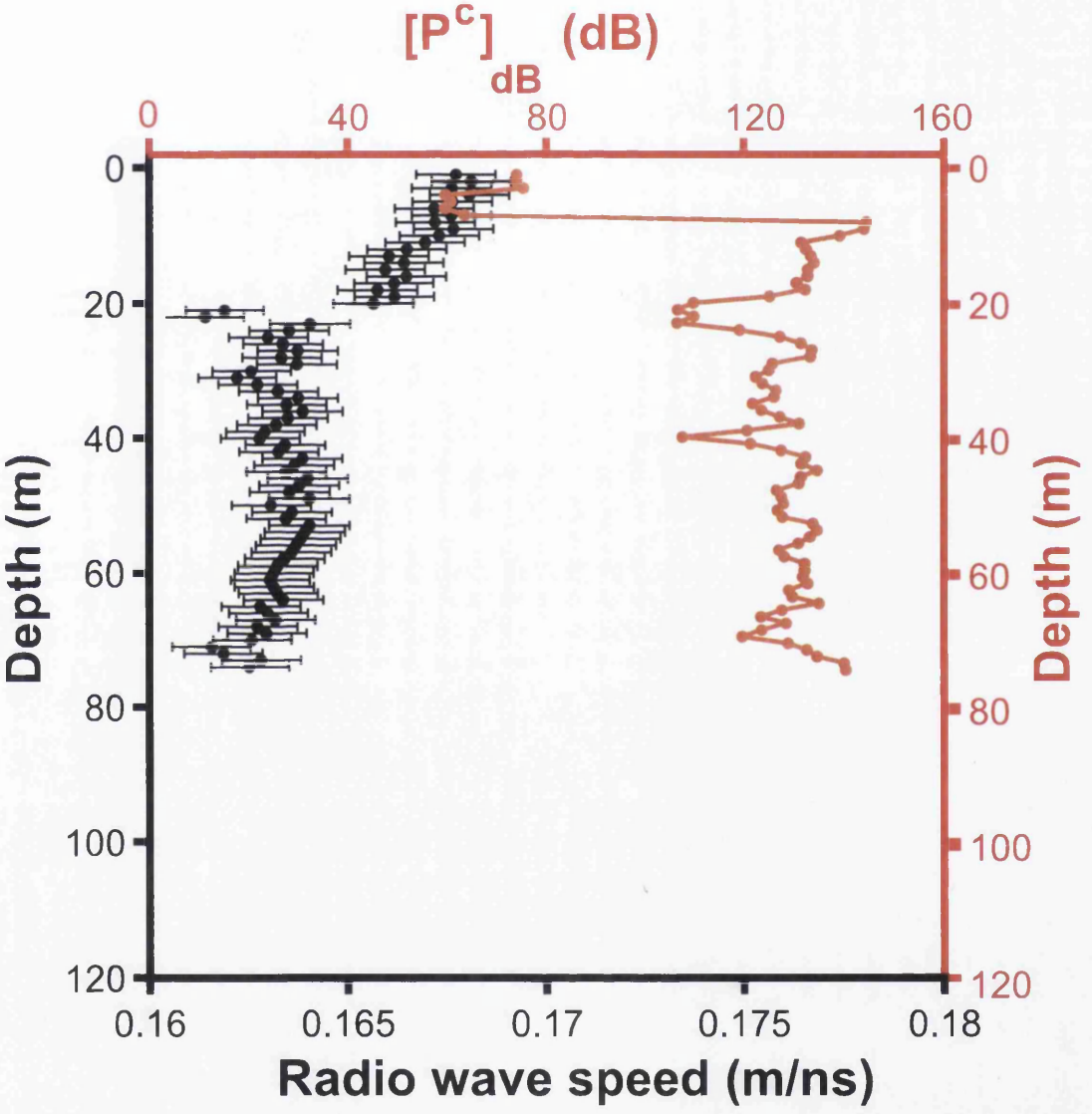

Figure 5.32: Radio wave speed (black) and $[P^c]_{dB}$ (red) profile for the survey B2h1h3

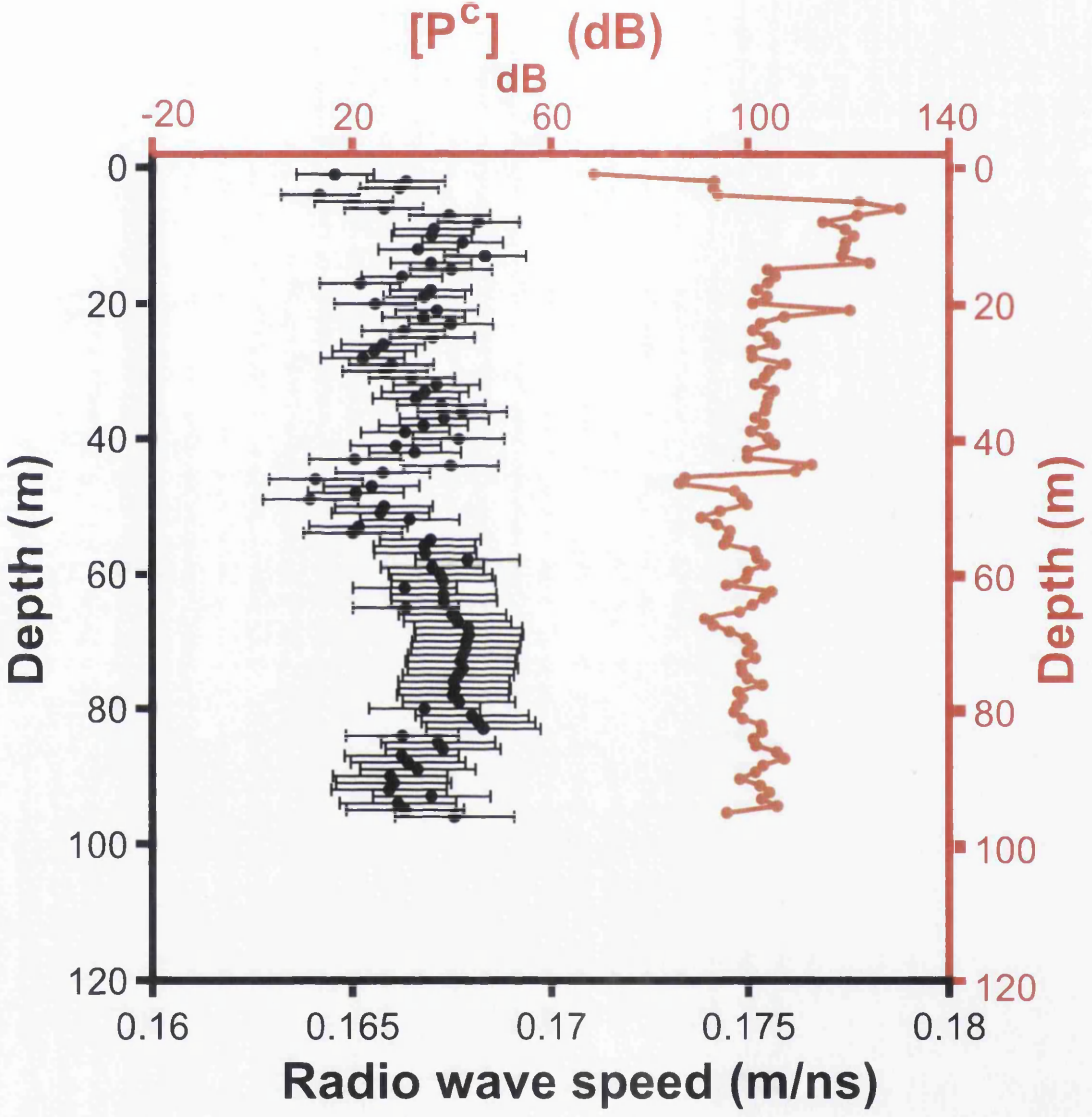

Figure 5.33: Radio wave speed (black) and $[P^c]_{dB}$ (red) profile for the survey Ch1h2

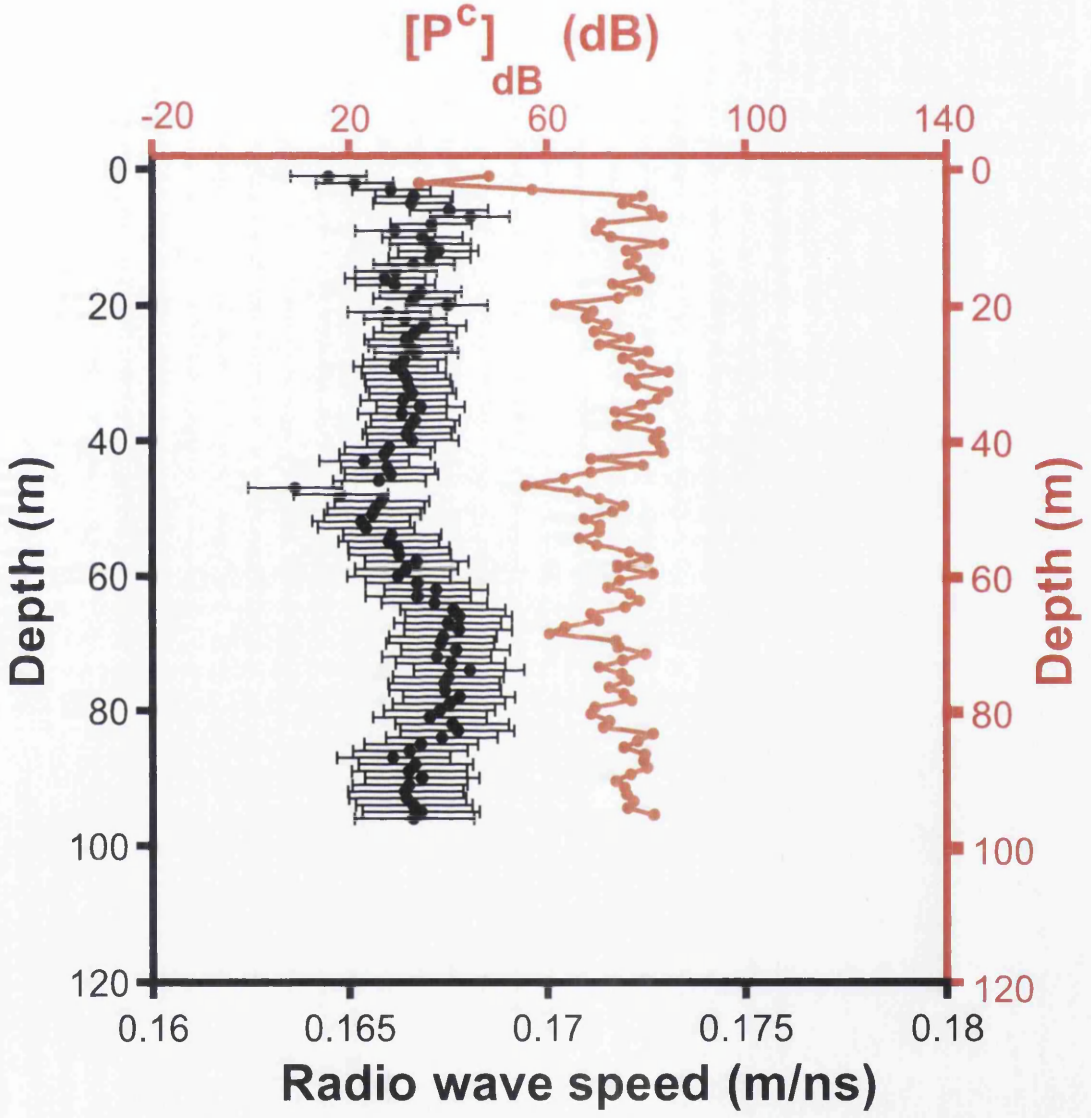

Figure 5.34: Radio wave speed (black) and $[P^c]_{dB}$ (red) profile for the survey Ch1h2$_1$.

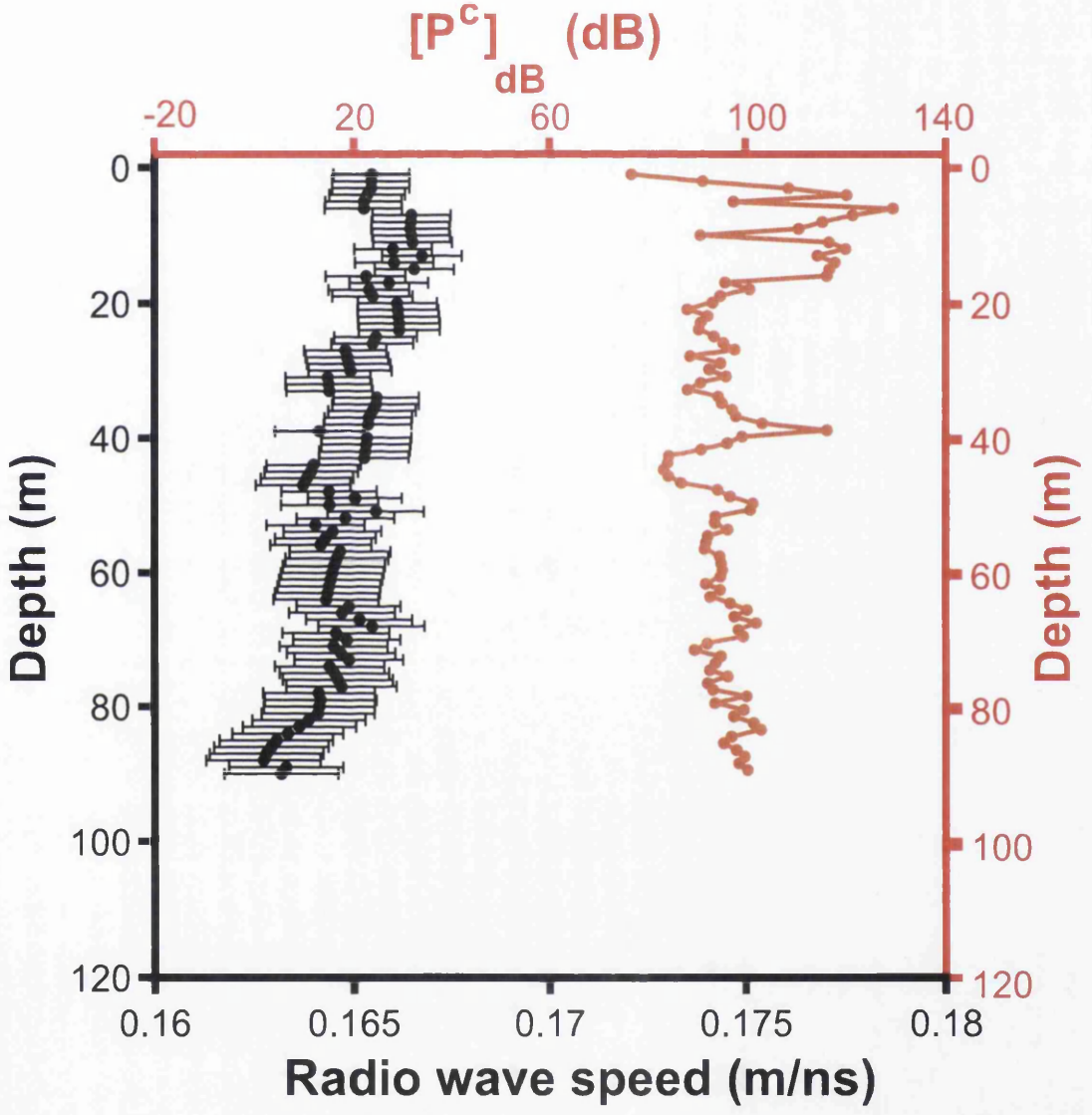

Figure 5.35: Radio wave speed (black) and $[P^c]_{dB}$ (red) profile for the survey Ch2h3.

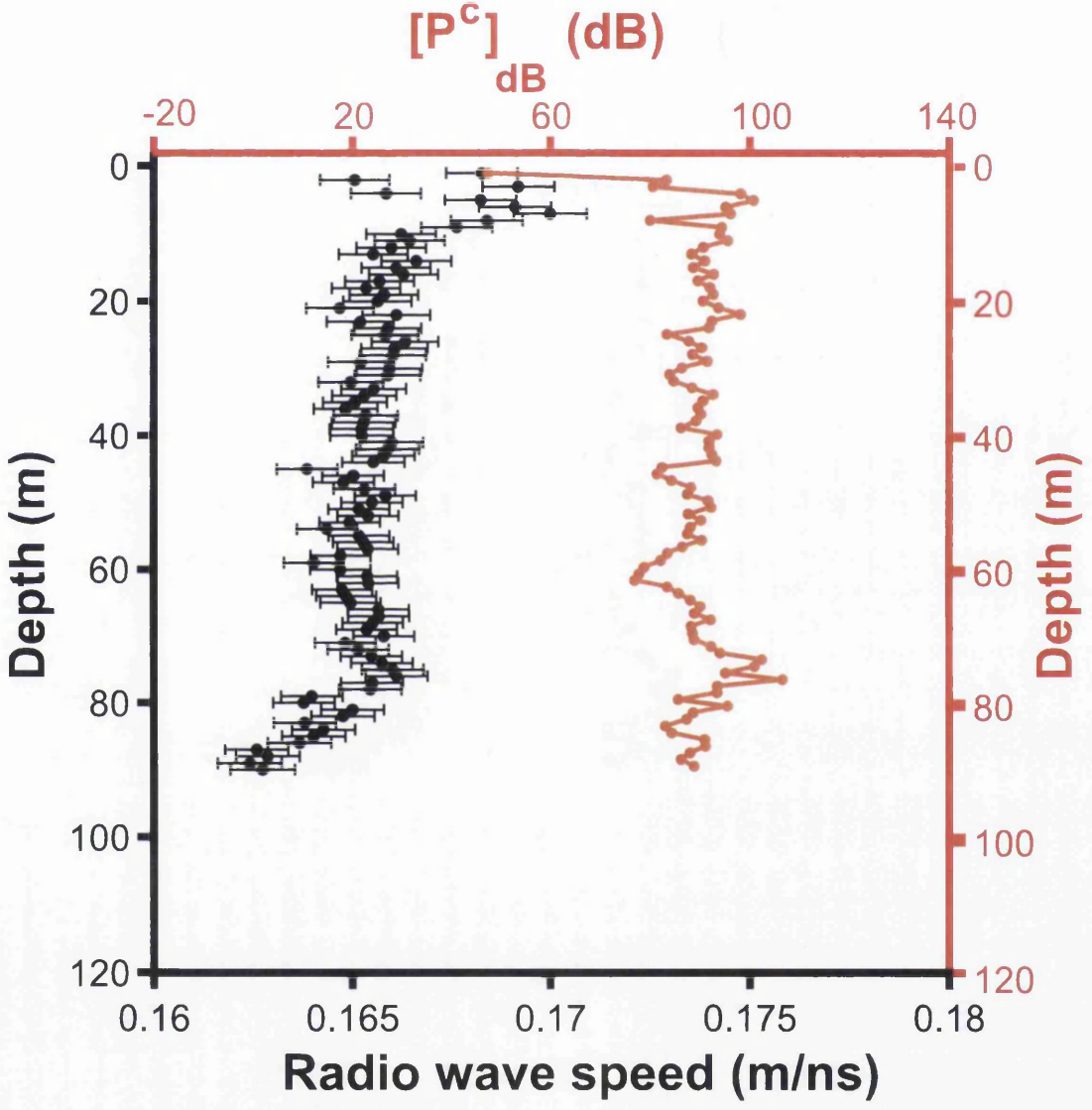

Figure 5.36: Radio wave speed (black) and $[P^c]_{dB}$ (red) profile for the survey Ch3h4.

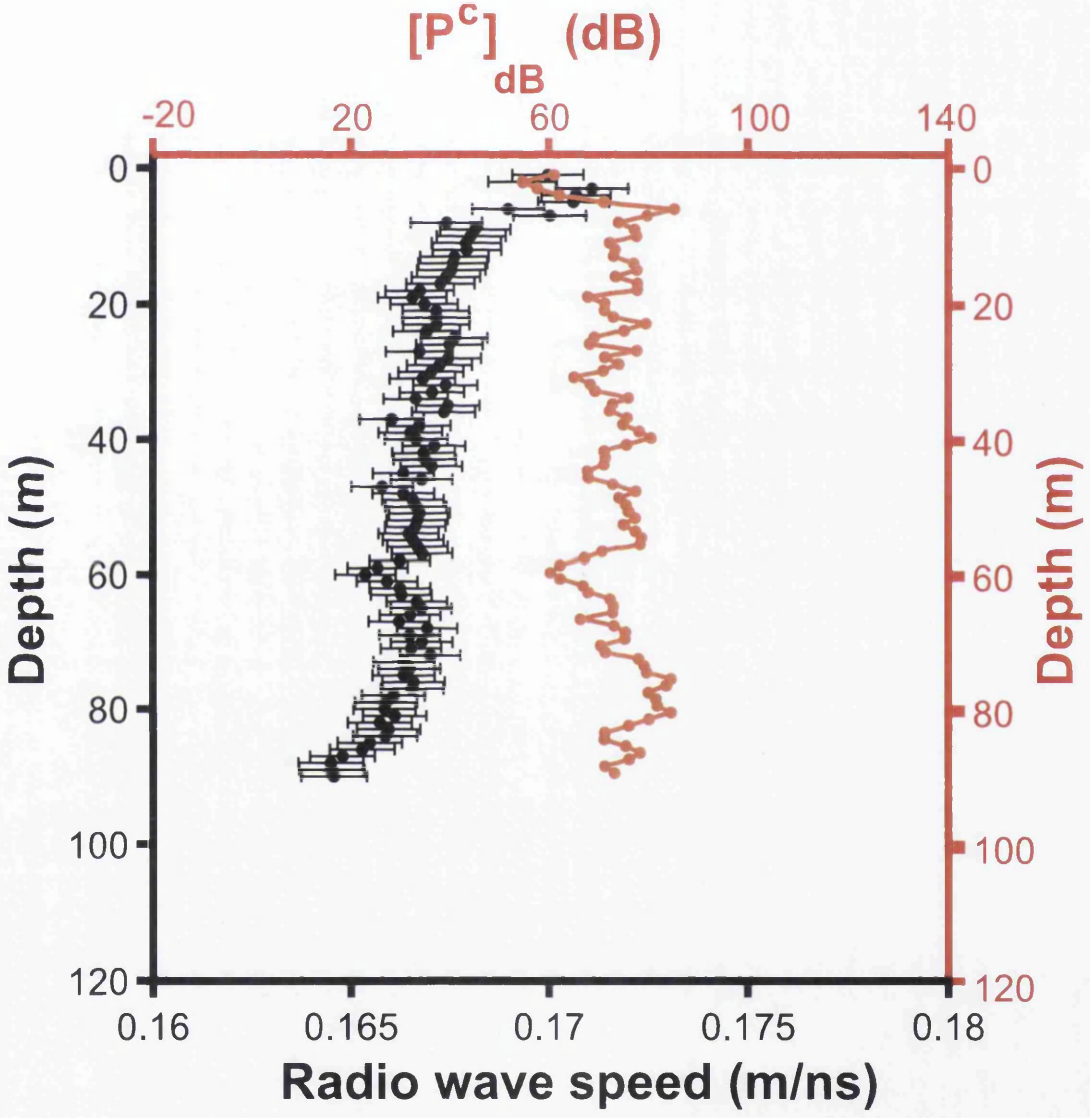

Figure 5.37: Radio wave speed (black) and $[P^c]_{dB}$ (red) profile for the survey Ch3h4$_1$.

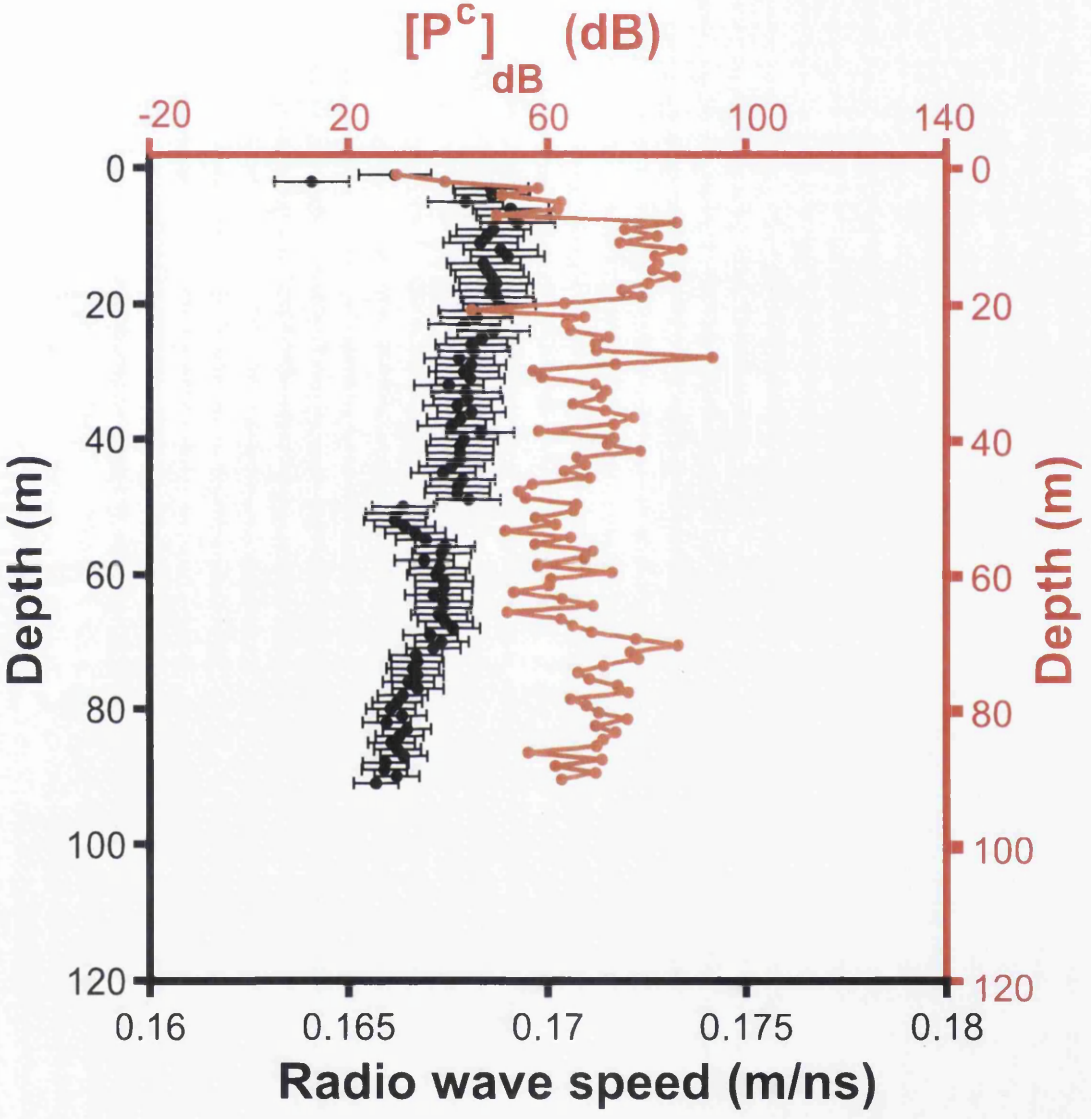

Figure 5.38: Radio wave speed (black) and $[P^c]_{dB}$ (red) profile for the survey Ch5h6$_1$.

5.27); the high-speed anomaly in Ah2h3 was not observed in the power profile. Power profiles also exhibit variability and showed evidence of correlation with the radio wave profiles; these include speed minima often associated with power minima (e.g. Ah1h2, Figure 5.25 at 25, 60 and 100 m depth and Ah3h5, Figure 5.28 at 30 m depth). Site A was also the location of Ah1h2, the deepest ZOP survey collected in the two campaigns. This survey reached the depth of 112 m and, remarkably, very little variation of radio wave speed with depth was observed. Meteorological data from Tarfala Research Station (Figure 5.21) show that no rainfall and no significant variations occurred during the surveying period.

Site B was located downglacier from A, in the upper ablation area of the glacier. This area was the only one investigated in both summers 2008 and 2009. The most recent survey (B1h3, Figure 5.30) do not support any evidence for a stratified structure; radio wave speed measured in the upper part of the ice column remains stable with depth with only minor variations at 25 and 40 m depth. The two surveys collected in 2008 (B2h1h2, Figure 5.31 and B2h1h3, Figure 5.32) are instead supportive of a 2 layer speed structure: radio wave speeds in the upper 20 m are markedly higher than those measured at greater depths. The transition between the high speed (dry) layer is marked with a sharp transition and a clear drop in radio wave speed. Speeds in the lower slow speed (wet layer) remained uniform with depth. Power profiles do not exhibit the same layered behaviour of the radio wave speed. However, as observed at site A, speed and power value do correlate in minima (e.g. at 39 m in Bh1h3, Figure 5.30; at 21 and 40 m in both the 2008 surveys, Figures 5.31 and 5.32).

Results at site C, located in the lower ablation area and below the riegel, shown a generally dry situation. At this site thee multi-frequency (100 and 250 MHz) and one 100 Mhz survey were collected. The multifrequency surveys showed no frequency-dependence of radio-wave speed estimates and the speed profiles are the same for the 100 and 250 MHz frequency. Instead, radar power clearly exhibits frequency-dependence since the 250 MHz returned power were considerably ($\sim$ 20 dB) lower than those acquired with the 100 MHz antennas. Radio wave speed profiles showed stability and no evidence of layering as observed at site B in 2008. Speeds were

stable with depth in one survey (Ch1h2, Figures 5.33, 5.34) whereas showed a slight decreases with depth in the others (Ch2h3, Ch3h4, Ch5h6). Power profiles confirmed the characteristics observed in the other sites with minima correlation (e.g. at 50 m in $Ch1h2_1$, Figure 5.34 and Ch2h3, Figure 5.35). Remarkably, the speed minima measured in $Ch3h4_1$ were correlated to power maxima (Figure 5.37). Site C was the only site where convincing evidences of speed decrease with depth were observed.

5.7 Hydrothermal structure of Storglaciären from ZOP surveys

5.7.1 Solid ice speed

Laboratory measurements of radio wave speed on solid glacier ice have yielded values of 0.168 $\pm$ 0.002 m/ns [*Robin et al.*, 1969; *Bogorodsky et al.*, 1985]. This value is typically used in literature to indicate radio wave speed of cold, polar glacier-ice with no water inclusions [*Macheret et al.*, 1993; *Murray et al.*, 2000a; *Bradford and Harper*, 2005; *Endres et al.*, 2009]. Remarkably, the vast majority of the speed estimates illustrated in this chapter (Figure 5.16) are lower than this value (indicated with a vertical solid line in Figure 5.16). As an example, a first-order interpretation of B2h1h2 and B2h2h3 using the Looyenga mixture equation (Equation 3.4) is given in Figure 5.39. The hydraulic structure from the two surveys is summarised as a two layer system with an upper layer with small amount of water content $W \sim 0.2$ % underlie by a lower layer with $W \sim 1$ %. Figure 5.39 shows also the temperature profile with depth collected by a thermistor string located at site B. Temperature data (provided by Rickard Pettersson at Uppsala University) were collected and processed as illustrated in *Pettersson et al.* [2004] and were published in *Gusmeroli et al.* [2010a]. At site B, Storglaciären is polythermal with a 20m thick cold surface layer (lowest temperature about -1.5°C) underlain by temperate ice at the pressure melting point (Figure 5.39, *Gusmeroli et al.* [2010a]. Positive water-contents should

not occur in cold glacier ice. Why do radio wave speeds measured in the cold ice are lower than the solid ice speed typical in radioglaciology?

Radio wave speeds estimates illustrated in this chapter were obtained from a radio-pulse radiated and received in water (Figure 5.4). There is thus a portion of the travelpath which travels in water, instead of ice. Since the dielectric contrast between water and ice is very high (Table 3.1) it is possible that only even a little portion of travelpath in water needs to be considered when measuring radio wave speed in glaciological ZOP surveys. From Figure 5.4 it is possible to write the travel time from the transmitted to the recorded signal T_M as a combination of three paths: the first from the transmitter to the wall of the first borehole (d_w), the second in the ice (d_i) and the third from the wall to the second borehole to the receiver (d_w). By defining v_w as the radio wave speed in water it follows that:

$$T_M = \frac{d_i}{v_i} + \frac{2d_w}{v_w}. \tag{5.27}$$

Equation 5.27 is in the form T_M=T_i+T_w. Speed estimates using T_M do not take into account the portion of travelpath travelled in water. The propagation speed in ice v_i is thus given by:

$$v_i = \frac{D_M - 2d_w}{T_M - 2d_w/v_w}, \tag{5.28}$$

Figure 5.40 shows the importance of including d_w (and thus using T_i instead of T_M) in radio wave speed estimates from ZOP collected in water-filled boreholes. v_M, the apparent speed is always lower than the v_i used for the model; more specifically the magnitude of the underestimation increases linearly with d_w (Figure 5.40a) and for example v_M from a ZOP in a subsurface with v_i=0.168 m/ns would be 0.165 m/ns for d_W=0.05. The sensitivity of this effect decreases with increasing distance between two boreholes (Figure 5.40. Therefore, since d_W at Storglaciären was measured to be between 0.03 and 0.05 m, it is reasonable to consider radio wave speeds profiles shown in Figure 5.39 as underestimated in their absolute magnitude. Correspondingly, water content values from B2h1h2 and B2h2h3 calculated using Equation 3.4 and radio wave speeds corrected for d_W=0.05 m matched current views on

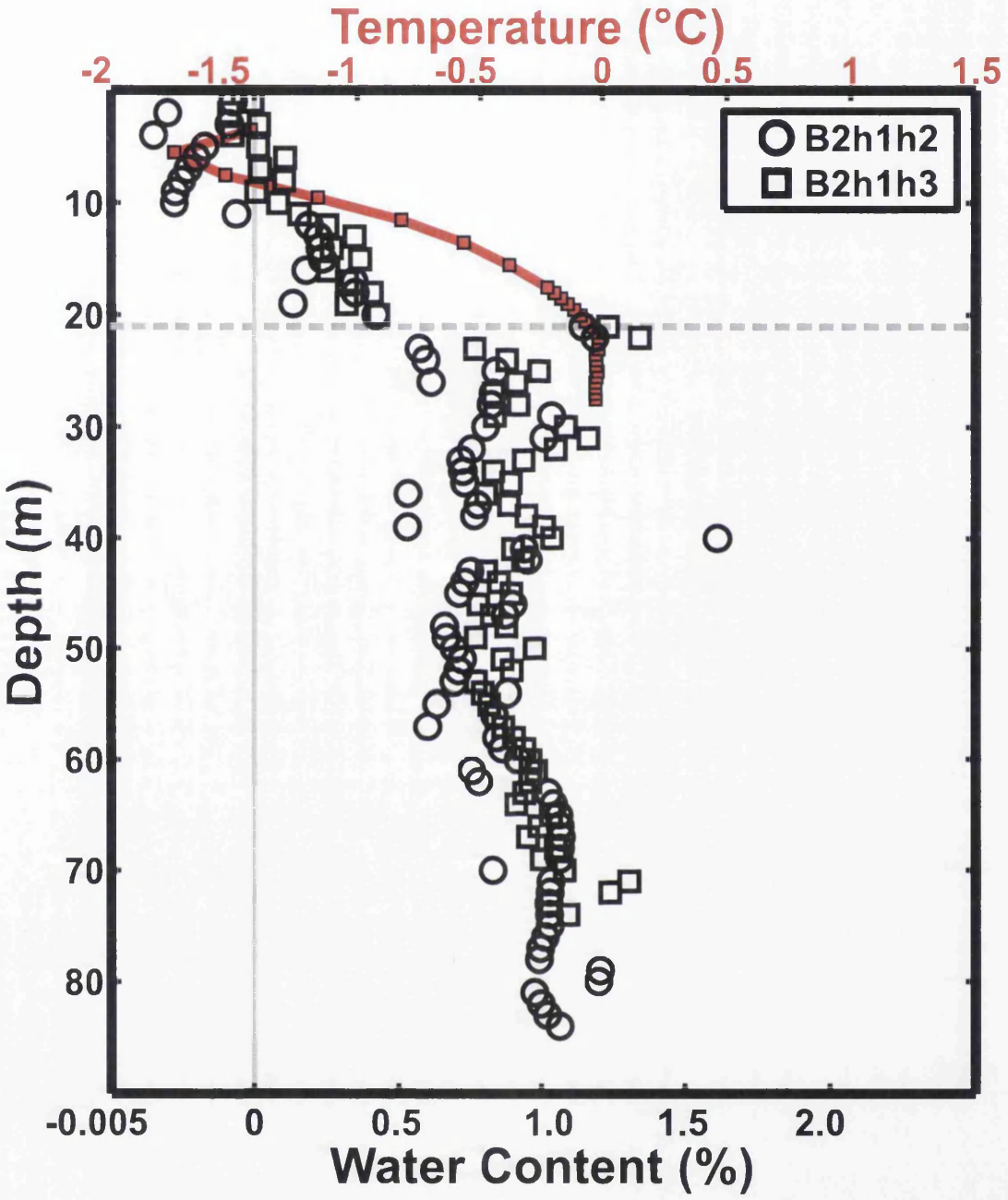

Figure 5.39: Water content profiles with depth at site B from the ZOP surveys colllected in summer 2008. Water content values were calculated using Equation 3.4. The red squares show the profile with depth from the thermistor string located where the ZOP surveys were acquired in summer 2008. The solid and the dashed gray lines indicate W=0% and the depth of the temperature-inferred CTS respectively.

radioglaciology since no water is present in the cold ice whereas some volumetric percentages of water are present in the temperate ice (Figure 5.41).

Radio wave speed profiles corrected for the borehole width are shown in Figure 5.42, the solid ice speed of 0.168 m/ns is also indicated in the Figure by a blue line. If the correction is taken into account radio wave speeds generally stabilise on the solid ice values (Figure 5.42. However, some regions areas present slower speeds indicative of volumetric water content. These regions are the deeper part of Ah1h2 (Figure 5.42a), at 30 m in Ah4h5 (Figure 5.42e), largely in the deeper regions of site B (Figure 5.42 from f to h) and only at considerable depth at site C (Figures 5.42 from i to n). The only site where speeds are typically lower than 0.168 m/ns is site B, where those measured in the deeper ice are as low as 0.165 m/ns.

5.7.2 Water content with depth

Speed profiles illustrated in Figure 5.42 can be transformed into water-content profiles by using the Looyenga equation (Equation 3.4). Errors in water content estimates are generated by the error in speed. These uncertainities can be calculated by combining the Looyenga equation (Equation 3.4) with the formal rules of error propagation (Equations 5.85.9 5.10 and 5.11). The procedure of computing error in water-content estimates in such a way was firstly proposed by *Barrett et al.* [2007] and subsequently applied in radioglaciological studies by *Gusmeroli et al.* [2008]. The error in speed estimates δ_v will generate an error in water content δ_W of [*Barrett et al.*, 2007]:

$$\delta_W = \frac{-2v^{-5/3}\delta_v c^{2/4}}{3(\varepsilon_w^{1/3} - \varepsilon_w^{1/3})}. \tag{5.29}$$

Resulting water content profiles for the radio wave speed estimates illustrated in Figure 5.42 calculated using Equation 3.4 are shown in Figure 5.43. Water contents measured at Storglaciären are typically low and less than 1 %. At site A, only three of the 5 surveys collected provided evidence of radio-wave speeds slow enough to be interpreted using Equation 3.4 for water-contents (Figure 5.43 from (a) to (c)). Site B presented much higher water content than site A (Figure 5.43 from (d) to (f) and

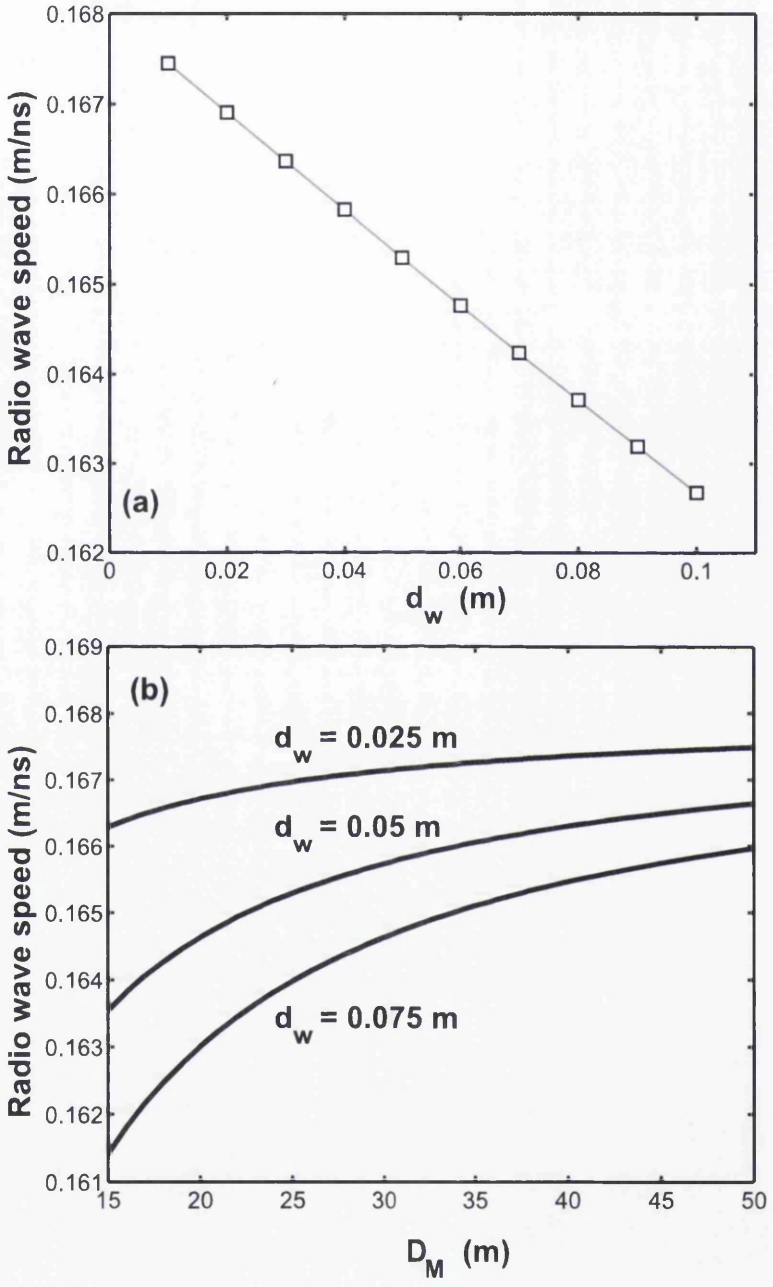

Figure 5.40: Effect of borehole width on radio wave speed estimates modeled using Equation 5.28 and v_i=0.168 m/ns. (a) v_M measured in a synthetic ZOP with D_M=25 m for different borehole width d_w. (b) v_M for different borehole wideness and different D_M.

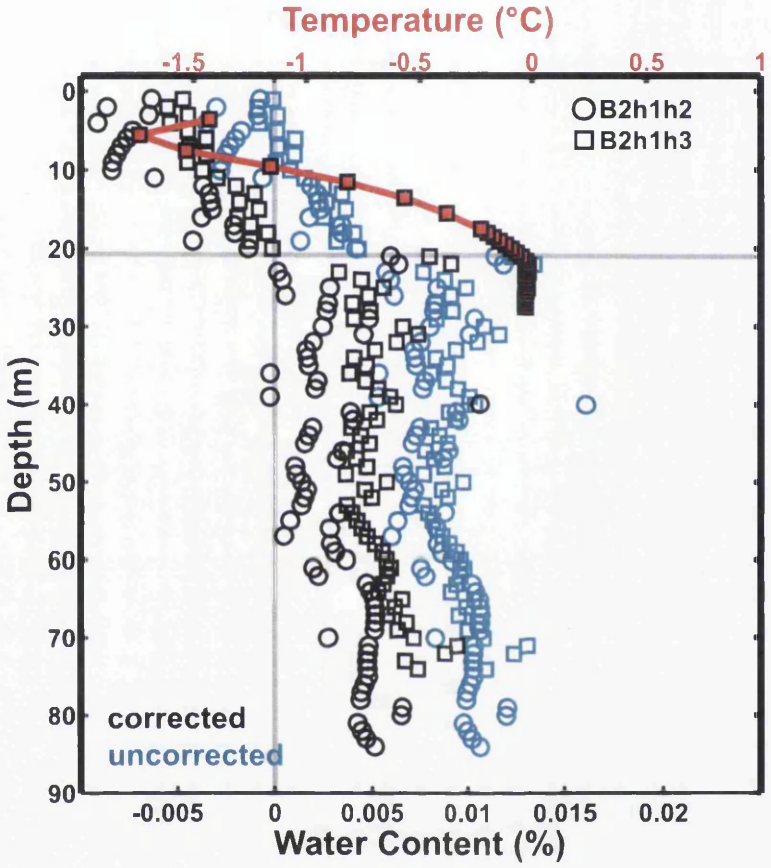

Figure 5.41: Difference in water content profiles with depth at site B from the ZOP surveys colllected in summer 2008. The black dots indicate profiles corrected for borehole wideness whereas blue profiles indicate the interpretation without the correction. The red squares show the profile with depth from the thermistor string located where the ZOP surveys were acquired in summer 2008. The horizontal line indicates the depth of the temperature-inferred CTS. The vertical line indicates water content = 0%.

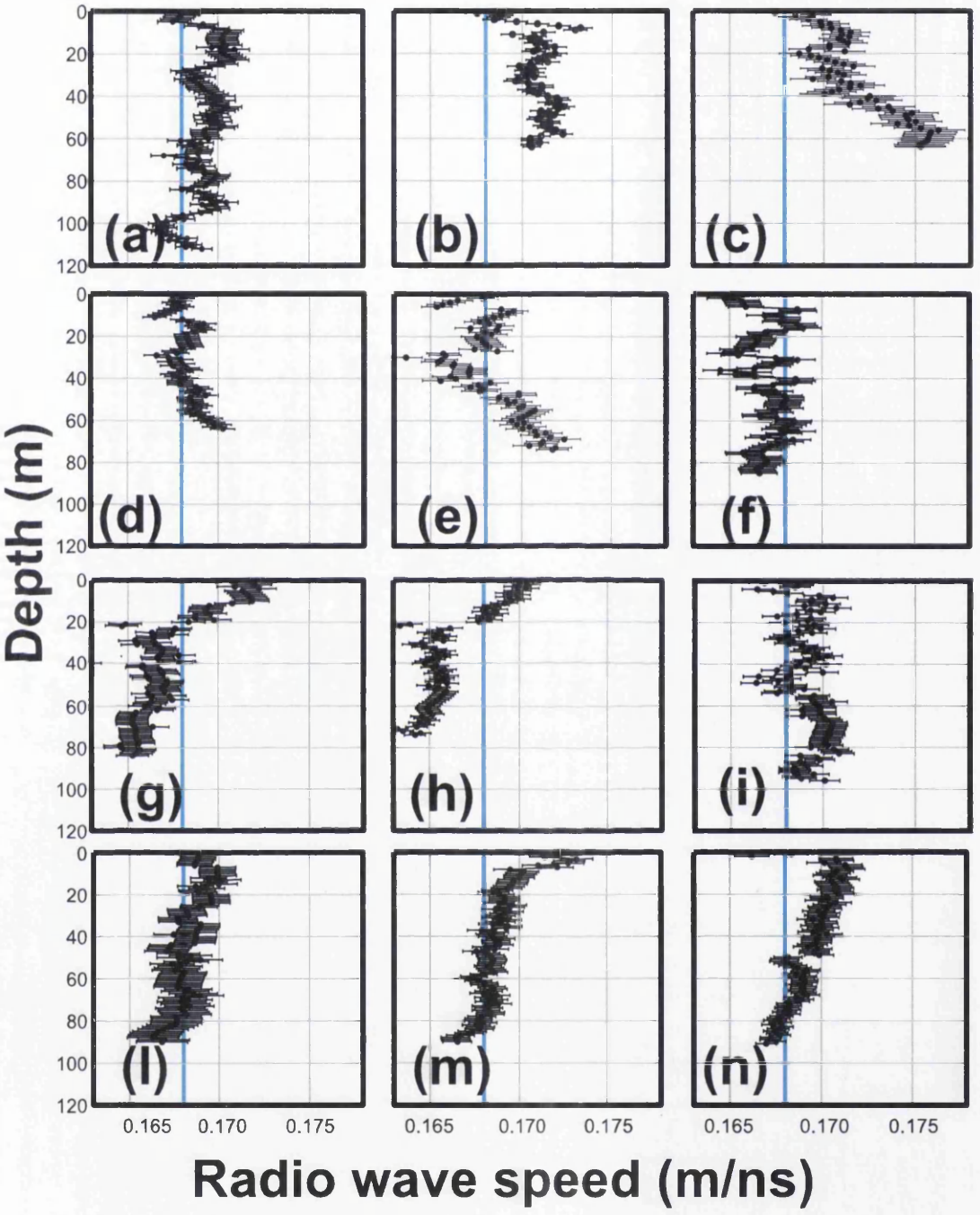

Figure 5.42: 100 MHz Radio wave speed profiles with depth as measured with ZOP surveys at Storglaciären. Profiles are corrected for the borehole width. (a) Ah1h2, (b) Ah1h3, (c) Ah2h3, (d) Ah3h5, (e) Ah4h5, (f) Bh1h3, (g) B2h1h2, (h) Bh2h1h3, (i) Ch1h2 (100 MHz, black dots; 250 MHz, red dots) , (l) Ch2h3, (m) Ch3h4, (n) Ch5h6.

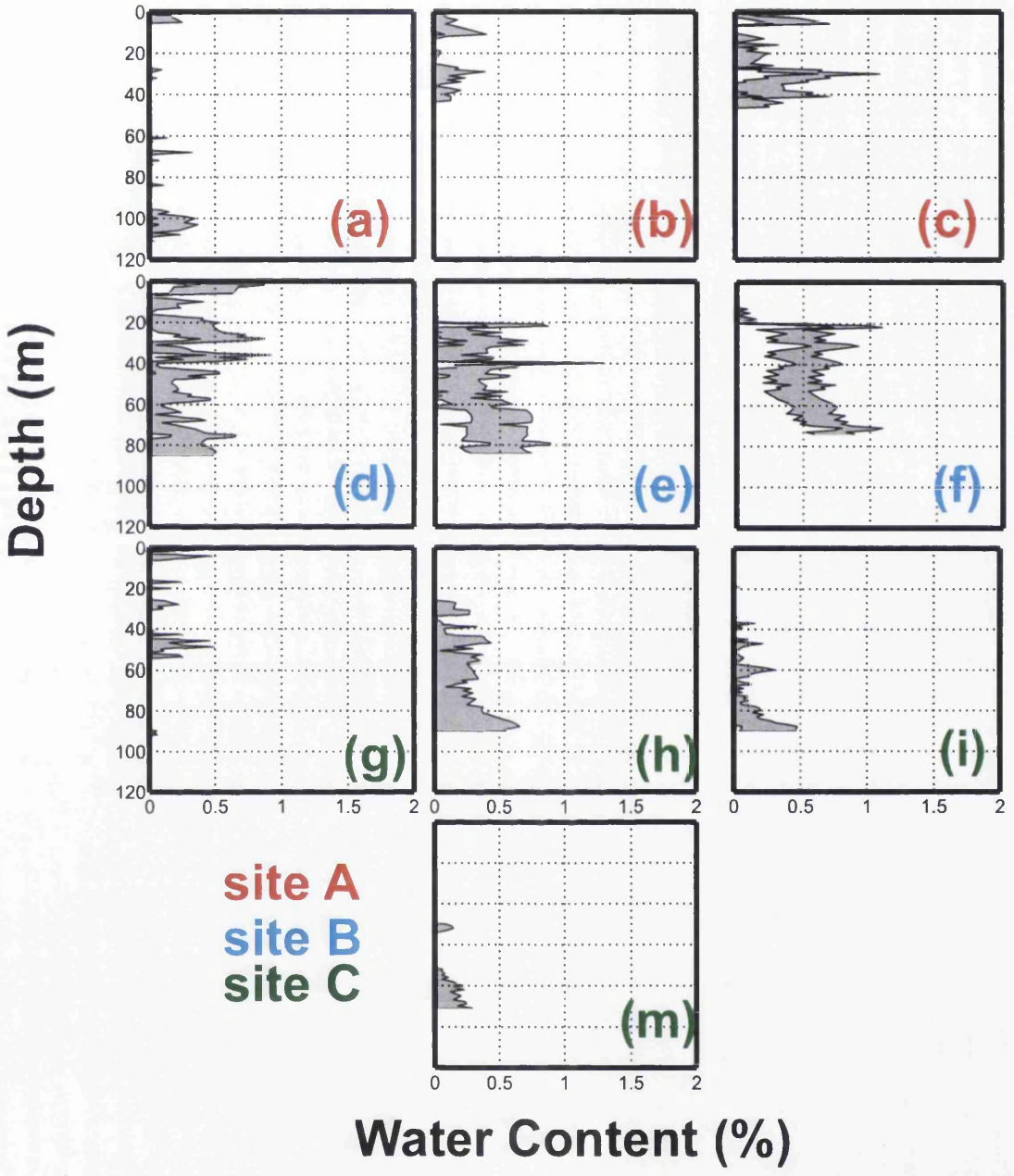

Figure 5.43: Water content profiles with depth as measured with ZOP surveys at Storglaciären. Profiles were obtained using Equation 3.4. Measurement error was calculated using Equation 5.29. (a) Ah1h2, (b) Ah3h5, (c) Ah4h5, (d) Bh1h3, (e) B2h1h2, (f) Bh2h1h3, (g) Ch1h2 , (h) Ch2h3, (i) Ch3h4, (m) Ch5h6. Note that Ah1h3 and Ah2h3 are not shown because radio wave speeds in these surveys were higher than the solid ice speed and thus no water-content was observed.

the large majority of the ice column is composed by glacier-ice with ~0.5% water content. Site C is similar to site A with W values lower than 0.5 %. Three of the four collected surveys at site C provided evidences of water-content increases with depth (Figures 5.43 from (h) to (m)).

5.8 Summary

A series of multi-frequency, multi-azimuthal zero offset borehole radar profiles were acquired at three different location in the ablation area of Storglaciären during two subsequent geophysical campaigns. A ZOP profile allows accurate reconstruction of radio wave speed and radar power variation throughout the ice column. The total number of surveys was 16 and the maximum depth sampled was 112 m from the glacier surface. Results supported spatial variability of both radio wave speed and power. No azimuthal and no frequency dependence of radio wave speed was observed. Conversely radar power was frequency dependent, since power measured with the 250 MHz antennas was much lower than that acquired with the 100 MHz ones. The vast majority of the surveys shows good correlation between speed and power especially in the location of minima. Radio wave speed distribution with depth, corrected for the fact that the radio pulse was radiated and received in water-filled boreholes, shows that water content at Storglaciären is less than 1%. This is in agreement with previous measurements using thermodynamics methods, but in disagreement with the often cited radioglaciological principle that radio wave speed in temperate ice should be considerably slower than 0.168 m/ns. Differences were observed between the three sites: site A, close to the accumulation area contained less water than site B, the wettest observed in the upper ablation area with water content up to 0.8%. At site C, located in the lower ablation area, three surveys on four provided evidence of water-content increase with depth.

Chapter 6

Seismic wave attenuation at Storglaciären

The vast majority of published works on glacier-ice water-content have considered the influence that water-content has on the propagation speed of geophysical signals such as electromagnetic [*Macheret et al.*, 1993; *Murray et al.*, 2000a; *Bradford and Harper*, 2005] and elastic [*Benjumea et al.*, 2003; *Navarro et al.*, 2005] waves. *Endres et al.* [2009] showed that by jointly inverting spatially-coincident radar and seismic wave speeds it is possible to obtain physically consistent water-content and pore-geometry estimates for a two-phase (ice-water) medium. However, since air bodies in the form of bubbles, englacial voids and fractures are commonly observed in glaciers [*Pohjola*, 1994], this interpretation is non-unique [*Bradford and Harper*, 2005; *Gusmeroli et al.*, 2008]. A 3-phase model should be considered in order to estimate volumetric content and geometry of both air and water inclusions within glacier-ice. As an example, relatively high electromagnetic (and low seismic) speeds could either be indicative of dry, bubble-free or wet, bubbly glacier-ice.

A few workers [*Macheret and Glazovsky*, 2000; *Bradford et al.*, 2009] included the presence of air bubbles in their water-content estimates. However, since these procedures did not consider electromagnetic wave speed being influenced by air-rich

features such as fractures and englacial voids, it is desirable that additional parameters, other than speed, are considered in the analysis to obtain more reliable water-content estimates. These parameters, rarely measured in glaciers, are radar and seismic attenuation; as stated by *Endres et al.* [2009], the combined use of radar and seismic speeds with corresponding attenuations would provide sufficient parameters to estimate the volumetric content and geometry of both air and water inclusions within glacier-ice. In fact, since propagation properties (speed and attenuation) of geophysical signals are sensitive to water, four independent parameters, jointly inverted, (instead of two) clearly add to the aim of describing glacier-ice properties using radar and seismic surveys. Furthermore, values of seismic attenuation are routinely used when exploring subglacial properties using seismic surveys [*Smith*, 1997, 2007; *Peters et al.*, 2008; *King et al.*, 2008] and uncertainities in these values often constitute limitations in the techniques used to derive bed properties [*Smith*, 2007].

This chapter will illustrate seismic wave attenuation's estimates from seismic refraction experiments acquired at Storglaciären in summer 2008. Seismic attenuation values will be expressed in terms of the P-wave quality factor Q_P estimated using methods from hydrocarbon exploration [*Tonn*, 1991; *Dasgupta and Clark*, 1998]. Contents of this chapter are published in *Gusmeroli et al.* [2010a].

6.1 Seismic attenuation and the spectral ratio method

Following the fundamental principles that control seismic wave attenuation and dispersion [*Futterman*, 1962] for the specific case of frequency-independent Q, the change in amplitude spectrum from S_0 to S_1 after travelling a distance, x, can be described by using the frequency-dependent attenuation coefficient, α [*Aki and Richards*, 2002]:

$$S_1 = GrS_0e^{-\alpha x}, \tag{6.1}$$

where G and r are the geometric spreading factor and energy partitioning losses at interfaces (when the wave crosses a boundary between two media) respectively: these two terms are treated as frequency-independent. By considering equation 3.12, equation 6.1 becomes:

$$S_1 = GrS_0 e^{-\frac{\pi f}{vQ}x}. \tag{6.2}$$

This equation provides the theoretical basis of the spectral ratio method, a popular method of obtaining frequency-independent Q estimates from field datasets such as vertical seismic profiles [*Tonn*, 1991; *Wang*, 2003] and surface reflection surveys [*Dasgupta and Clark*, 1998; *Reine et al.*, 2009].

Equation 6.2 implies that higher frequencies are preferentially attenuated. In this instance, the natural logarithm of the ratio between the attenuated and non-attenuated amplitude is (for constant Q and v) a linear function of frequency [*Tonn*, 1991]:

$$\ln\left(\frac{S_1}{S_0}\right) = -\frac{\pi f}{Qv}x + C, \tag{6.3}$$

where C is $\ln(Gr)$ and contains all frequency-independent terms. Equation 6.3 shows that $\ln(S_1/S_0)$ is linear in frequency with a slope, γ , given by:

$$\gamma = -\frac{\pi \Delta x}{Q}. \tag{6.4}$$

In typical experimental settings, the wavelet is sampled at two locations separated by a distance Δx and γ is converted to Q for the given $\Delta t = \Delta x/v$. When many pairs of attenuated signals are available, with a range of travel time differences, all of them sampling a volume considered to be characterised by a single Q, this Q can then be derived from a linear regression of spectral ratio slope, γ, against Δt (which is then directly estimated by the travel-times):

$$Q = -\frac{\pi}{m}, \tag{6.5}$$

where m is the slope of the regression line. Assuming constant Q within the medium, a more robust result can be derived by sampling the waves at a higher number of locations and such intensive sampling will be exploited in this chapter.

Shot	Date	Time
SG6j	06/07/2008	15.49
SG7j-1	07/07/2008	11.17
SG7j-2	07/07/2008	16.24

Table 6.1: Details of the seismic surveys used in the Q_P analysis at Storglaciären.

6.2 Field experiment, refraction surveys

Q_P estimates were obtained from seismic refraction surveys collected in the ablation area of Storglaciären (Figure 6.1). In this area the glacier has a cold-ice surface layer above a temperate core [*Holmlund and Eriksson*, 1989; *Pettersson et al.*, 2003]. At the time of the survey the glacier was snow-free (Figure 6.2) and the seismic line was located near a thermistor string which provided temperature data in the uppermost 28 m of ice (Figure 6.2). Data were acquired using a hammer-and-plate source and the receivers (24 x 100 Hz geophones) were positioned along a 115 m long line, transverse to glacier flow, with 5 m spacing (see Figure 6.1 for location and survey geometry). The distance between the source and closest-geophone was 5 m. The seismic line was repeated over two days at different times in order to detect any temporal variation in attenuation values (see Table 6.1 for details of the surveys).

6.3 Seismograms and seismic speed

Despite being collected at different moments (Table 6.1) the three seismograms clearly have similar carachteristics (Figure 6.3). In the seismograms is possible to differentiate two linear events at relatively low travel-times carachterised by different speed. Noticeble is the absence of a reflection at higher travel-times, reasonably expectable from the glacier-substrate interface. The faster event (dashed arrow in Figure 6.3) is recognizable throughout the whole geophone spread and is interpreted as refracted arrivals travelling in the uppermost part of the ice column. The second, slower event (solid arrow in Figure 6.3) is lower in frequency and is interpreted to

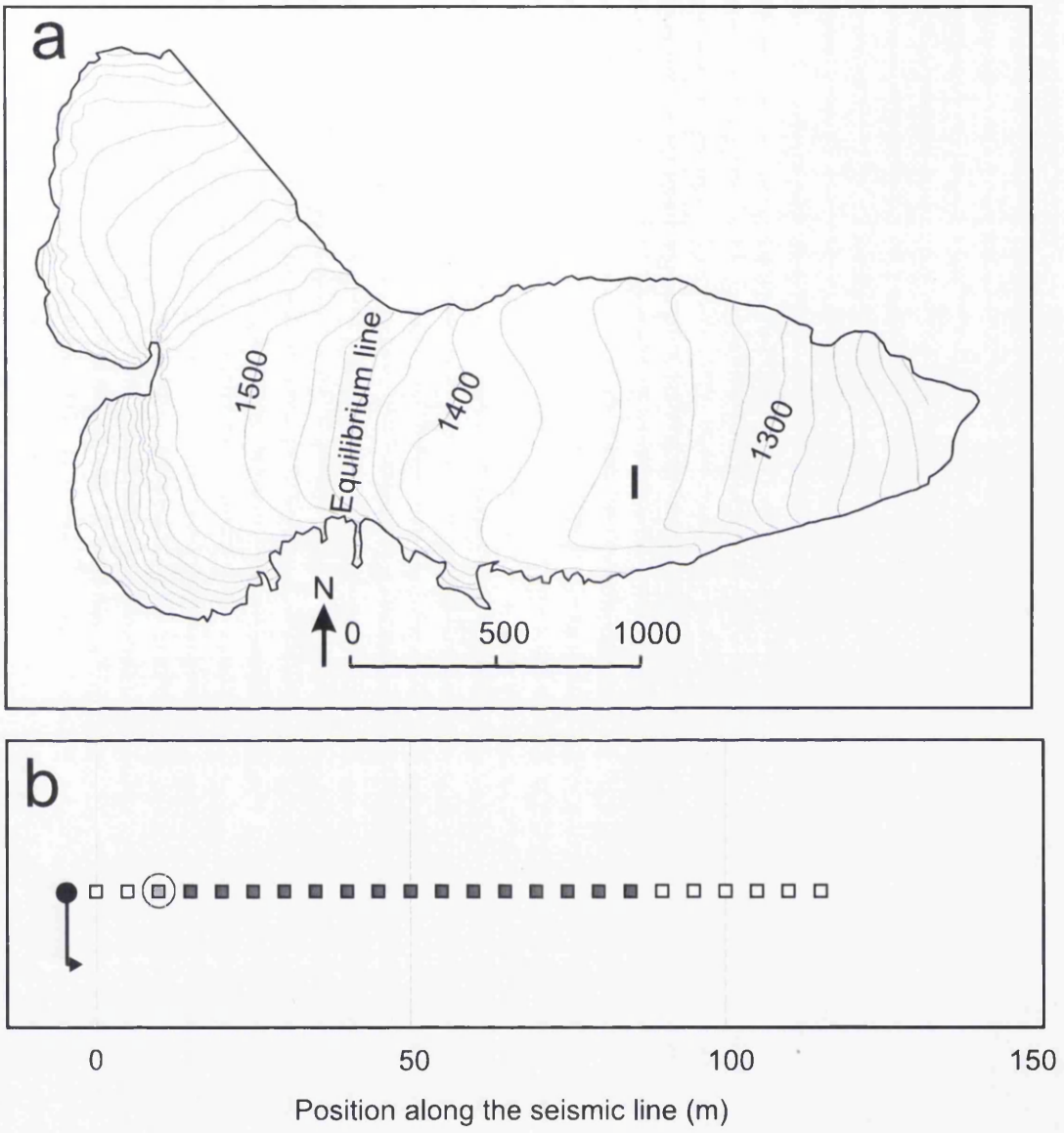

Figure 6.1: (a) Location of the seismic line at Storglaciären (67° 54'N, 18° 35'E). Surface elevation in meters above sea level. (b) Schematic of the survey. The black circle indicates the shot position; white and filled squares indicate unused and used geophones respectively. The arrow indicates the direction of the P-wave sampled. The circled geophone, located at 15 m from the source, was used as the reference arrival in the analysis (A_0 in equation 6.3).

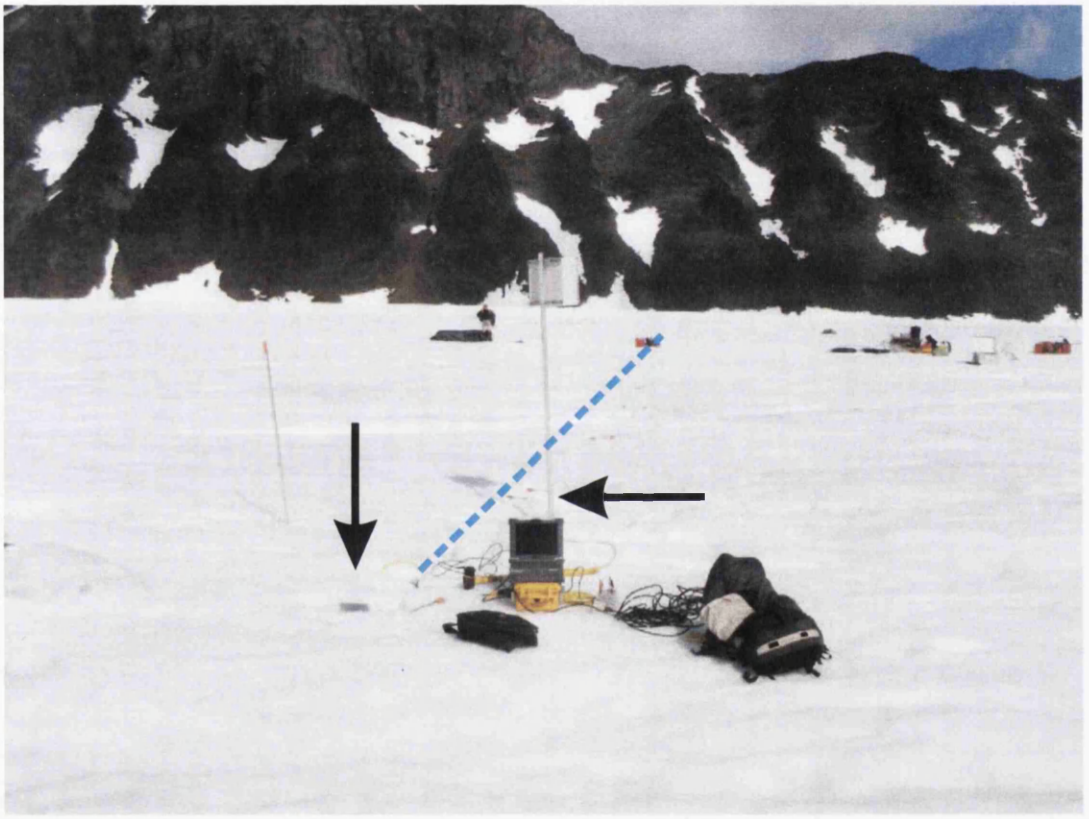

Figure 6.2: Photo of the location of the refraction surveys. The seismic line is indicated with the blue dashed line. The vertical arrow indicate the shot position whereas the horizontal line indicate the position of datalogger connected to the thermistor string.

be generated by Rayleigh waves which propagates along the free surface. The slower event, also known in seismological literature as *Ground roll* [*Sheriff and Geldart*, 1995], is only mentioned here as noise and will not be analysed. Seismic speeds for

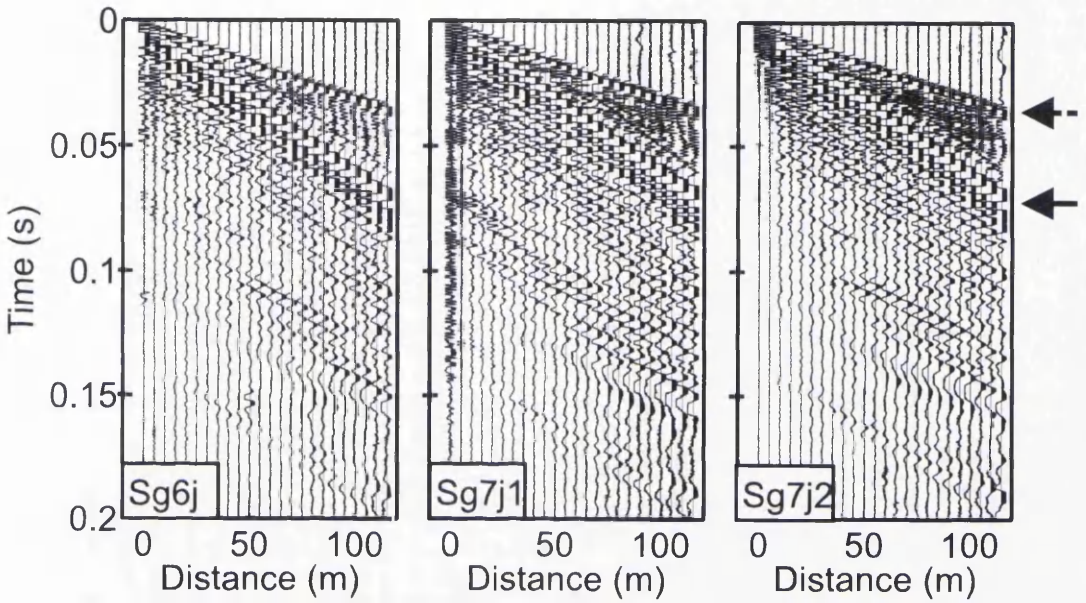

Figure 6.3: The three unprocessed seismograms collected at Storglaciären in July 2008. Dashed arrow indicates refracted first arrivals. Solid arrow indicates the ground roll (see text for explanations). See Table 6.1 for details on the surveys.

the refracted arrivals were calculated by picking the travel time of the first arriving energy directly from the seismograms 6.4. For refracted arrivals seismic velocity is the inverse of the slope of the line in a travel time *vs.* distance plot [*Sheriff and Geldart*, 1995]. Travel time of the first arrivals did not differ for the three surveys (Figure 6.4). And the calculated, averaged velocity was 3617±57 m/s.

6.4 Q_P analysis

Q_P estimates were obtained using the spectral ratio method [*Tonn*, 1991], for which the physical basis were explained in Section 4.1. The spectral ratio method allow Q_P estimates from seismic surveys by quantifying the attenuation of the high-frequency

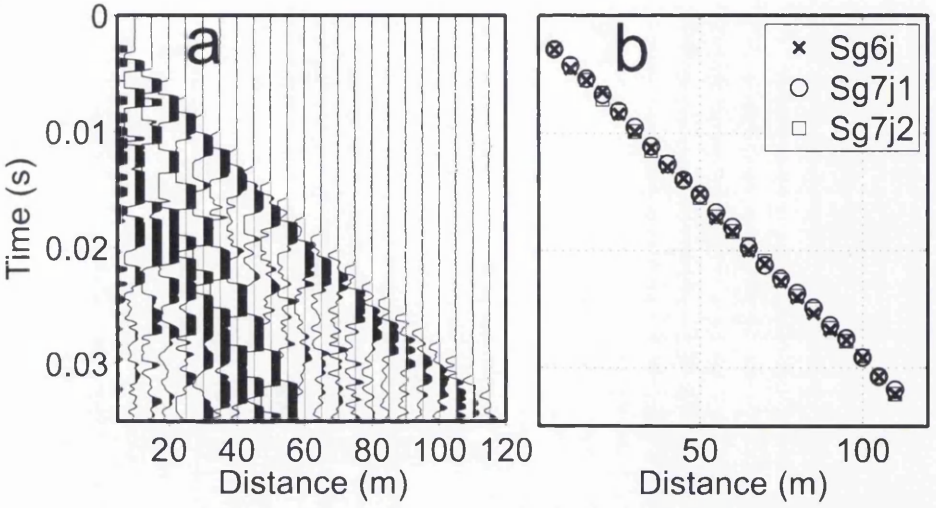

Figure 6.4: (a) Seismogram at Storglaciären showing the refracted arrivals. (b) Picked first arrivals of the refractions. No difference between travel-times (and thus speed) is observed.

component of the spectra predicted by equation 6.3. Equation 6.3 requires calculation of the amplitude spectra of a reference, unattenuated wavelet (S_0) and of an attenuated wavelet (S_1). Amplitude spectra were calculated by a short time Fourier transform on the first cycle of the wavelet using a cosine-tapered time window with a plateau from the first break of the arrival to its second subsequent zero crossing (Figure 6.5). The full window length (Figure 6.5) used to obtain the Fourier spectra included a taper before and after the plateau, the length of the taper was 10% of the length of the first cycle.

The spectral ratio in Figure 6.6 is an example of a Q_P estimate from SG7j1. The refraction arriving at 15 m offset is used as S_0 whereas the attenuated wavelet S_1 is computed from the refractions arriving at 60 m offset. Logarithm of the spectral ratio strongly decreases with frequency in the bandwidth 100-300 Hz (Figure 6.6b). From equation 6.4 Q_P can be estimated from the spectral ratio slope γ in the bandwidth 100-400 Hz for the particular pairs of arrivals (offset range, Δ_x=45 m) shown in Figure 6.6. Q_P is $\sim$ 6 for the 100-300 Hz bandwidth (Figure 6.6c) and is lower ($\sim$ 3) for the highest part of the frequency spectrum. The non-linearity of the

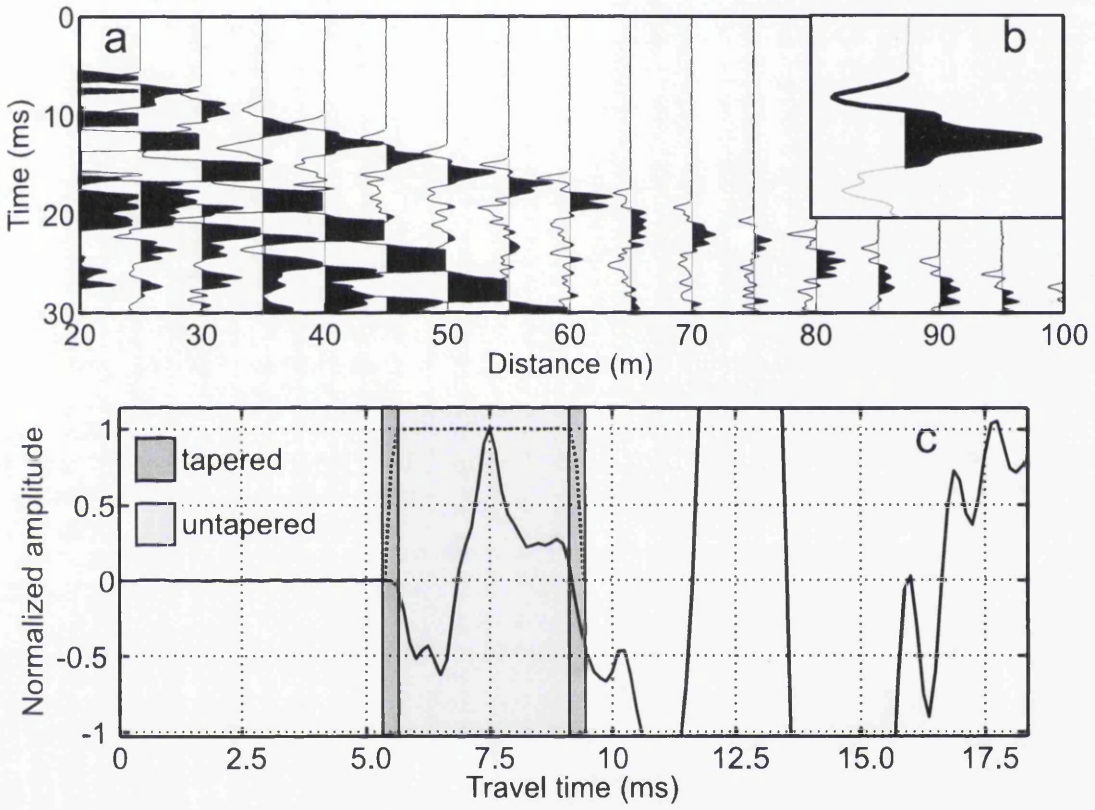

Figure 6.5: Example of unprocessed seismograms used in the computation of QP. (a) Sample data. (b) Extracted wavelet at 40m offset (c) Example of the taper (dotted line) applied to extract the first cycle of the refractions.

spectral-ratio-decrease with frequency (Figure 6.6) represent evidence of frequency dependence of Q_P.

6.4.1 Intensive sampling of the seismic wave

Q_P estimates in Figure 6.6 are obtained using the simplest application of the spectral ratio method since the wavelet is sampled at two locations. A novel application, where the wavelet is sampled at multiple locations is tested in this chapter. Figure 6.1b show a schematic of the seismic line with details on the approach exploited in this study: 15 consecutive refractions (filled squares in Figure 6.1b) will be used as attenuated wavelets (S_1) and compared with the unattenuated wavelet (S_0) extracted at 15 m offset (circled square in in Figure 6.1b). Since the reference wavelet recorded at position x attenuates to the wavelet recorded at $2x$ at the same rate that $2x$ decreases to $4x$, the position of S_0 has no implication on attenuation analysis and was arbitrarily chosen at 15 m offset. Refractions were not clearly distinguishable at high offsets and therefore part of the seismic line was not used in this analysis (white squares in Figure 6.1). In this process the selection of the bandwidth is important since the spectral ratios are representative of Q only in the region of the spectra where there is energy. For this dataset the choice to derive Q in the bandwidth 100-300 Hz is justified by two reasons: (i) the low frequency boundary was dictated by the 100 Hz geophones used in the data-collection and (ii) the high-frequency boundary was set at 300 Hz to avoid notches in the Fourier spectra that occur at 400-500 Hz (Figure 6.6). As shown in Figure 6.6 the spectrum of both arrivals is mostly concentrated in this bandwidth and decreases rapidly at frequencies higher than 300 Hz.

The natural logarithms of the spectral ratio (Figures 6.7 as example) between the reference spectra wavelet (arbitrarily picked as 15 m offset from the source, Figure 6.1b) and arrivals recorded at 15 subsequent geophones were then computed and plotted as function of frequency to derive the slope of the ln(spectral ratio), γ, which, according to equation 6.4, is a function of Q and the travel-time between

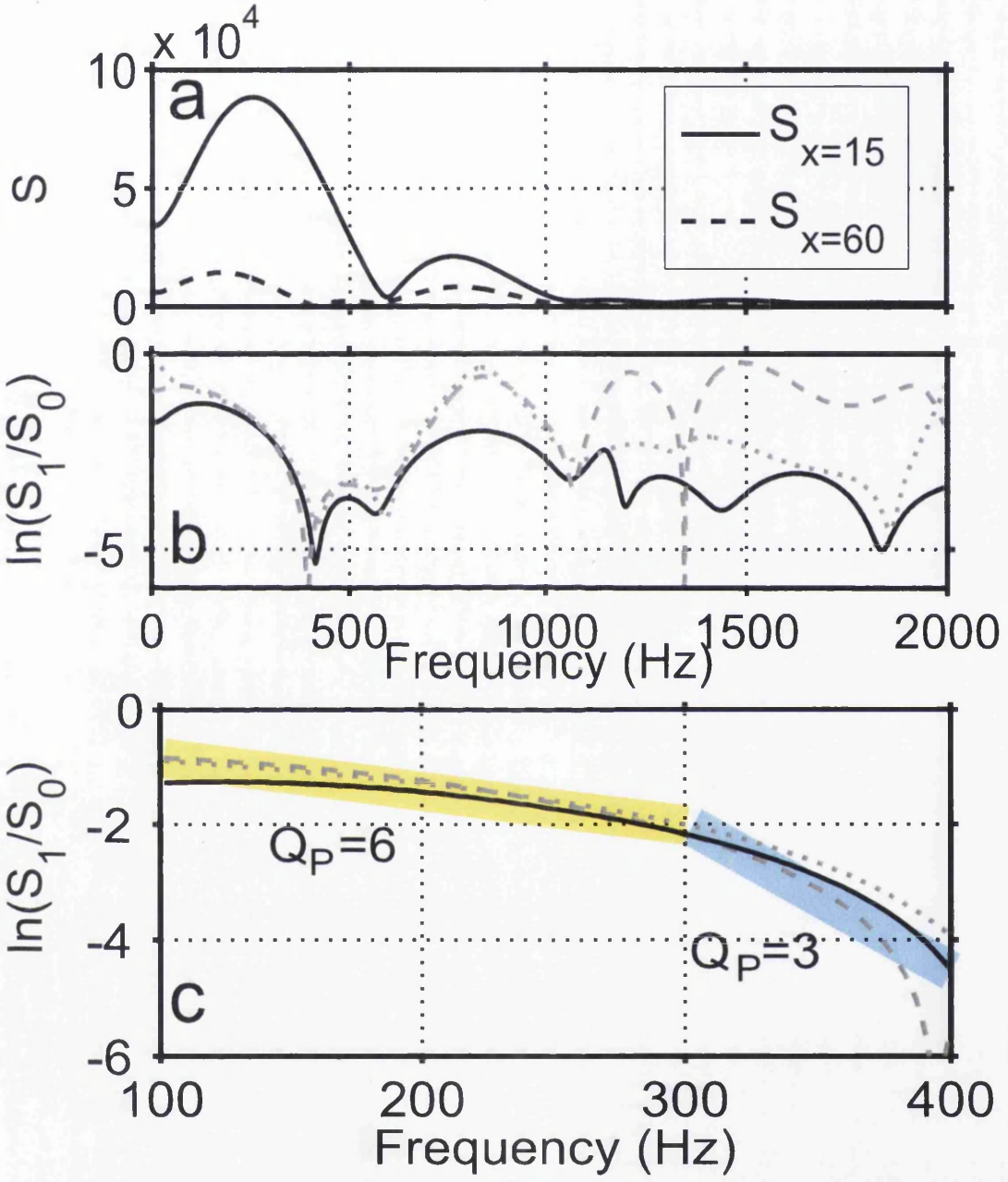

Figure 6.6: (a) Fourier spectra in the bandwidth 02000 Hz of the refractions arriving at 15(solid line) and 60 (dashed line) m. (b) Natural logarithm of the spectral ratio for the same arrivals (solid line) and for the pair $S_{x=20}/S_{x=65}$ (dotted gray line) and $S_{x=25}/S_{x=75}$ (dashed gray line)

the two arrivals. Figure 6.7 shows representative samples of spectral amplitudes and spectral ratios for similar pairs of arrivals in the three shots. γ estimates for the spectral ratios shown in Figure 6.7 are computed for clarity in Table 6.2. γ typically decreases by increasing the distance between the two pairs considered. Errors in γ estimates are low since the correlation between ln(spectral ratio) and frequency is generally good (Figures 6.7d,e, f). Table 6.2 includes, γ estimates for the spectral ratios depicted in Figure 6.7. Correlation coefficients, $\mathcal{R}^2$, and measurement error for γ estimates, δ_γ (the standard error of the regression analysis) are also included.

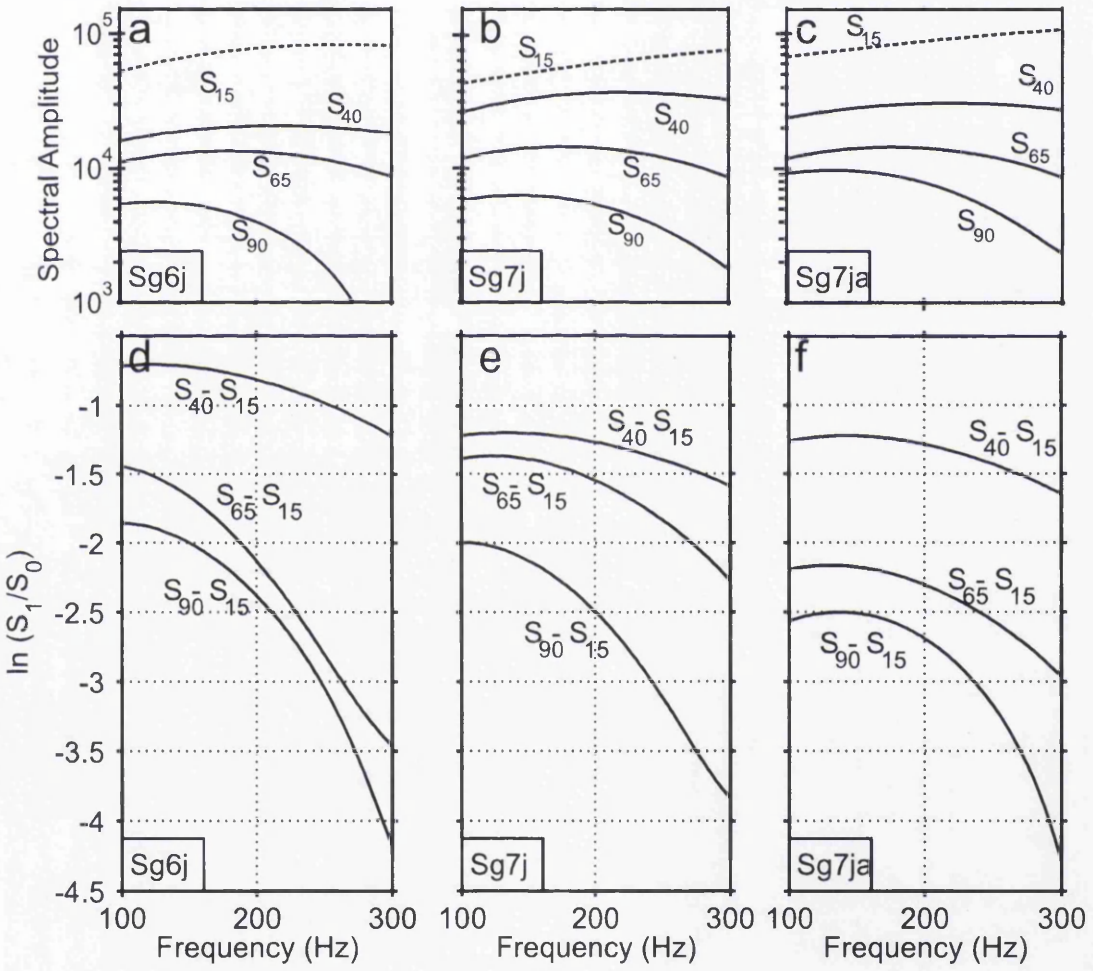

Figure 6.7: Examples of spectral amplitudes (a,b,c) and spectral ratios (e,f,g) between the reference wavelet, S_{15}, extracted at 15 m offset (dashed line in a, b and c) and other, subsequent arrivals.

Shot	pair	γ	δ_{gamma}	$\mathcal{R}^2$
SG6j	40-15	-0.0026	0.0001	0.97
	65-15	-0.0011	0.0002	0.97
	90-15	-0.0011	0.0003	0.91
SG7j-1	40-15	-0.0019	0.0001	0.87
	65-15	-0.0044	0.0001	0.89
	90-15	-0.0096	0.0002	0.94
SG7j-2	40-15	-0.0020	0.0001	0.83
	65-15	-0.0039	0.0001	0.88
	90-15	-0.0075	0.0004	0.79

Table 6.2: γ estimates with measurement error from the pairs of arrivals plotted in Figure 6.7

6.4.2 Q_P estimates

The key parameter used in the determination of Q_P, is γ, the slope of the regression line which relates the linear decay with frequency of the spectral ratios between two arrivals separated by the travel time Δt (Equations 6.3 and 6.4). Figure 6.8 shows how γ decreases in the three shots by increasing Δt, this behavior is a function of Q_P. General agreement between the three shots is observed. By assuming constant attenuation along the seismic line and by fitting a straight line to the γ vs. Δt pairs in all the three experiments a similar mean m (Equation 6.5) is obtained: $Q_P = 6\pm1$ (Figure 6.8a).

This average value represents a useful indication of the high seismic attenuation generally observed in our data, but is not the only way to interpret it. In fact, by considering all the datapoints in Figure 6.8, clear breaks-in-slope (Figure 6.8b, 6.8c, 6.8d) suggest that Q_P decreases at high Δt. Two regions of different slope are thus identified: one at low-central Δt (which corresponds to geophones positioned between 20 and 65 m) with higher Q_P (~ 8) and a second region at high Δt (between 65 and 90 m) with Q_P as low as 4. Results of the Q_P computation using all the receiver-pairs and dividing the datapoints into two regions are listed in Table 6.3. R^2 values are typically high, except at high Δt in SG6j (Figures 6.8a, 6.8b) where

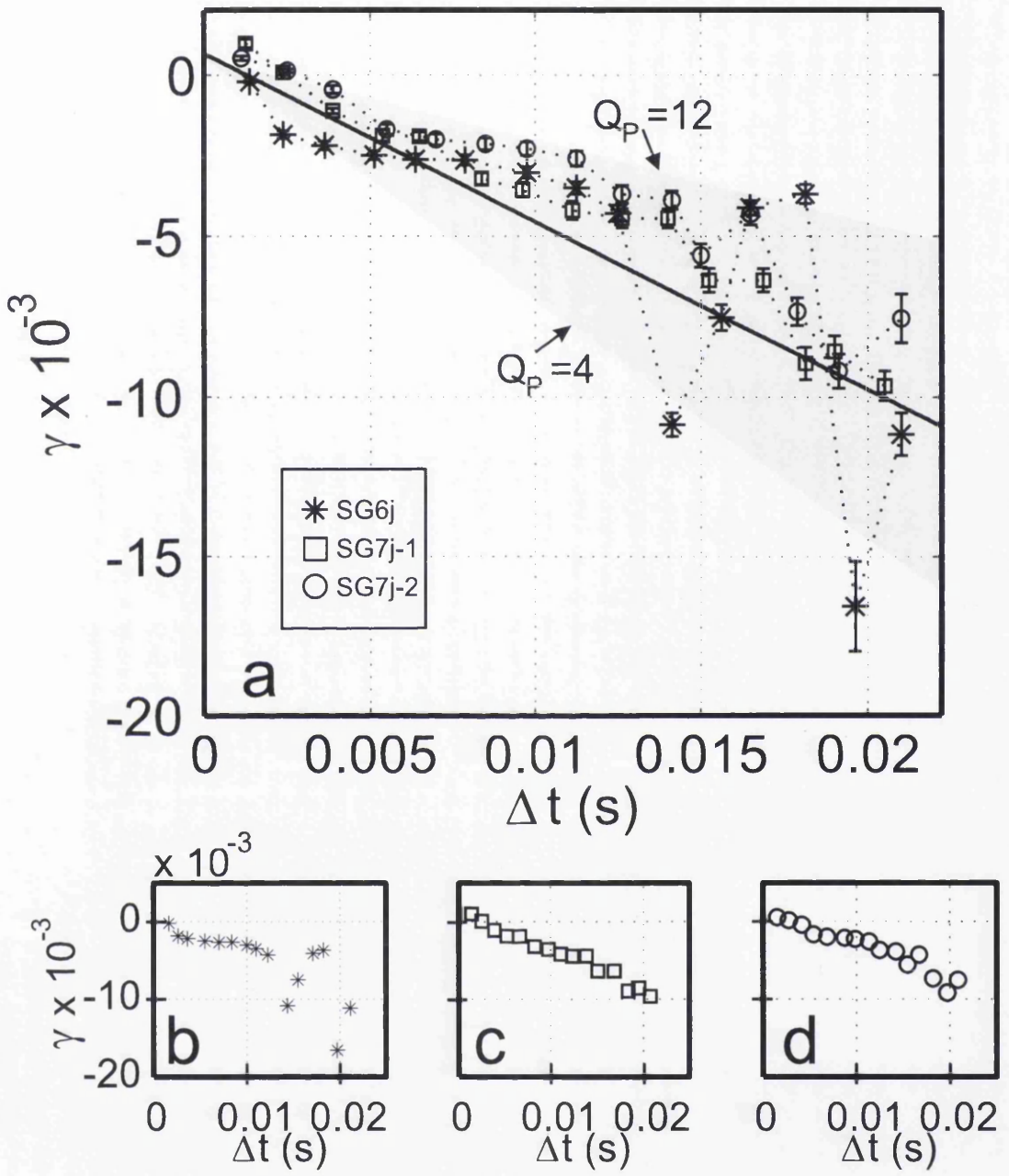

Figure 6.8: γ *vs.* Δt plots used in the Q_P estimates at Storglaciären. (a) Results for the three shots. The solid line indicates the best straight fit line obtained from the mean m in the three shots which gives $Q_P = 6 \pm 1$. The area marked in gray is bounded by two straight lines describing the highest and the lowest Q_P observed at SG (12 and 4 respectively). The three single shots are shown for clarity in (b), (c), and (d). Symbols listed in (a) are the same used in (b), (c) and (d). Details of the different shots are listed in Table 6.1

Shot	Q_P(all)	$\mathcal{R}^2$(all)	Q_P(20-65)	$\mathcal{R}^2$(20-65)	Q_P(65-90)	$\mathcal{R}^2$(65-90)
SG6j	6±2	0.58	6±2	0.62	6±7	0.12
SG7j-1	6±1	0.97	7±1	0.94	4±1	0.91
SG7j-2	7±1	0.91	9±1	0.92	5±1	0.72

Table 6.3: Q_P estimates for the uppermost ice of Storglaciären. all, 20-65 and 65-90 indicates the portion of the line considered in the analysis. $\mathcal{R}^2$ values are also given.

the accuracy appears to be low (probably noisy datapoints due to poor geophone coupling).

The results listed in Table 6.3 were calculated with equation 6.3 using the amplitude recorded in the receiver located at 15 m offset as S_0. Potential change in Q_P values by using different receivers as the reference were also investigated: Figure 6.9 shows that m and Q_P, for a given range of S_1, are the same even when different geophones are used. The only difference generated by changing the reference geophone are changes in intercept. Q_P is higher ($\sim$ 9) at low-central Δt whereas is clearly lower ($\sim$ 5) at higher travel-times (Figure 6.9).

6.5 Seismic attenuation and ice temperature

The first issue that needs to be addressed from the results in Table 6.3 is that these values are strikingly low compared to published examples for glacier-ice (Table 3.2). As mentioned in Section 3.2.1 there is much evidence supporting a strong temperature dependence of Q_P in glacier-ice [*Kuirowa*, 1964; *Clee et al.*, 1969; *Bentley and Kohnen*, 1976; *Jarvis and King*, 1993]. It is therefore reasonable to consider particularly high Q_P (such as those measured by *Bentley and Kohnen* [1976] at Byrd Station) to be typical of glacier-ice substantially colder than the melting point (the average temperature in *Bentley and Kohnen* [1976] of -28°C). *Jarvis and King* [1993] reported much higher attenuation in the more northern (thus warmer) Larsen Ice Shelf (ice temperature $\sim$ -10°C, from Reynolds, 1981; Vaughan and Doake, 1996).

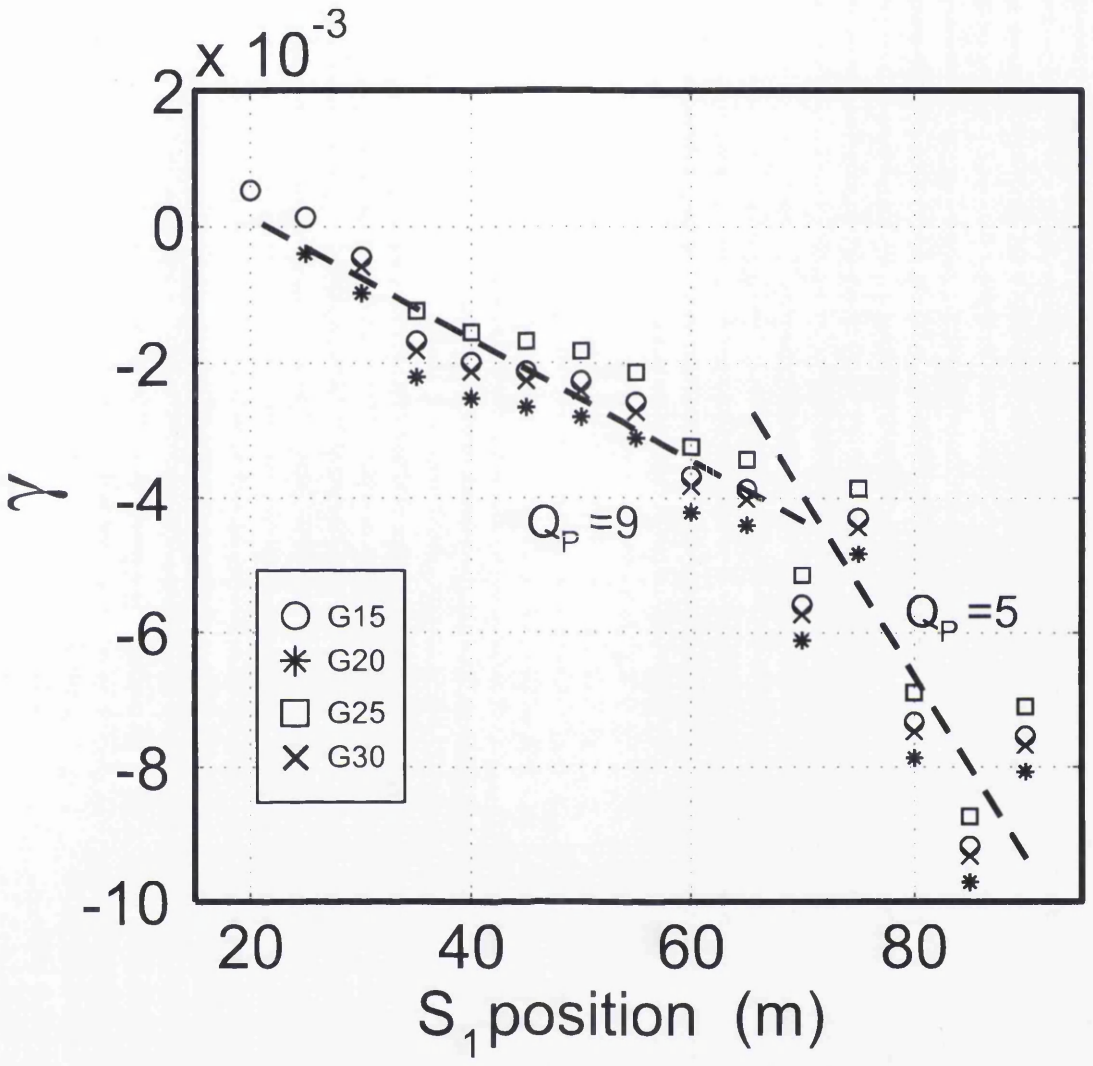

Figure 6.9: γ *vs.* Δt plot for SG7j-2 using different geophones as reference signal, A_0 in equation 6.3. Changes in slope, m, (and thus Q_P) are consistent along the seismic line even when different geophones are used. Changes in intercept are probably due to changes in the absolute amplitude of arrivals recorded at different geophones. Different symbols are for different reference-geophones. G15, G20, G25 and G30 indicate that the reference arrival has been extracted from the geophone located at 15, 20, 25 and 30 m respectively.

Using the central value of *Bentley and Kohnen* [1976], $Q_P = 714$ at 136 Hz, and deriving Q_P from α (equation 3.12) at 136 Hz for *Jarvis and King* [1993] we obtain $Q_P = 68$ at 136 Hz for the Larsen Ice Shelf: the seismic quality factor appears to be more than ten times higher by increasing ice temperature by $\sim$ 18°C. Estimates in temperate ice [*Westphal*, 1965; *Clee et al.*, 1969] are not easy to compare since they have been derived for much higher frequencies (kHz) than those reported in *Bentley and Kohnen* [1976], *Jarvis and King* [1993] and the study presented here.

The temperature profile with depth from a thermistor string adjacent to the seismic line is shown in Figure 6.10. Temperature data, provided by Rickard Pettersson, were collected and processed as described in *Pettersson et al.* [2004]. At this location Storglaciären is polythermal with a 20 m thick cold-surface layer (lowest temperature $\sim$ -1.5°C) underlain by temperate ice. The temperature profile is particularly important in the interpretation of Q_P but the interpretation is limitated by absence of knowledge on the depth-span at which Q_P estimates relate to. What depth is sampled by the propagating P wave?

One way to answer this question is by looking at the Fresnel volume: the finite volume of space around the geometric ray path that influences the propagation of a band-limited wave [*Spetzler and Snieder*, 2004]. Thus the maximum depth, q, sampled by a propagating P-wave is the radii of the Fresnel volume given by *Spetzler and Snieder* [2004] as:

$$q = \sqrt{\frac{3}{4}\frac{\lambda(x/2)^2}{x}}, \tag{6.6}$$

where λ and x are wavelength and offset respectively. Figure 6.10 shows the depth of the first Fresnel volume superimposed on the temperature profile for the bandwidth used in our study. The Fresnel volume increases with offset, changing from 12 to 25 m for 100 Hz energy. It is therefore likely that far-offset receivers sampled a wave which propagated in warmer ice than the one sampled by close-offset receivers. Thus if we define the maximum effective depth as that sampled by the lowest frequency (100 Hz) we can conclude that differences in m and Q_P observed in Figures 6.8 and 6.9 are probably due to the fact that earlier arrivals propagate principally in the

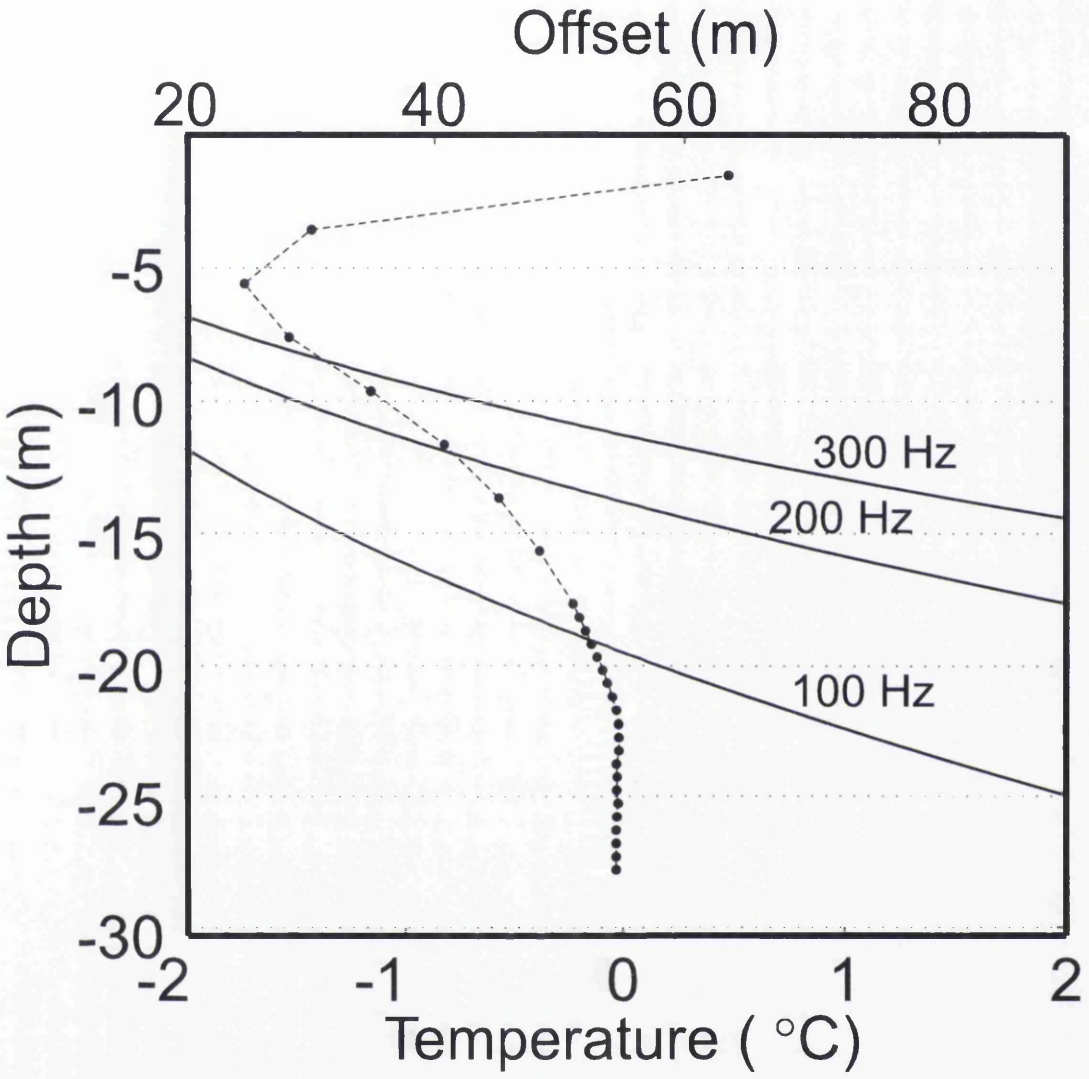

Figure 6.10: Temperature profile with depth (dots, dashed line) from the thermistor string located where the seismic line was acquired at Storglaciären. The maximum size of the radii of the first Fresnel volume (thus the depth sampled by the raypath) calculated using equation 6.6 is shown in black, solid lines. The Fresnel volume is frequency-dependent and this figure shows frequency used in our seismic attenuation analysis (100, 200 and 300 Hz). Temperature and Fresnel volume depth are plotted in the same figure to show how higher offsets are sampling warmer ice. Note that horizontal axes are different for temperature and Fresnel volume.

cold ice (with temperature around -1°C, Figure 6.10) whereas at higher Δt the low Q_P values are generated by a wave propagating in warmer ice, probably, at least partially, in the temperate ice.

6.6 Frequency dependence of Q

The methodology applied in this study appears to be an efficient tool for monitoring the thermal state of glaciers using frequency-independent Q_P estimates. The advantage of the frequency-independent estimate is that the variability in time of a number of γ, estimated in the frequency-domain is estimated: since the wave propagates deeper at high Δt, temperature-related variations in frequency-independent Q_P estimates were observed. Despite this fact, the deviations from linear in Figures 6.6 and 6.7 are indicating frequency-dependence of Q_P. It is thus worth providing an example of the calculation of Q_P when assumed to be frequency-dependent (and thus time-independent). This can be done by applying the method suggested by *Jeng et al.* [1999]: for each frequency the natural logarithm of the amplitude ratio $A_1(f)/A_0(f)$ is taken and plot against Δt. The slope of the regression line is $\pi f/Q$ which gives Q for that frequency (see equation 6.3). Figure 6.11 shows the spectrum of Q_P in the frequency range 50-200 Hz for the two shots collected on 7^{th} July. Absolute Q_P values seem slightly lower for the morning shot (SG7j-1) than the afternoon one (SG7-2). We can use this plot to obtain a single, frequency-independent, estimate of the attenuation coefficient α using equation 3.12. A linear regression in Figure 6.11 is in the form $Q = (\pi/\alpha v)f$. Thus α is derived using the slope of the line in Figure 6.11. This simple, though crude, calculation gives $\alpha = 3.47 \pm 0.68 \times 10^{-2}$ m^{-1} and $3.14 \pm 0.68 \times 10^{-2}$ m^{-1} for SG7j-1 and SG7j-2 respectively. These values are ~ 15 and ~ 150 times higher than those reported in *Jarvis and King* [1993] and *Bentley and Kohnen* [1976] respectively: further evidence that seismic attenuation is much higher in valley glaciers whose temperature is close to the melting point than in polar ice masses.

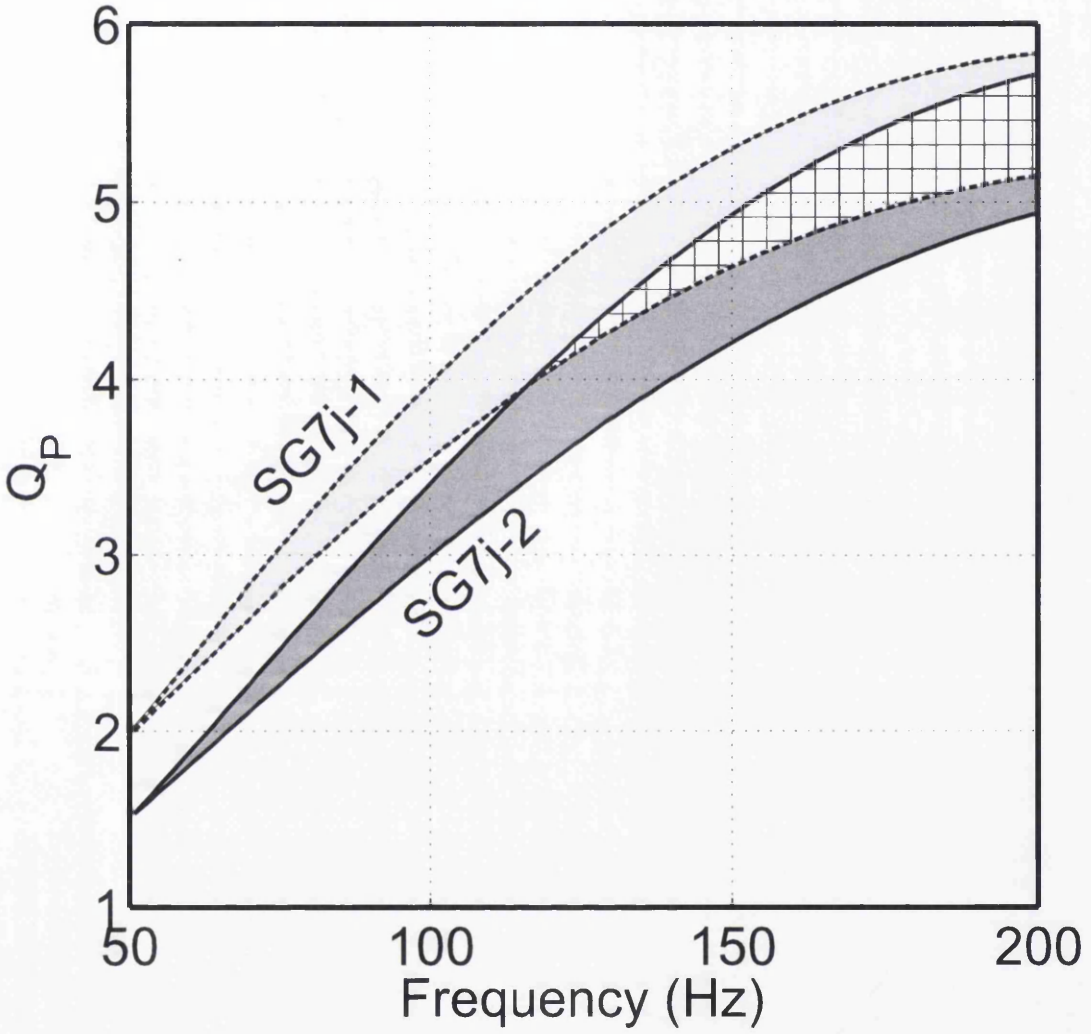

Figure 6.11: Attenuation spectrum for frequency-dependent Q_P computed using the spectral ratios and the Jeng and others' method. Only two shots are shown for clarity. Light and dark gray areas indicate the uncertainty in SG7j-1 and SG7j-2 respectively. The hatched area is common for both shots.

6.7 Temporal variations of Q

Temporal variations in Q_P or general seismic attenuation are neglected from our analysis. Despite the fact that the survey conditions may have been changed from the morning (low melt-rate) to the afternoon (high melt-rate) variations are insignificant in attenuation (and speed, see Figure 6.4) estimates. In fact, as discussed in Section 6.5, the depth of ice sampled by the data, is probably insensitive to surface variations. Minor exceptions include the anomalies observed at high Δt in SG6j (Figure 6.8b) and the slightly higher Q_P for the morning shot in the frequency dependent calculation (Figure 6.11). However, these are insufficient to confirm and discuss temporal Q_P variations.

6.8 Summary

Seismic refraction surveys have been carried out in the upper ablation area of Storglaciären, Sweden, in order to estimate seismic P-wave attenuation using the quality factor, Q_P. A methodology, based on the spectral ratio method, has been tested and discussed in terms of its capability to offer new insights into the geophysical characterisation of glacier-ice properties. Spectral analysis has been undertaken on 15 subsequent arrivals, covering a total geophone spread of 90 m. Results of this analysis show that average seismic attenuation in the uppermost 10-25 m of Storglaciären is very high ($Q_P \sim 6$), around 10 and 100 times higher than previously reported on the Larsen Ice Shelf [*Jarvis and King*, 1993] and at the Byrd Station [*Bentley and Kohnen*, 1976] respectively. Such differences are explained by considering that the average ice temperature which influences our data is $\sim$ -1°C whereas it was $\sim$ -10°C for *Jarvis and King* [1993] and $\sim$ -28°C for *Bentley and Kohnen* [1976]. In agreement with previous laboratory measurements [*Kuirowa*, 1964], further field evidence is provided that seismic attenuation in ice masses is significantly increased by raising ice temperature.

Q_P is lowered from $\sim$ 9 to $\sim$ 4 in the far-offset region of the seismic line. Since the wave propagates deeper at far-offsets this variation is interpreted by considering the ice temperature profile with depth in the study area: far-offset arrivals sampled deeper, warmer and thus more attenuative ice. Consequently this technique seems to be sensitively dependent on ice temperature. Future developments, perhaps combined with radar surveys and by moving the shot-position along the same seismic line, could offer new ways to detect the thermal state of ice-masses.

Chapter 7

Polythermal dynamics at Storglaciären

Results illustrated in chapters 4, 5 and 6 contribute toward the three most important aims of this thesis: (i) to understand the changes that occurred within the polythermal structure of Storglaciären in the last 20 years; (ii) measure the vertical distribution of water with depth and provide input for future models of polythermal glacier dynamics; and (iii) introduce novel in situ geophysical techniques to monitor glacier's temperature and water content.

Changes in the thermal structure of Storglaciären reported in Chapter 4 provide the opportunity to understand the interactions between climate and polythermal dynamics, this is a crucial point which has implications beyond glaciology (e.g. IPCC, [*Lemke et al.*, 2007]). This chapter is divided into three sections. First the spatiotemporal variations in the cold layer thickness illustrated in Chapter 4 will be discussed; particularly the sensitivity of the cold layer to changes in mass balance, climate, flow and water content will be explored using mass balance data provided by the Tarfala Research Station, simple models of polythermal glacier dynamics and previous studies. The second section will discuss the vertical distribution of water content at Storglaciären (Chapter 5) by directly comparing an independently made

calorimetric estimate of water content to the water content profiles derived at site B in 2008; some technical issues relate to borehole radar will also be analyzed, and a hypothesis for spatiotemporal variations in water content will be finally proposed. The third and last section will discuss the radar (Chapter 5) and seismic (Chapter 6) attenuation estimates observed at Storglaciären and their potential role in understanding glacier-ice properties.

7.1 Cold layer thinning

The cold surface layer of Storglaciären has been experiencing a continuous thinning, and volume loss, at a rate that seems largely unchanged since 1989 (Figure 4.32). The overall decrease of 22% of average thickness observed by *Pettersson et al.* [2003] agrees very well with the volume change observed in this study (Figure 7.1). The thinning is not accelerating, but is not slowing down either. From the linearity of the loss it can be hypothesised that the cold layer is slowly, but consistently thinning at an average rate of 0.75 m/a.

Despite the fact that the overall thinning-rate remained constant over 20 years, the decrease in cold ice changed spatially between the two comparisons (Figure 7.2). Strikingly, the thinning between 1989 and 2001 was largely confined to the margins and the central area was nearly unaffected by the loss, with thinning less than 3 m in 12 years (Figure 7.2). Conversely the cold layer thinning in the subsequent 8 years was higher than 15 m. The thickness pattern of the cold surface layer is governed by several factors including net-ablation, temperature gradient in the cold ice and water content at the CTS [*Blatter and Hutter*, 1991; *Moore et al.*, 1999; *Pettersson et al.*, 2003]. In this section the parameters that control the thickness of the cold surface layer and its spatiotemporal variations will be discussed. A similar analysis was done by *Pettersson et al.* [2007] and this section will combine the main findings of that study with the additional knowledge obtained by this PhD study (the 2009 map of the cold layer in Chapter 4 and the water content estimates in Chapter 5).

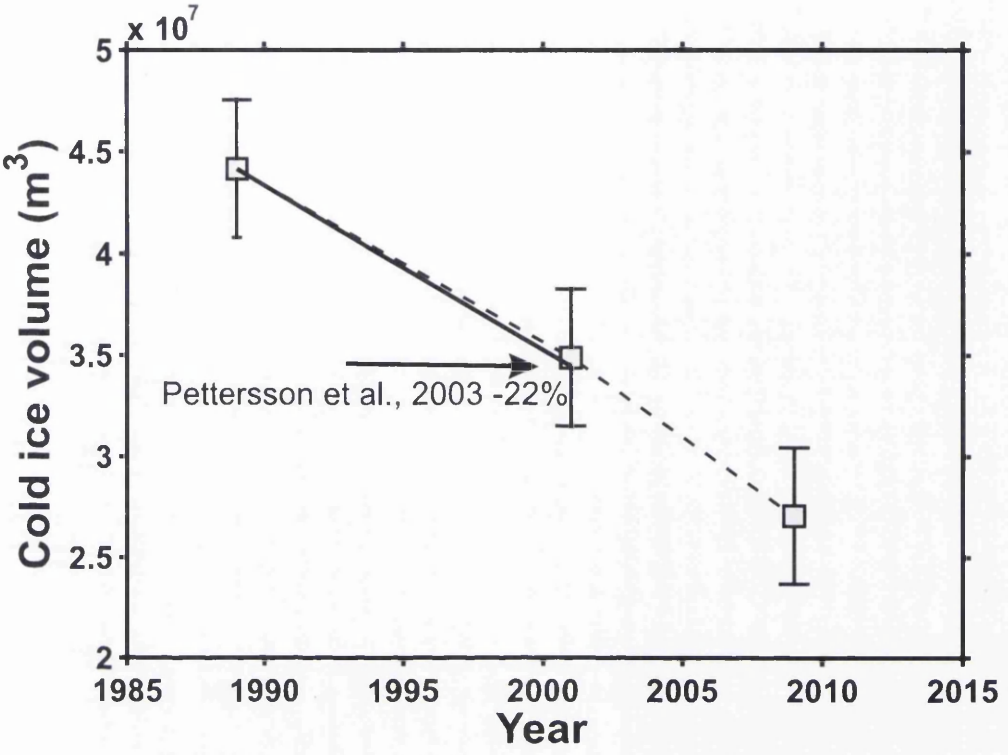

Figure 7.1: Volume loss of cold ice at Storglaciären between 1989 and 2009. This figure is the same as Figure 4.32. The only difference is that the value of thinning quoted in *Pettersson et al.* [2003] between 1989 and 2001 (22% of decrease in average cold layer thickness) is subtracted here from the 1989's cold ice volume estimate and indicated with the arrow. The two estimates (overall thinning and cold ice volume loss) agree very well.

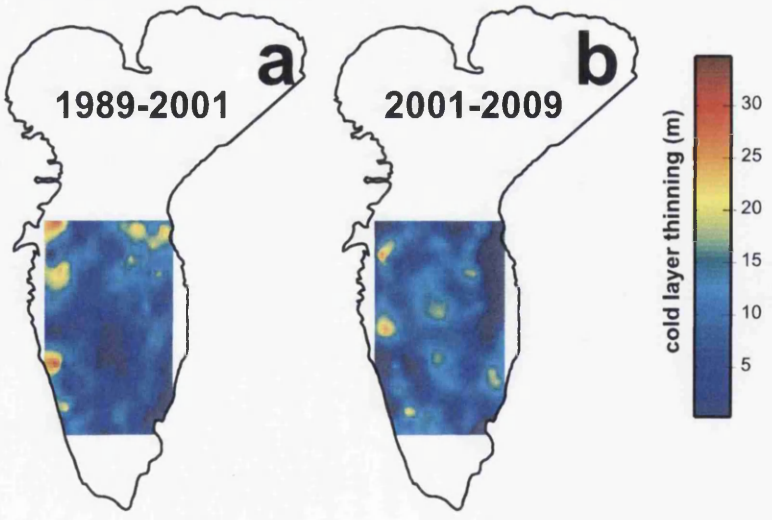

Figure 7.2: The thinning of the cold surface layer of Storglaciären by comparing different GPR surveys: 1989-2009 (a). 1989-2001 (b). 2001-2009 (c).

7.1.1 Accumulation and ablation

By looking at the mass balance of Storglaciären (Figure 7.3), we can observe how the changes in thermal structure between 1989 and 2001 reported in *Pettersson et al.* [2003] may be affected by different mass-balance regimes than those reported in this study. Mass balance fluctuations and more specifically the net-ablation are the dominant factor in controlling the cold surface layer thickness [*Pettersson et al.*, 2003, 2007]. The accumulation pattern on Storglaciären (e.g. [*Jansson and Pettersson*, 2007]) is shown in Figure 7.4a. Thickness changes in the cold surface layer (Figures 4.29, 7.4) appear to follow the pattern of the snow-cover and the thickest part of the layer (e.g. P in Figure 4.29) corresponds to an area with high accumulation and generally higher net-balance (*Pettersson et al.* [2007], Figure 7.4). Conversely thin snow covers correspond to high ablation-rates which results in thin cold-layer [*Pettersson et al.*, 2003]. There is however, no clear correspondence between snow-cover and the spatial extent of the thick cold-layer in the upper-northern side of the study area (A in Figure 4.29).

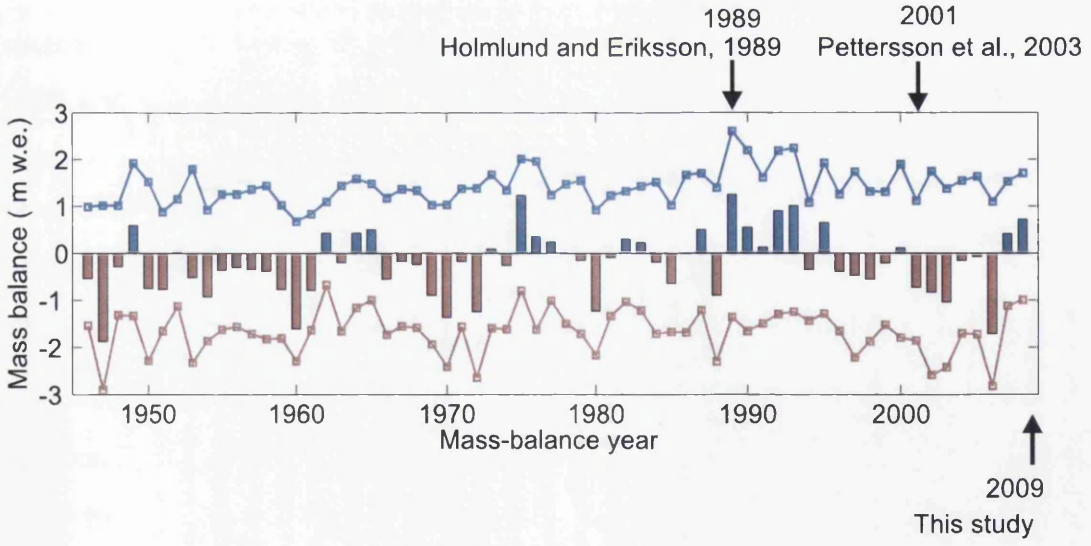

Figure 7.3: The mass balance series of Storglaciären from 1945 to 2008. The mass balance in the time-window analyzed in *Pettersson et al.* [2003] (1989-2001) was in equilibrium whereas from 2001 onwards, a series of negative years, including the 2006 maximum in negative loss are observed. Bars indicate the annual mass balance blue and red line indicate winter and summer mass balance respectively. Data courtesy of P. Jansson and Tarfala Research Station.

The presence of the thick-zone A can, however, still be explained in terms of snow cover. Despite the fact that snow thickness (Figure 7.4) in the proximity of A is only slightly higher, this portion of the ablation area of Storglaciären remained snow-covered longer than the rest of the glacier. The photo in Figure 5.3 was taken at the end of July 2008, zone A is still covered by snow whereas, for example, in proximity of TS (Figure 4.29) bare ice was observed one month earlier. Differences between snow-covered and bare-ice portion of a glacier were investigated in accumulation area ratio (AAR, e.g. *Dyurgerov et al.* [1996]; *Hock et al.* [2007]) studies at Storglaciären [*Hock et al.*, 2007]. A typical evolution of the snow cover at Storglaciären (Figure 7.5, [*Hock et al.*, 2007]) also confirms that the thick-zone A remained snow-covered for a longer time than other part of the ablation area.

Additional information on the mass balance patterns at Storglaciären were gathered using winter and summer mass balance maps described in *Jansson and Pettersson* [2007]. These maps covered the period between 1989 and 2001 and thus were appropriate for the first comparison. The second comparison, pertinent to this study, was calculated using snow depth and ablation values collected at the Tarfala Research Station for the period 2001-2008. Data for the hydrological years 2002 and 2003 are not available. Average winter (Figure 7.6) and summer (Figure 7.7) mass balance remained substantially unchanged in the two different time windows. No clear changes in either accumulation or ablation pattern are evident and therefore, as observed by *Pettersson et al.* [2003, 2007] for the first comparison, spatial changes in mass balance are not suspected to cause the observed thinning of the cold layer at Storglaciären.

A secondary comment on the spatial pattern of the cold layer is relevant to the flow. Since ice is advected from higher elevations towards the ablation zone one could hypothesize that thicker cold layer will be advected down glacier by the flow. According to this principle, the position of a thick cold layer in 1989 and be moved down glacier should be observable in 2009 nearer to the front of the glacier. However in neither of the three cold layer maps was this observed and the general spatial pattern appears not to be affected by the flow of the glacier. As an example, although thinner and

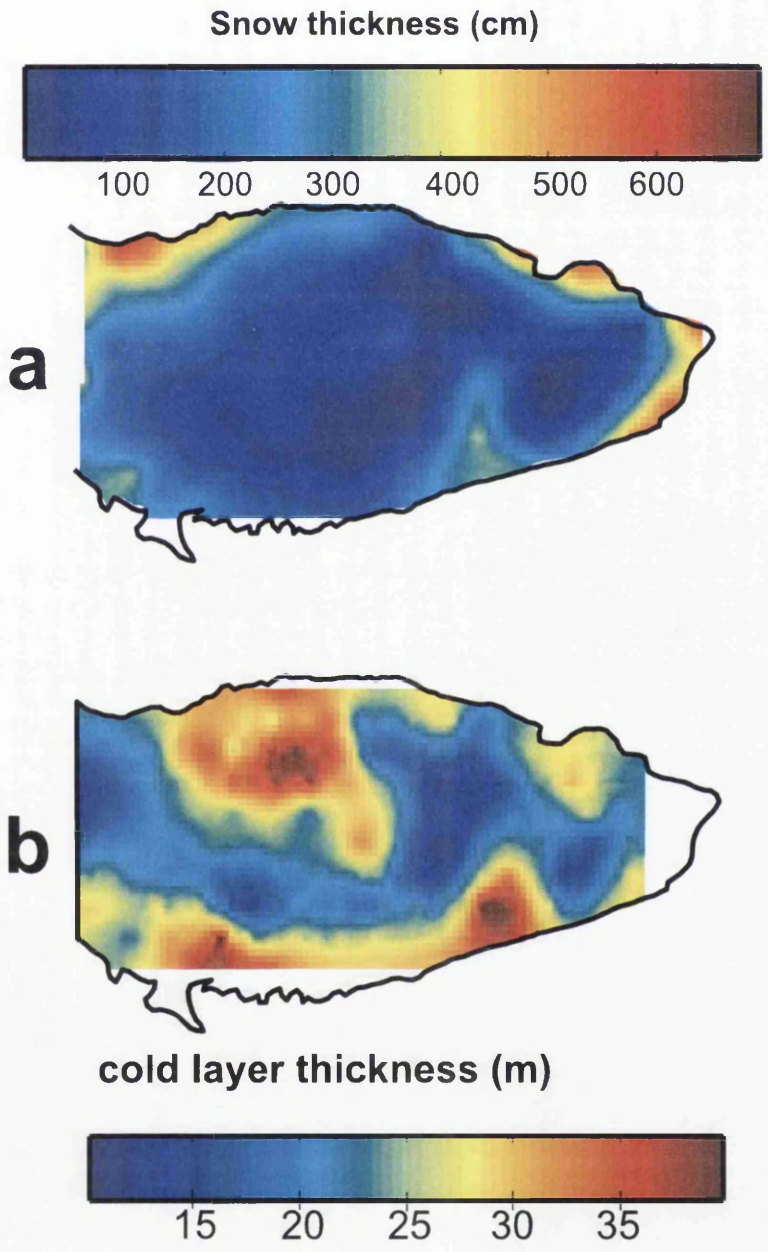

Figure 7.4: Comparison between the 2009 accumulation map at Storglaciären (a) and cold layer thickness in 2009 (b). Data in (a) courtesy of P. Jansson. Spatial characteristics of the glacier's mass balance were presented in *Jansson and Pettersson* [2007].

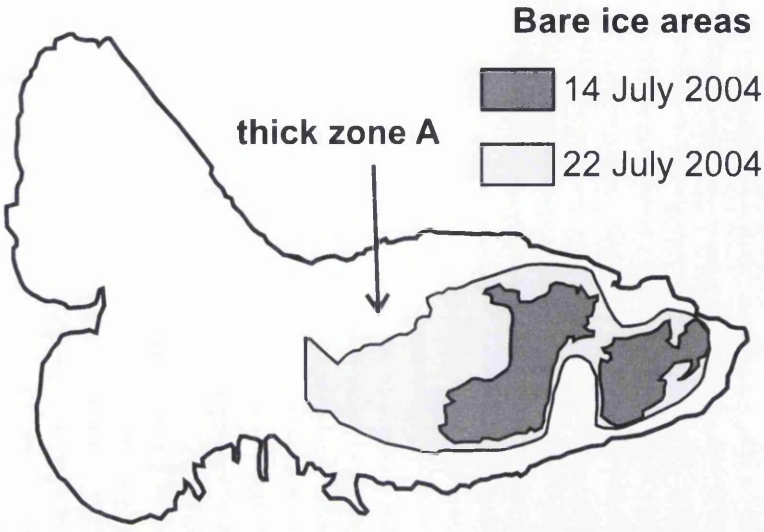

Figure 7.5: Accumulation area ratio evolution in the year 2004. Modified from *Hock et al.* [2007].

less extended, the thick-zone A (Figure 4.29) observed in 1989 is still present at approximately the same position 20 years later. Longitudinal ice velocities measured in the ablation area of Storglaciaren are $\sim$ 60 mm/d [*Hooke et al.*, 1989; *Jansson*, 1995]. It thus follows that in 20 years the longitudinal displacement experienced by a point on the ablation area is $\sim$ 400 m. Such a displacement should be identifiable if longitudinal flow had major effects on the spatial cold-layer pattern.

7.1.2 Dynamics of the CTS in polythermal glaciers

Theoretical studies [*Hutter et al.*, 1988, 1990; *Blatter and Hutter*, 1991; *Pettersson et al.*, 2007] and measurements [*Pettersson et al.*, 2003, 2004] suggest that temporal variations in cold layer thickness are controlled by climate, net-mass balance, heat conduction dynamics and ice flow. Forcing parameters which can cause temporal variation of the cold layer thickness have been summarised by *Pettersson* [2004] and are reported here in Figure 7.8 (modified from *Pettersson* [2004]). Forcing parameters are divided between those directly linked to climate (surface temperature and mass balance), thermodynamics (downward migration of the CTS due to refreezing of temperate ice) and ice flow (Figure 7.8).

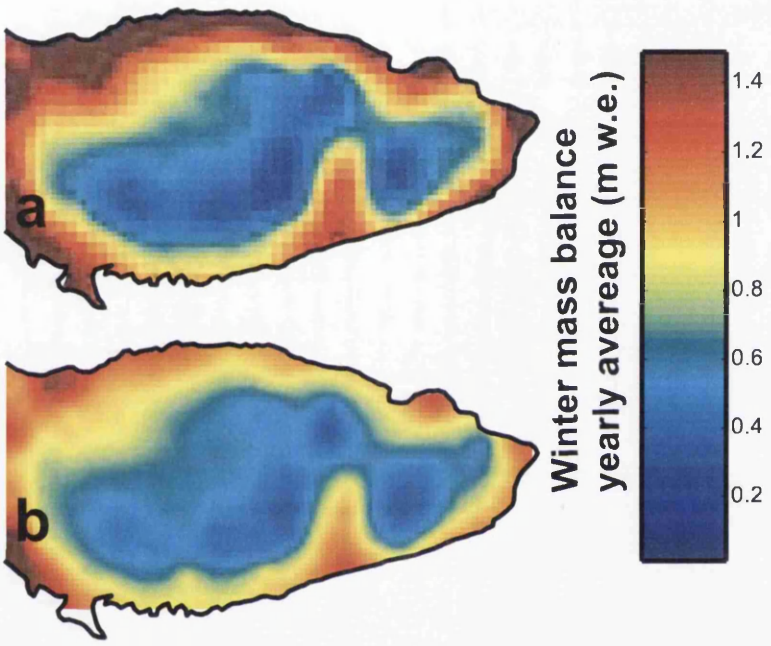

Figure 7.6: Yearly averaged winter mass balance of the period 1989-2000 (a) and for the period 2001-2009 (b). (a) was calculated from the grids discussed in *Jansson and Pettersson* [2007] whereas (b) was obtained from yearly ablation measurements at the Tarfala Research Station. In the calculation the hydrological years 2002 and 2003 are not included because the data were not available. The values in (b) were computed assuming a constant density of the snow cover of 400 Kg/m3. Although this value may not be appropriate for detailed mass balance study it is sufficient enough to the scope of (b) from which we wish to understand whether there are or not clear spatial variations in accumulation pattern.

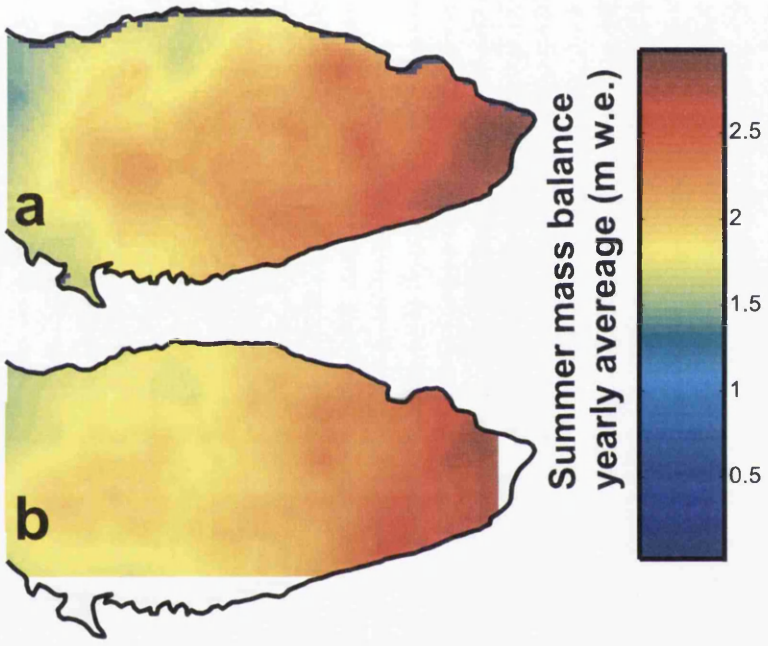

Figure 7.7: Yearly averaged summer mass balance of the period 1989-2000 (a) and for the period 2001-2009 (b). (a) was calculated from the maps discussed in *Jansson and Pettersson* [2007] whereas (b) was obtained from yearly ablation measurements at the Tarfala Research Station, in the calculation the hydrological years 2002 and 2003 are not included because the data were not available.

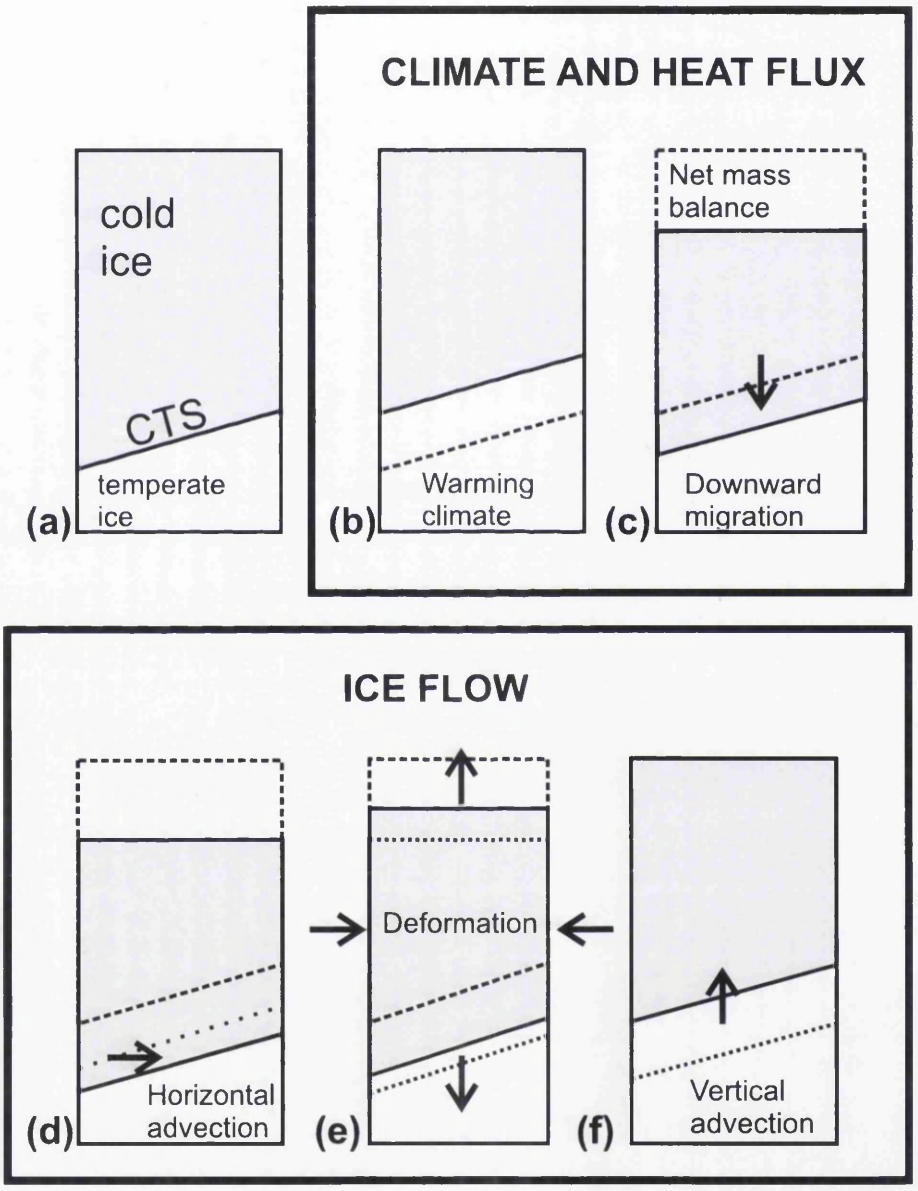

Figure 7.8: Conceptual model of changes in cold layer thickness, redrawn from *Pettersson* [2004]

Climate is obviously a dominant factor [*Pettersson et al.*, 2007]. The presence of permanently cold ice is itself caused by particularly cold winter temperatures, and the thickness of the cold ice is primarily determined by the temperature gradient throughout the cold layer. The stronger the gradient (e.g. the lower the average winter temperature) the thicker the layer. Conversely, in warmer climate the average winter temperature is not able to mantain the cold ice. A weaker temperature gradient caused by warmer winter temperatures was suggested as the primary cause of the cold layer thinning between 1989 and 2003 [*Pettersson et al.*, 2003, 2007].

Mass balance also plays a critical role in polythermal dynamics. As we have seen in section 7.1.1, the presence of the snow cover protects the underlying ice from ablation. Thicker snow cover typically corresponds to a thicker cold layer (Figures 7.4 and 7.5). However, a thick snow cover also insulates the glacier [*Hooke et al.*, 1983] and reduces the penetration of the winter cold wave. Thus, the presence of the snow layer acts in two opposite ways on the energy balance of the cold layer: (i) it protects the cold layer from ablation and (ii) it also insulates from cold temperatures, thus contributes toward a weaker temperature gradient which could therefore thin the layer. The interaction between these two aspects has never been investigated and the understanding is poor. Nevertheless it is very clear the effect that ablation has on cold layer: melting of ice at the surface causes a thinning of the cold layer. Additionally, refreezing of meltwater produces heat and this heat considerably warms up the ice [*Vincent et al.*, 2007].

The presence of a negative temperature gradient toward the surface (e.g. Figure 2.7) results in heat being conducted away from the CTS which will therefore migrate downward (Figure 7.8b). The downward migration of the CTS itself thickens the cold layer. This thickening is however counterbalanced by the net ablation at the surface. By excluding contributions from the flow regime, no changes in cold surface layer thickness should occur if the ablation rate at the surface is equal to the downward migration rate of the CTS [*Pettersson*, 2004]. The migration rate of the CTS is slowed down by higher ice water-content and by weaker temperature gradient in the cold ice [*Hutter et al.*, 1988, 1990; *Pettersson et al.*, 2007]. It thus follows that

a thinning in cold layer could be explained by either higher ablation rates, lower temperature gradient in the cold ice or higher water-contents [*Pettersson et al.*, 2007].

The role that ice flow has on polythermal glaciers dynamics is poorly understood. From the comparison obtained in this thesis (Figure 4.30) we can rule out a significant contribution from horizontal advection (Figure 7.8d). If a thicker cold layer is advected downglacier by the flow, thick areas (e.g. the thick-area A in Figure 4.29) in 1989 would be recognizable downglacier in 2001 and 2009. This is not observed. The contribution of deformation is largely non-investigated but can be important, the idea is that in compressive regimes the cold layer thickens (Figure 7.8d). Longitudinal velocities measured [*Hooke et al.*, 1989] and modelled [*Hanson*, 2005] just upglacier from A support the presence of a compressional regime (similar to the regime necessary to produce thrust fault). At this side of the glacier the flow is dominated by the dynamics generated in the northern accumulation basin (e.g. Figure 5.1) which flows into this area. High flow and quick closure of boreholes was also observed while drilling boreholes at site A (Chapter 5) in August 2009. Conversely vertical advection (Figure 7.8e) does not appear to be as efficient since the layer will be only shifted toward the vertical and no changes in thickness should occur.

7.1.3 Water contents and cold layer thinning

It has been shown that, according to theoretical models of CTS dynamics [*Hutter et al.*, 1988, 1990; *Blatter and Hutter*, 1991; *Hutter*, 1993], water content plays an important role in determining the migration-rate of the CTS. One simple way to describe the CTS migration-rate is by considering the propagation of a cold wave in temperate ice [*Hutter et al.*, 1990]. If an isothermal block of ice-water matrix whose temperature is at the melting point (θ_m) is considered and at the block-air interface a *cold source* with temperature $\theta_s < \theta_m$ is introduced, then heat flow be conducted away from the block toward the source and the temperature in the block will decrease below the freezing point until a thermodynamic equilibrium is reached. The freezing

front (CTS) thus propagates downward and, in thermodynamical equilibrium, the whole block of ice will reach the temperature θ_s. The migration rate of the CTS is directly related to the water content in the ice-water matrix [*Hutter et al.*, 1988, 1990]. Thermo-mechanical modelling suggests that liquid water content strongly inhibits the propagation of the freezing front (Figure 7.9 taken from *Hutter et al.* [1990]).

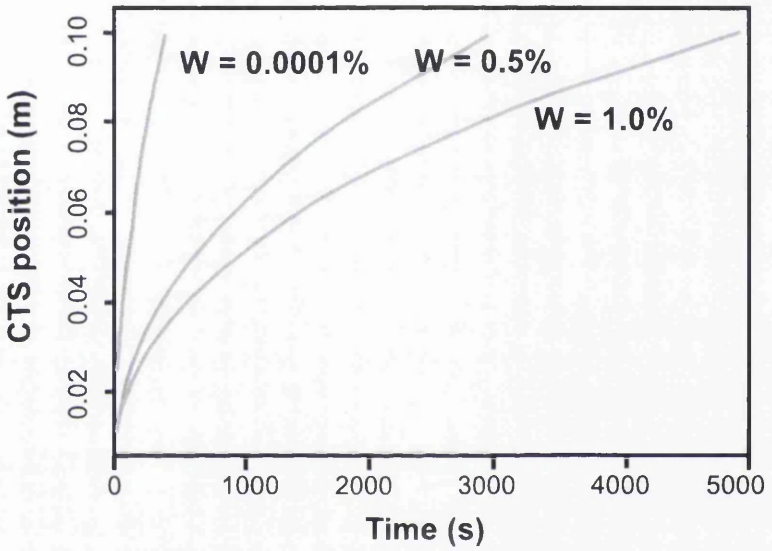

Figure 7.9: Position of the CTS as a function of time for θ_s=-5°C and various water contents. Modified from *Hutter et al.* [1990]. Note that length scales used in *Hutter et al.* [1990] are less than 0.25 m.

The migration rate of the CTS is given by the one-dimensional transition condition at the CTS [*Pettersson et al.*, 2007]:

$$\dot{a}_m = \frac{kC_p}{LW_{cts}} \frac{\partial \theta}{\partial z} + u_{CTS}. \tag{7.1}$$

where k, C_p, L, W_{cts} and u_{CTS} are thermal diffusivity of ice, the specific heat capacity, the latent heat of fusion, the water content and the vertical ice velocity at the CTS respectively. Equation 7.1 was used in the experimental studies of *Moore et al.* [1999], *Pettersson et al.* [2004] following the thermo-mechanical principles developed by *Hutter et al.* [1988, 1990]; *Blatter and Hutter* [1991] and *Hutter* [1993].

Typical values of $\partial\theta/dz$ observed or calculated for the cold side of the CTS in polythermal ice masses are between 0.03 to 0.05 °C/m [*Jania et al.*, 1996; *Ødegård et al.*, 1997; *Moore et al.*, 1999; *Lüthi et al.*, 2002; *Pettersson et al.*, 2004]. The emergence velocity u_{CTS} varies approximately between 1 and 2 m/a in the ablation area of Storglaciären [*Pettersson et al.*, 2007]. Using these parameters for Equation 7.1 we can quantify the role that water content plays in controlling the migration rate of the CTS (Figure 7.10). Important difference is observed between very-low water content values (e.g. less than 0.2 %) and water-contents typically observed at the CTS of Storglaciären ($\sim$ 0.7% [*Pettersson et al.*, 2004]). In nearly dry (thus with very low water content) the migration rate of the CTS reaches values $\sim$ 2 times higher than those observed for wetter ice (e.g. 0.7-0.8 %, Figure (7.10)).

There is thus a fundamental difference between water-free CTS and a wet CTS (Figure 7.10). In a water-free CTS the migration rate is very high and thus for low-water content areas we can expect a thick cold surface layer. This is in agreement with the thermo-mechanical modelling exercises described in *Pettersson et al.* [2007]. At high emergence velocity we observe high migration rate because of higher ice flux within the CTS (Figure 7.10). The migration rate of the CTS is higher for stronger temperature gradient: in colder climate the removal of ice from ablation is largely compensated by higher CTS migration rate. However, as pointed out by *Pettersson et al.* [2007], the lack of knowledge about spatial variability of water-content pose a strong limitation on our understanding in spatiotemporal dynamics of polythermal ice masses. Results explained in Chapter 5 provide a path to take in order to discuss some key aspects: is spatial variability in water content observed with borehole radar a possible cause for the complex thinning pattern observed throughout the years?

The location of the borehole radar experiment is shown, together with the relevant maps, in Figure 7.11. All the borehole radar sites were deliberately located in an area with thin cold surface layer (Figure 7.11) in order to allow penetration of the drill into warm ice. Strikingly, in all the three sites, the thickness of the layer was $\sim$ 20 m. As discussed in Section 7.1.1, the spatial pattern of the cold layer is primarily

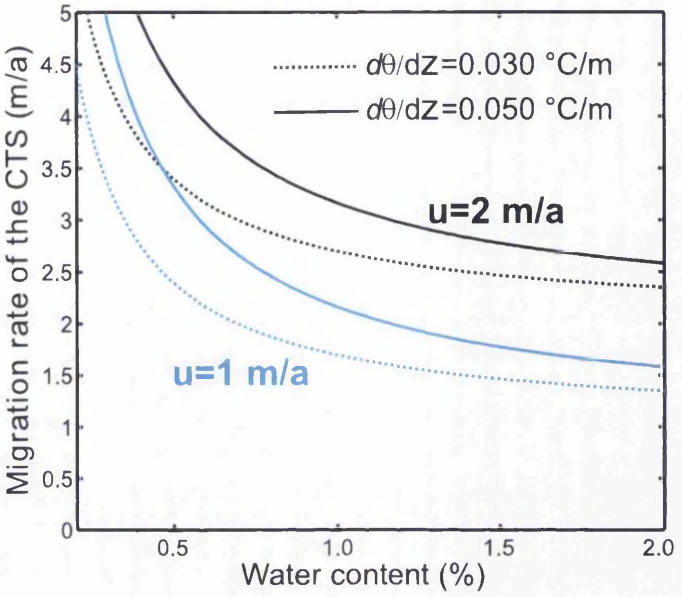

Figure 7.10: Migration of the CTS as function of water content according to Equation 7.1.

controlled by the snow-cover distribution on the glacier. While this is true for sites B and C (e.g. both sites were observed snow-free since mid-July in both campaigns) snow was still observed at site A at the end of August. It is thus possible that at site A refreezing of meltwater within the snow pack could produce sufficient heat to diminish the temperature gradient and thus cause a thinner layer.

Spatial variability of water contents measured with borehole radar was observed at the three sites (Figure 5.43). Water-contents at the CTS ($\sim$ 20 m in all the sites) varied as well between 0 and 1% and this variability is critical in terms of migration rate of the CTS since at low water contents (e.g. 0%) the migration rate of the CTS will be very high and the thinning rate will be negative (e.g. thickening). Conversely, for constant temperature gradient and the ablation rate, at 1 % water contents the migration rate is lower thus the thinning is higher. Borehole radar experiments measured water content with an accuracy of $\sim \pm$ 0.3 % ([*Gusmeroli et al.*, 2010b], Chapter 5). Such precision is too low to infer CTS dynamics. For example, the value of W_{cts}=0.5 $\pm$ 0.3 % supports negligible or higher-than-observed thinning rates depending if we consider its lower or upper boundary respectively. It

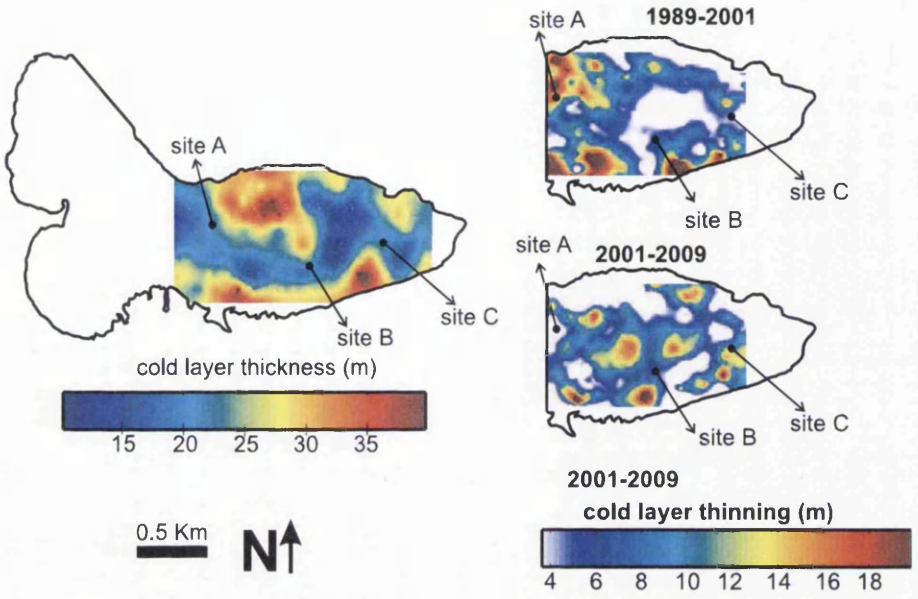

Figure 7.11: The cold surface layer in 2009 and the two thinning maps. The location of the borehole radar experiments described in Chapter 5 is indicated.

is thus possible that spatiotemporal variability of few 0.1s % in water-content can cause the complex spatial pattern of the thinning observed in Chapter 4 (Figure 7.11).

7.1.4 Cause of the thinning

An increase of 1°C in winter air temperature since the mid 1980s was proposed as the cause of the thinning between 1989 and 2001 [*Pettersson et al.*, 2003, 2007]. Air temperatures at the Tarfala Research Station shows that the increase observed for the previous comparison is still ongoing thus it is very likely that the thinning is directly connected to the warming climate. This is reasonable since a higher winter temperature results in a weaker temperature gradient within the cold layer and this in turn slows down the migration rate of the CTS. By considering the fact that the overall thinning rate is only slightly increased from that reported by *Pettersson et al.* [2003] a weakening of the gradient caused by the climatic warming in the 80s can thus explain the continuation and the slight increase of the thinning.

However as pointed out by *Pettersson et al.* [2007] we still can not assess the effect that water content has in these dynamics. A detailed series of radar-derived water-content estimates (see Chapter 4) validated with temperature profiles and calorimetric determinations (thus a combination of the field techniques illustrated in *Pettersson et al.* [2004], and in Chapter 5) would probably offer the way forward to obtain more information about spatiotemporal variation in water-content and its effect on CTS dynamics.

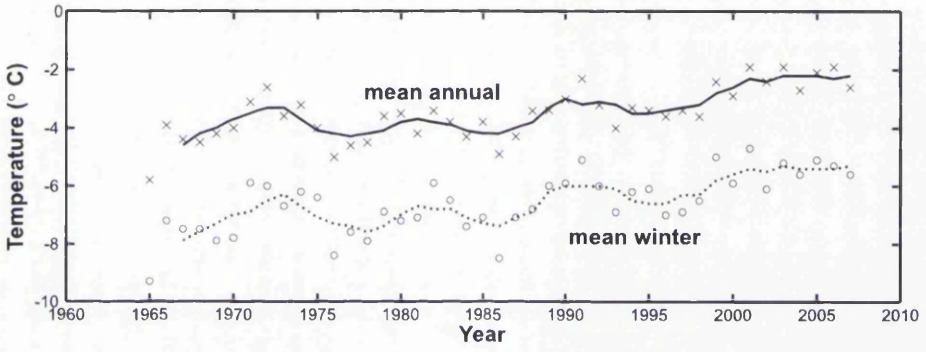

Figure 7.12: 1965-2007 air temperatures at the Tarfala Research Station (data courtesy of P. Jansson and Tarfala Research Station). Crosses and Circles are mean annual and mean winter temperature respectively. Solid and dashed lines indicate a 4 year running average on the mean values.

The thinning rate in the central part of the ablation area increased from negligible in 1989-2001 to higher than 1 m/a in 2001-2009 (Figure 7.11). A recent DEM comparison shows that this part of the glacier thickened between 1989 and 1999 [*Koblet et al.*, 2010]. This gain of mass appear to be a result of a thickening in the accumulation zone between 1969 and 1980 which propagated downglacier [*Koblet et al.*, 2010]. In the year 2000s there is no evidence supporting gain of mass in the ablation area. Thus we can explain low thinning-rates in the central part of the snout with high mass-flux and *vice versa*. These hypothesis can be tested by rigorous modelling exercises as it has been done in *Pettersson et al.* [2007] which are, however, beyond the scope of this PhD thesis.

7.1.5 Changes of the cold based areas

The thermal changes reported in this thesis are changes in thickness of the cold layer. No significant changes were observed between the frozen rim mapped by *Pettersson et al.* [2003] in 2001 and this study (Figure 4.34). *Pettersson* [2004] pointed out that changes in cold layer thickness can cause significant changes in cold-based areas only if the glacier occupies a wide valley with relatively non-steep topography. Storglaciären occupies a valley with steep sidewalls and thus changes in cold layer thickness only have minor effects on the regions of the glacier's bed that is cold based (Figure 7.13, *Pettersson* [2004]).

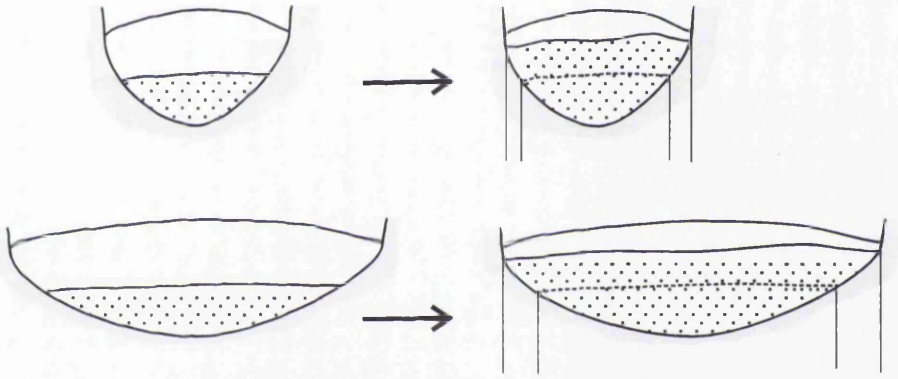

Figure 7.13: Conceptual model of changes in the cold based regions in a polythermal glacier. The changes are smaller on a glacier that occupies a steep valley. Modified from *Pettersson* [2004]

7.2 Water content distribution with depth

Borehole radar ZOP surveys (Chapter 5) have been used in this study to derive profiles of water-content with depth (Figure 5.43). The propagation speed of radio wave is slowed by the presence of water inclusion within ice (Figure 3.1) providing a method to measure water content (Chapter 3). Water content estimates using radio wave speed are frequent in literature (Chapter 2, Tables 2.1, 2.2 and 2.3). However, two main critiques should be addressed: (*i*) water content estimates using radio wave speed typically integrate over the volume illuminated by the radar, and

if larger water-bodies are present, these will be sampled and thus will contribute to the water-content determination [*Murray et al.*, 2000a]; (*ii*) petrophysical relationships (e.g. Equations 3.3, 3.4 and 3.6) used in the computation of water-content typically consider temperate glacier-ice as a two (ice-water) component mixture whereas glacier-ice is a multi-phase material with ice, water and air [*Bradford and Harper*, 2005; *Gusmeroli et al.*, 2008].

7.2.1 Correcting speed estimates for air content

The air-content distribution within the ice column was estimated using the model of *Bradford et al.* [2009], who calculated the air content within the temperate Bench Glacier by considering that, according to the ideal gas behavior, the volume of air trapped in the ice varies as a function of temperature and pressure. We can assume that the temperature follows the pressure field (Equation 2.5, [*Paterson*, 1994]). Thus, in the case of ideal gas behavior we can write the volume concentration of air, ϕ_a , as a function of pressure:

$$\phi_a = \mathcal{K} \times \left(\frac{\theta_0}{P} - \beta' \right), \tag{7.2}$$

where $\mathcal{K} = R/M \times \phi_{a1}$, ϕ_{a1} is the volume concentration of air within the ice at the glacier surface, R = 8.31 J/mol K is the universal gas constant, and $M = 25.8 \times 10^{-3}\mathrm{m}^3/\mathrm{mol}$ is the molar volume of the gas computed at θ_0 and atmospheric pressure $P_0 = 88160$ Pa. This value is the average summer value measured at the nearby Tarfala Research Station [Tarfala Research Station meteorological data, summer 2009].

By ignoring deviatoric stresses from the flow field, the hydrostatic pressure, P_z, can be written as a sum of discrete volume elements [*Bradford et al.*, 2009]:

$$P_z = g \sum_{k=1}^{n} (1 - \phi_{a(k)}) \rho_i \Delta z, \tag{7.3}$$

where g is the accelleration of gravity, $\rho_i = 917$ kg m^{-3} is the density of ice, and Δz is the discrete depth-step (1 m). The volumetric air content at any particular depth

is then given by combining equations 7.2 and 7.3, and by adding the atmospheric pressure, P_0, to the calculation:

$$\phi_{a(k+1)} = \frac{\mathcal{K}\theta_0}{\left[g\rho_i\Delta z \sum_{k=1}^{n}(1-\phi_{a(k)})\right]+P_0} - \mathcal{K}\beta'. \tag{7.4}$$

The effect of ϕ_a on radio-wave speed estimates can be quantified by considering v_m as the bulk radio-wave speed in the air-ice mixture defined by the sum of volumetric concentrations:

$$v_m = (1-\phi_a)v_{i'} + \phi_a c, \tag{7.5}$$

where the radio-wave speed estimate with the air component removed, $v_{i'}$, is given by:

$$v_{i'} = \frac{v_m - \phi_a c}{(1-\phi_a)}. \tag{7.6}$$

The correction outlined in this section simulates in a reasonable way the decrease of air content with increasing pressure in glaciers since equation 7.4 is primarily conditioned by the hydrostatic pressure, P_z. Numerical tests on equation 7.4 revealed that deviations from the melting point in the cold layer of Storglaciären (few K, Figure 2.7, *Pettersson et al.*, 2003) have a negligible effect on air content vs. depth values.

7.2.2 Water content profile at site B in 2008

Water content profiles obtained from ZOP profiles at site B in July 2008 are particularly important to discuss because the boreholes were drilled nearby a thermistor string which was recording temperature data (Figure 7.14, Section 2.5, Figure 2.7) when the ZOP were acquired. Additionally the surveys in 2008 showed the higher SNR observed in the two campaigns (Figure 5.18) and thus represent the highest quality dataset reported in this thesis. The thermistor string provides direct evidence of the glacier's thermal state at the study area but also represented the opportunity to directly compare radar-derived and calorimetry derived water content (Equation 7.1). Such a joint estimate of water content using both calorimetry

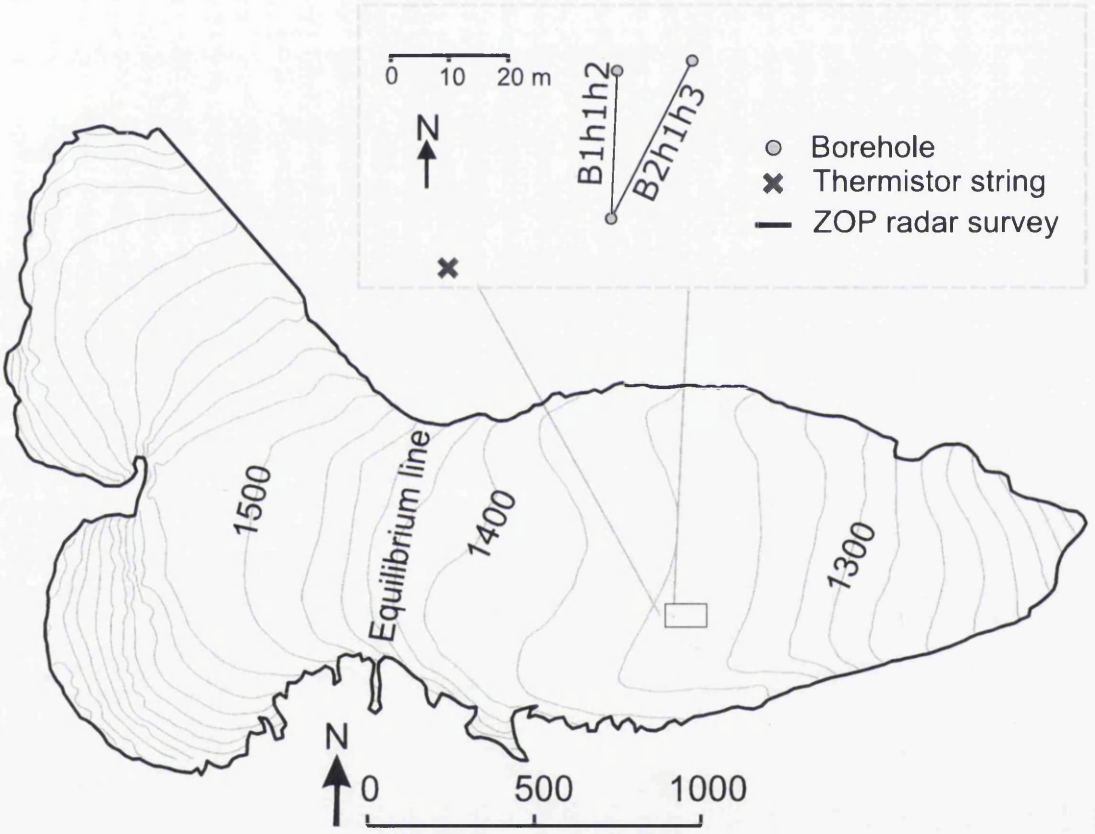

Figure 7.14: Map of the boreholes and thermistor string for the 2008 ZOPs.

and borehole radar has been shown in *Gusmeroli et al.* [2010b] and the following discussion closely follows that study. The calculation of calorimetric water content was done by Rickard Pettersson (personal communication, 2009) and is included in this thesis as an important, independently made, estimate of the same quantity at the CTS. The migration rate of the CTS in between May and August 2008 was -1.13±0.18 m/a and over the whole measurement period -1.23±0.25 m/a. The temperature gradient in the cold ice just above the CTS was -0.028 ±0.01°C/m in July 2008 and 0.04±0.02°C/m for the whole period. These values gives a water content of 0.6±0.1% for July 2008 (when our ZOP surveys were undertaken) and 0.8±0.1% for the whole measurement period.

Radio-wave speed profiles from the summer 2008 campaign (Figures 5.42g and 5.42h) were corrected for the presence of air bubbles in order to estimate water content with depth. The radio-wave speed measured close to the surface can be then used to estimate air content at the glacier surface, ϕ_{a1}, using equation 3.4, the air-content distribution with depth (using equation 7.4) and, consequently v_i' at any depth (equation 7.6). Calculated values for ϕ_{a1} are $4 \pm 2\%$ and $3 \pm 1\%$ for B2h1h2 and B2h1h3 respectively. These values progressively decrease with depth (equation 7.4, *Bradford et al.* [2009]). Figure 7.15 shows the resulting water-content profiles with depth which were calculated using equation 3.4.

Water-content profiles are corroborated by the temperature profile (Figure 7.15c): the cold surface layer is 20 m thick and in this layer water content in the mWS is equal to zero since all the intracrystalline water freezes once below the pressure melting point [e.g., *West et al.* [2007]]. The fact that the cold layer contains no microscopic water is also confirmed by looking at the radio-wave speed profiles (Figures 5.42g and 5.42h):speed is always higher than the commonly used value for solid, water-free ice (0.168 m/ns). Macroscopic water features can be present in the cold ice (e.g., from percolation of supraglacial water through fractures) but, for these two profiles, there are is no convincing evidence since no clear drops in speed are present in the profiles. Anomalously high water content values (generated from minima in radio-wave speed) are observed at the CTS (21 m, supported by the temperature

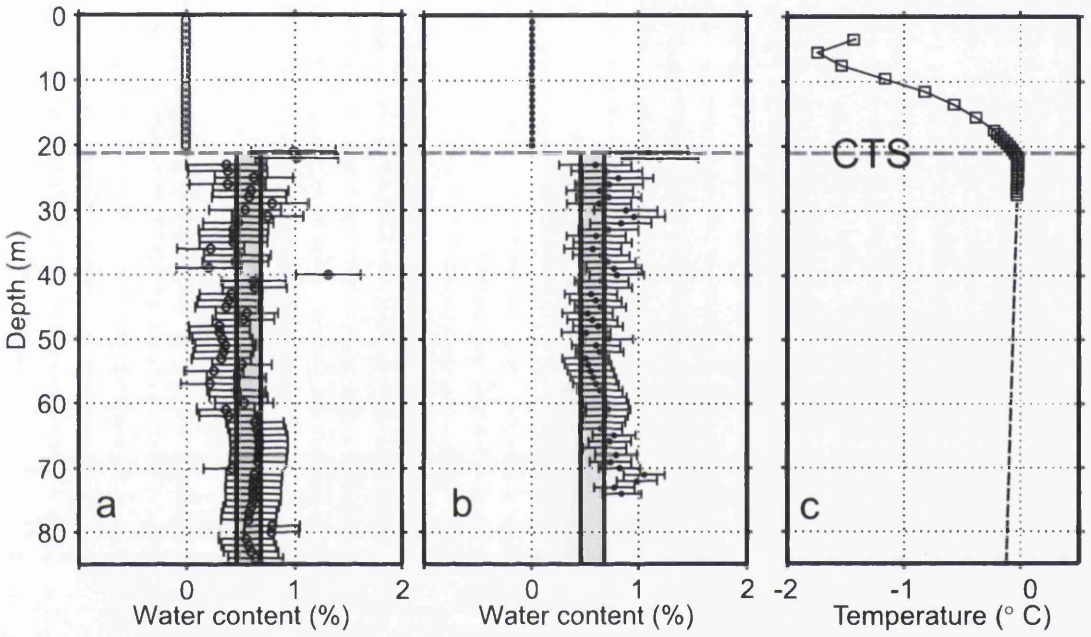

Figure 7.15: Water-content *vs.* depth model obtained from radio-wave speed analysis for two ZOP surveys in the ablation area of Storglaciären. (a) B2h1h2; (b) B2h1h3; (c) Temperature profile from the thermistors string located nearby the ZOP profiles. The cold ice is $\sim$ 21 m thick. Below this depth the ice is at the pressure melting point and contains water inclusions. Gray dashed line indicates CTS position. The gray shaded area show water content at the CTS measured with calorimetry (note that the measurement was at the CTS only, it is shown throughout the whole ice column to emphasise the uniformity of water content values).

profile in Figure 7.15) in both surveys and at 40 m in B2h1h2 (Figure 7.15a). At these locations, water content is around twice the mean values measured throughout the rest of the ice-column.

Satisfactory agreement in terms of both absolute values and general water distribution is observed between the two surveys and calorimetry. The mean water contents in the temperate ice are 0.5±0.3% and 0.7±0.2% for B2h1h2 and B2h1h3, respectively (stated uncertainties are the mean error throughout the whole profile). The variability of water content with depth is almost negligible in the temperate ice. Water-content values seem to stabilise on values ~0.6%. At depths deeper than ~60 m, the observed decrease in radio-wave speed results from slight increases in water content with depth, with values up to 1% in the deepest part of the surveys.

7.2.3 Critically refracted arrivals

The overall smooth trend of the water-content profiles (Figure 7.15) show the uniformity of water content in the mWS, and thus a layered model (e.g., alternation of water-free-ice and wet-ice layers) is not plausible. Such a layered structure could result from the fact that the most important source of water-content in glaciers (the entrapment at the close off [*Paterson*, 1971] is climatically driven and thus it varies in time. For example a period with high spring melt will produce large volumes of water within the firn aquifer. A low melt period followed by a high-melt period could result in the formation of a low water content layer overlain by a high water content layer.

The occurrence of critical refractions in ZOP surveys can reduce their ability to detect thin, high water-content layers [*West and Truss*, 2006]. In layered systems, with sharp changes in water content, the first arrival may not be the direct ray-path propagating between the inter-borehole region, but rather the critically-refracted ray-path [*Rucker and Ferré*, 2004]. When a slow-speed layer is located between two fast-speed layers, the critically-refracted path (dotted line in Figure 7.16a) only

partially propagates in the slow layer since it refracts at the interfaces and travels at the faster speed. Critically refracted arrivals cause overestimation of radio-wave speed in slow layers [*Rucker and Ferré*, 2004; *West and Truss*, 2006].

Nonetheless the ZOP technique is still used successfully to monitor hydrogeological processes [*Kuroda et al.*, 2009], and it is possible to validate water-content models inferred from the ZOP by identifying potential areas in the ZOP where the first-arriving enegy does not correspond to the direct ray-path [*Rucker and Ferré*, 2004; *Kuroda et al.*, 2009]. Specifically, where antennas are lowered through a high water-content layer that is adjacent to a lower water-content layer, the travel time of the critically-refracted first-arrival will decrease linearly as the antennas approach the boundary with the drier layer [*Rucker and Ferré*, 2004]. Consequently, a linear decrease in travel time would cause v_m to increase linearly if the effects of critical refraction were ignored. Areas where critically-refracted energy could be the energy arriving first are marked with arrows in Figure 6. If such minima in radio-wave speed were generated by critically-refracted arrivals it is likely that the water content at these locations would be underestimated.

To understand whether these minima in radio-wave speed represent high water-content layers, a ZOP model was generated [e.g., *Rucker and Ferré* [2004]; *West and Truss* [2006]], which simulates a high water-content layer surrounded by low water-content layers (Figure 7.16a). The model was run for 8 antenna depths to reproduce the minima in speed observed in the data, where the speed profile has characteristic features of critically refracted arrivals [*Rucker and Ferré*, 2004]. The contrast between the wet layer and the two dry layers (Figure 7.16a) is deliberately set to be high (nowhere in the ZOP do we observe such low radio-wave speeds due to high water content) in order to detect any serious misinterpretation of water content in the ZOP. Travel times and corresponding speeds assuming constant antenna separation (25 m) are then calculated using Snell's Law, which assumes geometric optics as an approximation of the propagation of EM radiation [*Telford et al.*, 1990] and the equations developed by *Rucker and Ferré* [2004] for ZOP. Since a pulse generated in the middle of the wet layer will refract critically at the boundary along the upper

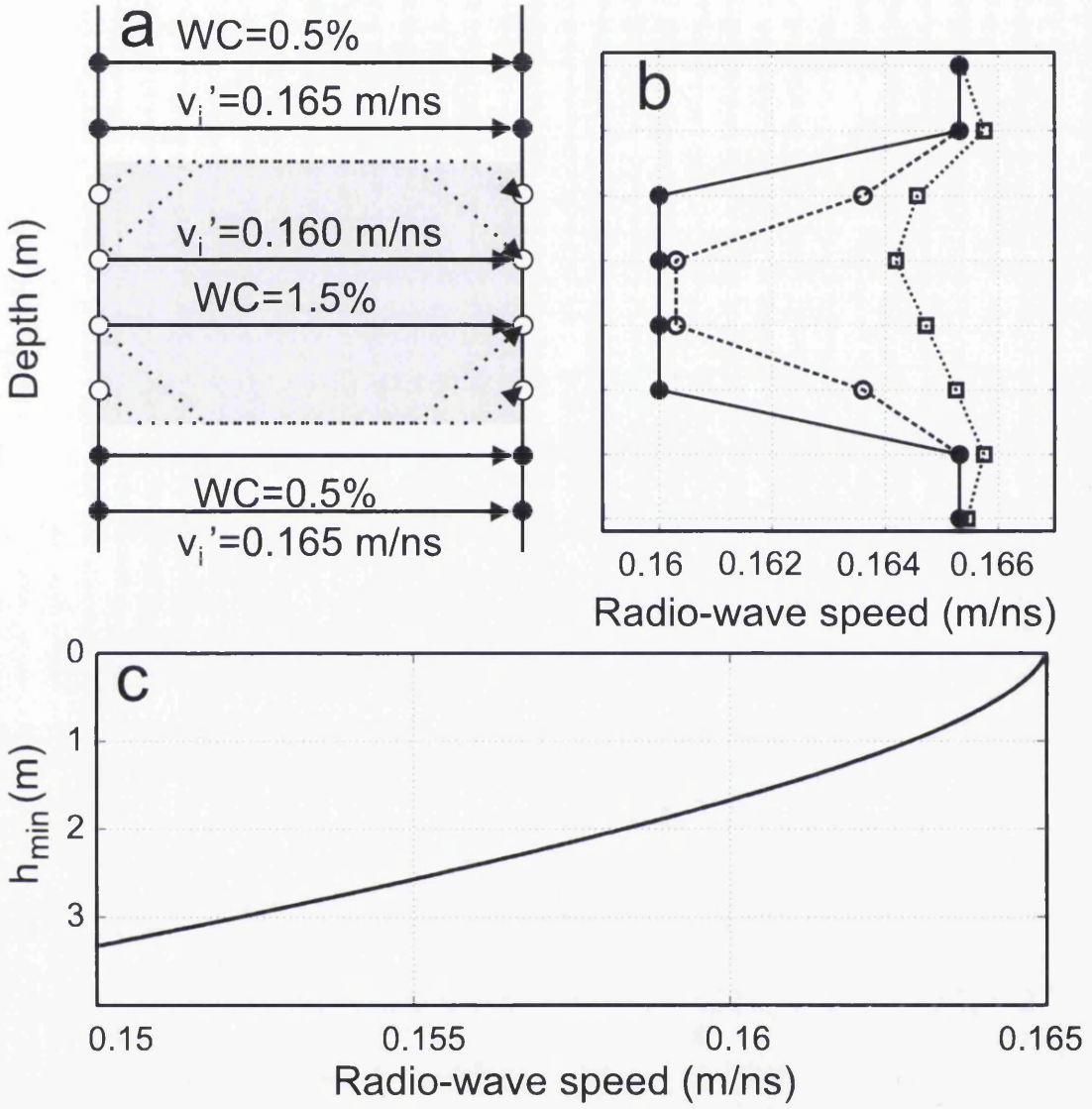

Figure 7.16: Simulated ZOP used to understand the potential for misleading interpretations introduced by critical refraction. Antenna separation is 25 m. (a) Schematic of the model input parameters. WC is water-content, black and white dots indicate antenna positions where the first arrivals are direct and critically-refracted rays respectively. Corresponding direct and critically-refracted raypaths are indicated with solid and dotted lines respectively. The low-speed (high water-content) layer is indicated by the gray area. (b) Speed models using the parameters illustrated in (a) from direct waves (solid line, black dots); critically-refracted waves (dashed line, white dots) and a comparison between 8 antenna depths (from 28 to 35 m) in ZOP1 (white dotted line, white squares; dashed arrow in figure 6). (c) Calculation of h_{min}.

and lower boundaries with the dry layers, the traveltime of the critically-refracted raypath is given by:

$$t_{\text{refr}} = \frac{x}{v_{\text{high}}} + z\left(\frac{2}{v_{\text{low}} \cos i_c} - \frac{2 \tan i_c}{v_{\text{high}}}\right), \tag{7.7}$$

[*Rucker and Ferré*, 2004], where v_{high} and v_{low} are radio-wave speeds though the dry and the wet layers respectively, z is the vertical distance from the antennae measurement depth to the interface between the two layers, and i_c is the critical angle defined by the Snell's Law:

$$i_c = \sin^{-1}\left(\frac{v_{\text{low}}}{v_{\text{high}}}\right). \tag{7.8}$$

Critically refracted waves (Figure 7.16b) always arrive before the direct arrivals in our model. However, the difference between the radio-wave speed measured using the two different arrivals becomes negligible especially in the centre of the layer. Figure 7.16b also shows part of the speed profile (antenna depths between 28 and 35 m). The speed minima in the data (squares in Figure 7.16b) are considerably smaller than the one caused by the modeled high water-content (W=1.5%) layer. Even if speed minima were caused by critically refracted arrivals, the underestimation of water content would only be minor and within the accuracy of our water content estimates (±0.3%).

Further evidence of the fact that critical refraction does not corrupt our interpretations is provided by looking at h_{min}, defined as the minimum thickness of a low speed layer for which the direct wave will be first-arriving energy [*Rucker and Ferré*, 2004]:

$$h_{\text{min}} \leq x\sqrt{\frac{v_{\text{high}} - v_{\text{low}}}{v_{\text{high}} + v_{\text{low}}}}. \tag{7.9}$$

h_{min} was computed from equation 7.9 using v_{high} = 0.165 m/ns and v_{low} using the likely spectrum of radio-wave speeds in temperate ice (from 0.15 m/ns to 0.165

m/ns). Figure 9c shows that the presence of very wet layers ($v_i = 0.15$ m/ns, water content $\sim 2.5\%$) would be correctly detected without any underestimation of water content if such layers were thicker than 3 m. For greater speeds (i.e. drier layers), the minimum detectable thickness decreases.

Since the aim of this modeling exercise was to validate the uniformity of water content in mWS we observe that the occurrence of critically refracted arrivals causes slight underestimation of water-content in high water-content layers which are not plausible in this data since radio-wave speed rarely decreases below 0.165 m/ns. The presence of high water content layers ($\phi_w > 1.5\%$) is plausible for radio-wave speed <0.163 m/ns but this case is never observed in the data.

7.2.4 Discrete water features

It is striking to observe how ZOP-derived micro-crystalline water-content values at the CTS are $\sim$ twice the average values measured in the rest of the temperate ice (Figure 7.15). This observation indicates either that the water content at the CTS is higher than the deeper ice or simply that, at this position, high water-content estimates result from the drop in v_m (Figures 5.31 and 5.32) due to the presence of larger (e.g., centimeter to decimeter size) water features of the MWS crossed during the raypath.

Powers of the first arrivals recorded at the CTS are also considerably lower ($\sim$ 20 dB) than average recorded throughout the whole ice column (Figures 5.31 and 5.32). Figure 5.31 shows how these low-speed, low-power arrivals only occur in two regions of the ice column, at the CTS and at 40 m depth. There are no reasons to believe that such an anomalous response would be caused simply by water-content changes since this response would have been observed more often within the temperate ice. Such a loss of energy and drop in speed can be explained by scattering and energy partitioning losses when the ray-path crosses an interface. It is therefore likely that those minima in v_m and power are due to local water features (e.g., water-filled

fractures, *Fountain et al.* [2005]) within the inter-borehole regions.

A travel-time model of a ZOP was used to further explore this possibility and predict the measured radio-wave speed when the raypaths intersect water features, such as water-filled fractures of variable size. Only two media are included, water-free ice with uniform radio-wave speed $v_i = 0.168$ m/ns and water with radio-wave speed $v_w = 0.033$ m/ns. The distance between the two boreholes, d_T, is assumed to be uniform throughout the profile (10 antenna depths with a 1-m of sampling interval). The water feature in the model is geometrically described by its horizontal width, d_w (or the portion of the raypath traveled in water) and height, n, as described in Figure 7.17. The true raypath in ice, d_i is thus the difference between d_T and d_w.

With this configuration, the measured radio-wave speed, v_m, at each antenna depth is given by:

$$v_m = \frac{d_T}{d_i/v_i + d_w/v_w}. \tag{7.10}$$

Re-arranging this equation allows calculation of the fracture width, d_w:

$$d_w = \frac{d_T}{v_i - v_w}\left(\frac{v_i v_w}{v_m} - v_w\right). \tag{7.11}$$

Figure 7.17 shows the simulation using equation 7.11 for a 25 m long inter-borehole region. We observe that even relatively small (e.g., 0.1 m wide) water features can decrease v_m and consequently cause under estimation of v_i. This effect, represented as negative spikes in v_m, can be seen in multiple antenna depths depending on the vertical elongation of the fracture. Minima in speed and power observed at the CTS typically intersect two antenna positions, meaning that the vertical elongation of the features causing this response is greater than 2 m: for this reason it is likely that the raypath does not travel around those objects but rather travels through them. *Fountain et al.* [2005] observed that fractures are the main transport route for water from the surface to the englacial system in glaciers and that they are more common than tubular conduits in the overdeepening of Storglaciären. This particular area of the glacier is also where our study was conducted. It is thus likely that such water-filled fractures are present at 20 and 40 m depth within the inter-borehole region in our survey. Such features would cause scattering, loss of energy due to

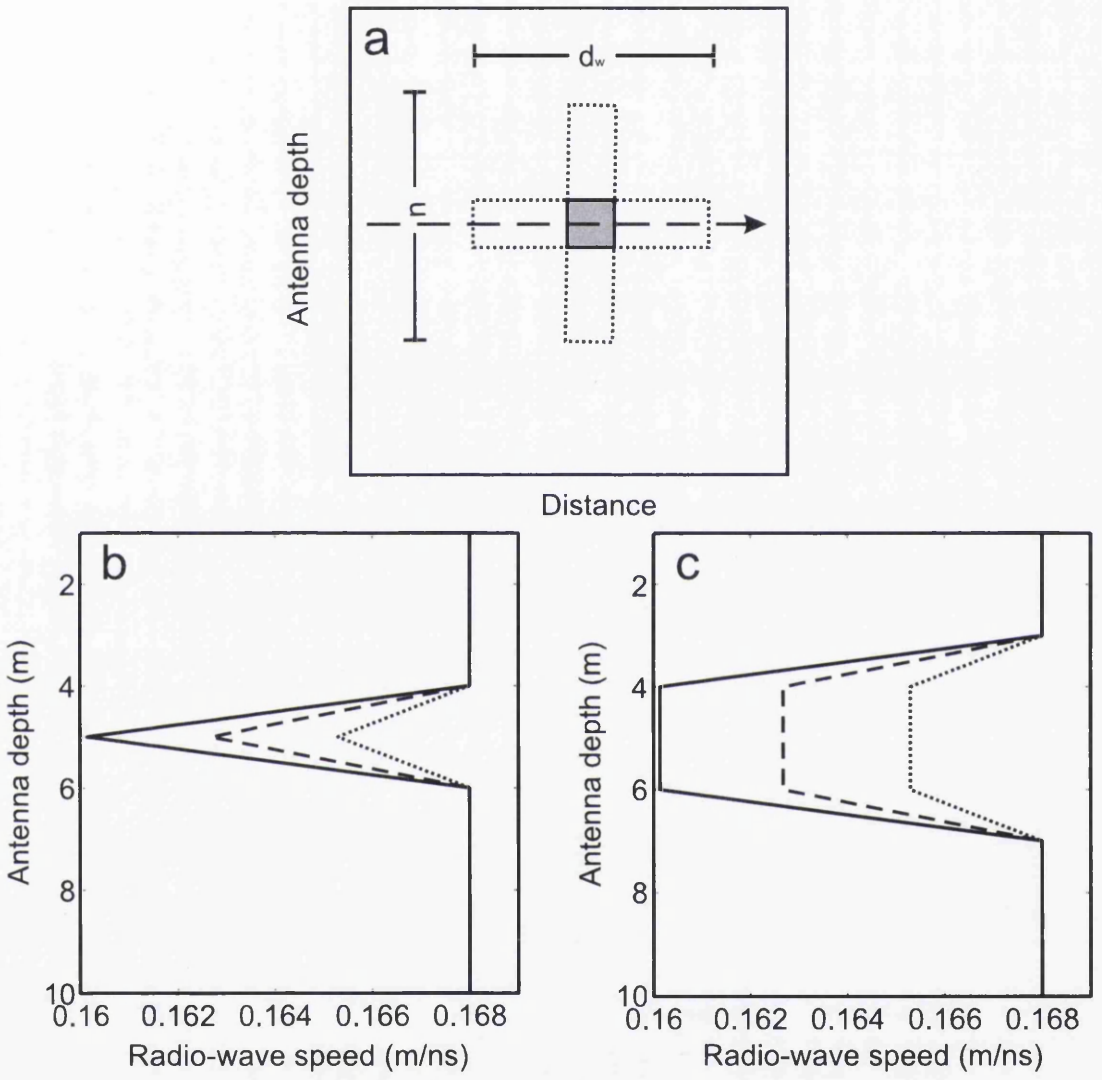

Figure 7.17: ZOP model including the presence of large (decimeter) water features using equation 7.10, $d_T = 25$ m, $v_i = 0.168$ m/ns and changing feature size. (a) Schematic of the model set-up: a 2D water feature geometrically described by its width d_w, and height n. (b,c) v_m for a water feature located at 5 m (b) and between 4 and 6 m depth (c) respectively. Note that the water feature in (a) is represented by the gray square. Dotted rectangles are included to show differently shaped water feature.

reflection and increase the travel time of the propagating wave, which then result in coincident low spikes in both measured radio-wave power and speed. We can roughly estimate the horizontal width of these fractures (equation 7.11) using the average unperturbed speed in the temperate ice (e.g., 0.165 m/ns) and the measured speed at the negative spike on each case (never lower than 0.162 m/ns). This calculation suggests that speed minima are caused by water features with d_w between 10 and 50 cm, consistent with the fracture interpretation.

7.2.5 Summary for site B

Temperature data, radar derived and calorimetry derived water-content estimates at site B (Figure 7.15) show that the hydraulic structure of this part of Storglaciären can be summarised by an upper, cold layer with 0% of volumetric water-content and a temperate core with a water content of $\sim 0.6 \pm 0.3\%$ (this value results from averaging the two surveys); the water content in the temperate ice does not vary significantly with depth and the system appears to be characterised by uniformity rather than variability. Calorimetric estimates of water content at the CTS ($0.6 \pm 0.1\%$) give similar results to the radar-derived values in the upper part of the temperate ice (Figure 7.15). Discrepancies between calorimetry and radar were observed at the CTS where the radar-derived water content is noticeably higher. These differences can be explained by considering that radar-derived water content estimates can be affected by discrete water features; in addition radar-derived water contents are a snapshot in time, while calorimetry-derived water content is an estimate over a longer interval.

Mean water-content values (both from radar and from calorimetry) are within the range of those derived by *Pettersson et al.* [2004] at the CTS of Storglaciären ($\phi_w = 0.6 \pm 0.3$ in this study in ~ 60 m depth of temperate ice and 0.8 ± 0.3 at the CTS in *Pettersson et al.*, 2004). By extending the analysis to deeper ice, it has been demonstrated that in the upper part of the temperate layer variations in water content are negligible. These estimates can be used to calculate ice viscosity for

both cold and temperate ice as shown in Equation 2.3. By empirically fitting the experimental results of *Duval* [1977] to a linear relationship between ϕ_w and A_0, it is possible to calculate A_{cold}=3.54 x 10^{-24} $Pa^{-3}s^{-1}$ and A_{warm}=12.83 $\pm$ 3.5 x 10^{-24} $Pa^{-3}s^{-1}$ (errors estimated using errors in ϕ_w): the whole temperate layer is thus between three and four times softer than the cold layer, a remarkable difference in terms of ice mechanics.

Liquid water in the mWS of glaciers potentially originates from four sources [*Paterson*, 1971]: (1) water input from the surface; (2) changes in the pressure melting point due to changes of the hydrostatic pressure; (3) water trapped in the ice of the accumulation area at the firn-ice transition; (4) melting due to the strain heating. Sources (1) and (2) are insignificant since the micro permeability of glacier ice is zero [*Lliboutry* [1971]; *Raymond and Harrison*, 1975] and (2) produces negligibly small quantities of water [*Pettersson et al.*, 2004; *Aschwanden and Blatter*, 2005]. Source (3), as argued by *Paterson* [1971], is the most important source of liquid water in temperate ice while source (4) is negligible at the CTS and in the upper part of the temperate ice, but becomes significant at depth [*Aschwanden and Blatter*, 2005]. The observed increase in water content with depth at depths greater than 60 m (Figure 7.15) can be explained with the predictions of *Aschwanden and Blatter* [2005; 2009].

7.2.6 Spatial variability in water content

The detailed discussion regarding the water content profiles at site B in 2008 can be applicable to other ZOP surveys. However, the lack of the comparison with the calorimetric estimates can raise objections on the interpretation including the fact that discrete water features and crevasses could corrupt it. Radio wave speed profiles from site to site varied considerably (Figure 5.43). From the surveys collected, a clear picture of water-content variations within Storglaciären is not immediate. Percentages of water were observed in some areas of the cold ice and this probably suggest that water percolates through fractures in the cold layer. The general agree-

ment on low water-content values within the temperate ice of Storglaciären (less than 1%) is perhaps the most important finding of this thesis. The upper boundary of W=1% has been indicated for the mWS in temperate ice [*Lliboutry*, 1976] and higher values should be therefore interpreted carefully since they may be greatly influenced by discrete water features in the MWS (Section 7.2.4 and *Murray et al.* [2000a]).

Water percentages at the site A were smaller than those measured at site B (Figure 5.43). At site A some water percentages were observed within the cold layer and this can be interpreted by considering the fact that site A is close to the equilibrium line altitude, some firn may be present and this firn could be porous and thus capable of storing small quantities of water (up to 0.5%). Additionally models suggest that close to the equilibrium line the production of water is lower than further down in the glacier (Figure 7.18, *Aschwanden and Blatter* [2005, 2009]). However, according to this model, water contents at site C should be higher than water contents at site B but this is not observed. On the other hand measurements in this thesis do not disagree with the increase of water content with depth predicted by *Aschwanden and Blatter* [2009]. The highest water content is observed at considerable depths, where the strain heating is larger.

Interestingly, the most important source of water content in glaciers: the water stored at the close-off [*Paterson*, 1971; *Pettersson et al.*, 2004] is at the same time the least understood (e.g. *Pettersson et al.* [2007]). Discrepancies between water content estimates in Figure 5.43 and the theoretical predictions by *Aschwanden and Blatter* [2005, 2009] could be explained by considering that there is very little knowledge on the spatial variability of water content at the close off. However, ZOP profiles, showed additional evidences of water content increases with depth. Such behaviour has been observed in Alpine cores [*Vallon et al.*, 1976], measured in Svalbard [*Jania et al.*, 2005] and predicted by models [*Aschwanden and Blatter*, 2005, 2009].

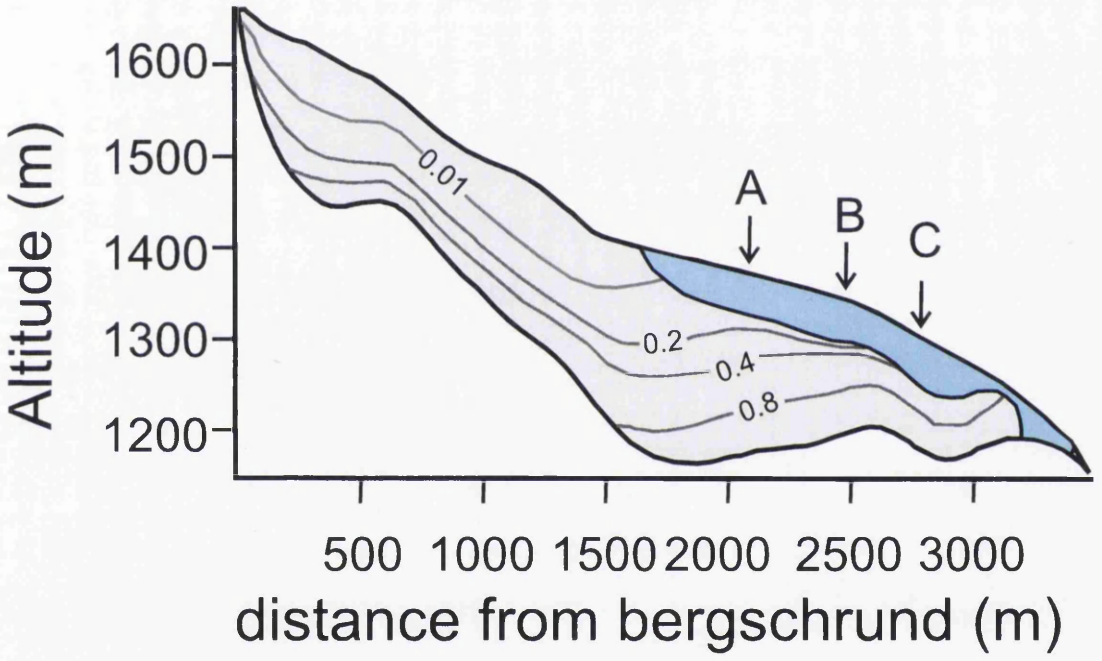

Figure 7.18: Water contents at Storglaciären computed by *Aschwanden and Blatter* [2009]. Water content values are (%). This figure was taken and modified from *Aschwanden and Blatter* [2009]. The model refers to the centre flow line of the glacier and thus both glacier and cold layer thickness are different than the real one where the ZOP surveys were acquired. Approximate location of the ZOP surveys is however indicated as a guide.

7.2.7 Temporal variability of water content

There is very poor understanding of temporal variability in water content. *Jania et al.* [2005] reported seasonal variations from 0.4 % to 2 % from the summer to spring at Hansbreen in Svalbard. Such a seasonal variation is presumably related to the amount of circulating meltwater in the macroscopic water system. Seasonal variation of microcrystalline water bodies implies some sort of percolation within porous temperate ice but this is not believed: microcrystalline water bodies are stored in small veins which can be blocked by air bubbles [*Lliboutry*, 1971; *Raymond and Harrison*, 1975; *Pettersson et al.*, 2004; *Gusmeroli et al.*, 2010b].

Inter-annual variation between summer 2008 and 2009 was observed at Site B. No water within the cold layer was inferred from the two surveys colllected in 2008 (Figure 7.15) but some water percentages, generated by lower speed, were found in 2009 (Figure 5.43d). Anomalously low radar power measured in the cold layer in the 2009 survey also suggest the presence of water (Figure 5.30). However, the upper 30 m of borehole 1 at site B in 2009 were drilled extremely slowly in order to obtain the borehole wide-enough for a 9 cm wide seismic source. The upper 30 m of the borehole were $\sim$ 10 cm wider than normally drilled boreholes. It has been demonstrated (Section 5.40) that borehole width affects measured speed; it is thus very likely that positive water percentages observed in the upper 20 m site B in 2008 are in fact caused by the exceptionally wider borehole 1 rather than water within the cold ice.

7.3 Radar and seismic attenuation

The main glaciological conclusions of this thesis were obtained using the well established correlation between radio wave speed and ice properties [*Macheret et al.*, 1993; *Murray et al.*, 2000a; *Navarro et al.*, 2005]. However radar power profiles illustrated in Chapter 5 and seismic attenuation estimates in Chapter 6 provide the

opportunity to discuss what can be learnt by measuring attenuation of these signals within ice masses. Recent glacio-geophysical literature motivates the importance of both radar and seismic attenuation in investigating bed properties [*Matsuoka et al.*, 2010; *Holland and Anandakrishnan*, 2009]; this is because the detection of wet,dry beds with radar or stiff,soft beds with seismic relies on accurate quantification of the returning signal compensated for the attenuation within the ice body. However as shown in Chapter 6 seismic Q_P values are lowered by ice temperature. Measuring power and/or attenuation of either seismic or radar signal could complement the established interpretations using speed. Ideally exctracting water-content, ice temperature, ice-thickness and subglacial conditions from a combination of radar and seismic surveys is the aim which could be addressed.

Joint estimates of radio wave speed and power variations with depth from ZOP radar surveys (Chapter 5) revealed that there is a correspondence between the two geophysical variables. In the vast majority of the surveys (Figures 5.25 to 5.38) the pattern of the radio wave speed profile is closely followed by the pattern of power profile and minima in speed very often correspond with minima in power. Disagreement between speed and power were only found at Site A where the boreholes were not as straight as the other two sites (Figures 5.22, 5.23, 5.24). All the power profiles presented in Chapter 5 show very little variation with depth and this, in agreement with speed, supports the fact that the water content within the temperate ice is low. Power profiles also exhibit a slight decrease with depth, this would imply higher attenuation due to water at depth and such a conclusion agrees with speed measurements: water content increases with depth.

Seismic attenuation values observed in this thesis only sampled the upper part of the ice column (Chapter 6). The lack of a consistent reflection from the bed (e.g. Figure 6.3) did not allow a direct comparison between Q_P values in the uppermost ice (Chapter 5, *Gusmeroli et al.* [2010a]) and bulk Q_P from the whole ice column which would then comprise of the water bodies in temperate ice. Q_P analysis from bed reflections has been undertaken on this PhD study also on a dataset acquired at midtre Lovénbreen in Svalbard but the poor data quality mainly determined by the

low SNR of the reflections did not allow successful estimates. As shown in Chapter 5, the frequency content of the wavelet needs to be extracted carefully and, for the refractions at Storglaciären the first arriving energy, composed by two nicely defined half cycles (Figure 6.5), was suitable for Q_P analysis.

7.4 Glaciological significance of this research

The 2009 map of the cold layer of Storglaciären and the comparison with previous surveys (Figure 4.30) shows that the thermal structure of the glacier is changing: the cold layer is slowly but persistently thinning (Figure 4.32) and if this continues the glacier may shift its thermal state from polythermal to temperate. The air temperature in the study area has been rising in the last decades (Figure 7.12). Since changes in thermal state are primarily controlled by climate, the observed thinning is assumed to be connected to the climatic warming.

Rises in englacial temperatures connected to atmospheric warming have been also recently reported in the European Alps [*Vincent et al.*, 2007] and in the Bolivian Andes [*Gilbert et al.*, 2010]. Such a combination of evidence worldwide suggests an important idea: englacial temperatures within ice masses are changing with climate and there is very little knowledge on the impact that these changes have on glacier-dynamics. A rise in englacial temperatures may shift the thermal regimes of high-altitude glaciers from cold to temperate (or at least temperate-based) [*Vincent et al.*, 2007; *Huggel*, 2009]. Rising englacial temperatures in steep glaciers currently frozen to the mountains can reduce the friction at their bed, increase ice-avalanching and thus constitute a increasing hazard for those populations who live nearby the glaciers [*Le Meur and Vincent*, 2006; *Vincent et al.*, 2007; *Huggel*, 2009]. Despite the fact that recent changes in glacier dynamics worldwide have been recently under great attention, the thermal evolution of glaciers over time has not been properly considered.

Thermal changes have profound effects on glacier dynamics: (i) warmer ice is softer,

a warmer glacier will deforms and moves differently; (ii) a change between cold-based and warm-based will allow an ice mass to slide on its bedrock; and (iii) when cold ice becomes temperate water-particles forms between crystals; these particles will additionally soften the ice. These fundamental relationships between a glacier thermal state and its dynamics should alert glaciologists on the importance of monitoring the thermal evolution with time, especially under a warming climate. Are the thermal structure observed in Greenland, Svalbard, Himalaya, Alaska, European Alps and Canadian Arctic changing with climate as it has been observed in the European Alps, Bolivian Andes and in this study? Can we compare the rate of changes observed at Storglaciären with other areas worldwide? Are hanging-wall glaciers and their potential hazards reacting similarly? These questions can be answered by intensifying our efforts to meticulously monitor englacial hydrothermal regimes using in situ geophysical and direct temperature measurements as it has been shown in the three results chapter of this thesis.

7.5 Summary

Spatiotemporal forcings responsible for the variation of the cold layer thickness have been discussed by looking at mass balance data, thermodynamics and weather data. Cold layer dynamics are dictated by complex interactions between climate, heat flux, mass balance and ice flow of which climate appears to be the most significant. Sample ZOP surveys from the 2008 campaign were directly compared to simultaneously acquired calorimetric estimates. The comparison shows that the water content distribution with depth in the upper ablation area of Storglaciären is relatively uniform. Water content distribution is interpreted in terms of ice viscosity: the whole temperate layer is between three and four times softer than the cold layer. Spatial and temporal variations of temperature and water-content in glaciers have profound effects on glacier dynamics, and the experiments outlined in this thesis provide a way to investigate these parameters.

Chapter 8

Conclusions

This PhD research aimed to investigate the spatial distribution of temperature and water-content within Storglaciären by using different geophysical surveys collected during three subsequent field campaigns (summer 2008, spring 2009 and summer 2009). Surface radar surveys were used to update our knowledge of the glacier's thermal regime, whereas borehole radar experiments allowed detailed sampling of the glacier dielectric properties with depth which were interpreted in terms of water-content. Additionally seismic refraction surveys have been studied in order to estimate the attenuation of P waves within the uppermost part of the ice column.

In Chapter 4, a series of common offset radar profiles was used to obtain an updated map of the polythermal structure of the glacier. The 2009 map was compared with previous maps of the polythermal structure of the glacier collected in 1989 [*Holmlund and Eriksson*, 1989] and 2001 [*Pettersson et al.*, 2003]. The comparison shows that the thinning of the cold layer observed between 1989 and 2001 [*Pettersson et al.*, 2003] is still ongoing. The thinning rate in the two time windows analyzed is approximately similar ($\sim$ 0.75 m/a). A volume calculation shows that the cold surface layer has lost one third of its volume in 20 years. Spatiotemporal variations in cold layer thickness are caused by complex interactions between climate, mass balance, ice flow, heat flux and water-content. Between these factors, the most

likely to cause thermal changes is the warming climate which is causing a weaker temperature gradient within the cold layer and thus causing the thinning. Rising englacial temperatures connected to atmospheric warming has been observed by repeated measurements in the European Alps [*Vincent et al.*, 2007] and inferred from heat-flux models in the Bolivian Andes [*Gilbert et al.*, 2010] and in West Antarctica [*Barrett et al.*, 2009]. There is increasing evidence that englacial temperatures are rising worldwide according to climate. The effect of these changes on glacier dynamics is largely unexplored and thus poorly understood.

Chapter 5 describe cross-borehole zero offset radar profiles acquired at three sites in Storglaciären. From these surveys 1 m depth-step profiles of radar wave speed and power up to 112 m depth were obtained. Radio wave speeds, interpreted in terms of ice water content, show that water content in the temperate ice of Storglaciären is generally low (<1%) and homogeneous with depth in the upper part of the temperate ice. An increase of water content due to strain-heating in the deepest part of the surveys (> 70 m) was observed. Spatial variability due to complex interactions between water-content generated at the close-off and water-content produced by strain heating was observed at the three sites. Additional evidence from temperature data was used to obtain a detailed model of the hydrothermal structure of the glacier at one site in the upper ablation area. Here the glacier is composed of a 20 m thick upper layer of cold, water-free ice, underlain by a temperate ice layer whose average water content is 0.6±0.3%. These findings imply that the whole temperate ice layer is from three to four times softer than the cold ice, and, consequently that realistic ice-flow models of polythermal glaciers should include the effect of water content on viscosity.

In Chapter 6 seismic refraction surveys were used to estimate seismic-wave attenuation using the spectral ratio method on the energy travelling in the uppermost ice with an average temperature of approximately -1 °C. Attenuation values were derived between 100 and 300 Hz using the P-wave quality factor, Q_P, the inverse of the internal friction. By assuming constant attenuation along the seismic line, mean Q_P was 6 ± 1. Q_P varied from 8 ± 1 to 5 ± 1 from the near-offset to the far-offset

region of the line, respectively. Since the wave propagates deeper at far offsets, this variation is interpreted by considering the temperature profile of the study area; far-offset arrivals sampled warmer and thus more-attenuative ice. This estimates are considerably lower than those reported for field studies in polar ice and, hence, are supportive of laboratory experiments that show attenuation increases with rising ice temperature.

8.1 Suggestions for further work

This research showed that in situ geophysical techniques can be used to constrain glaciological dynamics of a polythermal ice mass. Thermal structure was mapped with surface radar, water content distribution with depth was inferred from borehole radar surveys and the attenuation of seismic waves was studied as a tool to monitor englacial temperatures. The techniques discussed in this thesis can be applied elsewhere in glacierized areas. Cross-borehole radar surveys in particular, represent an appealing experiment to be conducted in other glaciological settings. In this section some suggestion for future research which have arisen after this PhD research will be discussed.

- *The cold layer of Storglaciären*: The 2009 cold layer map of the glacier represents a benchmark for continously monitoring the thermal structure of the glacier using radar surveys. The thermal-changes occurred between 1989 and 2001 were listed in the 2007 Fourth assessment of the IPCC [*Lemke et al.*, 2007] as additional evidence for changes in the cryosphere. It is very important to keep monitoring the cold layer of Storglaciären, especially after the observations made in this thesis that the thinning of the cold layer is an ongoing process. Future investigations could include surveying at different frequencies and installing a dense array of thermistors on the ablation area. In this way additional understanding of spatiotemporal changes in cold layer thickness can be achieved. Additional thermistor strings on the glacier will also allow fur-

ther calorimetry estimates of water content. Rigorous modelling efforts (not undertaken in this thesis) such as the study of *Pettersson et al.* [2007] are also recommended in understanding spatiotemporal variations of the cold layer.

- *Spatial variability of water content*: Water content estimates can be obtained with the methodologies described in Chapter 5. Cause for spatial variability remain, however, poorly understood. It has been pointed out that poor knowledge on the water entrapment at the close off is a limiting factor in understanding spatial variability. A combination of borehole radar surveys and calorimetric estimates in several part of the glacier could led towards a better understanding. Additionally, evidence from ice core could be beneficial.

- *Cross-borehole radar for glaciology*: It has been demonstrated (Chapter 5) a way to sample the dielectric properties of ice masses with depth. In this thesis this technique has been applied in measuring water content at Storglaciären, however other application are also possible. In cold ice masses, dielectric changes could be related to changes in crystal orientation fabric, a fundamental property for ice-flow modelling. Cross borehole radar experiments in cold glaciers could be the next step in exploring this technique in glaciology.

- *Thermal dynamics of glaciers*: Englacial temperatures are reacting to climate. This has been only recently reported in the literature as evidence for climatic warming. The consequences that thermal changes could have on glacier dynamics (e.g. icefalls, softening of ice, increasing sliding) are not-explored and largely not understood. Since temperature critically controls glacier motion it is essential that climatically-driven thermal variability will be (a) meticulously investigated as in Chapter 4 in other glacierized regions; and (b) included in models in order to understand its consequences on glacier-dynamics.

- *Petrophysics of radar and seismic attenuation*: Cross-borehole radar surveys (Chapter 5) allowed profiling of radar power which can be related to dielectric attenuation. Additionally a simple methodology to obtain seismic attenuation estimates has been described (Chapter 6). The next logical step is including

radar and seismic attenuation in petrophysical models in order to understand the effect that water-content has on attenuation of both geophysical quantities.

References

Aki, K., and P. Richards, *Quantitative seismology*, 2 ed., University Science Books, Sausalito, California, 2002.

Alley, R. B., M. Fahnestock, and I. Joughin, Understanding glacier flow in changing times, *Science*, *322*, 1061–1062, 2008.

Annan, A. P., *Ground penetrating radar workshop notes*, Brevik Place, Mississauga, Ontario, ONL4W 3R7, Canada, Sensors and Software Inc., 1091, 1999.

Aschwanden, A., and H. Blatter, Meltwater production due to strain heating in Storglaciären, Sweden, *Journal of Geophysical Research*, *110*, doi:10.1029/2005JF000,328, 2005.

Aschwanden, A., and H. Blatter, Mathematical modeling and numerical simulation of polythermal glaciers, *Journal of Geophysical Research*, *114*, doi:10.1029/2008JF001,028, 2009.

Bamber, J., Internal reflecting horizons in Spitsbergen glaciers, *Annals of Glaciology*, *9*, 5–10, 1987.

Barrett, B., Ground penetrating radar techniques for quantifying water distribution in glacial ice, Ph.D. thesis, The University of Leeds, 2007.

Barrett, B. E., T. Murray, and R. Clark, Errors in radar CMP velocity estimates due to survey geometry, and their implication for ice water content estimation, *Journal of Environmental and Engineering Geophysics*, *12*, 101–111, 2007.

Barrett, B. E., T. Murray, R. Clark, and K. Matsuoka, Distribution and character of water in a surge-type glacier revealed by multifrequency and multipolarisation ground-penetrating radar, *Journal of Geophysical Research*, *113*, doi:10.1029/2007TJF000,972, 2008.

Barrett, B. E., K. W. Nicholls, T. Murray, A. M. Smith, and D. G. Vaughan, Rapid recent warming on Rutford Ice Stream from borehole thermometry, *Geophysical Research Letters*, *36*, doi:10.1029/2008GL036,369, 2009.

Benjumea, B., Y. Y. Macheret, F. J. Navarro, and T. Teixidó, Estimation of water content in a temperate glacier from radar and seismic sounding data, *Annals of Glaciology*, *37*, 317–324, 2003.

Benn, D. I., and D. J. A. Evans, *Glaciers and glaciations*, Oxford University Press Inc., 198 Madison Avenue, New York, NY10016, 1998.

Bentley, C., and H. Kohnen, Seismic refraction measurements of internal friction in Antarctic Ice, *Journal of Geophysical Research*, *81*, 1519–1526, 1976.

Binley, A., P. Winship, R. Middleton, M. Pokar, and J. West, High-resolution characterization of vadose zone using cross-borehole radar, *Water Resource Research*, *37*, 2639–2652, 2001.

Binley, A., P. Winship, L. West, M. Pokar, and R. Middleton, Seasonal variation of moisture content in unsaturated sanstone inferred from borehole radar and resistivity profiles., *Journal of Hydrology*, *257*, 160–172, 2002.

Björnsson, H., Radio-echo sounding maps of Storglaciären, Isfallglaciären and Rabots Glaciär, Northern Sweden, *Geografiska Annaler*, *63*, 225–231, 1981.

Björnsson, H., Y. Gjessing, S. E. Hamran, J. O. Hagen, O. Liestol, O. F. Pálsson, and B. Erlingsson, The thermal regime of sub-polar glaciers mapped by multi-frequency radio echo sounding, *Journal of Glaciology*, *42*, 23–32, 1996.

Blankenship, D. D., C. R. Bentley, S. T. Rooney, and R. B. Alley, Seismic measurements reveal a saturated porous layer beneath an Antarctic ice stream, *Nature*, *322*, 54–57, 1986.

Blatter, H., On the thermal regime of an Arctic valley glacier: A study of White Glacier, Axel Heiberg Island, N.W.T., Canada, *Journal of Glaciology*, *33*, 200–211, 1987.

Blatter, H., and K. Hutter, Polythermal conditions in Arctic glaciers, *Journal of Glaciology*, *37*, 261–269, 1991.

Blatter, H., and G. Kappenberger, Mass balance and thermal regime of Laika ice cap, Coburg Island, *Journal of Glaciology*, *34*, 102–110, 1988.

Bogorodsky, V. V., C. R. Bentley, and P. E. Gudmandsen, *Radioglaciology*, D. Reidel Publishing Company, Dordrecht, 1985.

Bradford, J., and J. Harper, Wave field migration as a tool for estimating spatially continuous radar velocity and water-content in glaciers, *Geophysical Research Letters*, *32*, doi:10.1029/2004GL021,770, 2005.

Bradford, J., J. Nichols, T. Mikesell, and J. Harper, Continous profiles of electromagnetic wave velocity and water content in glaciers: an example from Bench Glacier, Alaska, USA, *Annals of Glaciology*, *50*, 1–9, 2009.

Brown, J., J. Harper, and J. Bradford, A radar transparent layer in a temperate glacier: Bench Glacier, Alaska, *Earth Surface Processes and Landforms*, *34*, 1497–1506, 2009.

Bull, C., Glaciological reconnaissance of the Sukkertoppen ice cap, south-west Greenland, *Journal of Glaciology*, *4*, 813–816, 1963.

Catania, G., T. Neumann, and S. Price, Characterizing englacial drainage in the ablation zone of the Greenland Ice Sheet, *Journal of Glaciology*, *54*, 567–578, 2008.

Chandler, D., B. Hubbard, A. Hubbard, T. Murray, and D. Rippin, Optimising ice flow law parameters using borehole deformation measurements and numerical modelling, *Geophysical Research Letters*, *35*, doi:10.1029/2008GL033,801, 2008.

Clarke, G. K. C., and R. H. Goodman, Radio echo soundings and ice-temperature measurements in a surge type glacier, *Journal of Glaciology*, *14*, 71–78, 1975.

Clee, T., J. Savage, and G. Neave, Internal friction in ice near its melting point, *Journal of Geophysical Research*, *74*, 973–980, 1969.

Comas, X., L. Slater, and A. Reeve, Spatial variability in biogenic gas accumulation is peat soils revealed by ground penetrating radar (GPR), *Geophysical Research Letters*, *32*, doi:10.1029/2004GL022,297, 2005.

Copland, L., and M. Sharp, Mapping thermal and hydrological conditions beneath a polythermal glacier with radio-echo sounding, *Journal of Glaciology*, *47*, 232–242, 2001.

Daniels, J. J., *Ground Penetrating Radar, 2nd Edition*, IEE Radar, Sonar, Navigation and Avionics Series 15, The Institution of Electrical Engineers, 2004.

Dasgupta, R., and R. Clark, Estimation of Q from surface seismic reflection data, *Geophysics*, *63*, 2120–2128, 1998.

Davis, J. L., and A. P. Annan, Ground-penetrating radar for high-resolution mapping of soil and rock stratigraphy, *Geophysical Prospecting*, *37*, 531–551, 1989.

Dowdeswell, J. A., and S. Evans, Investigations of the form and flow of ice sheets and glaciers using radio-echo sounding, *Reports on Progress in Physics*, *67*, 1821–1861, 2004.

Dowdeswell, J. A., D. J. Drewry, O. Liestøl, and O. Orheim, Radio echo-sounding of Spitsbergen glaciers problems in the interpretation of layer and bottom returns, *Journal of Glaciology*, *30*, 16–21, 1984.

Drewry, D. J., *Antarctica, Glaciological and Geophysical Folio*, University of Cambridge, Oxford, 1983.

Dupuy, D., Étude de la glace tempérée de glacier à l'aide de mesures thermiques et diélectriques, Ph.D. thesis, Univ. de Grenoble, France, 1970.

Duval, P., The role of water content on the creep rate of polycrystalline ice, *International Associations of Hydrological Sciences publication*, *118*, 29–33, 1977.

Dvorkin, J., and A. Nur, Dynamic poroelasticity a unified model with the squirt and the Biot mechanisms, *Geophysics*, *58*, 524–533, 1993.

Dyurgerov, M., V. Uvarov, and T. Kostjashkina, Mass balance and runoff of Tuyuksu glacier and ther north slope of the Zailiyskiy Alatau Range, *Zeitschrift für Gletscherkunde und Glazialgeologie*, *32*, 1996.

Eisen, O., A. Bauder, M. Lüthi, P. Riesen, and M. Funk, Deducing the thermal structure in the tongue of Gornergletcher, Switzerland, from radar surveys and borehole measurements, *Annals of Glaciology*, *50*, 63–70, 2009.

Endres, L. A., T. Murray, A. D. Booth, and L. J. West, A new framework for estimating englacial water content and pore geometry using combined radar and seismic wave velocities, *Geophysical Research Letters*, *36*, doi:10.1029/2008GL036,876, 2009.

Eriksson, M. G., H. Björnsson, U. C. Herzfeld, and P. Holmlund, The botton topography of Storglaciären. a new map based on old and new ice depth measurements, analyzed with geostatistical methods, *Forskningsrapportserien*, 1994, STOU-NG 95, 48p.

Flowers, G., and G. Clarke, Surface and bed topography of Trapridge glacier, Yukon territory, Canada: Digital elevation models and derived hydraulic geometry, *Journal of Glaciology*, *45*, 165–174, 1999.

Fountain, A. G., and J. S. Walder, Water flow through temperate glaciers, *Review of Geophysics*, *36*, 299–328, 1998.

Fountain, A. G., R. W. Jacobel, R. Schlichting, and P. Jansson, Fractures as the main pathways of water flow in temperate glaciers, *Nature*, *433*, 618–621, 2005.

Fowler, A. C., On the transport of moisture in polythermal glaciers, *Geophysics Astrophysics and Fluid Dynamics*, *28*, 201–224, 1984.

Fowler, A. C., and D. A. Larson, On the flow of polythermal glaciers. i. model and preliminary analysis, *Proceedings of the Royal Society of London. Series A, Mathematical and Physical Sciences*, *363*, 217–242, 1978.

Futterman, W., Dispersive body waves, *Journal of Geophysical Research*, *67*, 5279–5291, 1962.

Garbarino, M., E. Lingua, T. Nagel, D. Godone, and R. Motta, Patterns of larch establishment following deglaciation of Ventina glacier, central Italian Alps, *Forest Ecology and Management*, *259*, 583–590, 2010.

Gilbert, A., P. Wagnon, C. Vincent, P. Ginot, and M. Funk, Atmospheric warming at a high-elevation tropical site revealed by englacial temperatures at Illimani, Bolivia (6340 m above sea level, 16°S, 67°W), *Journal of Geophysical Research*, *115*, doi:10.1029/2009JD012,961, 2010.

Glen, J. W., The creep of polycrystalline ice, *Proceedings of the Royal Society of London - Series A*, *228*, 519–538, 1955.

Greaves, R. J., D. P. Lesmes, J. M. Lee, and M. N. Toksoz, Velocity variation and water content estimated from multi-offset, ground-penetrating radar, *Geophysics*, *61*, 683–695, 1996.

Griffiths, D. J., *Introduction to Electrodynamics, 3rd Edition*, Prentice-Hall International, Inc., 1999.

Grudd, H., and T. Schneider, Air temperature at Tarfala Research Station, *Geografiska Annaler*, *74*, 115–120, 1996.

Gulley, J. D., D. I. . Benn, D. Müller, and A. Luckman, A cut-and-closure origin for englacial conduits in uncrevassed regions of polythermal glaciers, *Journal of Glaciology*, *55*, 66–80, 2009.

Gusmeroli, A., T. Murray, B. Barrett, R. Clark, and A. Booth, Estimates of water content in glacier ice using vertical radar profiles: a modified interpretation from Falljökull, Iceland., *Journal of Glaciology*, *54*, 939–942, 2008.

Gusmeroli, A., R. Clark, T. Murray, A. Booth, B. Barrett, and B. Kulessa, Seismic waves attenuation in the uppermost ice of Storglaciären, *Journal of Glaciology*, *56*, 249–255, 2010a.

Gusmeroli, A., T. Murray, P. Jansson, R. Pettersson, A. Achwanden, and A. Booth, Vertical distribution of water within the polythermal Storglaciären, Sweden., *Journal of Geophysical Research, in press*, 2010b.

Haeberli, W., Eistemperaturen in den Alpen, *Zeitschrift für Gletscherkunde und Glazialgeologie*, *11*, 203–220, 1976.

Hambrey, M., T. Murray, N. Glasser, A. Hubbard, B. Hubbard, G. Stuart, S. Hansen, and J. Kohler, Structure and changing dynamics of a polythermal valley glacier on a centennial time scale: midre Lovénbreen, Svalbard, *Journal of Geophysical Research*, *105*, doi:10.1029/2004JF000,128, 2005.

Hamran, S. E., E. Aarholt, J. O. Hagen, and P. Mo, Estimation of relative water content in sub-polar glacier using surface-penetration radar, *Journal of Glaciology*, *42*, 533–537, 1996.

Hanson, B., A fully three-dimensional finite-element model applied to velocities on Storglaciären, Sweden., *Journal of Glaciology*, *41*, 91–102, 2005.

Henry, T. A., and R. J. White, The temperature of Sukkertoppen ice cap, *Journal of Glaciology*, *5*, 265, 1964.

Herzfeld, U., M. Eriksson, and P. Holmlund, On the influence of Kriging parameters on the cartographic output, a study in mapping subglacial topography, *Mathematical Geology*, *25*, 881–900, 1993.

Hock, R., D. Kootstra, and C. Reijmer, Deriving glacier mass balance from acumulation area ratio on storglaciären, sweden, *IAHS Publication*, pp. 163–170, 2007.

Hock, R., M. de Woul, V. Radić, and M. Dyurgerov, Mountain glaciers and ice caps around Antarctica make a large sea-level rise contribution, *Geophysical Research Letters*, *36*, doi:10.1029/2008GL037,020, 2009.

Holland, C., and S. Anandakrishnan, Subglacial seismic reflection strategies when source amplitude and medium attenuation are poorly known, *Journal of Glaciology*, *55*, 931–937, 2009.

Holmlund, P., and M. Eriksson, The cold surface layer on Storglaciären, *Geografiska-Annaler*, *71*, 241–244, 1989.

Holmlund, P., and P. Jansson, The Tarfala mass balance program, *Geografiska Annaler*, *81*, 115–120, 1999.

Holmlund, P., and P. Jansson, Glaciological research at Tarfala Research Station, *Stockholm University*, 2002.

Holmlund, P., J. O. Näslund, and C. Richardson, Radar suveys on Scandinavian glaciers, in search for useful climate archives, *Geografiska Annaler*, *78*, 147–154, 1996.

Hooke, R. L., *Principles of glacier mechanics*, Cambridge University Press, Cambridge, UK, 2005.

Hooke, R. L., J. E. Gould, and J. Brzozowski, Near-surface temperatures near and below the equilibrium line on polar and supolar glaciers, *Zeitschrift für Gletscherkunde and Glazialgeologie*, *19*, 1–25, 1983.

Hooke, R. L., P. Calla, P. Holmlund, M. Nillsson, and A. Stroeven, A 3 year record of seasonal variations in surface velocity, Storglaciären. Sweden, *Journal of Glaciology*, *35*, 235–247, 1989.

Howat, I. M., I. Joughin, and T. Scambos, Rapid changes in ice discharge from Greenland outlet glaciers, *Science*, *315*, 1559–1561, 2007.

Hubbard, B., A. Hubbard, H. M. Mader, J. Tison, K. Grust, and P. W. Nienow, Spatial variability in the water content and rheology of temperate glaciers: Glacier de Tsanfleuron, Switzerland., *Annals of Glaciology*, *37*, 1–6, 2003.

Huggel, C., Recent extreme slope failures in glacial environments: effects of thermal perturbation, *Quaternary Science Reviews*, *28*, 1119–1130, 2009.

Huisman, J., S. Hubbard, J. Redman, and A. Annan, Measuring soil water-content with ground penetrating radar: a review., *Vadose Zone Journal*, *2*, 476–491, 2003.

Hutter, K., Thermo-mechanically coupled ice-sheet repsonse - cold, polythermal, temperate., *Journal of Glaciology*, *39*, 65–85, 1993.

Hutter, K., H. Blatter, and M. Funk, A model computation of moisture content in polythermal glaciers, *Journal of Geophysical Research*, *93*, 12,20512,214, 1988.

Hutter, K., A. Zyrd, and H. Röthlisberger, On the numerical solution of Stefan problems in temperate ice., *Journal of Glaciology*, *36*, 41–48, 1990.

Irvine-Fynn, T. D. L., B. J. Moorman, J. L. M. Williams, and F. S. A. Walter, Seasonal changes in ground-penetrating radar signature observed at a polythermal glacier, Bylot Island, Canada, *Earth Surface Processes and Landforms*, *31*, 892–909, 2006.

Isaaks, E., and R. Srivastava, *An introduction to applied geostatistic*, Oxford University Press, New York, 1989.

Jacobel, R., and S. Anderson, Interpretation of radio-echo return from internal water bodies in Variegated Glacier, Alaska, *Journal of Glaciology*, *33*, 319–323, 1987.

Janetti, E., M. Riva, S. Straface, and A. Guadagnini, Stochastic characterization of the Montalto Uffugo research site (Italy) by geostatistical inversion of moment equations of groundwater flow, *Journal of Hydrology*, *381*, 42–51, 2010.

Jania, J., D. Mochnacki, and B. Gadek, The thermal structure of Hansbreen, a tidewater glacier in southern Spitsbergen, Svalbard, *Polar Research*, *15*, 53–66, 1996.

Jania, J., et al., Temporal changes in the radiophysical properties of a polythermal glacier in Spitsbergen, *Annals of Glaciology*, *42*, 125–134, 2005.

Jansson, P., Water pressure and basal sliding on Storglaciären, northern Sweden., *Journal of Glaciology*, *41*, 232–240, 1995.

Jansson, P., Dynamics and hydrology of a small polythermal valley glacier, *Geografiska Annaler*, *78*, 171–180, 1996.

Jansson, P., and R. Pettersson, Spatial and temporal characteristics of a long mass balance record, Storglaciären, Sweden, *Arctic, Antarctic and Alpine Research*, *30*, 432–437, 2007.

Jansson, P., R. Hock, and T. Schneider, The concept of glacier storage: A review, *Journal of Hydrology*, *282*, 116–129, 2003.

Jarvis, E., and E. King, The seismic wavefield recorded on an Antarctic ice shelf, *Journal of Seismic Exploration*, *2*, 69–86, 1993.

Jeng, Y., J. Ysai, and S. Chen, An improved method of determining near-surface Q, *Geophysics*, *65*, 1780–1787, 1999.

Johnston, D., M. Toksöz, and A. Timur, Attenuation of seismic waves in dry and saturated rocks, ii: Mechanisms, *Geophysics*, *44*, 691–711, 1979.

King, E. C., A. M. Smith, T. Murray, and G. W. Stuart, Glacier-bed charachteristic of midtre Lovénbreen, *Journal of Glaciology*, *54*, 145–156, 2008.

Knopoff, L., Q, *Rev. Geophys.*, *2*, 625–660, 1964.

Koblet, T., I. G. Roer, M. Zemp, P. Jansson, P. Thee, W. Haeberli, and P. Holmlund, Determination of length, area and volume changes at Storglaciären, Sweden, from multi-temporal aerial images, *The Cryosphere discussion*, *4*, 347–379, 2010.

Kohler, J., J. Moore, M. Kennet, R. Engest, and H. Elveh, Using ground-penetrating radar to image previous years' summer surfaces for mass-balance measurements, *Annals of Glaciology*, *24*, 355–360, 1997.

Kotlyakov, V. M., and Y. Y. Macheret, Radio echo-sounding of subpolar glaciers in Svalbard: Some problems and results of Soviet studies, *Annals of Glaciology*, *9*, 151–159, 1987.

Kuirowa, D., *Internal friction of ice*, Institute of Low Temperature Science Hokkaido University Contribution, A-18, 1-62, 1964.

Kulessa, B., A. Booth, A. Hobbs, and A. Hubbard, Automated monitoring of subglacial hydrological processes with ground-penetrating radar (GPR) at high temporal resolution: scope and potential pitfalls, *Geophysical Research Letters*, *35*, doi:10.1029/2008GL035,855, 2008.

Kuroda, S., H. Jang, and H. Kim, Time-lapse borehole radar monitoring of an infiltration experiments in the vadose zone., *Journal of Applied Geophysics*, *67*, 361–366, 2009.

Le Meur, E., and C. Vincent, Monitoring of the Taconnaz ice fall (French Alps) using measurements of mass balance, surface velocities and ice cliff position, *Cold Regions Science and Technology*, *46*, 1–11, 2006.

Lemke, P., et al., *Observations: Changes in Snow, Ice and Frozen Ground. In: Climate Change 2007: The Physical Science Basis. Contribution of Working Group I to the Fourth Assessment Report of the Intergovernmental Panel on Climate Change [Solomon, S., D. Qin, M. Manning, Z. Chen, M. Marquis, K.B. Averyt, M. Tignor and H.L. Miller (eds.)]*, Cambridge University Press, Cambridge, UK and New York, NY, USA, 2007.

Lliboutry, L., Permeability, brine content and temperature of temperate ice, *Journal of Glaciology*, *10*, 15–29, 1971.

Lliboutry, L., Physical processes in temperate glaciers, *Journal of Glaciology*, *16*, 151–158, 1976.

Loewe, F., The temperature of Sukkertoppen ice cap, *Journal of Glaciology*, *6*, 179, 1966.

Looyenga, M., Dielectric constants of heterogeneous mixtures, *Physica*, *31*, 401–406, 1965.

Lüthi, M., M. Funk, A. Iken, S. Gogineni, and M. Truffer, Mechanisms of fast flow in Jakobshavn Isbrae, west Greenland. part iii: Measurements of

ice deformation, temperature and cross-hole conductivity in boreholes to the bedrock, *Journal of Glaciology*, *48*, 369–385, 2002.

MacGregor, J., D. Winebrenner, H. Conway, K. Matsuoka, P. Mayewski, and G. Clow, Modeling englacial radar attenuation at Siple Dome, West Antarctica, using ice chemistry and temperature data, *Journal of Geophysical Research*, *112*, doi:10.1029/2006JF000,717, 2007.

Macheret, Y. Y., and A. F. Glazovsky, Estimation of absolute water content in Spitsbergen glaciers from radar sounding data, *Polar Research*, *19*, 205–216, 2000.

Macheret, Y. Y., M. Y. Moskalevsky, and E. V. Vasilenko, Velocity of radiowaves in glaciers as an indicator of their hydrothermal state, structure and regime, *Journal of Glaciology*, *39*, 373–384, 1993.

Mader, H., Observations of the water-vein system in polycristalline ice, *Journal of Glaciology*, *38*, 333–347, 1992.

Maohuan, H., On the temperature distribution of glaciers in China, *Journal of Glaciology*, *36*, 210–216, 1990.

Martinez, M., X. Lana, and E. Giunito, Shear-wave attenuation tomography of the lithosphere-astenosphere beneath the Mediterranean region, *Tectonophysics*, *481*, 51–67, 2008.

Matsuoka, K., S. Uratsuka, S. Fujita, and F. Nishio, Ice-flow induced scattering zone within the Antarctic ice sheet revealed by high-frequency airborne radar., *Journal of Glaciology*, *50*, 382–388, 2004.

Matsuoka, K., D. Morse, and C. Raymond, Estimating englacial radar attenuation using depth profiles of the returned power, central West Antarctica, *Journal of Geophysical Research*, *115*, doi:10.1029/2009JF001,496, 2010.

Meier, M. F., M. B. Dyurgerov, U. K. Rick, S. O'Neel, W. T. Pfeffer, R. S. Anderson, S. P. Anderson, and A. F. Glazovsky, Glaciers dominate eustatic sea-level rise in the 21st century, *Science*, *317*, DOI:10.1126/science.1143,906, 2007.

Moore, J. C., A. Pälli, F. Ludwig, H. Blatter, J. Jania, B. Gadek, P. Glowacki, D. Mochnacki, and E. Isaksson, High-resolution hydrothermal structure of Hansbreen, Spitsbergen, mapped by ground-penetrating radar, *Journal of Glaciology*, *45*, 524–532, 1999.

Murray, T., D. L. Gooch, and G. W. Stuart, Structures within the surge front at Bakaninbreen, Svalbard, using ground-penetrating radar, *Annals of Glaciology*, *24*, 122–129, 1997.

Murray, T., G. W. Stuart, M. Fry, N. Gamble, and M. D. Crabtree, Englacial water distribution in a temperate glacier from surface and borehole radar velocity analysis, *Journal of Glaciology*, *46*, 389–398, 2000a.

Murray, T., G. W. Stuart, P. J. Miller, J. Woodward, A. Smith, P. R. Porter, and H. Jiskoot, Glacier surge propagation by thermal evolution at the bed, *Journal of Geophysical Research*, *105*, 13,491–13,507, 2000b.

Murray, T., A. Booth, and D. M. Rippin, Water content of glacier-ice: Limitations on estimates from velocity analysis of surface ground-penetrating radar surveys, *Journal of Environmental and Engineering Geophysics*, *12*, 87–99, 2007.

Murray, T., H. Corr, A. Forieri, and A. Smith, Contrasts in hydrology between regions of basal deformation and sliding beneath Rutford Ice Stream, West Antarctica, mapped using radar and seismic data, *Geophysical Research Letters*, *35*, doi:10.1029/2008GL033,681, 2008.

Nas, B., and A. Berktay, Groundwater quality mapping in urban groundwater using GIS, *Environmental Monitoring and Assessment*, *160*, 215–227, 2010.

Navarro, F., J. Otero, Y. Macheret, E. Vasilenko, J. Lapazaran, A. Alhlström, and F. Machío, Radioglaciological studies on Hurd Peninsula glaciers, Livingston Island, Antarctica, *Annals of Glaciology*, *50*, 17–24, 2009.

Navarro, F. J., Y. Y. Macheret, and B. Benjumea, Application of radar and seismic methods for the investigation of temperate glaciers, *Journal of Applied Geophysics*, *57*, 193–211, 2005.

Nye, J., The geometry of water veins and nodes in polycristalline ice, *Journal of Glaciology*, *35*, 17–22, 1989.

Ødegård, R. S., J. Hagen, and S. Hamran, Comparison of radio- echo sounding (30-1000 mhz) and high-resolution borehole-temperature mea- surements at Finsterwalderbreen, southern Spitsbergen, Svalbard, *Annals of Glaciology*, *24*, 262–267, 1997.

Paren, J. G., Dielectric properties of ice. chapter 6 :field experiments on axel heiberg island, Ph.D. thesis, University of Cambridge, 1970.

Parizek, B. R., and R. B. Alley, Implications of increased Greenland surface melt under global-warming scenarios: ice-sheet simulations, *Quaternary Science Reviews*, *23*, 1013–1027, 2004.

Paterson, W. S. B., Temperature measurements in Athabasca Glacier, Alberta, Canada, *Journal of Glaciology*, *10*, 339–349, 1971.

Paterson, W. S. B., *The Physics of Glaciers*, Butterworth-Heineman, Oxford, 1994.

Peters, L., S. Anandakrishnan, C. Holland, H. Horgan, D. Blankenship, and D. Voigt, Seismic detection of a subglacial lake near the South Pole, Antarctica, *Geophys. Res. Lett.*, *35*, doi:10.1029/2008GL035,704, 2008.

Peterson, J., Pre-inversion corrections and analysis of radar tomographic data., *Journal of Environmental and Engineering Geophysics*, *6*, 1–18, 2001.

Pettersson, R., Dynamics of the cold surface layer of Storglaciären, Sweden, Ph.D. thesis, Stockholm University, 2004.

Pettersson, R., Frequency dependence of scattering from the cold-temperate transition surface in a polythermal glacier, *Radio Science*, *40*, doi:10.1029/2004RS003,090, 2005.

Pettersson, R., P. Jansson, and P. Holmlund, Cold surface layer thinning on Storglaciären, Sweden, observed by repeated ground penetrating radar surveys, *Journal of Geophysical Research*, *108*, doi:10.1029/2003JF000,024, 2003.

Pettersson, R., P. Jansson, and H. Blatter, Spatial variability in water content at the cold-temperate transition surface of the polythermal Storglaciären, Sweden, *Journal of Geophysical Research*, *109*, doi:10.1029/2003JF000,110, 2004.

Pettersson, R., P. Jansson, H. Huwald, and H. Blatter, Spatial pattern and stability of the cold surface layer of Storglaciären,Sweden, *Journal of Glaciology*, *53*, 99–109, 2007.

Pohjola, V., Tv-video observations of englacial voids in Storglaciären, Sweden, *J. Glaciol.*, *40*, 231–240, 1994.

Rabus, B. T., and K. A. Echelmeyer, The flow of a polythermal glacier: McCall, Alaska, USA, *Journal of Glaciology*, *43*, 522–536, 1997.

Raymond, C. F., and W. D. Harrison, Some observations on the behavior of the liquid and gas phases in temperate glacier ice, *Journal of Glaciology*, *14*, 213–233, 1975.

Reine, C., M. van der Baan, and R. Clark, The robustness of seismic attenuation measurements using fixed- and variable-window time-frequency transforms, *Geophysics*, *72*, WA 123–WA 135, 2009.

Reynolds, J., The distribution of mean annual temperature in the Antarctic Peninsula, *British Antarctic Survey Bullettin*, *54*, 123–133, 1981.

Reynolds, J. M., *An introduction to applied and environmental geophysics*, John Wiley & Sons Ltd, 1997.

Robin, G., *Seismic shooting and related investigations; Norwegian-British-Swedish Antarctic Expedition 1949-1952: Glaciology III, Scientific Results, Vol V*, 1958.

Robin, G., Velocity of radio waves in ice by means of a bore-hole interferometric technique, *Journal of Glaciology*, *15*, 151–158, 1975.

Robin, G., S. Evans, and J. Bailey, Interpretation of radio-echo sounding in polar ice sheets, *Philosophical Transactions of the Royal Society of London, Series A*, *256*, 437–505, 1969.

Rucker, D., and T. Ferré, Correcting water content measurement errors associated with critically refracted first arrivals on zero offset profiling borehole ground penetrating radar profiles., *Vadose Zone Journal*, *3*, 278–287, 2004.

Sams, M., J. Neep, M. Worthington, and M. King, The measurement of velocity dispersion and frequency-dependent intrinsic attenuation in sedimentary rocks, *Geophysics*, *62*, 1456–1464, 1997.

Schytt, V., Notes on glaciological activities in Kebnekaise, Sweden during 1965, *Geografiska Annaler*, *48*, 43–50, 1966.

Schytt, V., Notes on glaciological activities in Kebnekaise, Sweden during 1966 and 1967, *Geografiska Annaler*, *50*, 111–120, 1968.

Sheriff, R. E., and L. P. Geldart, *Exploration Seismology., 2nd Edition*, Cambridge University Press, Cambridge, 1995.

Smith, A., Subglacial bed properties from normal-incidence seismic reflection data, *J. Environ. Eng. Geophys.*, *12*, 313, 2007.

Smith, A. M., Basal conditions on Rutford Ice Stream, West Antarctica, from seismic observations., *Journal of Geophysical Research*, *102*, 543–552, 1997.

Smith, A. M., T. Murray, K. W. Nicholls, K. Makinson, G. Adalgeirsdottir, A. Behar, and D. G. Vaughan, Rapid erosion and drumlin formation observed beneath a fast-flowing Antarctic ice stream., *Geology*, *35*, 127–130, 2005.

Smith, B. M. E., and S. Evans, Radio echo sounding: Absorption and scattering by water inclusion and ice lenses., *Journal of Glaciology*, *11*, 133–146, 1972.

Solomon, S., et al., *Technical Summary. In: Climate Change 2007: The Physical Science Basis. Contribution of Working Group I to the Fourth Assessment Report of the Intergovernmental Panel on Climate Change [Solomon, S., D. Qin, M. Manning, Z. Chen, M. Marquis, K.B. Averyt, M. Tignor and H.L. Miller (eds.)]*, Cambridge University Press, Cambridge, UK and New York, NY, USA, 2007.

Spencer, T., C. Edwards, and J. Sonnan, Seismic-wave attenuation in nonresolvable cyclic stratification, *Geophysics*, *47*, 16–24, 1982.

Spetzler, H., and D. Anderson, The effect of temperature and partial melting on velocity and attenuation in a simple binary system, *Journal of Geophysical Research*, *73*, 6051–6080, 1968.

Spetzler, J., and R. Snieder, The Fresnel volume and transmitted waves, *Geophysics*, *60*, 653–663, 2004.

Stuart, G., T. Murray, N. Gamble, K. Hayes, and A. Hodson, Characterization of englacial channels by ground-penetrating radar: An example from austre Brøggerbreen, Svalbard, *Journal of Geophysical Research*, *108*, doi:10.1029/2003JB002,435, 2003.

Suter, S., M. Laternser, W. Haeberli, R. Frauenfelder, and M. Hoezle, Cold firn and ice of high-altitude glaciers in the Alps: measurements and distribution modelling, *Journal of Glaciology*, *47*, 85–96, 2001.

Telford, W., L. Geldart, and R. Sheriff, *Applied geophysics*, Cambridge University Press, Cambridge, UK, 1990.

Toksöz, M., and D. Johnston, *Seismic wave attenuation*, SEG Geophysical Reprint Series, Tulsa: Society of Exploration Geophysics, 1981.

Toksöz, M., D. Johnston, and A.Timur, Attenuation of sesimic waves in dry and saturated rocks, i: Laboratory measurements, *Geophysics*, *44*, 681–690, 1979.

Toms, J., T. M. Müller, and B. Gurevich, Seismic attenuation in porous rocks with random patchy saturation, *Geophysical Prospecting*, *55*, 671–678, 2007.

Tonn, R., The determination of the seismic quality factor Q from VSP data: a comparison of different computational method, *Geophysical Prospecting*, *39*, 1–27, 1991.

Topping, J., *Errors observation and their treatment.*, Chapman and Hall, Science Paperbacks, London, 1972.

Vallon, M. J., J. Petit, and B. Fabre, Study of an ice core the the bedrock in the accumulation zone of an alpine glacier, *Journal of Glaciology*, *17*, 13–28, 1976.

van der Wal, R. S. W., W. Boot, M. R. van der Broeke, C. J. P. P. Smeets, C. H. Reijmer, and J. Oerlemans, Large and rapide melti-induced velocity changes in the ablation zone of the Greenland Ice Sheet, *Science*, *321*, 111–113, 2008.

Vaughan, D., and C. Doake, Recent atmospheric warming and retreat of ice shelves on the Antarctic Peninsula, *Nature*, *379*, 328–331, 1996.

Vincent, C., E. LeMeur, D. Six, P. Possenti, E. Lefebvre, and M. Funk, Climate warming revealed by englacial temperatures at Col du Dôme (4250 m, Mont Blanc area), *Geophysical Research Letters*, *34*, doi:10.1029/2007GL029,933, 2007.

Walford, M., M. Jennett, and P. Holmlund, Interpretation of radio-echoes from Storglaciären, Sweden., *Journal of Glaciology*, *35*, 39–49, 1986.

Wang, Y., Quantifying the effectiveness of stabilised inverse Q filtering, *Geophysics*, *68*, 337–345, 2003.

West, J., and S. Truss, Borehole time domain reflectometry in layered sandstone: Impact of measurement technique on vadose zone process identification, *Journal of Hydrology*, *319*, 143–162, 2006.

West, L., D. Rippin, T.Murray, H. Mader, and B. Hubbard, Dielectric permittivity measurements on ice cores: implications for interpretation of glacial unfrozen water content, *Journal of Environmental and Engineering Geophysics*, *12*, 37–45, 2007.

Westphal, J., In situ attenuation measurements in glacial ice., *Journal of Geophysical Research*, *70*, 1949–1853, 1965.

Winkler, K., and A. Nur, Seismic attenuation: Effect of pore fluids and frictional sliding, *Geophysics*, *47*, 1–14, 1982.

Zwally, H. J., W. Abdalati, T. Herring, K. Larson, J. Saba, and K. Steffen, Surface melt-induced acceleration of Greenland ice-sheet flow, *Science*, *297*, 218–222, 2002.